Towards *ab initio* assisted materials design: DFT based thermodynamics up to the melting point

Dissertation
zur Erlangung des akademischen Grades
Doktor der Naturwissenschaften (Dr. rer. nat.)
vorgelegt dem
Department Physik der Fakultät für Naturwissenschaften
an der Universität Paderborn

Blazej Grabowski

Promotionskommission
Vorsitzender   Prof. Dr. phil. Klaus Lischka
Gutachter   Prof. Dr. rer. nat. Wolf Gero Schmidt
Gutachter   Prof. Dr. rer. nat. Jörg Neugebauer

Tag der Einreichung: 20. Oktober, 2009
Tag der mündlichen Prüfung: 08. Dezember, 2009

To Anna, Maximilian, Christoph, Barbara, and Stanislaw.

Acknowledgments

Abstract

Metals are ubiquitous in numerous aspects of our lives, due to the possibility of adjusting their properties to a wide range of technological needs (light-weight, high-strength, durability, etc.). The ability to provide such a large variability in metallic properties is based on a profound knowledge gathered over centuries of research. One might, therefore, be tempted to consider the task of metal research as being completed in general. This is however by far not the case. The reason is the tremendous complexity of such materials at microscopic scales, which is actually the origin of their versatility. This complexity is still poorly understood and most traditional approaches are facing fundamental difficulties in providing further progress.

A very recent approach to enable further progress is so called *ab initio* methods. Their basic idea is to start the materials description directly at the electronic scale, in contrast to many traditional approaches which focus on the meso-/macroscopic scale. The key advantage of *ab initio* methods is their derivation from universal quantum mechanical laws which allow, in principle, to fully incorporate the complexity inherent to metallic materials. The actual application of these methods faces serious challenges: (i) A direct quantum mechanical solution is not feasible and approximations are unavoidable. For instance, the density functional theory (DFT), a particularly successful *ab initio* approach, relies in practical applications on the so called exchange-correlation functional, which cannot be systematically improved. (ii) Despite various approximations, *ab initio* calculations are computationally highly demanding and the development of advanced simulation techniques is needed. (iii) Typically, only $T = 0$ K conditions are considered and the extension to finite temperatures – crucial for metals – is related to even larger CPU requirements.

The general objective of the present work is to address various aspects related to these challenges. For that purpose, a systematic and with respect to numerical accuracy fully controlled DFT study of thermodynamic properties for an extensive set of metals is provided. A special focus is on the assessment of the predictive power of present day's exchange-correlation functionals and on the influence of temperature in the full temperature window from zero Kelvin up to the melting point. We study in detail the central thermodynamic quantity, the free energy surface, and show that a high quality prediction of its temperature and volume dependence is crucial to guarantee an unbiased description of derived materials properties. This turns out to be particularly challenging at high temperatures due to the fact that the numerical/controllable errors propagate in a strongly increasing fashion with temperature. We therefore developed and applied a set of novel approaches going significantly beyond previous studies: 1) A method to efficiently assess the controllable errors in all relevant free energy contributions and to reduce them to a few meV/atom even at the highest temperatures. 2) A hierarchical coarse graining scheme to efficiently determine the anharmonic free energy contribution, which accounts for the atomic interaction beyond the simple analytic harmonic description and which therefore usually represents a formidable computational challenge. 3) A general and intuitive treatment of the free energy contribution due to point defects from which the standard approaches can be easily derived as approximations.

Our methods can be applied to resolve long standing uncertainties about physical mechanisms such as, e.g., the evaluation of the effects eventually leading to the transition from the solid to the liquid phase. One of these decisive problems, which remained unresolved for over 90 years, is the detailed balance of contributions to the heat capacity of a metal before melting. Investigating the example of aluminum in detail, our approach allowed for the first time an accurate quantification of all relevant excitation mechanisms and thus to settle a long standing debate. These findings indicate that the methods developed and applied in this study represent an important step towards the general goal of a materials design solely on the computer.

Contents

Chapter 1

Motivation: *Ab initio* assisted metals design

1.1 General ideas and philosophy

The ever ongoing demand for increasing performance, quality, and price reduction of steel and other metals has lead to a change in the philosophy of designing such materials. Traditionally, metals were designed based on physical understanding derived from the mesoscopic and macroscopic scale (top-down approaches). A wide range of elaborated methods has been developed (e.g. Refs. [1, 2]) over the past decades allowing to perform efficient and accurate macroscopic simulations, for instance to simulate a car crash. Despite their advantages and successes, there are however fundamental difficulties in using top-down approaches: Their application often requires expensive or partly even inaccessible experimental input and they need to be re-derived for each material class anew. Rather recently, an alternative approach has therefore attracted a lot of attention in metals design. The key idea is to start from the same fundamental principles as nature does which amounts to describing the interaction between electrons and nuclei, the basic constituents of any material, using quantum mechanics (bottom-up approach). The basis for these bottom-up approaches are so called *ab initio* methods, the Latin term for *from the beginning*, and their crucial advantage is that they, in principle, allow reliable predictions without the need of any experimental input.

In various branches of the metals science community, the *ab initio* approach is expected to be the future key to a large variety of metals science issues as the following selected expert statements may illustrate: "Conventional materials design hits upon its limits for the newly developed high manganese steels. We need to understand the atomistic interactions among the various alloying elements to predict ordered and defect structures which affect the mechanical properties." (Prof. W. Bleck [3]) – "Mesoscopic models need energetic and kinetic data which is practically not accessible by experiment. Examples are interface energies of metastable phases or mobilities in multicomponent systems. *Ab initio* is the unrivaled approach capable of providing such data." (Prof. G. Gottstein [4]) – "In designing and optimizing new steels, it is often helpful to decompose the complex processes into sub processes and to understand each independent of the others. For such purposes, *ab initio* methods become increasingly important, since they allow to perform 'virtual' experiments. A prominent example is the study of hydrogen behavior in metals." (Dr. H.-P. Schmitz [5]) – "We need modeling approaches taking advantage of the new *ab initio* methods, in order to support specific material data acquisition for an understanding of physically based models. This will facilitate a faster development of such models and make them applicable to conventional fabrication routes of semi-finished high quality aluminum products made from more recycling friendly alloys." (Prof. J. Hirsch [6]).

Let us discuss one specific example in more detail: the application of *ab initio* methods as a tool to provide input parameters to meso/macroscopic approaches. We focus hereby in particular on the so called CALPHAD approach [7]. The CALPHAD approach is a widely used method in materials design for predicting phase diagrams as a function of temperature and concentration for multi-component materials. Such phase diagrams are fundamental tools for engineers when determining processing routes (road maps [8]) to design materials. An important difficulty related to the typical CALPHAD approach is however the fact that it requires experimental input. The reason is an often challenging and expensive sample preparation and the necessity of high precision measurements. Further, from a principle point of view, some necessary input (e.g., energetics of metastable phases) is missing due to the lack of corresponding samples. The *ab initio* approach constitutes therefore a very promising possibility to provide the missing experimental data [9]. Further, it would also provide a reference to evaluate the physical concepts that enter the interpolation formulas used in CALPHAD (e.g., with respect to stacking fault energies or magnetism).

The quantum mechanical and electrostatical concepts, upon which *ab initio* approaches are based, are well established and have been verified in numerous experimental studies (see e.g. the collection in Ref. [10]). Therefore, at energy scales relevant for materials science, any such problem could be in principle solved by applying the *ab initio* concept. However, a direct solution of the underlying quantum mechanical equation – the Schrödinger equation – would be restricted to a few electrons. This is a serious limitation since realistic materials science problems require the description of a huge number of nuclei ($\approx 10^{23}$ in one cubic centimeter) with each having up to a hundred electrons. In order to make an application of *ab initio* techniques nonetheless feasible, a combination of numerically highly efficient methods and various physically justified approximations is indispensable. The development and falsification of these methods and approximations cannot be performed by tackling directly such complex problems as mentioned above (multicomponent systems, non-periodic structures, metastable phases) where *ab initio* is expected to **predict** properties. It is mandatory to address these challenges first for simple materials systems and problems for which sufficient experimental data are available which can be used to **falsify** the developments and approximations. The general goal of the present study is to address the latter issue.

1.2   Goals of the present work: Achievable accuracy and efficiency

There are various *ab initio* approaches available,[1] out of which one is exceptionally well suited for the application to metals: the density functional theory (DFT [12]; introduced in detail in Sec. 2.1). For that reason, the focus of the present study is on DFT based *ab initio* calculations. In general, DFT assisted metals design faces the following challenges:

A. *Extension to finite temperatures.*
   Originally, DFT has been designed and applied as a ground state theory and therefore the directly accessible materials properties refer to $T = 0$ K. For realistic simulations, in particular for metals, the extension to finite temperatures is necessary. Calculating materials properties at finite temperatures results however in a large increase in computational effort. This is due to the dramatically increased number of accessible microscopic configurations as compared to $T = 0$ K. In fact, calculating finite temperature properties is only feasible using statistical approaches. Therefore, the development and improvement of the combination of DFT and statistical approaches is crucial.

---

[1]The existing *ab initio* approaches can be roughly grouped into density functional theory based, Hartree-Fock based, and quantum Monte Carlo based [11].

B. *Assessment of the systematic error.*
   Formally, DFT is an exact theory. In practice however, the so called exchange-correlation (xc) functional (see Sec. 2.1.6) needs to be approximated, since the exact functional, mathematically proven to exist, is not known. This approximation causes an unknown systematic error, because there exists no practical approach to systematically improve the accuracy of the xc functional. It is therefore necessary to systematically assess the achievable accuracy of calculated materials properties.

C. *Assessment of controllable errors.*
   Any practical realization of DFT is based on a set of specific parameters. These parameters control for instance how formally infinite sums or continuous integrals are mapped onto practical finite sums and discrete integrals. There is no principle difficulty arising from this mapping since the introduced errors can always be controlled by scanning the corresponding parameter space, even though at an increased computational cost. In actual calculations however, the assessment of these controllable errors is rarely done when it comes to finite temperature calculations (challenge A) which themselves require highly increased computational resources. A challenge is therefore to develop a detailed understanding of the dependence of the controllable errors on the various parameters for finite temperature properties. This will allow to devise optimum parameters, i.e., the ones yielding the desired accuracy with lowest computational cost.

The present thesis aims at tackling several aspects of these challenges. For that purpose and according to the philosophy introduced in Sec. 1.1, we focus on the thermodynamics of simple – i.e., elementary and non-magnetic – metals, which are experimentally well investigated. In particular, we employ a hierarchical scheme, in order to study the various excitation mechanisms contributing to the equilibrium thermodynamic properties. This scheme is illustrated in Fig. 1.1 and its key steps (levels) are:

I. The basis of the present thesis is a systematic study of the two dominating excitation mechanisms (challenge A): the electronic and the quasiharmonic one. A key point distinguishing these investigations from previous ones is the large and comparable set of investigated metals and the wide range of studied thermodynamic properties. Moreover, we perform all calculations using two complementary xc functionals (challenge B) and put special emphasis on numerically highly converged thermodynamic properties with an assessment of the remaining numerical error (challenge C). As a further special feature, we provide a systematic comparison of DFT results with data obtained using the CALPHAD method discussed in Sec. 1.1. We focus hereby on the key quantity of the CALPHAD approach: the free energy at constant pressure.

II. Based on the results from LEVEL I, two representative elements are identified, for which the quasiharmonic calculations are extended beyond the conventionally applied scheme by including the explicit dependence on the electronic temperature. Typically, also the corresponding theoretical background is not treated and we therefore present a discussion of the necessary formalism (Sec. 2.1.3) and its implementation (Sec. 3.3.4). These developments eventually allow to calculate the phonon shift due to electronic temperature and further to investigate its influence on thermodynamic properties.

III. On LEVEL III of the hierarchy, the excitation spectrum is further extended such as to include all relevant mechanisms contributing to thermodynamic properties of the studied elements. The additionally included contributions, the explicitly anharmonic and the vacancy
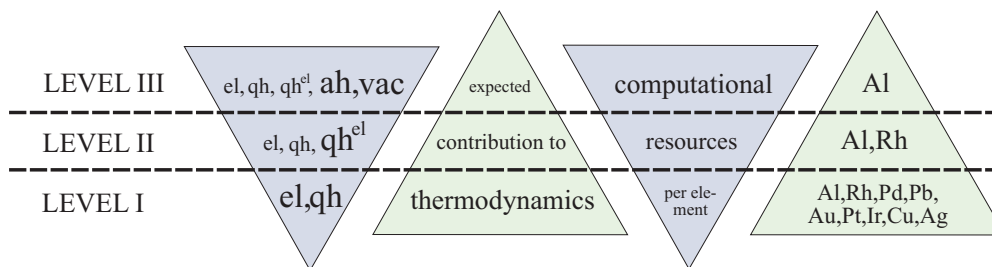
Figure 1.1: Schematic illustration of the hierarchical approach to thermodynamic properties employed in the present thesis. As shown by the first (from left) triangle the number of considered excitation mechanisms increases with the level. The abbreviations stand for: el=electronic, qh=quasiharmonic, qh^{el}=qh + the influence of electronic temperature (cf. Sec. 3.3.4), ah=explicitly anharmonic, and vac=vacancies. At each level the newly included contributions are emphasized by a larger fontsize. The second triangle indicates the expected contribution of the newly included excitations to thermodynamic properties and the third triangle the corresponding CPU requirements. The last triangle shows the elements considered at each level.

one, constitute a tremendous theoretical challenge: For instance, a molecular dynamics based calculation of the anharmonic part of the free energy would necessitate computational time in the range of several CPU years when using standard methods even on high performance computers (challenge A). In order to make such a study nonetheless feasible, we have developed a fully DFT based coarse graining technique in configuration space and succeeded in reducing the number of configurations from 10^6 to a few hundreds at the highest and thus computationally most expensive level. Using this approach we were able to guarantee a numerical accuracy of better than 1 meV/atom (challenge C) - remaining errors can thus be exclusively related to the xc functional (challenge B). As will be discussed in Sec. 2.3.5, it is useful to reconsider the anharmonicity calculations using complementary methods, which include quantum mechanical effects. In order to estimate the resulting corrections, we have calculated the anharmonic phonon shift in aluminum using quantum mechanical perturbation theory up to fourth order.

The methods developed and applied within this hierarchical scheme provide a complete description of all physically relevant contributions to the free energy of a non-magnetic elementary metal. Based on this knowledge we can computationally address key questions of materials design. For example, the highly accurate approach will allow us to tackle a long standing debate about the dominating physical mechanisms determining the isobaric heat capacity of aluminum close to the melting point. Furthermore, the obtained DFT results provide a sound basis for evaluating theoretical approaches for larger scale applications. For example, inter-atomic potentials such as the embedded atom method (EAM) are widely applied for finite temperature properties of several million atoms, although they are designed by fitting to a limited range of usually temperature independent data. Based on the complete set of DFT calculated excitation mechanisms for aluminum, we will therefore perform a detailed evaluation of the quality of three state-of-the-art EAM parametrizations. The examples chosen in this study shall demonstrate the capability of DFT based thermodynamics to open new and exciting routes towards an *ab initio* assisted materials design.

Chapter 2

Theoretical background

A key objective of this thesis is to identify and develop efficient *ab initio* approaches to predict materials properties at finite temperatures. For that purpose, concepts from thermodynamics, statistics, and quantum mechanics need to be combined. One of the central quantities in thermodynamics is the free energy surface $F(V, T)$ as a function of volume V and temperature T. It is a thermodynamic potential and therefore fully determines all thermodynamic properties, for example the isobaric heat capacity $C_P(T)$ ($P =$ pressure) or the adiabatic bulk modulus $B_S(T)$ ($S =$ entropy):

$$C_P(T) = -T \left(\frac{\partial^2 F(V, T)}{\partial T^2} \right)_{V,P}, \qquad B_S(T) = V \left(\frac{\partial^2 F(V, T)}{\partial V^2} \right)_{T,S}. \tag{2.1}$$

According to statistical physics, F is fully determined by the partition function Z according to

$$F(V, T) = -k_\mathrm{B} T \ln Z(V, T), \tag{2.2}$$

where k_B is the Boltzmann constant, and

$$Z(V, T) = \sum_\xi e^{-\beta E_\xi(V)}, \tag{2.3}$$

with $\beta = (k_\mathrm{B} T)^{-1}$. In Eq. (2.3), E_ξ is the volume dependent but temperature independent ξth energy level of the considered system. The sum runs over all such energy levels including possible degeneracies. These energies can be fully determined using the concepts of quantum mechanics.

The detailed determination of the E_ξ and subsequently of F for realistic solid state materials uses an involved apparatus of numerous methods developed over the past decades. A schematic overview illustrating the task to be accomplished and the relation of various key concepts is given in Fig. 2.1. The remainder of this chapter and Chap. 3 address the various parts of Fig. 2.1 in detail.

2.1 From quantum mechanics to density functional theory

2.1.1 Motivation

The basic quantum mechanical principles are: The motion and interaction of microscopic particles (electrons and nuclei in the present case) cannot be described/predicted on an individual basis. Their behavior can be only captured in a statistical fashion, i.e., based on probabilities for ensembles of particles. The probabilities can be described by wave mechanics, which accounts for the observed
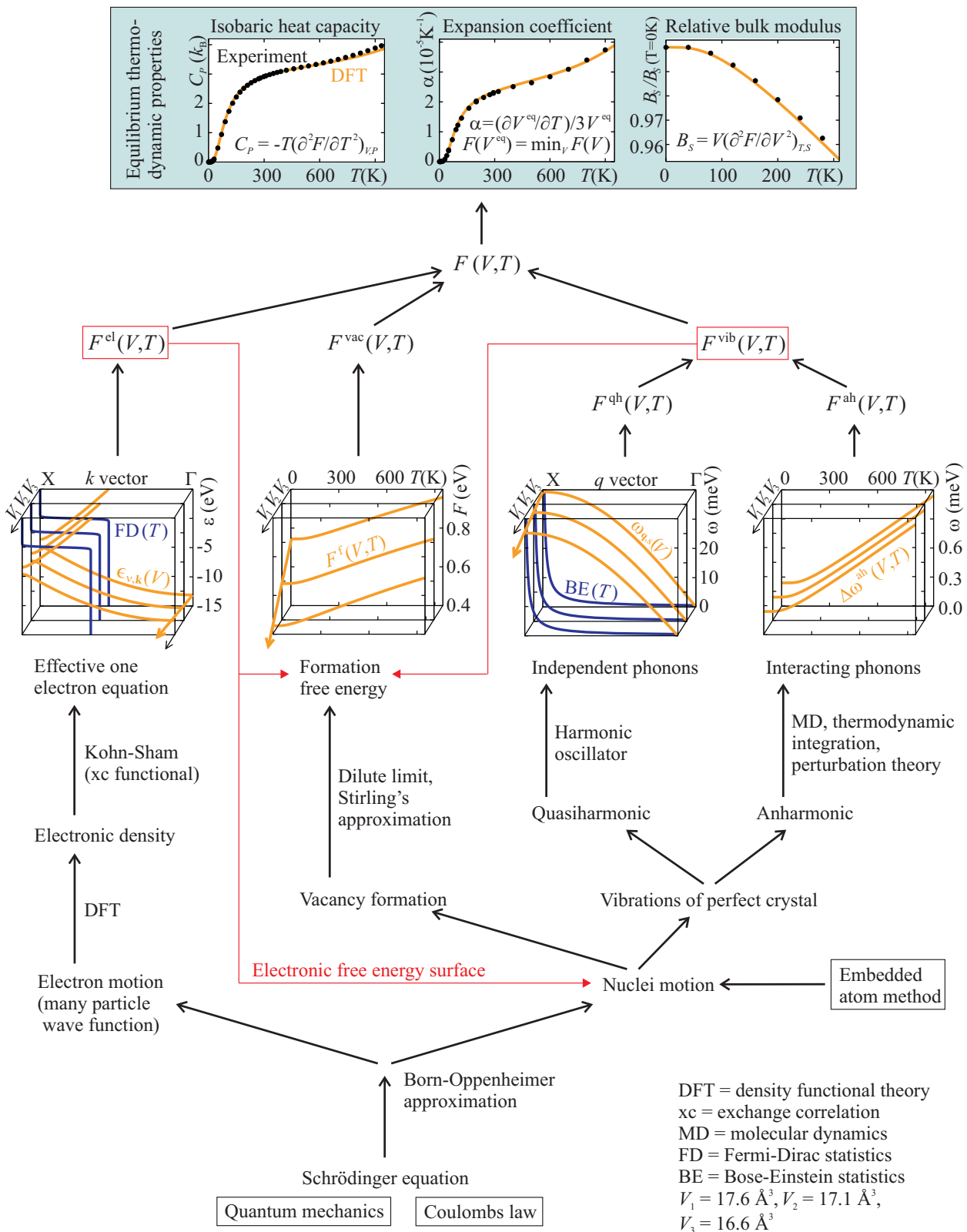
Figure 2.1: Schematic visualization of the *ab initio* approach that is developed in this thesis and employed to derive equilibrium thermodynamic properties of non-magnetic elementary metals. The plotted data are for aluminum and highlight some of the results of this work. Experimental values are from Refs. [13], [14], and [15], for C_P, α, and B_S, respectively. The various expressions and symbols will be defined in this and the following chapter, except for F^{vib} which denotes the vibrational free energy and which is defined only here for the purpose of a convenient representation.

interference phenomena and the impossibility of localization. These principles are embodied in the Schrödinger equation, which additionally incorporates Coulomb's law. We are interested only in equilibrium properties here, for which it is sufficient to consider the time independent Schrödinger equation:

$$\hat{H}\Psi_\xi = E_\xi\Psi_\xi. \tag{2.4}$$

Here, the E_ξ are the energy levels entering Eq. (2.3). Further, $\Psi_\xi = \Psi_\xi(\{\mathbf{r}_i\}, \{\mathbf{R}_I\})$ is the many-body wave function of the ξth energy depending on the set of electronic coordinates $\{\mathbf{r}_i\}$, where i runs over all electrons in the system, and on the set of nuclei coordinates $\{\mathbf{R}_I\}$ with I running over all nuclei. The Ψ_ξ contain the full information about the system and they must obey the fundamental requirement of antisymmetry with respect to the interchange of electrons which are identical particles (fermions)

$$\Psi_\xi(\mathbf{r}_1,\dots,\mathbf{r}_i,\dots,\mathbf{r}_j,\dots,\mathbf{r}_{N_e},\{\mathbf{R}_I\}) = -\Psi_\xi(\mathbf{r}_1,\dots,\mathbf{r}_j,\dots,\mathbf{r}_i,\dots,\mathbf{r}_{N_e},\{\mathbf{R}_I\}), \tag{2.5}$$

where N_e is the number of electrons. In principle, also nuclei of the same species are identical particles and would need to obey either a symmetry or antisymmetry condition depending on the number of fermions they are composed of [16]. In crystals however, the motion of the nuclei is fixed to the vicinity of their crystallographic positions and this renders the nuclei distinguishable. Further in Eq. (2.4), $\hat{H}$ is the Hamilton operator given by:

$$\hat{H} = \hat{T}^{\mathrm{el}} + \hat{T}^{\mathrm{nuc}} + \hat{V}^{\mathrm{el}} + \hat{V}^{\mathrm{nuc}} + \hat{V}^{\mathrm{e\text{-}n}}. \tag{2.6}$$

The operators on the right are the kinetic energy for the electrons (nuclei) $\hat{T}^{\mathrm{el}}$ ($\hat{T}^{\mathrm{nuc}}$), the electron-electron repulsion $\hat{V}^{\mathrm{el}}$, the nucleus-nucleus repulsion $\hat{V}^{\mathrm{nuc}}$, and the electron-nucleus attraction $\hat{V}^{\mathrm{e\text{-}n}}$ given by:

$$\hat{T}^{\mathrm{el}}(\{\mathbf{r}_i\}) = -\sum_i^{N_e} \frac{\hbar^2}{2m_e}\nabla_i^2, \tag{2.7}$$

$$\hat{T}^{\mathrm{nuc}}(\{\mathbf{R}_I\}) = -\sum_I^{N_n} \frac{\hbar^2}{2M_I}\nabla_I^2, \tag{2.8}$$

$$\hat{V}^{\mathrm{el}}(\{\mathbf{r}_i\}) = \frac{1}{2}\sum_i^{N_e}\sum_{j\neq i}^{N_e} \frac{e^2}{4\pi\epsilon_0|\mathbf{r}_i - \mathbf{r}_j|}, \tag{2.9}$$

$$\hat{V}^{\mathrm{nuc}}(\{\mathbf{R}_I\}) = \frac{1}{2}\sum_I^{N_n}\sum_{J\neq I}^{N_n} \frac{Z_I Z_J e^2}{4\pi\epsilon_0|\mathbf{R}_I - \mathbf{R}_J|}, \tag{2.10}$$

$$\hat{V}^{\mathrm{e\text{-}n}}(\{\mathbf{r}_i\},\{\mathbf{R}_I\}) = -\sum_i^{N_e}\sum_I^{N_n} \frac{Z_I e^2}{4\pi\epsilon_0|\mathbf{r}_i - \mathbf{R}_I|}. \tag{2.11}$$

Here, $\hbar$ is the reduced Planck constant, m_e the electron mass, e the elementary charge, ϵ_0 the electric constant, N_n the number of nuclei, and M_I (Z_I) the mass (proton number) of nucleus I. At this point, the *ab initio* problem is fully defined: Only known fundamental constants enter the various formulas and thus a unique solution of Eq. (2.4) could in principle be obtained. However, the numerical effort to directly solve Eq. (2.4) is not practical even for systems with a few electrons. In order to illustrate this in a bit more detail, we show how one could proceed in solving it numerically.

   Let us sketch the procedure for a simple system consisting of one nucleus at $\mathbf{R}$, containing one proton, and of one electron at $\mathbf{r}$, i.e., the hydrogen atom: First, we need to construct a box

around the atom, realized by energetic barriers, to fix the atom in space. The box needs to be large enough to capture the relevant physics, which is technically ensured by converging its size. A reasonable box size for the present problem is $20\,a_0$ [17] ($a_0 := 1$ Bohr radius ≈ 0.05 nm). Next, we need to discretize the box introducing another convergence parameter, the corresponding mesh which we assume here for simplicity to be equidistant. A reasonable mesh distance is $0.1\,a_0 =: \delta$ [17] yielding a mesh of $200^3 = 8 \cdot 10^6 =: N_{\mathrm{mesh}}^3$. The possible positions of the electron and the nucleus are thus $\mathbf{r} = \delta(x, y, z)$ and $\mathbf{R} = \delta(x', y', z')$ with x, y, z, x', y', and z' integers each running over $1 \ldots N_{\mathrm{mesh}}$. The wave function becomes in the discrete case a vector indexed by all possible configurations the system can assume: $\Psi_{x,y,z,x',y',z'}$, i.e., a vector of size $(N_{\mathrm{mesh}}^3)^2$ (for convenience, we drop the index ξ on Ψ in this example). The Hamilton operator becomes a quadratic matrix, $\mathbf{H}$, of size $(N_{\mathrm{mesh}}^3)^2 \times (N_{\mathrm{mesh}}^3)^2$ with rows and columns indexed accordingly. The attractive electron-nucleus term, the only Coulomb term for the hydrogen atom, affects only the diagonal elements of the matrix contributing a term proportional to $1/|(x, y, z) - (x', y', z')|$. To render the infinite value occurring for $(x, y, z) = (x', y', z')$ finite, an infinitesimal parameter can be added to the denominator. The kinetic energy operators can be, for the present purpose, approximated by the central finite difference

$$\nabla_x^2 \Psi_{x,y,z,x',y',z'} \approx \frac{1}{\delta^2} \left(\Psi_{x+1,y,z,x',y',z'} - 2\Psi_{x,y,z,x',y',z'} + \Psi_{x-1,y,z,x',y',z'} \right),$$

$$\nabla_y^2 \Psi_{x,y,z,x',y',z'} \approx \frac{1}{\delta^2} \left(\Psi_{x,y+1,z,x',y',z'} - 2\Psi_{x,y,z,x',y',z'} + \Psi_{x,y-1,z,x',y',z'} \right), \tag{2.12}$$

and so on for z, x', y' z'. Equation (2.12) makes clear that the kinetic energy operator is non-local in the chosen real space representation. In this approximation, it contributes a finite value to all neighboring sites at $x - 1$, $x + 1$, $y - 1$, and so on, and thus makes the Hamilton matrix $\mathbf{H}$ non-diagonal, e.g.,

$$\begin{aligned}
H_{x,y,z,x',y',z';\, x-1,y,z,x',y',z'} &= -\hbar^2/(2m_e\delta^2), \\
H_{x,y,z,x',y',z';\, x,y,z,x'-1,y',z'} &= -\hbar^2/(2M\delta^2),
\end{aligned} \tag{2.13}$$

(M: proton mass). Having constructed $\mathbf{H}$, the solution of the discretized Schrödinger equation is obtained by diagonalizing $\mathbf{H}$, i.e., by solving its eigenvalue equation. In principle, this is a standard algebraic problem for a sparse matrix, however, for a matrix of extremely huge size: $(N_{\mathrm{mesh}}^3)^2 \times (N_{\mathrm{mesh}}^3)^2 = 64 \cdot 10^{12} \times 64 \cdot 10^{12}$. The currently largest manageable eigenvalue problems[1] are performed on matrix sizes in the range of $10^{12} \times 10^{12}$. Thus, the matrix of the electron-nucleus problem is in the range of technically diagonalizable matrices provided one employs today's world's highest performance algorithms and computer hardware.

For a general problem, the Hamilton matrix will have the schematic form given in Fig. 2.2 and its size s will scale as:

$$s(N_{\mathrm{mesh}}^3, N_e, N_n) = (N_{\mathrm{mesh}}^3)^{N_e+N_n} \times (N_{\mathrm{mesh}}^3)^{N_e+N_n}. \tag{2.14}$$

It is clear that, for any problem larger than the hydrogen atom, a direct solution is not practical in the next decades even if we assume that Moore's law will continue to hold. For instance, if we consider only a single aluminum atom, the atom with the smallest number of electrons ($N_e = 13$) out of the studied elements, the matrix size (for the same box size) is $s(N_{\mathrm{mesh}} = 200, N_e = 13, N_n = 1) \approx 10^{96} \times 10^{96}$.

---

[1]Such eigenvalue problems are performed by Internet search engines [18]. The matrix size is determined by the number of web pages available in the Internet, which was $\approx 10^{12}$ in 2008 [19]. However, strictly speaking, in these algorithms only the lowest eigenvalue is determined (using the so called power method) rather than the full eigenvalue problem [20].
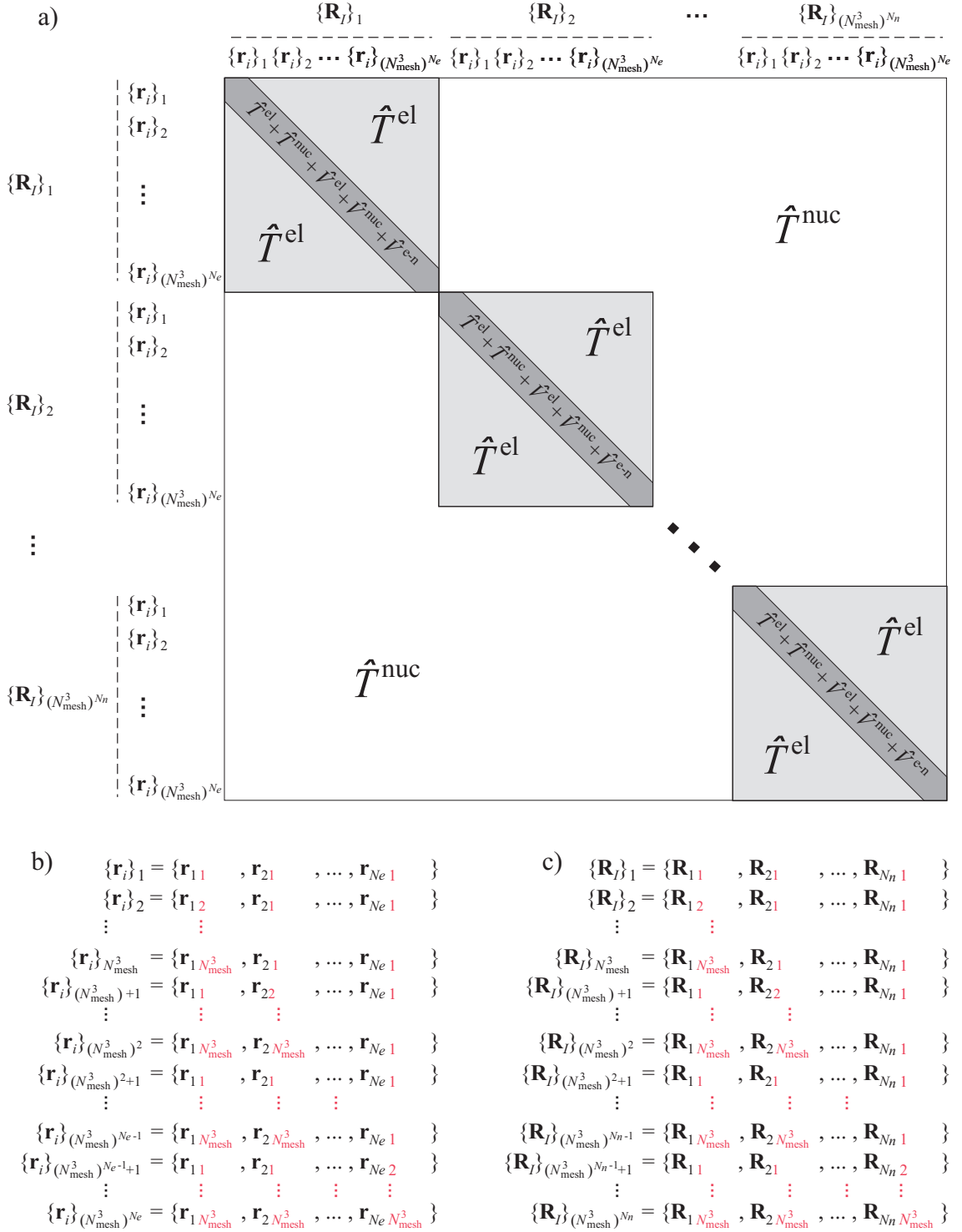
Figure 2.2: a) Schematic visualization of the Hamiltonian matrix for a system of N_e electrons, with coordinates $\{\mathbf{r}_i\}$, and N_n nuclei, with coordinates $\{\mathbf{R}_I\}$, discretized onto a $N_{\mathrm{mesh}} \times N_{\mathrm{mesh}} \times N_{\mathrm{mesh}}$ mesh. The rows and columns are indexed by the possible microscopic configurations of the system enumerated as shown in b) and c). On the right hand side of the equations in b) and c) the black index runs over the electrons and nuclei, respectively, while the red index runs over the mesh. In a), the dashed lines indicate that the nuclei configuration is the same for all electronic configurations captured by the line. Further, the placement of the operators indicates which part of the matrix is affected. For instance, $\hat{T}^{\mathrm{el}} + \hat{T}^{\mathrm{nuc}} + \hat{V}^{\mathrm{el}} + \hat{V}^{\mathrm{nuc}} + \hat{V}^{\mathrm{e\text{-}n}}$ affects only the dark shaded diagonal of the matrix.

Table 2.1: Electron mass, m_e, to nucleus mass, M_I, ratio for the studied elements ($I =$ Al, Cu, ...). Additionally, the actual values for the off diagonal elements within the central finite difference method are shown. Note that in the first column we set $M_I = m_e$ for comparison. The mesh distance is $\delta = 0.1\,a_0$.

M_I	m_e	M_{Al}	M_{Cu}	M_{Rh}	M_{Pd}	M_{Ag}	M_{Ir}	M_{Pt}	M_{Au}	M_{Pb}
m_e/M_I (10^{-6})	—	20.3	8.6	5.3	5.2	5.1	2.9	2.8	2.8	2.6
$\frac{-\hbar^2}{2M_I\delta^2}$ (meV)	$-1.3 \cdot 10^6$	-27.7	-11.7	-7.3	-7.0	-6.9	-3.9	-3.8	-3.8	-3.6

A complete solution is, however, not needed to obtain accurate results. Numerous approximations have been developed which allow a numerically efficient treatment capturing the important physics. A major role is played hereby by the Born-Oppenheimer approximation, which decouples the electron and nucleus motion, and by density functional theory which removes the dependence of s on N_e. These concepts are introduced in the following.

2.1.2 Born-Oppenheimer approximation

Inspection of Eqs. (2.7) and (2.8) reveals that the kinetic energy operators for the electrons and nuclei differ by a factor of m_e/M_I. Tab. 2.1 shows this factor and actual values using the central finite difference method for the studied elements. For the lightest element, aluminum, the off diagonal elements [Eq. (2.13)] produced by the nucleus kinetic energy are five orders of magnitude smaller than the off diagonal elements produced by the electron kinetic energy. Physically, this means that the electrons can follow the nuclei almost instantaneously and can therefore relax virtually to their ground state for each nuclei configuration on the time scale of atomic motion as given e.g. by atomic vibrations. This observation suggests that decoupling the motion of electrons and nuclei completely, i.e., accounting only for the electronic ground state at each nuclei configuration, will be a reasonable approximation. This is the essence of the Born-Oppenheimer approximation [21].

The formal introduction of the Born-Oppenheimer approximation is a three step procedure. In a first step, we define an auxiliary Hamilton operator by:

$$\hat{H}^{\mathrm{el}} \; := \; \hat{H} - \hat{T}^{\mathrm{nuc}} \; = \; \hat{T}^{\mathrm{el}} + \hat{V}^{\mathrm{el}} + \hat{V}^{\mathrm{nuc}} + \hat{V}^{\text{e-n}}. \tag{2.15}$$

We call $\hat{H}^{\mathrm{el}}$ an electronic Hamilton operator, because it contains only non-local terms in the electronic coordinates after subtracting $\hat{T}^{\mathrm{nuc}}$. The corresponding eigenvalue equation, the electronic Schrödinger equation, reads

$$\hat{H}^{\mathrm{el}} \, \psi_{\tilde{\nu}} = E_{\tilde{\nu}}^{\mathrm{el}} \, \psi_{\tilde{\nu}}, \tag{2.16}$$

where $\psi_{\tilde{\nu}} = \psi_{\tilde{\nu}}(\{\mathbf{r}_i\}, \{\mathbf{R}_I\})$ and $E_{\tilde{\nu}}^{\mathrm{el}}$ are the corresponding $\tilde{\nu}$'th eigenfunction and eigenvalue. An important observation is that a complete solution to Eq. (2.16) can be obtained by solving an eigenvalue equation for each nuclei configuration separately, which is due to the fact that $\hat{H}^{\mathrm{el}}$ corresponds to a block diagonal matrix. As a consequence, we can relabel the eigenvalues as $E_{\tilde{\nu}}^{\mathrm{el}} = E_{\nu}^{\mathrm{el}}(\{\mathbf{R}_I\})$ and the eigenfunctions as $\psi_{\tilde{\nu}}(\{\mathbf{r}_i\}, \{\mathbf{R}_I\}) = \psi_{\nu}(\{\mathbf{r}_i\}; \{\mathbf{R}_I\})$, with ν running only over the eigenfunctions for a fixed nuclei configuration and with the semicolon indicating that the set $\{\mathbf{R}_I\}$ is treated as a parameter.

In a second step, we reintroduce the kinetic energy operator of the nuclei by defining a nuclei

operator $\hat{H}_\nu^{\text{nuc}}$ as

$$\hat{H}_\nu^{\text{nuc}}(\{\mathbf{R}_I\}) \;=\; \hat{T}^{\text{nuc}}(\{\mathbf{R}_I\}) + \hat{1} E_\nu^{\text{el}}(\{\mathbf{R}_I\}), \tag{2.17}$$

where $\hat{1}$ is the identity operator. Similarly as $\hat{H}^{\text{el}}$, $\hat{H}_\nu^{\text{nuc}}$ is block diagonal, having only coupling terms in $\{\mathbf{R}_I\}$ but none in ν, and therefore its eigenfunctions Λ and eigenvalues E^{nuc} can be labeled by ν and an index μ running over all eigenfunctions for a fixed ν, i.e.:

$$\begin{aligned}
\hat{H}_\nu^{\text{nuc}}(\{\mathbf{R}_I\})\, \Lambda_{\nu,\mu}(\{\mathbf{R}_I\}) \;&= \\
\left[\hat{T}^{\text{nuc}}(\{\mathbf{R}_I\}) + \hat{1} E_\nu^{\text{el}}(\{\mathbf{R}_I\})\right] \Lambda_{\nu,\mu}(\{\mathbf{R}_I\}) \;&= \; E_{\nu,\mu}^{\text{nuc}}\, \Lambda_{\nu,\mu}(\{\mathbf{R}_I\}).
\end{aligned} \tag{2.18}$$

The key point of Eq. (2.18), called the nuclei Schrödinger equation, is that each of the E_ν^{el} describes a potential energy surface (PES) in which the nuclei move. Particularly, once ν has been fixed to some value, say $\nu = \nu'$, the nuclei move only in the potential energy surface given by $E_{\nu'}^{\text{el}}$ without changing to another E_ν^{el}.

The final step of the Born-Oppenheimer approximation is then to approximate the eigenvalues E_ξ of the original Schrödinger equation, Eq. (2.4), by the eigenvalues $E_{\nu,\mu}^{\text{nuc}}$, i.e.:

$$E_\xi \approx E_{\nu,\mu}^{\text{nuc}}. \tag{2.19}$$

As shown in Ref. [22], this approximation is equivalent to neglecting terms which couple the electronic wave functions ψ_ν to the nuclei wave functions $\Lambda_{\nu,\mu}$. These terms will be small and the approximation therefore reasonable when $m_e/M_I \ll 1$ as for the studied elements. Application of Eq. (2.19) decouples the original Schrödinger equation, Eq. (2.4), into two block diagonal eigenvalue equations, Eqs. (2.16) and (2.18), and the full problem scales therefore as:

$$s(N_{\text{mesh}}, N_e, N_n) \;=\; (N_{\text{mesh}}^3)^{N_n} \cdot \underbrace{\left[(N_{\text{mesh}}^3)^{N_e} \times (N_{\text{mesh}}^3)^{N_e}\right]}_{\substack{\text{Electronic Schrödinger eq.} \\ \text{for fixed nuclei coordinates}}} + \; (N_{\text{mesh}}^3)^{N_e} \cdot \underbrace{\left[(N_{\text{mesh}}^3)^{N_n} \times (N_{\text{mesh}}^3)^{N_n}\right]}_{\substack{\text{Nuclei Schrödinger eq.} \\ \text{for fixed electronic PES}}}.$$
$$\tag{2.20}$$

The symbolic notation, used here and frequently in the following to indicate the dimensions of a problem, is explained in App. A.1.1. Equation (2.20) means that the original problem represented by one large matrix, Eq. (2.14), has been transformed into various smaller matrix equations. The remaining smaller matrix equations are however still too large to be solved directly. The actual advantage of applying the Born-Oppenheimer approximation is that further approximations and reformulations can be performed for the electrons and nuclei *separately*.

In typical applications of the Born-Oppenheimer approximation a further approximation is implicitly performed. Out of the various potential energy surfaces, E_ν^{el}, only the energetically lowest one (denoted as E_g^{el}), i.e., the one corresponding to the electronic ground state at $T = 0$ K, is considered. Temperature dependence enters subsequently by determining the nuclei motion on E_g^{el}. Such an approach is however not fully correct since at finite temperatures the nuclei motion will be determined by the thermodynamic electronic ground state which corresponds to the minimal electronic free energy rather than by the $T = 0$ K electronic ground state E_g^{el} [23]. Put differently, the motion of the nuclei at some finite temperature will be determined by several E_ν^{el} and the specific contribution of each E_ν^{el} will be weighted according to the temperature. It is important to stress that this coupling of different E_ν^{el} is not contained in Eq. (2.18), it only enters when the E_ν^{el} are inserted into the partition function, Eq. (2.3). This fact is exploited in the next section.

2.1.3 Free energy Born-Oppenheimer approximation

In order to derive the dependence of the nuclei motion on the electronic free energy, we pursue the following strategy. We apply the Born-Oppenheimer approximation to the partition function and transform the latter such as to separate a sum over the electronic eigenvalues E_ν^{el} which we identify with the electronic free energy. Let us thus apply Eq. (2.19) and insert the $E_{\nu,\mu}^{\text{nuc}}$ into the partition function, Eq. (2.3),

$$Z = \sum_{\nu,\mu} e^{-\beta E_{\nu,\mu}^{\text{nuc}}} = \sum_\nu \left(\sum_\mu e^{-\beta E_{\nu,\mu}^{\text{nuc}}} \right), \tag{2.21}$$

where the sum has been adjusted to correspond to the new indices. We can use Eq. (2.18) to transform the partition function further. For that purpose, we multiply Eq. (2.18) from left with $\Lambda_{\nu,\mu}^*$ and integrate over the nuclei coordinates to obtain (using Dirac's notation; see App. A.1.3):

$$\langle \Lambda_{\nu,\mu}| \left(\hat{T}^{\text{nuc}} + \hat{1} E_\nu^{\text{el}} \right) |\Lambda_{\nu,\mu}\rangle = E_{\nu,\mu}^{\text{nuc}}. \tag{2.22}$$

Inserting into Eq. (2.21) yields

$$Z = \sum_\nu \left(\sum_\mu e^{-\beta\langle \Lambda_{\nu,\mu}|(\hat{T}^{\text{nuc}}+\hat{1} E_\nu^{\text{el}})|\Lambda_{\nu,\mu}\rangle} \right) = \sum_\nu \left(\sum_\mu \langle \Lambda_{\nu,\mu}|e^{-\beta(\hat{T}^{\text{nuc}}+\hat{1} E_\nu^{\text{el}})}|\Lambda_{\nu,\mu}\rangle \right), \tag{2.23}$$

where we have used Eqs. (A.4) and (A.5), which is possible since the $\Lambda_{\nu,\mu}$ are eigenfunctions of $\left(\hat{T}^{\text{nuc}} + \hat{1} E_\nu^{\text{el}} \right)$. It would be desirable to factorize the exponential to separate the E_ν^{el}. This factorization needs however to be performed with caution since $\hat{T}^{\text{nuc}}$ and $\hat{1} E_\nu^{\text{el}}$ are non-commuting operators (both act on $\{\mathbf{R}_I\}$). Therefore, we have to apply the so called Zassenhaus formula [24]:

$$e^{-\beta(\hat{T}^{\text{nuc}}+\hat{1} E_\nu^{\text{el}})} = e^{-\beta\hat{T}^{\text{nuc}}} e^{-\beta\hat{1} E_\nu^{\text{el}}} e^{\beta^2/2 [\hat{T}^{\text{nuc}},\hat{1} E_\nu^{\text{el}}]} e^{-\beta^3/6 \left(2[\hat{1} E_\nu^{\text{el}},[\hat{T}^{\text{nuc}},\hat{1} E_\nu^{\text{el}}]]+[\hat{T}^{\text{nuc}},[\hat{T}^{\text{nuc}},\hat{1} E_\nu^{\text{el}}]]\right)} \cdots . \tag{2.24}$$

Here, we have used the commutator as given in Eq. (A.3) and the dots denote exponentials corresponding to higher orders in β and with increasingly nested commutators. An explicit formula for the higher order terms is given in Ref. [24]. In Ref. [25], it is shown that exponentials corresponding to orders β^2 and higher will be small if $m_e \ll M_I$, i.e., under the same condition as needed for the Born-Oppenheimer approximation. It is therefore justified to approximate

$$e^{-\beta(\hat{T}^{\text{nuc}}+\hat{1} E_\nu^{\text{el}})} \approx e^{-\beta\hat{T}^{\text{nuc}}} e^{-\beta\hat{1} E_\nu^{\text{el}}}, \tag{2.25}$$

in any case in which the Born-Oppenheimer approximation is justified. Using Eq. (2.25), the invariance property of the trace, Eq. (A.7), and the fact that $(e^{-\beta\hat{T}^{\text{nuc}}}e^{-\beta\hat{1} E_\nu^{\text{el}}})$ corresponds to a block diagonal matrix (which allows to choose the same basis for different ν, e.g., $\nu = \nu'$ with a fixed ν') yields

$$\begin{aligned} Z &= \sum_\nu \left(\sum_\mu \langle \Lambda_{\nu,\mu}|e^{-\beta\hat{T}^{\text{nuc}}} e^{-\beta\hat{1} E_\nu^{\text{el}}}|\Lambda_{\nu,\mu}\rangle \right) \\ &= \sum_\nu \left(\sum_\mu \langle \Lambda_{\nu',\mu}|e^{-\beta\hat{T}^{\text{nuc}}} e^{-\beta\hat{1} E_\nu^{\text{el}}}|\Lambda_{\nu',\mu}\rangle \right) \\ &= \sum_\mu \langle \Lambda_{\nu',\mu}|e^{-\beta\hat{T}^{\text{nuc}}} \left(\sum_\nu e^{-\beta\hat{1} E_\nu^{\text{el}}} \right) |\Lambda_{\nu',\mu}\rangle = \sum_\mu \langle \Lambda_{\nu',\mu}|e^{-\beta\hat{T}^{\text{nuc}}} e^{-\beta\hat{1} F^{\text{el}}}|\Lambda_{\nu',\mu}\rangle, \end{aligned} \tag{2.26}$$

with the electronic free energy defined by:

$$F^{\text{el}}(\{\mathbf{R}_I\}) := -k_{\text{B}}T\ln\sum_\nu e^{-\beta E_\nu^{\text{el}}(\{\mathbf{R}_I\})}. \tag{2.27}$$

In order to recombine the exponentials again, we need to apply the Baker-Campbell-Hausdorff formula which reads [24]:

$$e^{-\beta\hat{T}^{\text{nuc}}}\,e^{-\beta\hat{1}F^{\text{el}}} = e^{-\beta\left(\hat{T}^{\text{nuc}}+\hat{1}F^{\text{el}}\right)-\beta^2/2[\hat{T}^{\text{nuc}},\hat{1}F^{\text{el}}]]-\beta^3/6[[\hat{T}^{\text{nuc}},\hat{1}F^{\text{el}}],\hat{1}F^{\text{el}}-\hat{T}^{\text{nuc}}]\cdots}. \tag{2.28}$$

However, the terms in the exponential of order β^2 and higher correspond again to terms which are small if $m_e \ll M_I$ and we approximate therefore:

$$e^{-\beta\hat{T}^{\text{nuc}}}\,e^{-\beta\hat{1}F^{\text{el}}} \approx e^{-\beta\left(\hat{T}^{\text{nuc}}+\hat{1}F^{\text{el}}\right)}. \tag{2.29}$$

In fact, it is shown in Ref. [25] that the terms neglected in Eq. (2.29) lead to contributions which are of the same order as the contributions from the neglected terms in Eq. (2.25) having however the opposite sign. Therefore, the approximations performed in Eqs. (2.25) and (2.29) partially compensate each other. Inserting Eq. (2.29) into Eq. (2.26) yields for the partition function:

$$Z = \sum_\mu \langle\Lambda_\mu|e^{-\beta\left(\hat{T}^{\text{nuc}}+\hat{1}F^{\text{el}}\right)}|\Lambda_\mu\rangle. \tag{2.30}$$

Next we define the eigenvalue equation

$$\left(\hat{T}^{\text{nuc}} + \hat{1}F^{\text{el}}\right)\tilde{\Lambda}_\mu = \tilde{E}_\mu^{\text{nuc}}\tilde{\Lambda}_\mu, \tag{2.31}$$

with the eigenfunctions $\tilde{\Lambda}_\mu$ and eigenvalues $\tilde{E}_\mu^{\text{nuc}}$, and we call it effective nuclei Schrödinger equation. Equation (2.31) describes the nuclei motion in the electronic free energy surface (FES) corresponding to the thermodynamic ground state. Using Eqs. (2.31) and (A.7), we can conveniently rewrite Z as:

$$Z = \sum_\mu e^{-\beta\tilde{E}_\mu^{\text{nuc}}}. \tag{2.32}$$

In summary, we have therefore the following chain of key equations and flow of key quantities:

$$\hat{H}^{\text{el}}\,\psi_\nu = \boxed{E_\nu^{\text{el}}(\{\mathbf{R}_I\})}\,\psi_\nu \tag{2.33}$$

$$\boxed{F^{\text{el}}(\{\mathbf{R}_I\})} = -k_{\text{B}}T\ln\sum_\nu e^{-\beta\boxed{E_\nu^{\text{el}}(\{\mathbf{R}_I\})}} \tag{2.34}$$

$$\left\{\hat{T}^{\text{nuc}} + \hat{1}\boxed{F^{\text{el}}(\{\mathbf{R}_I\})}\right\}\tilde{\Lambda}_\mu = \boxed{\tilde{E}_\mu^{\text{nuc}}}\,\tilde{\Lambda}_\mu \tag{2.35}$$

$$F = -k_{\text{B}}T\ln\sum_\mu e^{-\beta\boxed{\tilde{E}_\mu^{\text{nuc}}}}. \tag{2.36}$$
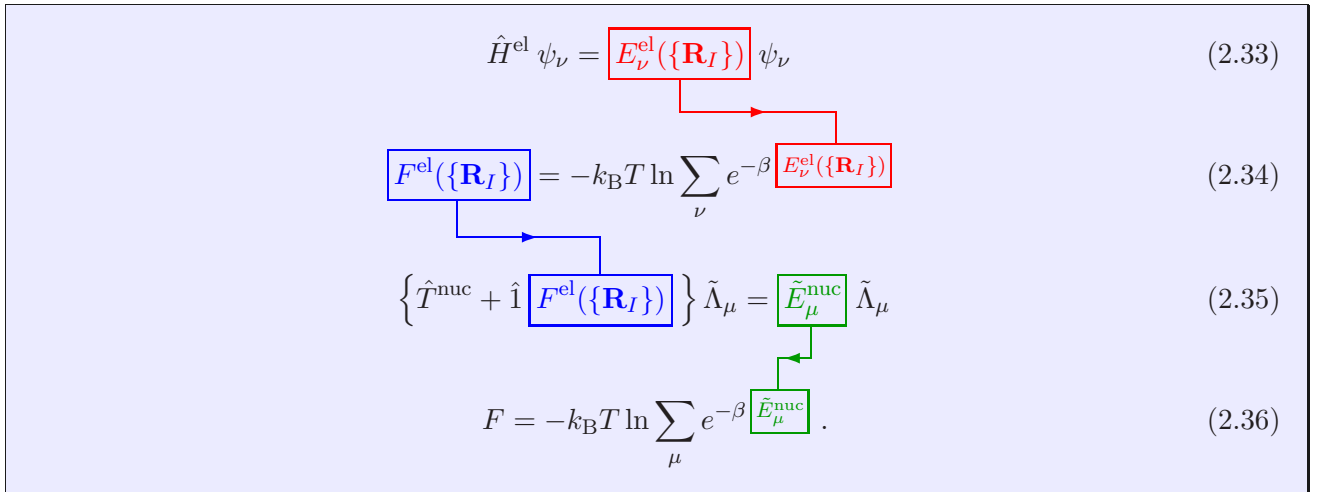
Performing both approximations, Eqs. (2.25) and (2.29), is referred to as the free energy Born-Oppenheimer (FEBO) approximation. The FEBO approximation has been introduced by Cao and Berne in 1993 [25]. We stress that it is an additional approximation to the original Born-Oppenheimer one, requiring however the same condition ($m_e/M_I \ll 1$) to be applicable. The scaling within the FEBO approximation changes to

$$s(N_{\mathrm{mesh}}, N_e, N_n) \;=\; (N_{\mathrm{mesh}}^3)^{N_n} \cdot \underbrace{\left\{ s^{\mathrm{el}} := \left[(N_{\mathrm{mesh}}^3)^{N_e} \times (N_{\mathrm{mesh}}^3)^{N_e} \right] \right\}}_{\substack{\text{Electronic Schrödinger eq.} \\ \text{for fixed nuclei coordinates}}} \;+\; \underbrace{\left[(N_{\mathrm{mesh}}^3)^{N_n} \times (N_{\mathrm{mesh}}^3)^{N_n} \right]}_{\substack{\text{Effective nuclei Schrödinger eq.} \\ \text{for electronic ground state FES}}},$$
$$(2.37)$$

where we have defined for future reference $s^{\mathrm{el}} = s^{\mathrm{el}}(N_{\mathrm{mesh}}, N_e)$, the scaling of the electronic Schrödinger equation for fixed nuclei coordinates. In comparison with the scaling within the Born-Oppenheimer approximation, Eq. (2.20), the prefactor $(N_{\mathrm{mesh}}^3)^{N_e}$ has been removed rendering the second term on the right hand site of Eq. (2.37) to be independent of N_e.

From this point on, we can discuss the electronic Schrödinger equation, Eq. (2.16), and the effective nuclei Schrödinger equation, Eq. (2.31), separately.

2.1.4   Density functional theory

For the remainder of Sec. 2.1, we concentrate on the electronic Schrödinger equation for a fixed nuclei configuration:
$$\hat{H}^{\mathrm{el}}\, \psi_\nu(\{\mathbf{r}_i\}; \{\mathbf{R}_I\}) = E_\nu^{\mathrm{el}}(\{\mathbf{R}_I\})\, \psi_\nu(\{\mathbf{r}_i\}; \{\mathbf{R}_I\}). \tag{2.38}$$

A direct solution for more than two electrons is still an infeasible task. In fact, the estimations performed in Sec. 2.1.1 for the system of one electron and one nucleus can be taken directly over for two electrons.

In 1964, Hohenberg and Kohn [12] showed that the ground state E_g^{el} of Eq. (2.38) is uniquely determined by a functional of the electron density ρ which is given in terms of the electronic wave function $\psi_\nu(\{\mathbf{r}_i\}) = \psi_\nu(\{\mathbf{r}_i\}; \{\mathbf{R}_I\})$ by:

$$\rho(\mathbf{r}) := \rho(\mathbf{r}_1) = N_e \int \dots \int |\psi_\nu(\{\mathbf{r}_i\})|^2 d\mathbf{r}_2 d\mathbf{r}_3 \dots d\mathbf{r}_{N_e}. \tag{2.39}$$

The crucial observation is that $\rho(\mathbf{r})$ is only a function of the three spatial variables, in contrast to $\psi_\nu(\{\mathbf{r}_i\})$ which is a function of $3N_e$ variables, and that a functional is the central equation instead of an eigenvalue equation. Thus, the scaling reduces as

$$s^{\mathrm{el}}(N_{\mathrm{mesh}}, N_e) = (N_{\mathrm{mesh}}^3)^{N_e} \times (N_{\mathrm{mesh}}^3)^{N_e} \quad \rightarrow \quad s^{\mathrm{DFT}}(N_{\mathrm{mesh}}) = N_{\mathrm{mesh}}^3, \tag{2.40}$$

with the DFT scaling s^{DFT}. The corresponding theory is called the density functional theory (DFT) and it is important to stress that, despite the tremendous reduction of variables, DFT is in principle exact. It is only the practical realization which makes an approximation necessary. The derivation by Hohenberg and Kohn [12] is the most often presented formulation of DFT. However, E_g^{el} corresponds to a single electronic PES, the $T = 0$ K one, and as discussed in Sec. 2.1.2, it is not sufficient for our purposes to have only a single PES available. In 1965, Mermin [26] showed that there exists also a functional of the electronic density which uniquely determines the thermodynamic ground state FES, i.e., F^{el}. We therefore consider here Mermin's extended formulation, the finite temperature DFT. Further, we rely on the Levy constrained search formulation [27, 28], which is more generally applicable than the original approach by Hohenberg and Kohn/Mermin [12, 26].

In order to introduce finite temperature DFT formally, we need to generalize the notion of the free energy. Specifically, we define a free energy functional $\widetilde{F}^{\text{el}}$ constructed from an entropy and an inner energy contribution by:

$$\widetilde{F}^{\text{el}}[\{p_\nu\}, \{\psi_\nu\}] = T \underbrace{k_B \sum_\nu p_\nu \ln p_\nu}_{\text{(negative) Entropy term}} + \underbrace{\sum_\nu p_\nu \langle \psi_\nu | \hat{H}^{\text{el}} | \psi_\nu \rangle}_{\text{Inner energy contribution}} . \tag{2.41}$$

Here, the p_ν are weights which determine the contribution of the corresponding ψ_ν to the free energy and which must satisfy:

$$p_\nu \geq 0 \quad \text{and} \quad \sum_\nu p_\nu = 1. \tag{2.42}$$

The free energy functional, Eq. (2.41), is constructed such that its minimum with respect to $\{p_\nu\}$ and $\{\psi_\nu\}$ will always correspond to the free energy defined in Eq. (2.27) [29], i.e.:

$$F^{\text{el}} = -k_B T \ln \sum_\nu e^{-\beta E_\nu^{\text{el}}} = \min_{\{p_\nu\}, \{\psi_\nu\}} \widetilde{F}^{\text{el}}[\{p_\nu\}, \{\psi_\nu\}]. \tag{2.43}$$

We can now perform the key step of DFT which is to rewrite the minimization as:

$$F^{\text{el}} = \min_\rho \left(\min_{\{p_\nu\}, \{\psi_\nu\}}^{\rho} \widetilde{F}^{\text{el}}[\{p_\nu\}, \{\psi_\nu\}] \right). \tag{2.44}$$

Here, the inner minimization is constrained in the sense that only sets of $(\{p_\nu\}, \{\psi_\nu\})$ are allowed which yield ρ, using a generalized version of Eq. (2.39):

$$\rho(\mathbf{r}) := \rho(\mathbf{r}_1) = N_e \sum_\nu p_\nu \int \ldots \int |\psi_\nu(\{\mathbf{r}_i\})|^2 d\mathbf{r}_2 d\mathbf{r}_3 \ldots d\mathbf{r}_{N_e}. \tag{2.45}$$

The outer minimization relaxes then this condition by allowing to search for the minimum among all electronic densities ρ which satisfy [29]:

$$\rho(\mathbf{r}) \geqslant 0, \quad \int \rho(\mathbf{r}) d\mathbf{r} = N_e, \quad \text{and} \quad \int |\nabla \rho(\mathbf{r})^{1/2}|^2 d\mathbf{r} < \infty. \tag{2.46}$$

These conditions guarantee that the electronic density corresponds to an antisymmetric wave function describing N_e electrons [30]. Using Eqs. (2.15) and (2.41), we can rewrite the inner minimization from Eq. (2.44) as:

$$\min_{\{p_\nu\}, \{\psi_\nu\}}^{\rho} \widetilde{F}^{\text{el}}[\{p_\nu\}, \{\psi_\nu\}] = \min_{\{p_\nu\}, \{\psi_\nu\}}^{\rho} \left[\sum_\nu p_\nu \left(k_B T \ln p_\nu + \langle \psi_\nu | \hat{T}^{\text{el}} + \hat{V}^{\text{el}} + \hat{V}^{\text{nuc}} + \hat{V}^{\text{e-n}} | \psi_\nu \rangle \right) \right]$$

$$= \mathcal{F}[\rho] + \int \rho(\mathbf{r}) v(\mathbf{r}) d\mathbf{r} + V^{\text{nuc}}. \tag{2.47}$$

Here, we have defined the functional $\mathcal{F}[\rho]$, the external potential $v(\mathbf{r})$, and the scalar quantity V^{nuc} by

$$\mathcal{F}[\rho] := \min_{\{p_\nu\}, \{\psi_\nu\}}^{\rho} \left[\sum_\nu p_\nu \left(k_B T \ln p_\nu + \langle \psi_\nu | \hat{T}^{\text{el}} + \hat{V}^{\text{el}} | \psi_\nu \rangle \right) \right], \tag{2.48}$$

$$\hat{V}^{\text{e-n}} = -\sum_i^{N_e} \sum_I^{N_n} \frac{Z_I e^2}{4\pi\epsilon_0 |\mathbf{r}_i - \mathbf{R}_I|} =: \sum_i^{N_e} v(\mathbf{r}_i), \tag{2.49}$$

$$\sum_\nu p_\nu \langle \psi_\nu | \hat{V}^{\text{nuc}} | \psi_\nu \rangle = \frac{1}{2} \sum_I^{N_n} \sum_{J \neq I}^{N_n} \frac{Z_I Z_J e^2}{4\pi\epsilon_0 |\mathbf{R}_I - \mathbf{R}_J|} =: V^{\text{nuc}}, \tag{2.50}$$

and finally used the fact that:

$$
\begin{aligned}
\sum_\nu p_\nu \langle \psi_\nu | \hat{V}^{\text{e-n}} | \psi_\nu \rangle \quad &= \quad \sum_\nu p_\nu \int \sum_i^{N_e} v(\mathbf{r}_i) |\psi_\nu(\{\mathbf{r}_i\})|^2 \, d\mathbf{r}_i \\
&= \quad \int v(\mathbf{r}) d\mathbf{r} \left[N_e \sum_\nu p_\nu \int \cdots \int |\psi_\nu(\{\mathbf{r}_i\})|^2 \, d\mathbf{r}_2 \ldots d\mathbf{r}_{N_e} \right] \\
\overset{\text{Eq. (2.45)}}{=} \quad &\int v(\mathbf{r}) \rho(\mathbf{r}) d\mathbf{r}.
\end{aligned}
\tag{2.51}
$$

To obtain the second equality in Eq. (2.51), the symmetry of $|\psi_\nu(\{\mathbf{r}_i\})|^2$ with respect to an interchange of particle variables $\mathbf{r}_i$ and $\mathbf{r}_1$ was used [cf. Eq. (2.5)]. Inserting Eq. (2.47) into Eq. (2.44) gives:

$$F^{\text{el}} = \min_\rho \left(\mathcal{F}[\rho] + \int \rho(\mathbf{r}) v(\mathbf{r}) d\mathbf{r} \right) + V^{\text{nuc}}. \tag{2.52}$$

This is the final equation of finite temperature DFT. It states that the electronic free energy at thermal equilibrium, F^{el}, can be determined by minimizing the functional $\mathcal{F}[\rho] + \int \rho(\mathbf{r}) v(\mathbf{r}) d\mathbf{r}$ with respect to the electronic density ρ, while V^{nuc} is only a scalar shift. An important observation is that $\mathcal{F}[\rho]$ does not depend on the external potential $v(\mathbf{r})$, i.e., it is a universal functional of ρ only, likewise applicable to atoms, molecules, or crystals. However, the exact functional form of $\mathcal{F}[\rho]$ is not known and, in practice, one therefore relies on approximations which are discussed in the following. Before, let us briefly comment on the presented derivation of Eq. (2.52).

The steps leading to Eq. (2.52) seem rather straightforward. In fact, the key step is the separation of the minimization as given in Eq. (2.44) which allows the introduction of the functional $\mathcal{F}[\rho]$ in Eq. (2.47). It is however important to stress that an indispensable requirement for such a separation and for the correct minimization of $\mathcal{F}[\rho]$ is the knowledge of the domain of electronic densities which are admissible. Specifically, only those densities are admissible which are derivable from an antisymmetric wave function [Eq. (2.5)]. The determination of the conditions identifying such densities is rather involved [30] and the conditions are therefore given here, in Eq. (2.46), without proof.

2.1.5   Kohn-Sham approach

Equation (2.52) asserts only that a functional $\mathcal{F}[\rho]$ must exist, but it gives no prescription of how to construct it. In 1965, Kohn and Sham [31] developed an indirect approach to handle this problem. The basic idea is to introduce an auxiliary system of non-interacting electrons in addition to the actual system of interest containing electron interactions. The auxiliary system is solved exactly (this is straightforward since no interactions are present) and additionally the classical electron interaction is included. As it turns out empirically, this accounts for the major part of the physics contained in the actual interacting system and the remaining part can be approximated very efficiently with a "simple" functional dependence. To introduce the Kohn-Sham approach formally, we need first to formulate the minimization of Eq. (2.52) in terms of a functional derivative.

The minimum search in Eq. (2.52) is equivalent [29] to performing a variation of

$$\delta \left[\mathcal{F}[\rho] + \int \rho(\mathbf{r})v(\mathbf{r})d\mathbf{r} - \mu \left(\int \rho(\mathbf{r})d\mathbf{r} - N_e \right) \right] = 0, \tag{2.53}$$

where $\mu \left(\int \rho(\mathbf{r})d\mathbf{r} - N_e \right)$, with the Lagrange multiplier μ, is included in order to guarantee particle conservation, i.e., that ρ integrates to N_e [cf. Eq. (2.46)]. Carrying out the variation yields the Euler-Lagrange equation [29]:

$$\mu = v(\mathbf{r}) + \frac{\delta \mathcal{F}[\rho]}{\delta \rho(\mathbf{r})}. \tag{2.54}$$

We can now proceed with the Kohn-Sham (KS) approach. DFT and thus Eq. (2.54) is applicable to any electronic system, in particular to a system of non-interacting electrons, i.e., one without $\hat{V}^{\mathrm{el}}$, for which:

$$\mathcal{F}^{\mathrm{KS}}[\rho] := \mathcal{F}[\rho] = \min_{\{p_\nu\}, \{\psi_\nu\}}^{\rho} \left[\sum_\nu p_\nu \left(k_{\mathrm{B}}T \ln p_\nu + \langle \psi_\nu | \hat{T}^{\mathrm{el}} | \psi_\nu \rangle \right) \right]. \tag{2.55}$$

We hence introduce such a system with N_e electrons and require that its electronic density equals the density of our interacting system. This can be achieved by varying the external potential of the non-interacting system, which we call the effective potential, $v^{\mathrm{eff}}(\mathbf{r})$. We thus have two Euler-Lagrange equations providing the same density and thus the same μ:

1) Interacting system:

$$\mu = v(\mathbf{r}) + \frac{\delta \mathcal{F}[\rho]}{\delta \rho}. \tag{2.56}$$

2) Non-interacting system:

$$\mu = v^{\mathrm{eff}}(\mathbf{r}) + \frac{\delta \mathcal{F}^{\mathrm{KS}}[\rho]}{\delta \rho}. \tag{2.57}$$

Combining Eqs. (2.56) and (2.57) gives for the effective potential:

$$v^{\mathrm{eff}}(\mathbf{r}) = v(\mathbf{r}) + \frac{\delta \mathcal{F}[\rho]}{\delta \rho} - \frac{\delta \mathcal{F}^{\mathrm{KS}}[\rho]}{\delta \rho}. \tag{2.58}$$

To proceed further, we now introduce the first key step of the Kohn-Sham approach, namely the separation of the interacting system into:

$$\mathcal{F}[\rho] = \mathcal{F}^{\mathrm{KS}}[\rho] + E^{\mathrm{H}}[\rho] + E^{\mathrm{xc}}[\rho]. \tag{2.59}$$

Here, $E^{\mathrm{H}}[\rho]$ is the so called Hartree energy functional which accounts for the classical part of the electron-electron interaction,

$$E^{\mathrm{H}}[\rho] = \frac{1}{2} \int \frac{\rho(\mathbf{r})\rho(\mathbf{r}')}{|\mathbf{r} - \mathbf{r}'|} d\mathbf{r}d\mathbf{r}', \tag{2.60}$$

and $E^{\mathrm{xc}}[\rho]$ is the exchange-correlation functional which formally accounts for the unknown difference between $\mathcal{F}^{\mathrm{KS}}[\rho] + E^{\mathrm{H}}[\rho]$ and the fully interacting system. The functional dependence of $E^{\mathrm{xc}}[\rho]$ is not known as is the case for $\mathcal{F}[\rho]$. However, and this is the actual merit of this approach, the functional dependence of $E^{\mathrm{xc}}[\rho]$ can be approximated to good accuracy using simple formulas as opposed to $\mathcal{F}[\rho]$. This is a consequence of the fact that $\mathcal{F}^{\mathrm{KS}}[\rho] + E^{\mathrm{H}}[\rho]$ contains already a major part of the physics of the interacting system. The exchange-correlation functional is discussed further

in the following section. Inserting Eq. (2.59) into Eq. (2.58) yields:

$$v^{\text{eff}}(\mathbf{r}) = v(\mathbf{r}) + \frac{\delta E^{\text{H}}[\rho]}{\delta \rho} + \frac{\delta E^{\text{xc}}[\rho]}{\delta \rho} = v(\mathbf{r}) + \frac{1}{2} \int \frac{\rho(\mathbf{r}')}{|\mathbf{r} - \mathbf{r}'|} d\mathbf{r}' + \frac{\delta E^{\text{xc}}[\rho]}{\delta \rho}. \qquad (2.61)$$

This is the final equation for the effective potential of the non-interacting system, which can be evaluated assuming we have approximated $E^{\text{xc}}[\rho]$. Due to the second and third term on the right hand side this potential is in fact a functional of the density, i.e., $v^{\text{eff}}(\mathbf{r}) = v^{\text{eff}}[\rho](\mathbf{r})$. This dependence causes however a difficulty since, while we have a prescription of how to calculate v^{eff} from ρ, we have no prescription of how to obtain ρ. The solution to this issue is given by the second key step of the Kohn-Sham approach: Up to this point, we have treated the non-interacting system using DFT, but we can as well use a standard quantum mechanical approach based on an eigenvalue equation. This is straightforward due to the missing interactions. The full solution of the non-interacting system can be therefore obtained by solving the Kohn-Sham eigenvalue equation

$$\hat{H}^{\text{KS}}[\rho] \, \varphi_i(\mathbf{r}) = \epsilon_i \varphi_i(\mathbf{r}), \qquad (2.62)$$

where ϵ_i and φ_i are the ith eigenvalue and eigenfunction, and where the Kohn-Sham Hamiltonian $\hat{H}^{\text{KS}}$ assumes an effective one particle form:

$$\hat{H}^{\text{KS}}[\rho] = -\frac{1}{2}\nabla^2 + v^{\text{eff}}[\rho](\mathbf{r}). \qquad (2.63)$$

The eigenfunctions φ_i can be used to obtain the electronic density of the non-interacting system by

$$\rho(\mathbf{r}) = \sum_i f_i |\varphi_i(\mathbf{r})|^2, \qquad (2.64)$$

where f_i is the Fermi-Dirac function:

$$f_i = \left\{ 1 + e^{(\epsilon_i - \mu)/(k_{\text{B}}T)} \right\}^{-1}. \qquad (2.65)$$

The origin of the Fermi-Dirac function is the fact that even non-interacting electrons need to obey antisymmetry with respect to particle interchange. Its maximal value is 1 which means that a particular energy level can be occupied by at most one electron (Pauli principle). An example Fermi-Dirac function is plotted in Fig. 2.1 [denoted as FD(T)]. With Eqs. (2.63) to (2.65), we have obtained a prescription for calculating ρ from v^{eff}. If we finally combine both approaches, the standard quantum mechanical and the DFT approach, we arrive at a set of fully coupled equations:

$$\boxed{v^{\text{eff}}[\rho](\mathbf{r}) = v(\mathbf{r}) + \delta E^{\text{xc}}[\rho]/\delta\rho + \tfrac{1}{2}\int d\mathbf{r}' \, \rho(\mathbf{r}')/(|\mathbf{r} - \mathbf{r}'|)}$$

$\rho(\mathbf{r})$ \qquad\qquad $v^{\text{eff}}(\mathbf{r})$ \qquad\qquad $\varphi_i^{\text{start}}(\mathbf{r})$

$$\boxed{\rho(\mathbf{r}) = \sum_i f_i |\varphi_i(\mathbf{r})|^2} \qquad\qquad \boxed{\left\{ -\nabla^2 + v^{\text{eff}}(\mathbf{r}) \right\} \varphi_i(\mathbf{r}) = \epsilon_i \varphi_i(\mathbf{r})}$$

$$\varphi_i(\mathbf{r}) \qquad\qquad\qquad\qquad\qquad (2.66)$$
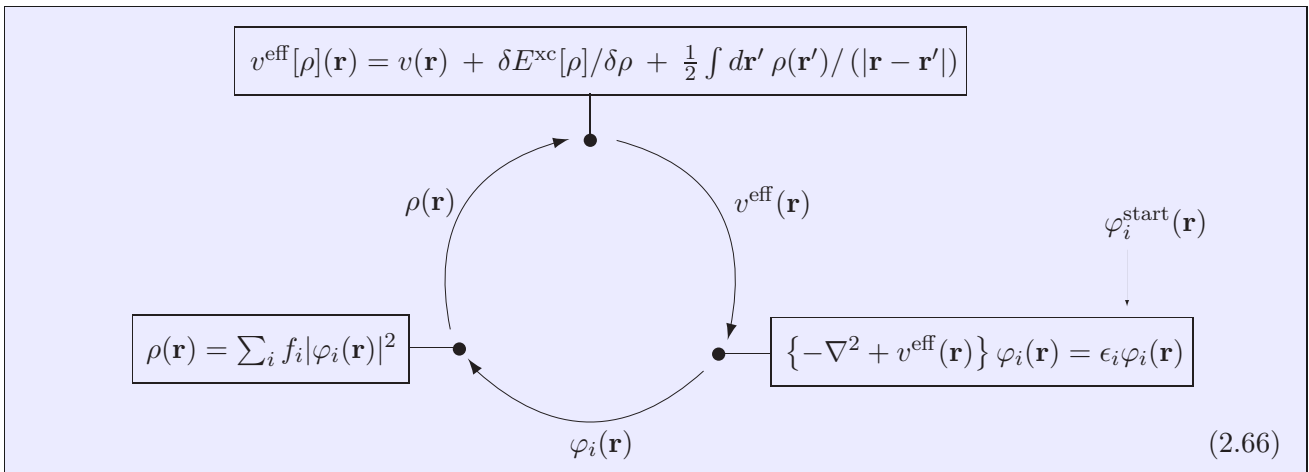
This cycle of equations is called the self consistency cycle. At start, one needs initial wave functions $\varphi_i^{\mathrm{start}}$ which can be constructed for instance from random numbers. The equations are then calculated self consistently until convergence has been achieved, i.e., until φ_i, ρ, and v^{eff} do not change significantly anymore. The converged φ_i and the f_i can be used to calculate $\mathcal{F}^{\mathrm{KS}}$, which contains a kinetic energy contribution [this is the only contribution to the inner energy for a non-interacting system; cf Eq. (2.41)] and an entropy contribution [29]:

$$\mathcal{F}^{\mathrm{KS}}\left[\{\varphi_i[\rho]\}, \{f_i[\rho]\}\right] = \underbrace{-\frac{1}{2}\sum_i f_i \int \varphi_i(\mathbf{r})\nabla^2\varphi_i(\mathbf{r})d\mathbf{r}}_{\text{Kinetic energy contribution}} - T\ \underbrace{k_{\mathrm{B}}\sum_i\left[f_i \ln f_i + (1 - f_i)\ln(1 - f_i)\right]}_{\text{Entropy contribution}}.$$

(2.67)

Here, we have indicated that $\mathcal{F}^{\mathrm{KS}}$ depends implicitly on ρ through the self consistency cycle. Equation (2.67) completes the solution of the non-interacting system. The equilibrium electronic free energy of the system of interest including interactions can be finally obtained using Eqs. (2.52) and (2.59):

$$F^{\mathrm{el}} = \mathcal{F}^{\mathrm{KS}}[\rho] + E^{\mathrm{H}}[\rho] + E^{\mathrm{xc}}[\rho] + \int \rho(\mathbf{r})v(\mathbf{r})d\mathbf{r} + V^{\mathrm{nuc}}. \tag{2.68}$$

All terms are now explicitly given except for the exchange-correlation functional $E^{\mathrm{xc}}[\rho]$ which is discussed in the next section.

Let us summarize DFT and the Kohn-Sham approach with the key equations and their scaling properties:

1) Many electron eigenvalue equation:

$$\left.\begin{array}{l}\hat{H}^{\mathrm{el}}\psi_\nu = E_\nu^{\mathrm{el}}\psi_\nu \\[2mm] F^{\mathrm{el}} = -k_{\mathrm{B}}T\ln\sum_\nu e^{-\beta E_\nu^{\mathrm{el}}}\end{array}\right\} \quad \text{with} \quad s^{\mathrm{el}}(N_{\mathrm{mesh}}, N_e) = (N_{\mathrm{mesh}}^3)^{N_e} \times (N_{\mathrm{mesh}}^3)^{N_e}.$$

(2.69)

$\downarrow$ DFT

2) Electronic density functional:

$$F^{\mathrm{el}} = \min_\rho\left(\mathcal{F}[\rho] + \int \rho(\mathbf{r})v(\mathbf{r})d\mathbf{r}\right) + V^{\mathrm{nuc}} \quad \text{with} \quad s^{\mathrm{DFT}}(N_{\mathrm{mesh}}) = N_{\mathrm{mesh}}^3. \tag{2.70}$$

$\downarrow$ Kohn-Sham

3) Self consistent effective one electron eigenvalue equation:

$$\left.\begin{array}{l}\left(-\frac{1}{2}\nabla^2 + v^{\mathrm{eff}}(\mathbf{r})\right)\varphi_i(\mathbf{r}) = \epsilon_i\varphi_i(\mathbf{r}), \quad \rho = \sum_i f_i|\varphi_i|^2 \\[2mm] F^{\mathrm{el}} = \mathcal{F}^{\mathrm{KS}}[\rho] + E^{\mathrm{H}}[\rho] + E^{\mathrm{xc}}[\rho] + \int \rho(\mathbf{r})v(\mathbf{r})d\mathbf{r} + V^{\mathrm{nuc}}\end{array}\right\} \quad \text{with} \quad \begin{array}{l}s^{\mathrm{KS}}(N_{\mathrm{mesh}}, N^{\mathrm{it}}) = \\[1mm] = N^{\mathrm{it}}\cdot(N_{\mathrm{mesh}}^3 \times N_{\mathrm{mesh}}^3).\end{array}$$

(2.71)

In Eq. (2.71), we have introduced s^{KS} the scaling function of the Kohn-Sham approach. It represents a one particle matrix equation, which is a consequence of the introduction of the effective one electron eigenvalue equation. We need, however, to solve an eigenvalue equation at each iteration step of the self consistency cycle, Eq. (2.66), which results in N^{it} eigenvalue equations, with N^{it} the number of iterations steps required for self consistency.

We finally remark that the usual Kohn-Sham approach, as presented here, is not applicable in every case. Levy [32] and Lieb [28] have shown that there are physically reasonable interacting systems which produce electronic densities that cannot be obtained from a pure ground state of a non-interacting system. This means that if we are to use the occupation numbers as given by Eq. (2.65), no effective potential for the non-interacting system can be constructed such as to yield the density of the interacting system. Situations of this kind often arise for degenerate systems and it is then possible to derive a more general Kohn-Sham formalism [33] which uses ensembles of the degenerate ground states to describe the density. In this general approach, the occupation numbers in Eq. (2.64) do not decrease monotonically with energy, in fact some of the occupation numbers below μ from Eq. (2.65) can go to zero leaving holes and some well above μ can become 1. Further, Englisch and Englisch [34] have shown that in rare cases there are even systems which cannot be described by this generalized Kohn-Sham procedure. However, these issues are of no concern for the present study: As remarked in Refs. [35] and [36], if Eqs. (2.62) and (2.64) are not applicable the self consistency cycle, Eq. (2.66), will not converge. Such a situation did not occur in the presented calculations.

2.1.6   Exchange correlation functional

We now turn to the discussion of the exchange-correlation energy functional $E^{\text{xc}}[\rho]$ which is formally defined by Eq. (2.59). This is the remaining component of the Kohn-Sham approach to be determined.

The exact functional dependence of $E^{\text{xc}}[\rho]$ is not known. There are however certain formal properties and exact relations which must be fulfilled, like for instance the norm conservation for the so called exchange-correlation hole [36]. Those can be used as guidelines in constructing/improving functionals and, by now, a large set is available in literature. Two popular functionals representing two important families of $E^{\text{xc}}[\rho]$ functionals are the local density approximation (LDA) and the generalized gradient approximation by Perdew-Burke-Ernzerhof (GGA-PBE) [37]. LDA and GGA-PBE have been widely applied to $T = 0$ K properties and have proven to be very reliable.[2]

The idea behind the LDA is to assume that the exchange-correlation energy is local, i.e., that it depends only on the value of the electronic density at a single space point [29]. The actual dependence is derived from the homogeneous electron gas and reads:

$$E^{\text{xc}}[\rho] = \int \rho(\mathbf{r}) \, \epsilon_{\text{heg}}^{\text{xc}}(\rho(\mathbf{r})) \, d\mathbf{r}. \tag{2.72}$$

Here, $\epsilon_{\text{heg}}^{\text{xc}}(\rho)$ is the exchange-correlation energy per particle of a homogeneous electron gas (heg) with the density ρ. Note that $\epsilon_{\text{heg}}^{\text{xc}}(\rho)$ is merely a function and not a functional, since it depends on a single density value. It is convenient to split $\epsilon_{\text{heg}}^{\text{xc}}$ into an exchange part, $\epsilon_{\text{heg}}^{\text{x}}$, and a correlation part, $\epsilon_{\text{heg}}^{\text{c}}$, as: $\epsilon_{\text{heg}}^{\text{xc}} = \epsilon_{\text{heg}}^{\text{x}} + \epsilon_{\text{heg}}^{\text{c}}$. The exchange part can be derived exactly analytically and is given

---

[2]One of many examples is the study performed in Ref. [38], where the $T = 0$ K energetics for a wide range of intermetallics was computed with LDA and GGA, showing good agreement with experiment. In Ref. [38], the PW91 [39] parametrization of GGA was employed. However, the PW91 and the PBE parametrization typically yield very similar results [37].

by [29]:

$$\epsilon_{\text{heg}}^{\text{x}}(\rho) = -\frac{3}{4}\left(\frac{3}{\pi}\right)^{1/3}\rho^{4/3}. \tag{2.73}$$

In contrast, the analytical dependence of $\epsilon_{\text{heg}}^{\text{c}}$ is not known. However, numerical results (based on quantum Monte Carlo calculations) have been obtained for a wide range of densities [40] and interpolations allow to obtain $\epsilon_{\text{heg}}^{\text{c}}$ for any density. In principle, it is also possible to derive an exchange-correlation energy for the homogeneous electron gas which contains an explicit temperature dependence [29]. The resulting corrections to the free energy are however small compared to the error introduced by LDA in general [23]. We will not consider such temperature dependent exchange-correlation functionals.

Due to the assumptions made, the LDA yields exact results only for the homogeneous electron gas. Despite this restriction and its simplicity, the LDA has turned out to provide accuracies sufficient to address a wide variety of material science issues and has been used successfully for many years [41]. The enormous success of LDA is attributed to the fact that its derivation is based on a physical system (homogeneous electron gas). This ensures that LDA reproduces the above mentioned norm conservation and further important relations for the exchange-correlation hole (see e.g. Ref. [29] for details).

The exact exchange-correlation energy depends on electron density values at all space points. Therefore, a natural extension of the LDA seems to be a systematic increase of the space points which contribute to E^{xc}, for instance by including more and more neighboring points. The latter is equivalent to performing an expansion in terms of the gradient of the electronic density. Exchange correlation energy functionals of this kind are termed gradient expansion approximation (GEA) and belong to the set of semi-local functionals. It turns out however that such a systematic increase of gradient orders is not applicable [42]: The analytical and computational complexity becomes higher with each order while the achievable accuracy drops as compared to LDA. This unintuitive loss in accuracy is due to the fact that, in contrast to LDA, the GEA is not derived from a physical system and it therefore does not fulfill the exact relations. In order to remove this deficiency of the GEA, a generalized approach, i.e., the generalized gradient approach (GGA), has been developed. Within GGA the exchange-correlation energy is given by:

$$E^{\text{xc}}[\rho] = \int f^{\text{xc}}(\rho(\mathbf{r}), \nabla\rho(\mathbf{r}))\, d\mathbf{r}. \tag{2.74}$$

Here, f^{xc} is a general function of the density and of its gradient at a single space point. The important difference to a GEA functional is that within GGA an arbitrary dependence on ρ and $\nabla\rho$ can be implemented into f^{xc} while for a GEA functional a systematic power-series-like gradient expansion is performed. The general f^{xc} function gives GGA a greater flexibility which can be used to construct functionals that fulfill the exact relations.[3] One of the most reliable and therefore prominent functionals of this type is the GGA-PBE functional.

Further improvements of the exchange-correlation energy functionals proceed along the lines of incorporating more non-locality. One such group of functionals are metaGGAs [42] and another are explicitly orbital dependent functionals [42]. Both groups are however still in their infancy and

---

[3]There exists also another philosophy to constructing GGA functionals. The f^{xc} function is constructed such as to reproduce a certain set of experimental values rather than fulfill the exact relations. This approach is referred to as semi-empirical and it is used predominantly in quantum chemistry calculations [36]. A prominent functional of this type is BLYP [36]. To distinguish the semi-empirical and the approach presented in the main text, the latter is referred to as *ab initio* or non-empirical. The non-empirical approach is predominantly used in condensed matter theory and a prominent functional of this type, besides the PBE functional, is the PW91 [39] functional.

the complexity and computational requirements of these functionals are significantly increased as compared to LDA and GGA. We will not consider them in this study.

We finally comment on the philosophy with respect to the exchange-correlation functional taken in this work. Since there exists no feasible way to systematically improve the exchange-correlation functional as shown by the GEA functionals, we regard the errors introduced by LDA and GGA-PBE as being uncontrollable. In contrast, all other approximations introduced subsequently will be controllable in the sense that some convergence parameter can always be used to reduce the corresponding error.

2.1.7 Periodic approach

The matrix corresponding to the Kohn-Sham eigenvalue equation scales as $s^{\mathrm{KS}}(N_{\mathrm{mesh}}) = (N_{\mathrm{mesh}}^3 \times N_{\mathrm{mesh}}^3)$ (with $N^{\mathrm{it}} = 1$). Let us roughly estimate the size of a crystal that would be accessible based on this equation. For that purpose, we consider however a more realistic situation than the one sketched in Sec. 2.1.1 where we relied on the world's most powerful computer machines. We assume now a single node with, say, 16 GB of memory.[4] If we further represent our matrix by single precision numbers (i.e., 4 bytes), we can store $\approx 63,000 \times 63,000$ elements and thus increase N_{mesh} to ≈ 40. Using the mesh distance from Sec. 2.1.1, $\delta = 0.1a_0$, we are then able to describe a cell of $4 \times 4 \times 4\ a_0^3 (= 4^3 a_0^3)$. A typical unit cell of the considered elements is however $\approx 8^3 a_0^3$ (4 atoms) large, and thus too large to be fully captured by the mesh. In fact, due to the cubic scaling, we would need already $1,000$ GB (i.e., 1 TB) of memory to discretize a $8^3 a_0^3$ unit cell. In Sec. 3.4.3, we will show that cell sizes of at least $16^3 a_0^3$ (32 atoms) are necessary to describe thermodynamic properties, which is clearly not manageable if we tackle the Kohn-Sham equation directly as described. In order to proceed, we need to further exploit the underlying physics and symmetry of the system under study.

An inherent property of crystals is their periodicity. A more suitable basis, as compared to the real space basis used above, is therefore a plane wave, i.e., periodic or reciprocal, basis. Using a plane wave basis has in fact two advantages: 1) Only a small number of basis elements needs to be considered explicitly in the calculation, since they describe already accurately the properties of the system. 2) Surface effects are removed which allows to describe thermodynamic properties accurately using smaller cell sizes. Strictly speaking, 1) is only valid if the strong oscillations of the electronic wave function close to the ionic cores are removed. This can be achieved by employing the PAW method and is described in Sec. 2.1.8. In the following, we implicitly assume that the PAW method is employed and discuss the periodic ansatz with the general aim of rewriting the Kohn-Sham equations in reciprocal space. We put special emphasis on revealing the role played by two important parameters that are crucial to obtain the desired convergence: the k sampling and the plane wave cutoff.

Every crystal structure can be classified into one of 14 Bravais lattices (see e.g. Ref. [43]). A Bravais lattice consists of all points with position vectors $\mathbf{R}$ of the form

$$\mathbf{R} = n_1\mathbf{a}_1 + n_2\mathbf{a}_2 + n_3\mathbf{a}_3, \quad \text{with} \quad n_1, n_2, n_3 \in \mathbb{Z}, \tag{2.75}$$

and with lattice vectors $\mathbf{a}_1$, $\mathbf{a}_2$, and $\mathbf{a}_3$. Specifically, the investigated elements belong to the face-centered-cubic (fcc) Bravais lattice. The fcc lattice vectors can be specified in two different but equivalent ways corresponding to the conventional unit cell or the primitive unit cell. The first one, emphasizing the cubic symmetry, will be employed in Sec. 2.3.2. Here, we utilize the primitive cell

---

[4]Currently available RAM sizes in the high performance computing sector are in the range of 2 to 64 GB.

with lattice vectors

$$\mathbf{a}_1 = \frac{a^{\text{lat}}}{2}\,(0,1,1), \quad \mathbf{a}_2 = \frac{a^{\text{lat}}}{2}\,(1,0,1), \quad \mathbf{a}_3 = \frac{a^{\text{lat}}}{2}\,(1,1,0), \tag{2.76}$$

where a^{lat} denotes the lattice constant. The real space representation, Eq. (2.75), has a corresponding representation in reciprocal space, which is defined as the lattice of vectors $\mathbf{G}$ fulfilling:

$$e^{i\mathbf{G}\cdot\mathbf{R}} = e^{i2\pi n} = 1, \quad \text{with} \quad n \in \mathbb{Z}. \tag{2.77}$$

Equation (2.77) is satisfied if

$$\mathbf{G} = k_1\mathbf{b}_1 + k_2\mathbf{b}_2 + k_3\mathbf{b}_3, \quad \text{with} \quad k_1, k_2, k_3 \in \mathbb{Z}, \tag{2.78}$$

and with the reciprocal lattice vectors uniquely determined by

$$\mathbf{b}_1 = \frac{2\pi}{V}\,\mathbf{a}_2 \times \mathbf{a}_3, \qquad \mathbf{b}_2 = \frac{2\pi}{V}\,\mathbf{a}_3 \times \mathbf{a}_1, \qquad \mathbf{b}_3 = \frac{2\pi}{V}\,\mathbf{a}_1 \times \mathbf{a}_2, \tag{2.79}$$

where

$$V = \mathbf{a}_1 \cdot (\mathbf{a}_2 \times \mathbf{a}_3) = (a^{\text{lat}})^3/4 \tag{2.80}$$

is the volume of the (real space) fcc primitive unit cell. With these definitions and considering the fact that the periodicity of the lattice implies $v^{\text{eff}}(\mathbf{r}) = v^{\text{eff}}(\mathbf{r} + \mathbf{R})$, we can expand the effective potential by

$$v^{\text{eff}}(\mathbf{r}) = \frac{1}{V} \sum_{\mathbf{G}} v_{\mathbf{G}}^{\text{eff}}\, e^{i\mathbf{G}\cdot\mathbf{r}}, \tag{2.81}$$

where $v_{\mathbf{G}}^{\text{eff}}$ are reciprocal expansion coefficients. The sum in Eq. (2.81) runs only over the reciprocal lattice vectors $\mathbf{G}$ rather than over all possible plane waves, to ensure the periodicity of the potential in real space. The wave function, which does not need to have this symmetry, can be expanded using Bloch's theorem [44, 45] as

$$\varphi_i(\mathbf{r}) = \varphi_{\nu,\mathbf{k}}(\mathbf{r}) = e^{i\mathbf{k}\cdot\mathbf{r}} \sum_{\mathbf{G}} c_{\nu,\mathbf{k}+\mathbf{G}}\, e^{i\mathbf{G}\cdot\mathbf{r}}, \tag{2.82}$$

with expansion coefficients $c_{\nu,\mathbf{k}+\mathbf{G}}$ and with the wave vector $\mathbf{k}$ lying inside the so called first Brillouin zone which is spanned by the vectors $\mathbf{b}_1$, $\mathbf{b}_2$, and $\mathbf{b}_3$ from Eq. (2.79). We note two important observations about Eq. (2.82): 1) A given eigenfunction $\varphi_i(\mathbf{r})$ of the periodic real space Kohn-Sham equation can be expanded using again the reciprocal lattice vectors $\mathbf{G}$ which now however, in contrast to Eq. (2.81), depend on a specific wave vector $\mathbf{k}$ and which are modulated by a plane wave $e^{i\mathbf{k}\cdot\mathbf{r}}$ of this wave vector. 2) Wave functions of different $\mathbf{k}$ do not couple to each other and can be therefore treated separately. The latter point allows also to split the original index i into an index $\mathbf{k}$ and an index ν which denotes the solutions for a fixed $\mathbf{k}$. Inserting Eqs. (2.81) and (2.82) into Eq. (2.62) yields

$$\frac{\hbar^2}{2m_e} \sum_{\mathbf{G}} |\mathbf{k}+\mathbf{G}|^2 c_{\nu,\mathbf{k}+\mathbf{G}}\, e^{i(\mathbf{k}+\mathbf{G})\cdot\mathbf{r}} + \frac{1}{V} \sum_{\mathbf{G},\mathbf{G}'} v_{\mathbf{G}'}^{\text{eff}}\, c_{\nu,\mathbf{k}+\mathbf{G}}\, e^{i(\mathbf{k}+\mathbf{G}+\mathbf{G}')\cdot\mathbf{r}} = \epsilon_{\nu,\mathbf{k}} \sum_{\mathbf{G}} c_{\nu,\mathbf{k}+\mathbf{G}}\, e^{i(\mathbf{k}+\mathbf{G})\cdot\mathbf{r}}, \tag{2.83}$$

where the indices of the eigenvalues, $\epsilon_i = \epsilon_{\nu,\mathbf{k}}$, have been adjusted to correspond to Eq. (2.82). Since the set of $\mathbf{G}$ vectors is infinite, we can shift the summation in the second term on the left

side to $\tilde{\mathbf{G}} = \mathbf{G} + \mathbf{G}'$ and then rename the index $\tilde{\mathbf{G}} \to \mathbf{G}$:

$$\frac{1}{V} \sum_{\mathbf{G},\mathbf{G}'} v_{\mathbf{G}'}^{\mathrm{eff}}\, c_{\nu,\mathbf{k}+\mathbf{G}}\, e^{i(\mathbf{k}+\mathbf{G}+\mathbf{G}')\cdot\mathbf{r}} = \frac{1}{V} \sum_{\tilde{\mathbf{G}},\mathbf{G}'} v_{\mathbf{G}'}^{\mathrm{eff}}\, c_{\nu,\mathbf{k}+\tilde{\mathbf{G}}-\mathbf{G}'}\, e^{i(\mathbf{k}+\tilde{\mathbf{G}})\cdot\mathbf{r}}$$

$$= \frac{1}{V} \sum_{\mathbf{G},\mathbf{G}'} v_{\mathbf{G}'}^{\mathrm{eff}}\, c_{\nu,\mathbf{k}+\mathbf{G}-\mathbf{G}'}\, e^{i(\mathbf{k}+\mathbf{G})\cdot\mathbf{r}}. \qquad (2.84)$$

Inserting Eq. (2.84) into Eq. (2.83) gives

$$\sum_{\mathbf{G}} \left[\left(\frac{\hbar^2}{2m_e}|\mathbf{k}+\mathbf{G}|^2 - \epsilon_{\nu,\mathbf{k}} \right) c_{\nu,\mathbf{k}+\mathbf{G}} + \frac{1}{V} \sum_{\mathbf{G}'} v_{\mathbf{G}'}^{\mathrm{eff}}\, c_{\nu,\mathbf{k}+\mathbf{G}-\mathbf{G}'} \right] e^{i(\mathbf{k}+\mathbf{G})\cdot\mathbf{r}} = 0, \qquad (2.85)$$

and finally, since Eq. (2.85) needs to be satisfied for all $\mathbf{r}$, we have:

$$\left(\frac{\hbar^2}{2m_e}|\mathbf{k}+\mathbf{G}|^2 - \epsilon_{\nu,\mathbf{k}} \right) c_{\nu,\mathbf{k}+\mathbf{G}} + \frac{1}{V} \sum_{\mathbf{G}'} v_{\mathbf{G}'}^{\mathrm{eff}}\, c_{\nu,\mathbf{k}+\mathbf{G}-\mathbf{G}'} = 0. \qquad (2.86)$$

Equation (2.86) is the final expression for the reciprocal Kohn-Sham equation. Similarly as Eq. (2.82), it couples only expansion coefficients $c_{\nu,\mathbf{k}+\mathbf{G}}$ for the same vector $\mathbf{k}$, i.e., it is block diagonal ($\alpha_i = \mathbf{k}$ and $\beta_j = \mathbf{G}$). This allows to treat $\mathbf{k}$ as a parameter and the corresponding eigenvalue equation independently of the equations for all the other $\mathbf{k}$ vectors. From a technical viewpoint, this fact allows to parallelize computations in a straightforward manner. The density of the $\mathbf{k}$ vectors, which we call k sampling in the following, becomes only important when calculating for instance the kinetic energy contribution to $\mathcal{F}^{\mathrm{KS}}$ from Eq. (2.67):

$$-\frac{\hbar^2}{2m_e} \sum_{\nu,\mathbf{k}} f_{\nu,\mathbf{k}} \int \varphi_{\nu,\mathbf{k}}(\mathbf{r}) \nabla^2 \varphi_{\nu,\mathbf{k}}(\mathbf{r}) d\mathbf{r} = \frac{\hbar^2}{2m_e} \sum_{\nu,\mathbf{k}} f_{\nu,\mathbf{k}} \sum_{\mathbf{G}} |\mathbf{k}+\mathbf{G}|^2\, |c_{\nu,\mathbf{k}+\mathbf{G}}|^2. \qquad (2.87)$$

Here, the summation, $\sum_i = \sum_{\nu,\mathbf{k}}$, and the occupation numbers, $f_i = f_{\nu,\mathbf{k}}$, have been adjusted to correspond to Eq. (2.82) and the orthonormality of plane waves has been used. In principle, the k sampling needs to be infinitely dense (within the first Brillouin zone) for a macroscopic crystal. It turns out however that the dependence of $\mathcal{F}^{\mathrm{KS}}$ (and other properties) on $\mathbf{k}$ is smooth and a rather small mesh can be used to accurately describe materials properties. [An example for the dependence of $\epsilon_{\nu,\mathbf{k}}$ on $\mathbf{k}$ along special high symmetry directions (introduced in Sec. 2.4.1) including additionally the volume dependence is given in Fig. 2.1 for the case of aluminum.] At this point it is however important to distinguish metallic systems as investigated in the present study from semiconductors and insulators. For the latter, rather small k samplings are often sufficient. In contrast, for metals, denser meshes are required as a consequence of the sharp interface at the Fermi surface. In calculating thermodynamic properties of metals the convergence aspect of the k sampling becomes therefore particularly important. This will be investigated in Sec. 3.4.2. In performing k sampling tests, one should consider that a larger crystal cell in real space leads to a smaller Brillouin zone in reciprocal space so that less $\mathbf{k}$ vectors suffice for the sums in Eq. (2.87). For a convenient comparison between the k samplings of different supercells, we will use the unit kp·atom, which is obtained by multiplying the number of k points with the number of atoms in the supercell, and which takes the inverse relation between real and reciprocal spaces into account.

Equation (2.86) can be considered as a matrix equation in $\mathbf{G}$ and $\mathbf{G}'$ and its solution (with the aim of determining the $c_{\nu,\mathbf{k}+\mathbf{G}}$) scales therefore as $s(g) = g^3 \times g^3$ where g is the number of

G vectors along 1 dimension. In principle, g would need to go to infinity. Similarly as for the k sampling, it turns out however that (if the PAW method is employed) only small **G** vectors contribute significantly to the expansion in Eq. (2.82). We therefore introduce a plane wave cutoff, E^{cut}, such that only **G** vectors are considered which fulfill

$$\frac{\hbar^2}{2m_e}|\mathbf{G}+\mathbf{k}|^2 < E^{\mathrm{cut}} \qquad \Rightarrow \qquad |\mathbf{G}+\mathbf{k}| < \sqrt{\frac{2m_e}{\hbar^2}E^{\mathrm{cut}}}, \qquad (2.88)$$

or using the reduced quantities explained in App. A.1.2:

$$|\mathbf{G}_{a_0}+\mathbf{k}_{a_0}| < \sqrt{2E_h^{\mathrm{cut}}} \qquad \text{and} \qquad |\mathbf{G}_{a_0}+\mathbf{k}_{a_0}| < \sqrt{E_r^{\mathrm{cut}}}. \qquad (2.89)$$

Thus, the allowed vectors lie within a sphere of radius $\sqrt{2m_e E^{\mathrm{cut}}/\hbar^2}$. Let us now reconsider the estimation from the beginning of this section, i.e., 16 GB of memory allowing to store a matrix of size $63,000 \times 63,000$. For the purpose of an estimation, we can choose $\mathbf{k} = 0$ and further assume that the number of plane waves, N^{PW}, inside the sphere can be obtained from the volume of the sphere, $4\pi/3\,(2m_e E^{\mathrm{cut}}/\hbar^2)^{3/2}$, divided by the volume of the Brillouin zone, $\mathbf{b}_1 \cdot (\mathbf{b}_2 \times \mathbf{b}_3) = 8\pi^3/V$, i.e.:

$$N^{\mathrm{PW}} \approx \frac{V}{6\pi^2}\left(\frac{2m_e}{\hbar^2}E^{\mathrm{cut}}\right)^{3/2}. \qquad (2.90)$$

Choosing aluminum as an example, we can take E^{cut} to be 14 Ry (see App. A.1.2 for atomic units) which is a very well converged cutoff (cf. Sec. 3.4.4.3). Solving Eq. (2.90) for the real space volume V and using the maximum allowed $N^{\mathrm{PW}} = 63,000$ yields $V \approx 40^3 a_0^3$, i.e., significantly larger than the $V \approx 4^3 a_0^3$ achieved within the real space approach. Thus, by rewriting the Kohn-Sham equation in reciprocal space and introducing a plane wave cutoff we are able to address cell sizes which are large enough to calculate converged thermodynamic properties (cf. the discussion at the beginning of the section). We stress however that the presented estimation has primarily relied on the information about the converged plane wave cutoff obtained from the detailed convergence tests performed within this work. Such convergence issues become particularly important when calculating finite temperature properties.

The transition from the real to the reciprocal space changes the scaling of the Kohn-Sham approach as follows:

$$\underbrace{s^{\mathrm{KS}} = N^{\mathrm{it}} \cdot (N_{\mathrm{mesh}}^3 \times N_{\mathrm{mesh}}^3)}_{\text{Real space Kohn-Sham equation}} \quad \rightarrow \quad \underbrace{\begin{aligned} s^{\mathrm{KS}} &= N^{\mathrm{it}} N_k \cdot \left[N^{\mathrm{PW}} \times N^{\mathrm{PW}}\right] \\ &= N^{\mathrm{it}} N_k \cdot \left[(a^{\mathrm{lat}})^3 (E^{\mathrm{cut}})^{3/2} \times (a^{\mathrm{lat}})^3 (E^{\mathrm{cut}})^{3/2}\right]. \end{aligned}}_{\text{Reciprocal Kohn-Sham equation}} \qquad (2.91)$$

Here, we have introduced N_k, the number of **k** vectors included in the k sampling, to account for the fact that the matrix constructed from the N^{PW} **G** and N^{PW} **G**$'$ vectors needs to be solved for each such **k** vector. We have also used Eqs. (2.80) and (2.90) to express N^{PW} in terms of a^{lat} and E^{cut}. In fact, in actual implementations, the solution of the Kohn-Sham equation does not scale as given in Eq. (2.91). Highly optimized routines allow to improve the scaling considerably, however, the actual realization and implementation is far more complex (and can differ among different codes) than the presented derivation, which aims at introducing the key convergence parameters, k sampling and plane wave cutoff. We briefly comment on four important ideas which further reduce the involved computational effort, while details can be found for example in Refs. [46] or [47].

The first idea is to calculate only the energetically lowest $\epsilon_{\nu,\mathbf{k}}$, in particular those that will be actually occupied by the electrons at thermal equilibrium. For such a purpose, very efficient techniques have been developed [46] which do not need to diagonalize the Hamiltonian matrix as a whole. They rely instead on self consistent minimization techniques which use computationally far less expensive operations as compared to a direct diagonalization. The scaling is then approximately linear with N_e^3 (the cubic dependence is due to the necessary orthogonalization of the electronic orbitals). The second idea is to use specific mixing schemes for the electronic density within the self consistency cycle, Eq. (2.66). The density as obtained from the Kohn-Sham equation is not taken directly to calculate the effective potential but it is mixed with previous densities. This procedure introduces a certain memory effect which reduces N^{it} the number of self consistency cycles. The third idea is to calculate not all of the contributions to the Kohn-Sham Hamiltonian in reciprocal space, but to take the most convenient representation (reciprocal or real space) for each contribution. For instance, a good representation for the kinetic energy is the reciprocal space in which it is diagonal. In contrast, the exchange-correlation energy is diagonal in real space in which it is therefore calculated. Such a dual space approach is only possible because there are methods available (Fast Fourier Transforms [48]) which transform quantities from one to the other space very efficiently. Finally, the fourth idea is to employ point symmetries to reduce the k sampling to include only the inequivalent or irreducible $\mathbf{k}$ vectors, i.e., $N_k \rightarrow N_k^{\text{irr}}$, with N_k^{irr} the number of irreducible $\mathbf{k}$ vectors. Symmetries will be considered in more detail in the context of the quasiharmonic approximation used to describe nuclei motion (Sec. 2.3.4). Based on these optimizations, the solution of the Kohn-Sham equation scales as (cf. App. A.1.1 for the notation convention)

$$
s^{\text{KS}} = N^{\text{it}}\, N_k \cdot \left[(a^{\text{lat}})^3 (E^{\text{cut}})^{3/2} \times (a^{\text{lat}})^3 (E^{\text{cut}})^{3/2} \right] \quad \rightarrow \quad
\begin{aligned}
s^{\text{KS}}(a^{\text{lat}}, E^{\text{cut}}, N_k^{\text{irr}}, N_e, N^{\text{it}}) &= \\
= \underbrace{(a^{\text{lat}})^3\, (E^{\text{cut}})^{3/2}\, N_k^{\text{irr}}\, N_e^3\, N^{\text{it}}}_{\text{Optimized Kohn-Sham equation}},
\end{aligned}
$$
$$(2.92)$$

which applies to both CPU time and memory.

2.1.8 LAPW+lo, PAW, and pseudopotentials

In the vicinity of the nuclei positions $\mathbf{R}_I$, the effective Kohn-Sham potential, $v^{\text{eff}}(\mathbf{r})$, is dominated by the strong Coulomb repulsion produced by the nuclei, $v(\mathbf{r}) = \sum_I^{N_n} Z_I e^2 / (4\pi\epsilon_0 |\mathbf{r} - \mathbf{R}_I|)$ [cf. Eqs. (2.49) and (2.51)]. This causes the Kohn-Sham wave functions $\varphi_{\nu,\mathbf{k}}(\mathbf{r})$ to oscillate strongly in this region which can be understood as follows: Classically, if an electron approaches the nucleus its potential energy decreases while the kinetic energy increases such as to keep the total energy constant. Quantum mechanically, an increase in kinetic energy corresponds to an increase in the oscillations of the wave function.

A plane wave description of these strong oscillations would require a large cutoff in Eq. (2.88) obviating a treatment in reciprocal space. In order to circumvent this difficulty, the following decomposition of the full crystal wave function might seem reasonable:

$$
\varphi_{\nu,\mathbf{k}}(\mathbf{r}) = \underbrace{\widetilde{\varphi}_{\nu,\mathbf{k}}(\mathbf{r} \notin \Omega_I)}_{\substack{\text{Smooth wave function,} \\ \text{suited for plane waves}}} + \underbrace{\varphi_{\nu,\mathbf{k}}^{\Omega}(\mathbf{r} \in \Omega_I)}_{\substack{\text{Strong oscillations at nucleus,} \\ \text{suited for atomic basis}}} .
$$
$$(2.93)$$

Here, the real space has been divided into two distinct regions: One region consists of non-overlapping spheres which are centered at the ionic positions. The sphere corresponding to ion

I has a volume of Ω_I. In this region, $\varphi_{\nu,\mathbf{k}}^{\Omega}(\mathbf{r} \in \Omega_I)$ describes the strongly oscillating crystal wave function and it is well suited to be described by an atomic like basis. The other region consists of all the remaining space not covered by the spheres. Here, $\widetilde{\varphi}_{\nu,\mathbf{k}}(\mathbf{r} \notin \Omega_I)$ describes the smooth crystal wave function and it is well suited for a plane wave description.

It turns out however that a major problem of Eq. (2.93) is the matching of the two wave functions from the distinct regions. This problem has two aspects: 1) The wave functions need to match in real space at the interfaces of the spheres. This can be accomplished efficiently. 2) The wave functions need to match also in energy space. This requires an additional self consistency loop which is computationally highly expensive [49]. One possible approach to overcome 2) is to perform the energy matching only up to the first order of a Taylor expansion. Since this so called linearization procedure is an approximation, additional orbitals inside Ω_I (referred to as local orbitals) are introduced to reduce the corresponding error. Methods based on this approach are called linearized augmented plane waves plus local orbitals (LAPW+lo) and despite the approximation introduced by the linearization, they are considered as the most accurate methods presently available for solving the Kohn-Sham equation [50]. They are however also the computationally most expensive methods and, for the system sizes required in this study (up to 500 atoms), we had to apply a numerically more efficient method, the projector augmented wave (PAW) approach introduced next. Nonetheless, we will use the LAPW+lo method as a reference for validating the so called PAW potentials using smaller system sizes.

The PAW method [51] approaches the time consuming energy matching problem (and in fact the real space matching at the same time) from a conceptually different direction. Within PAW the decomposition in Eq. (2.93) is reformulated to:

$$\varphi_{\nu,\mathbf{k}}(\mathbf{r}) = \underbrace{\widetilde{\varphi}_{\nu,\mathbf{k}}(\mathbf{r})}_{\substack{\text{Smooth wave function} \\ \text{over the full crystal}}} - \underbrace{\widetilde{\varphi}_{\nu,\mathbf{k}}^{\Omega}(\mathbf{r} \in \Omega_I)}_{\substack{\text{Smooth wave function} \\ \text{inside spheres}}} + \underbrace{\varphi_{\nu,\mathbf{k}}^{\Omega}(\mathbf{r} \in \Omega_I)}_{\substack{\text{Strongly oscillating wave} \\ \text{function inside spheres}}} . \qquad (2.94)$$

Here, in contrast to Eq. (2.93), the smooth wave function $\widetilde{\varphi}_{\nu,\mathbf{k}}(\mathbf{r})$ is allowed to extend over the full crystal, i.e., also in the spheres. To compensate for the contribution of $\widetilde{\varphi}_{\nu,\mathbf{k}}(\mathbf{r})$ inside Ω_I, a new smooth function $\widetilde{\varphi}_{\nu,\mathbf{k}}^{\Omega}(\mathbf{r} \in \Omega_I)$ is introduced which equals $\widetilde{\varphi}_{\nu,\mathbf{k}}(\mathbf{r})$ in Ω_I and is zero otherwise. Therefore, Eq. (2.94) is effectively identical to Eq. (2.93). A key point of the PAW method is now to treat

$$\Delta\varphi_{\nu,\mathbf{k}}^{\Omega}(\mathbf{r} \in \Omega_I) = \varphi_{\nu,\mathbf{k}}^{\Omega}(\mathbf{r} \in \Omega_I) - \widetilde{\varphi}_{\nu,\mathbf{k}}^{\Omega}(\mathbf{r} \in \Omega_I) \qquad (2.95)$$

as a single object. In particular, the aim is to construct a convenient basis to expand it, i.e., a basis from which only a few elements suffice to describe $\Delta\varphi_{\nu,\mathbf{k}}^{\Omega}(\mathbf{r} \in \Omega_I)$ accurately. This approach has the following major advantage. The matching in real space and energy space is fully incorporated into the construction of the basis. This construction is however performed once and can be then applied to any PAW calculation. In a sense, the matching, in particular the time consuming self consistency cycle for the energy matching, is outsourced from the actual calculation into the PAW basis of $\Delta\varphi_{\nu,\mathbf{k}}^{\Omega}$.

The actual construction of a convenient basis for $\Delta\varphi_{\nu,\mathbf{k}}^{\Omega}$ is an involved matter and in fact based on empiricism and experience. We mention briefly only the key aspects. The expansion reads:

$$\Delta\varphi_{\nu,\mathbf{k}}^{\Omega}(\mathbf{r} \in \Omega) = \sum_{I,\mu} c_{I,\mu} \Delta\phi_{I,\mu}(\mathbf{r} - \mathbf{R}_I) = \sum_{I,\mu} c_{I,\mu} \left[\phi_{I,\mu}(\mathbf{r} - \mathbf{R}_I) - \widetilde{\phi}_{I,\mu}(\mathbf{r} - \mathbf{R}_I) \right]. \qquad (2.96)$$

Here, $c_{I,\mu}$ are the expansion coefficients and $\Delta\phi_{I,\mu}$ the basis elements with μ running over basis

functions for a single ion I at $\mathbf{R}_I$. The basis elements $\Delta\phi_{I,\mu}$ are constructed from two parts $\phi_{I,\mu}$ and $\widetilde{\phi}_{I,\mu}$. The first part $\phi_{I,\mu}$ is called the atomic partial basis and is readily accessible. It corresponds to a basis of a single isolated ion, i.e., to the eigenfunctions of a corresponding Kohn-Sham equation. Constructed in this way, it turns out empirically that only a few elements $\phi_{I,\mu}$ suffice to accurately describe $\varphi_{\nu,\mathbf{k}}^{\Omega}$. Therefore, the second part $\widetilde{\phi}_{I,\mu}$, which is called auxiliary partial basis, needs to be adjusted such that $\widetilde{\varphi}_{\nu,\mathbf{k}}^{\Omega}$ is removed from $\varphi_{\nu,\mathbf{k}}^{\Omega}$ in order to satisfy Eq. (2.95). Further, each element $\widetilde{\phi}_{I,\mu}$ needs to approach its dual part $\phi_{I,\mu}$ smoothly at the interface of Ω_I in order to guarantee that $\Delta\varphi_{\nu,\mathbf{k}}^{\Omega}$ vanishes outside Ω_I. In practice, an auxiliary partial basis is obtained by solving a Kohn-Sham equation of an artificial isolated ion with the strong Coulomb potential replaced by an artificially smooth potential. This potential is fine tuned such that the corresponding eigenfunctions have the desired properties. Finally, also the coefficients $c_{I,\mu}$ need to be determined. For that purpose, note that $\Delta\varphi_{\nu,\mathbf{k}}^{\Omega}$ needs to depend on $\widetilde{\varphi}_{\nu,\mathbf{k}}(\mathbf{r})$ due to $\widetilde{\varphi}_{\nu,\mathbf{k}}^{\Omega}$. Imposing additionally (for simplicity) a linearity constraint one obtains [51]:

$$c_{I,\mu} = \langle\widetilde{p}_{I,\mu}|\widetilde{\varphi}_{\nu,\mathbf{k}}\rangle, \qquad \text{with} \qquad \langle\widetilde{p}_{I,\mu}|\widetilde{\phi}_{J,\xi}\rangle = \delta_{I,J}\delta_{\mu,\xi}. \qquad (2.97)$$

Here, $\widetilde{p}_{I,\mu} = \widetilde{p}_{I,\mu}(\mathbf{r})$ are the so called projector functions. They are typically constructed from the $\widetilde{\phi}_{I,\mu}$ with some optimized analytical dependence [51, 52].

In summary, there are three sets of functions $\{\phi_{I,\mu}\}$, $\{\widetilde{\phi}_{I,\mu}\}$, and $\{\widetilde{p}_{I,\mu}\}$ within the PAW method which need to be determined for each species and also for each xc functional separately beforehand. Their dependence is then stored in so called PAW potentials and imported in actual PAW calculations. In fact, since these functions are solutions to isolated ions, only their radial part needs to be stored explicitly while the angular part can be treated efficiently analytically.

In principle, the PAW method is a formally exact way to transform the original wave function. In practice, the expansion in Eq. (2.96) is finite and the quality of the basis must be checked, i.e., the quality of the PAW potential. We use here PAW potentials [53] as provided with the VASP code [46]. In addition to the finite basis approximation, these potentials treat only the valence electrons explicitly while the core electrons are treated within the frozen core approximation. This approximation exploits the fact that for most materials properties the strongly localized core electrons do not participate in the chemical bonding and their wave functions retain the form found for isolated atoms, i.e., they are frozen [54]. To validate if both approximations, the finite basis and the frozen core, are justifiable, the reliability of the used PAW potentials will be cross checked against the LAPW+lo method (Sec. 4.1.2). This comparison has in fact a further advantage which concerns the heavier elements in our study (Ir, Pt, Au). For these elements, the core electrons are expected to behave relativistically, since they attain high kinetic energies. Such effects (within the scalar relativistic approximation) are in principle included during the construction of the frozen core for the PAW potentials. Since the employed LAPW+lo method explicitly contains scalar relativistic effects for the core electrons, the cross checks will implicitly include also this evaluation.

We need to comment on an important consequence of the wave function decomposition as used in the PAW method. This issue will lead to the introduction of a new convergence parameter. The Kohn-Sham equation within the PAW method is formulated in terms of the smooth wave functions $\widetilde{\varphi}_{\nu,\mathbf{k}}$ and reads [53, 55]:

$$\hat{H}^{\mathrm{PAW}}\,\widetilde{\varphi}_{\nu,\mathbf{k}} = \epsilon_{\nu,\mathbf{k}}\,\hat{O}\,\widetilde{\varphi}_{\nu,\mathbf{k}}. \qquad (2.98)$$

Here, $\hat{O}$ is the overlap matrix which is given by

$$\hat{O} = \hat{1} + \sum_{I,J,\mu,\xi} |\widetilde{p}_{I,\mu}\rangle \left[\langle\phi_{I,\mu}|\phi_{J,\xi}\rangle - \langle\widetilde{\phi}_{I,\mu}|\widetilde{\phi}_{J,\xi}\rangle\right] \langle\widetilde{p}_{J,\xi}|, \qquad (2.99)$$

and which renders Eq. (2.98) a generalized eigenvalue problem. Further in Eq. (2.98), $\hat{H}^{\mathrm{PAW}}$ is the PAW Hamiltonian which is more complex than the original Kohn-Sham Hamiltonian $\hat{H}^{\mathrm{KS}}$, Eq. (2.63), due to non-local terms. It reads[5] [53]

$$\hat{H}^{\mathrm{PAW}} = \hat{H}^{\mathrm{PAW}}[\widetilde{\rho}, \rho^{\Omega}, \widetilde{\rho}^{\Omega}, \rho^{\mathrm{aug}}]$$

$$= \underbrace{\hat{H}^{\mathrm{rKS}}[\widetilde{\rho} + \rho^{\mathrm{aug}}]}_{\substack{\text{Local;} \\ \text{plane waves}}} + \sum_{I,J,\mu,\xi} |\widetilde{p}_{I,\mu}\rangle \underbrace{\left[\langle \phi_{I,\mu}| \, \hat{H}^{\mathrm{rKS}}[\rho^{\Omega}] \, |\phi_{J,\xi}\rangle - \langle \widetilde{\phi}_{I,\mu}| \, \hat{H}^{\mathrm{rKS}}[\widetilde{\rho}^{\Omega} + \rho^{\mathrm{aug}}] \, |\widetilde{\phi}_{J,\xi}\rangle \right]}_{\text{Non local; spherical basis on radial grid}} \langle \widetilde{p}_{J,\xi}|,$$

$$(2.100)$$

where $\hat{H}^{\mathrm{rKS}}$ is a reduced Kohn-Sham Hamiltonian given by

$$\hat{H}^{\mathrm{rKS}} = \hat{H}^{\mathrm{KS}} - v(\mathbf{r}), \tag{2.101}$$

and where the electronic charge densities $\widetilde{\rho}$, ρ^{Ω}, $\widetilde{\rho}^{\Omega}$, and ρ^{aug} read:

$$\text{Plane wave grid} \;\rightarrow\; \widetilde{\rho}(\mathbf{r}) \;=\; \sum_{\nu,\mathbf{k}} f_{\nu,\mathbf{k}} |\widetilde{\varphi}_{\nu,\mathbf{k}}(\mathbf{r})|^2,$$

$$\text{Radial grid} \quad\rightarrow\; \begin{cases} \rho^{\Omega}(\mathbf{r}) \;=\; \displaystyle\sum_{I,J,\mu,\xi} \phi_{I,\mu}^*(\mathbf{r} - \mathbf{R}_I)\, \phi_{J,\xi}(\mathbf{r} - \mathbf{R}_I) \; \sum_{\nu,\mathbf{k}} f_{\nu,\mathbf{k}} \, \langle \widetilde{\varphi}_{\nu,\mathbf{k}}|\widetilde{p}_{I,\mu}\rangle \langle \widetilde{p}_{J,\xi}|\widetilde{\varphi}_{\nu,\mathbf{k}}\rangle, \\[2ex] \widetilde{\rho}^{\Omega}(\mathbf{r}) \;=\; \displaystyle\sum_{I,J,\mu,\xi} \widetilde{\phi}_{I,\mu}^*(\mathbf{r} - \mathbf{R}_I)\, \widetilde{\phi}_{J,\xi}(\mathbf{r} - \mathbf{R}_I) \; \sum_{\nu,\mathbf{k}} f_{\nu,\mathbf{k}} \, \langle \widetilde{\varphi}_{\nu,\mathbf{k}}|\widetilde{p}_{I,\mu}\rangle \langle \widetilde{p}_{J,\xi}|\widetilde{\varphi}_{\nu,\mathbf{k}}\rangle, \end{cases}$$

$$\text{Both grids} \quad\rightarrow\; \rho^{\mathrm{aug}}(\mathbf{r}) \;=\; \text{augmentation (or compensation) charges.} \tag{2.102}$$

We have indicated in Eqs. (2.100) and (2.102) in which basis, i.e., on which grid, the various terms are calculated. Similarly as for the wave function, Eq. (2.94), the PAW Hamiltonian and the PAW charge densities separate into a smooth part which can be conveniently calculated on a plane wave grid and an oscillating part inside the spheres which can be efficiently treated on a radial grid. In this respect, a note on the terms $\langle \widetilde{\varphi}_{\nu,\mathbf{k}}|\widetilde{p}_{I,\mu}\rangle$ which enter ρ^{Ω} and $\widetilde{\rho}^{\Omega}$ might be useful. These terms must be first calculated on a plane wave grid and thus the projector functions need to be transformed from their radial representation onto plane waves. However, the latter transformation needs to be performed only once at the beginning of the calculation and further $\langle \widetilde{\varphi}_{\nu,\mathbf{k}}|\widetilde{p}_{I,\mu}\rangle$ includes a sum over the reciprocal vectors which renders these quantities mere numbers multiplying the radial part $[\phi_{I,\mu}^*(\mathbf{r} - \mathbf{R}_I)\, \phi_{J,\xi}(\mathbf{r} - \mathbf{R}_I)]$. Also, possibly large reciprocal vectors (i.e., beyond E^{cut}) in the plane wave representation of the projectors are of no concern, since they are simply cut of when multiplied with the corresponding zero components from $\widetilde{\varphi}_{\nu,\mathbf{k}}$.

A complete separation of the PAW Hamiltonian into plane wave and radial components, however, cannot be achieved. There is one quantity the augmentation charge ρ^{aug} which enters both Hamiltonian parts and which must be therefore calculated on both grids. This fact is indicated in Eq. (2.100) by the blue color. The origin of the augmentation charge is the need to cancel a

---

[5]For the sake of clarity, we have omitted here the contribution of the core charges (corresponding to the quantities n_c, $\widetilde{n}_c$, n_{Zc}, and $\widetilde{n}_{Zc}$ in Ref. [53]) and of two further terms connected to the augmentation charge (corresponding to the terms $\sum_L \int \widetilde{v}_{\mathrm{eff}}(\mathbf{r}) \hat{Q}_{ij}^L(\mathbf{r}) d\mathbf{r}$ and $\sum_L \int_{\Omega r} \widetilde{v}_{\mathrm{eff}}^1(\mathbf{r}) \hat{Q}_{ij}^L(\mathbf{r}) d\mathbf{r}$ in Ref. [53]). The omitted terms however do not change the conclusions drawn in the main text.

spurious electrostatic interaction between the charges in different spheres. An actual construction scheme for ρ^{aug} is given for instance in Ref. [53]. The point of concern here is that its plane wave representation needs to contain components significantly beyond E^{cut}. In order to avoid an increase in E^{cut}, a dual grid technique is frequently employed [53, 55]. Within this approach, a second, dense real space grid (augmentation grid; corresponding to high reciprocal components) is introduced in addition to the usual plane wave grid, in order to treat the augmentation charges efficiently, while the "usual" plane wave grid is used for the time consuming operations of the Kohn-Sham equation [53]. The density of the augmentation grid however corresponds to a new, third convergence parameter besides the k sampling and plane wave cutoff. We will investigate in Sec. 3.4.1 the influence of the augmentation grid on thermodynamic properties.

Finally in this section, we discuss the pseudopotential method which is an approximation to the frozen core PAW method. In particular, we focus on the norm conserving pseudopotential approach [56] in the separable Kleinman-Bylander form [57] which has the following Kohn-Sham equation

$$\hat{H}^{\mathrm{PP}}\,\widetilde{\varphi}_{\nu,\mathbf{k}} \;=\; \epsilon_{\nu,\mathbf{k}}\,\widetilde{\varphi}_{\nu,\mathbf{k}}, \tag{2.103}$$

with the pseudopotential (PP) Hamiltonian given by:

$$\hat{H}^{\mathrm{PP}}[\widetilde{\rho}] \;=\; \hat{H}^{\mathrm{rKS}}[\widetilde{\rho}] \;+\; \underbrace{\hat{V}^{\mathrm{PP}}_{I,\mu'} \;+\; \sum_{I,\mu}\,|\Delta\hat{V}_{I,\mu}\widetilde{\phi}^{\mathrm{PP}}_{I,\mu}\rangle\left[\langle\widetilde{\phi}^{\mathrm{PP}}_{I,\mu}|\,\Delta\hat{V}_{I,\mu}\,|\widetilde{\phi}^{\mathrm{PP}}_{I,\mu}\rangle\right]^{-1}\langle\widetilde{\phi}^{\mathrm{PP}}_{I,\mu}\Delta\hat{V}_{I,\mu}|}_{\text{PP contribution; independent of density, i.e., }\textbf{fixed}\text{ during calculation}}. \tag{2.104}$$

Here, $\Delta\hat{V}_{I,\mu} = \hat{V}^{\mathrm{PP}}_{I,\mu} - \hat{V}^{\mathrm{PP}}_{I,\mu'}$ and the $\widetilde{\phi}^{\mathrm{PP}}_{I,\mu}$ are obtained from solving a Kohn-Sham equation of an artificial isolated ion with the strong Coulomb potential replaced by $\hat{V}^{\mathrm{PP}}_{I,\mu}$. This procedure is analogous to determining the auxiliary partial basis $\widetilde{\phi}_{I,\mu}$ for the PAW potentials. In fact, the solutions $\phi_{I,\mu}$ to a Kohn-Sham calculation of an isolated atom (including the Coulomb potential) are also here used to determine the shape of $\widetilde{\phi}^{\mathrm{PP}}_{I,\mu}$. In particular, the artificial potential $\hat{V}^{\mathrm{PP}}_{I,\mu}$ is fine tuned such that:

1) the eigenvalues corresponding to $\widetilde{\phi}^{\mathrm{PP}}_{I,\mu}$ equal the eigenvalues corresponding to $\phi_{I,\mu}$,

2) $\widetilde{\phi}^{\mathrm{PP}}_{I,\mu}$ and $\phi_{I,\mu}$ match outside Ω_I,

3) the norms $\int|\widetilde{\phi}^{\mathrm{PP}}_{I,\mu}|^2 d\mathbf{r}$ and $\int|\phi_{I,\mu}|^2 d\mathbf{r}$ are equal inside Ω_I (norm conservation),

4) the radial part of $\widetilde{\phi}^{\mathrm{PP}}_{I,\mu}$ has no nodes.

Further in Eq. (2.104), $\hat{V}^{\mathrm{PP}}_{I,\mu'}$ is the so called local potential and corresponds to $\hat{V}^{\mathrm{PP}}_{I,\mu}$ for a fixed $\mu = \mu'$. For a sufficiently large basis $\widetilde{\phi}^{\mathrm{PP}}_{I,\mu}$ (with respect to the atomic quantum number μ), the choice of $\hat{V}^{\mathrm{PP}}_{I,\mu'}$ is arbitrary. Since however the summation in Eq. (2.104) is typically truncated for lower μ, the local potential needs to be chosen such that it adequately reproduces the scattering properties in the higher angular momentum channels [56]. As in the case of the PAW potentials, $\widetilde{\phi}^{\mathrm{PP}}_{I,\mu}$, $\hat{V}^{\mathrm{PP}}_{I,\mu'}$, and $\widetilde{\phi}^{\mathrm{PP}}_{I,\mu}$ are determined beforehand, stored on radial grids in so called pseudopotentials, and then imported during actual calculations.

The reason for introducing the norm conserving pseudopotential method are the following advantages as compared to the PAW method:

1) The overlap matrix $\hat{O}$, Eq. (2.99), reduces to $\hat{1}$ due to norm conservation. This reduces the pseudopotential Kohn-Sham equation, Eq. (2.103), to an ordinary eigenvalue problem which is computationally less expensive than a generalized one.

2) Another consequence of norm conservation is that the spurious electrostatic interaction between different spheres is removed. Therefore, the augmentation charge needs not to be introduced and the only convergence parameters remain the k sampling and the plane wave cutoff.

3) The PP contribution to Eq. (2.104) is independent of the electronic density. Therefore, it needs to be calculated once at the beginning of a calculation and does not have to be self consistently updated. In fact, the PP contribution can be systematically derived from a Taylor expansion of the non-local contribution to the PAW Hamiltonian, Eq. (2.100) [58]. The local potential $\hat{V}_{I,\mu'}^{\mathrm{PP}}$ corresponds then to the first order term and the non-local term of the PP contribution, i.e., the third term in Eq. (2.104), corresponds to the second order term. In this respect, the PAW potential can be viewed as a dynamic pseudopotential which adapts to the actual environment.

4) For some elements (aluminum in the present case), it is possible to generate pseudopotentials which yield accurate results based on smoother wave functions as compared to the PAW. Thus, the employed E^{cut} can be chosen smaller reducing the computational effort.

We will apply the pseudopotential approach for the time consuming calculations of anharmonic contributions in aluminum. For the other elements in this study the pseudopotential method is not well suited. It would produce "harder" wave functions than the PAW method, i.e., wave functions with larger reciprocal components, especially for the transition metals [59].

2.2 Capturing electronic bonding effectively: The EAM approach

DFT, the Kohn-Sham ansatz, the periodic representation, and the PAW method allow to solve quantum mechanical electronic systems that are not addressable using the original electronic Schrödinger equation, Eq. (2.38). At present, structures of up to ≈ 1000 atoms can be investigated based on the combination of these approaches. As shown in Sec. 3.4.3, these system sizes are sufficient to calculate accurate thermodynamic properties of elementary crystalline metals as intended here. In general however, a variety of materials science issues will not be describable with this size restriction. An example is the study of grain boundary migration which makes system sizes of several $10,000$ atoms necessary [60]. Additionally, there is often also a time restriction when considering dynamical phenomena. To address such issues nonetheless, the application of empirical approaches is unavoidable. Such approaches capture the electronic bonding only effectively and are therefore orders of magnitude faster than DFT but consequently significantly less accurate. For metals, one particularly convenient empirical approach is the embedded atom method (EAM) [61]. So far however, a well founded evaluation of the capability of the EAM approach to yield sound thermodynamic properties up to the melting point, was hampered by the lack of reference data. Based on our DFT calculations we will be able to fill this gap. In particular, we will investigate three different EAM parametrizations for aluminum introduced in Sec. 4.5. In the following we discuss briefly the theoretical background of the EAM approach, while details can be found for instance in Ref. [61].
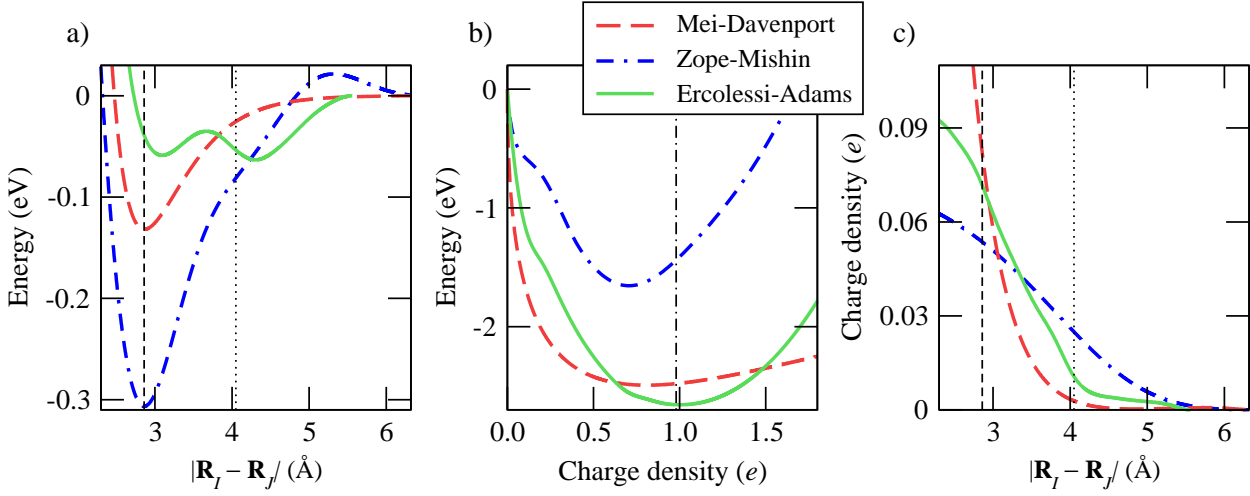
Figure 2.3: The three EAM parametrizations for aluminum (Mei-Davenport [62], Zope-Mishin [63], and Ercolessi-Adams [64]) employed in this work. a) The pair potential v^{pair} as a function of the distance between two atoms. The vertical dashed (dotted) line marks the distance to the first (second) nearest neighbor in fcc aluminum. Both distances are similar for all parametrizations. b) The embedding energy f^{emb} as a function of the local density ρ_I, which is the sum of charge densities of all neighboring atoms inside a certain cutoff radius. The charge density is given in units of the electronic charge e. The vertical dot-dashed line marks ρ_I for fcc aluminum at the equilibrium lattice constant. c) Charge density ρ^{at} as a function of the distance between two atoms. The meaning of the vertical lines is as in a).

The total energy E^{EAM} of an elementary material composed of N_n atoms reads within the EAM approach [61]

$$E^{\text{EAM}}(\{\mathbf{R}_I\}) = \frac{1}{2} \sum_{I}^{N_n} \sum_{J \neq I}^{N_n} v^{\text{pair}}(|\mathbf{R}_I - \mathbf{R}_J|) + \sum_{I}^{N_n} f^{\text{emb}}(\rho_I), \qquad (2.105)$$

with the local electron density ρ_I given by:

$$\rho_I = \sum_{J \neq I}^{N_n} \rho_J^{\text{at}}(|\mathbf{R}_I - \mathbf{R}_J|). \qquad (2.106)$$

Equation (2.105) provides a means to calculate the energy for any given atomic configuration $\{\mathbf{R}_I\}$ using only the three one dimensional and beforehand parametrized functions v^{pair}, f^{emb}, and ρ^{at}. Examples for these functions are given in Fig. 2.3. The pair potential v^{pair} can be interpreted as an electrostatic interaction between two atoms [61]. If v^{pair} would be the only term contributing to E^{EAM}, the bond strength would be coordination independent, i.e., the bond energy of two atoms I and J would always be a constant regardless of how many further atoms are placed near I and J. This coordination independence strikingly contradicts the true physical behavior observed in metallic systems [61]. The key idea of the EAM approach is to introduce an embedding energy f^{emb} which accounts exactly for this missing dependence. It is a function of the local electron density ρ_I which is produced by the spherically symmetric atomic densities ρ_J^{at} of all atoms inside a certain cutoff radius, except for I.

The EAM approach can be also motivated by starting with the Kohn-Sham expression Eq. (2.68) [in fact the $T = 0$ K version of Eq. (2.68) is used] and performing two crude approximations which

lead directly to Eq. (2.105) [61]. Despite this formal connection, however, no unique way exists to determine v^{pair}, f^{emb}, and ρ^{emb} from an underlying theory [65]. Consequently, various schemes have been developed and we discuss three possibilities in Sec. 4.5. Assuming that we have determined these functions, Eq. (2.105) allows to treat system sizes in the range of 10^7 atoms on present day high performance computers [66].

In order to show how the EAM approach is incorporated into the so far discussed methodology, let us reconsider Eqs. (2.33) to (2.36) and combine them with Eq. (2.105):

$$E^{\mathrm{EAM}}(\{\mathbf{R}_I\}) = \frac{1}{2}\sum_I^{N_n}\sum_{J \neq I}^{N_n} v^{\mathrm{pair}}(|\mathbf{R}_I - \mathbf{R}_J|) + \sum_I^{N_n} f^{\mathrm{emb}}(\rho_I) \tag{2.107}$$

$$\left\{ \hat{T}^{\mathrm{nuc}} + \hat{1}\, E^{\mathrm{EAM}}(\{\mathbf{R}_I\}) \right\} \Lambda_\mu^{\mathrm{EAM}} = E_\mu^{\mathrm{nuc,EAM}}\, \Lambda_\mu^{\mathrm{EAM}} \tag{2.108}$$

$$F \approx F^{\mathrm{EAM}} = -k_{\mathrm{B}}T \ln \sum_\mu e^{-\beta E_\mu^{\mathrm{nuc,EAM}}}. \tag{2.109}$$

Thus, $E^{\mathrm{EAM}}(\{\mathbf{R}_I\})$ replaces the electronic free energy surface $F^{\mathrm{el}}(\{\mathbf{R}_I\})$ and determines now fully the nuclei motion. We have indicated this fact by introducing corresponding eigenfunctions $\Lambda_\mu^{\mathrm{EAM}}$ and eigenvalues $E_\mu^{\mathrm{nuc,EAM}}$ and the subsequently resulting free energy F^{EAM}. The methods developed in Sec. 2.3 for solving the nuclei equations, Eqs. (2.108) and (2.109), can be fully applied regardless of which of the surfaces, $F^{\mathrm{el}}(\{\mathbf{R}_I\})$ or $E^{\mathrm{EAM}}(\{\mathbf{R}_I\})$, is used. We stress however that if we employ the EAM approach, the electron system is treated effectively at $T = 0$ K and we have no access to the contribution of the electrons to the free energy.

2.3 Exploring the nuclei phase space

2.3.1 Motivation

In Secs. 2.3 and 3.1, we will be concerned with solving Eq. (2.35), i.e.,

$$\left\{ \hat{T}^{\mathrm{nuc}}(\{\mathbf{R}_I\}) + \hat{1} F^{\mathrm{el}}(\{\mathbf{R}_I\}) \right\} \tilde{\Lambda}_\mu(\{\mathbf{R}_I\}) = \tilde{E}_\mu^{\mathrm{nuc}}\, \tilde{\Lambda}_\mu(\{\mathbf{R}_I\}) \tag{2.110}$$

and subsequently Eq. (2.36):

$$F = -k_{\mathrm{B}}T \ln \sum_\mu e^{-\beta \tilde{E}_\mu^{\mathrm{nuc}}}. \tag{2.111}$$

Using Eqs. (2.37), (2.69) to (2.71), (2.91), and (2.92), we have the scaling behavior of the full problem, i.e., involving the calculation of $F^{\mathrm{el}}(\{\mathbf{R}_I\})$, given by:

$$s = (N_{\mathrm{mesh}}^3)^{N_n} \cdot \underbrace{s^{\mathrm{KS}}(a^{\mathrm{lat}}, E^{\mathrm{cut}}, N_k^{\mathrm{irr}}, N_e, N^{\mathrm{it}})}_{\substack{\text{Optimized Kohn-Sham eq.} \\ \text{for fixed nuclei coordinates}}} + \underbrace{\left[(N_{\mathrm{mesh}}^3)^{N_n} \times (N_{\mathrm{mesh}}^3)^{N_n} \right]}_{\substack{\text{Effective nuclei Schrödinger eq.} \\ \text{for electronic ground state FES}}}. \tag{2.112}$$

We have hereby written in black the part of the problem that has been transformed into a solvable expression by the methods introduced in Secs. 2.1.4 to 2.1.8, whereas red marks the two parts

that render the full solution at this stage infeasible: 1) We need to solve the Kohn-Sham equation $(N_{\text{mesh}}^3)^{N_n}$ times, i.e., for each nuclei configuration. If we take $N_{\text{mesh}} = 200$ from the example in Sec. 2.1.1, $N_n = 2$, and 1 CPU hour for one Kohn-Sham equation, we would need a calculation time of 10^{10} years. 2) As for the solution of the effective nuclei Schrödinger equation, we can apply the estimations performed in Sec. 2.1.1 replacing the electron and nucleus system by two nuclei.

Inspection of the nuclei Schrödinger equation reveals that it scales exactly as the electronic Schrödinger equation, Eqs. (2.38) and (2.40), but with N_e replaced by N_n. An intuitive way to proceed might therefore be the application of DFT and the Kohn-Sham ansatz to remove the dependence on N_n and to render issue 2) feasible. Indeed, such approaches are developed in the field of nuclear physics [67]. For the case of thermodynamic properties of crystals however, a conceptually different approach needs to be applied. The reason is the different physical nature of the electronic and nuclei systems:

A) Focusing on metals, the valence electrons are free to move across the full crystal. In quantum mechanical terms, an electron wave function extends over the full crystal and the overlap with the wave functions of other electrons is significant. Due to this overlap, quantum mechanical many-body effects need to be accounted for as it is done in DFT and the Kohn-Sham ansatz.

B) In contrast, the nuclei are closely bound to their $T = 0$ K equilibrium positions. This holds true even if we consider thermal vibrations. The different one nucleus wave functions therefore practically do not overlap and quantum mechanical many-body effects are negligible. Instead, there are two other very important aspects that need to be accounted for: First, the nuclei motion is strongly coupled in a classical fashion due to the presence of the valence electrons, i.e., due to $F^{\text{el}}(\{\mathbf{R}_I\})$. This is the origin of thermal vibrations and the major contribution to all thermodynamic properties. Second, even though quantum mechanical many-body effects are not present, each of the nuclei must be treated quantum mechanically. This means that the uncertainty principle, i.e., the impossibility to localize a particle in both real and reciprocal space, must be obeyed. The consideration of this principle is crucial for thermodynamic properties at low temperatures.

An adequate approach to efficiently cover the issues in B) is the quasiharmonic approximation. The quasiharmonic approximation is a perturbative approach respecting the special role played by the $T = 0$ K equilibrium positions of the nuclei, $\{\mathbf{R}_I^0\}$, by expanding $F^{\text{el}}(\{\mathbf{R}_I\})$ in a Taylor series up to second order at $\{\mathbf{R}_I^0\}$. Considering only the second order term allows computationally an extremely efficient treatment. Nonetheless, it describes a major part of the classical coupling of the nuclei, while the rather small effects beyond the quasiharmonic approximation can be taken into account by two distinct approaches which will be discussed in Sec. 2.3.5. The quasiharmonic approach neglects by definition quantum mechanical **many-body** effects, which enables to solve the resulting Hamiltonian using a standard procedure, which is the correspondence principle. This means that, in a first step, we can define a purely classical variable $\mathbf{U}(\mathbf{R}_I^0)$, which denotes the displacement of nucleus I out of $\mathbf{R}_I^0$, i.e.,

$$\mathbf{U}(\mathbf{R}_I^0) \; = \; \mathbf{R}_I - \mathbf{R}_I^0, \tag{2.113}$$

and a corresponding classical momentum $\mathbf{P}(\mathbf{R}_I^0)$. This allows to solve the classical Hamilton function and by requiring that $\mathbf{U}(\mathbf{R}_I^0)$ and $\mathbf{P}(\mathbf{R}_I^0)$ obey the standard canonical commutation relations, we obtain the quantum mechanical result. This procedure fully takes into account the quantum mechanical nature of each of the nuclei discussed above in B), i.e., quantum mechanical **one-body** effects. A further advantage of the quasiharmonic approximation is the fact that it tackles both of

the difficulties with Eq. (2.112), issues 1) and 2), at the same time. Before discussing these issues in detail and introducing the quasiharmonic approximation formally, we need to briefly comment on defect formation and to introduce the supercell concept in the next section.

As schematically shown in Fig. 2.1, the step preceding the quasiharmonic approximation, which separates the vibrations of the perfect crystal into quasiharmonic and anharmonic vibrations, is the separation of the nuclei motion into vacancy formation and perfect crystal vibrations. Within the present work, an intuitive model was developed to perform the latter separation. We therefore postpone the discussion of this step to the methodological part, Chap. 3. We note here that in calculating vacancy properties, we will need to apply the quasiharmonic approach to a perfect crystal and to a crystal containing a vacancy. Due to the break of translational symmetry, some of the equations given below need to be modified for the vacancy crystal. We will address this issue in Sec. 3.3.3.

2.3.2 Supercell approach

So far, for the discussion of the electronic free energy, it was sufficient to consider a crystal lattice as being defined by the primitive lattice vectors, Eqs. (2.75) and (2.76). These definitions correspond, however, to the equilibrium positions $\{\mathbf{R}_I^0\}$ of the nuclei at $T = 0$ K. In order to be able to describe nuclei vibrations at finite temperatures within a periodic ansatz, we introduce the so called supercell approach which will lead to a new convergence parameter, the supercell size. This approach is also needed to describe defect structures, such as vacancies or self interstitials.

A supercell is defined to be a multiple of either the primitive unit cell, Eq. (2.76), or of an equivalent unit cell. Specifically, we will use cubic supercells (sc)

$$\mathbf{s}_1 = n^{\text{sc}} \mathbf{a}_1', \quad \mathbf{s}_2 = n^{\text{sc}} \mathbf{a}_2', \quad \mathbf{s}_3 = n^{\text{sc}} \mathbf{a}_3', \tag{2.114}$$

built up from the conventional fcc unit cell, which is given by the lattice vectors

$$\mathbf{a}_1' = a^{\text{lat}}(1,0,0), \quad \mathbf{a}_2' = a^{\text{lat}}(0,1,0), \quad \mathbf{a}_3' = a^{\text{lat}}(0,0,1), \tag{2.115}$$

and by four atoms placed at:

$$\mathbf{R}_1^0 = a^{\text{lat}}(0,0,0), \quad \mathbf{R}_2^0 = \frac{a^{\text{lat}}}{2}(0,1,1), \quad \mathbf{R}_3^0 = \frac{a^{\text{lat}}}{2}(1,0,1), \quad \mathbf{R}_4^0 = \frac{a^{\text{lat}}}{2}(1,1,0). \tag{2.116}$$

The employed supercell sizes in the present study and the corresponding numbers N_n of atoms per supercell will be:

$$n^{\text{sc}} \in \{1,2,3,4,5\} \quad \Rightarrow \quad N_n \in \{4,32,108,256,500\}. \tag{2.117}$$

The reason for constructing cubic supercells are symmetry compatibility and efficient defect-defect screening. After setting up the supercell, the atoms within are allowed to freely vibrate around $\mathbf{R}_I^0$ according to the given temperature. Beyond the supercell, we have however periodic boundary conditions, which are implicit due to solving the Kohn-Sham equation in reciprocal space, and hence, to each atom there is an infinite number of image atoms, i.e., atoms that move identically to the original atom. In terms of the displacement $\mathbf{U}(\mathbf{R}_I^0)$, we have

$$\mathbf{U}(\mathbf{R}_I^0 + n_1\mathbf{s}_1 + n_2\mathbf{s}_2 + n_3\mathbf{s}_3) = \mathbf{U}(\mathbf{R}_I^0), \tag{2.118}$$

for any integers n_1, n_2, and n_3. The consequence of this implicit periodicity is best discussed in reciprocal space. Let us therefore calculate $\mathbf{U}_{\mathbf{q}}$, the Fourier transform of all real space displacements,

i.e., also those beyond the supercell, which is given by:[6]

$$\mathbf{U_q} \;=\; N_n^{-1/2}\, N_s^{-3} \sum_{I}^{N_n} \sum_{n_1}^{N_s} \sum_{n_2}^{N_s} \sum_{n_3}^{N_s} \mathbf{U}(\mathbf{R}_I^0 + n_1\mathbf{s}_1 + n_2\mathbf{s}_2 + n_3\mathbf{s}_3)\, e^{-i\mathbf{q}\cdot(\mathbf{R}_I^0 + n_1\mathbf{s}_1 + n_2\mathbf{s}_2 + n_3\mathbf{s}_3)}. \quad (2.119)$$

Here, $\mathbf{q}$ is a plane wave vector corresponding to the nuclei displacements. Further, the first sum runs over all N_n nuclei within the supercell and the corresponding normalization factor $N_n^{-1/2}$ is split symmetrically to this Fourier transform and its inverse given below in Eq. (2.128). The remaining sums run each over N_s integers, where N_s needs to go in principle to infinity to account for the periodicity. The resulting value of the sums however does not diverge, which becomes apparent when Eq. (2.119) is rewritten using Eq. (2.118):

$$\mathbf{U_q} \;=\; N_n^{-1/2} \sum_{I}^{N_n} \mathbf{U}(\mathbf{R}_I^0)\, e^{-i\mathbf{q}\cdot\mathbf{R}_I^0} \times$$

$$\times \underbrace{\left[N_s^{-1} \sum_{n_1}^{N_s} e^{-in_1\mathbf{q}\cdot\mathbf{s}_1} \right] \left[N_s^{-1} \sum_{n_2}^{N_s} e^{-in_2\mathbf{q}\cdot\mathbf{s}_2} \right] \left[N_s^{-1} \sum_{n_3}^{N_s} e^{-in_3\mathbf{q}\cdot\mathbf{s}_3} \right]}_{\substack{\text{1 for } N_s \to \infty \text{ and } \mathbf{q} = \mathbf{G}^{\mathrm{sc}} \\ \text{0 for } N_s \to \infty \text{ and } \mathbf{q} \neq \mathbf{G}^{\mathrm{sc}}}}. \quad (2.120)$$

In general, a sum $1/N \sum_n^N e^{-ixn}$ for $N \to \infty$ is 1 if x is a multiple of 2π and 0 otherwise. Equation (2.120) will therefore be identical to 0 unless $\mathbf{q} \cdot \mathbf{s}_1 = 2\pi n$, $n \in \mathbb{Z}$, and similarly for $\mathbf{q} \cdot \mathbf{s}_2$ and $\mathbf{q} \cdot \mathbf{s}_3$. This is an analogous requirement to Eq. (2.77) however with $\mathbf{R}$ replaced by $\mathbf{s}_1$, $\mathbf{s}_2$, and $\mathbf{s}_3$ and therefore $\mathbf{q}$ vectors satisfying these conditions will lie on a supercell reciprocal lattice defined by

$$\mathbf{G}^{\mathrm{sc}} = k_1\mathbf{b}_1^{\mathrm{sc}} + k_2\mathbf{b}_2^{\mathrm{sc}} + k_3\mathbf{b}_3^{\mathrm{sc}} \quad \text{with} \quad k_1, k_2, k_3 \in \mathbb{Z}, \quad (2.121)$$

and with the supercell reciprocal lattice vectors uniquely determined by

$$\mathbf{b}_1^{\mathrm{sc}} = \frac{2\pi}{\Omega}\, \mathbf{s}_2 \times \mathbf{s}_3, \qquad \mathbf{b}_2^{\mathrm{sc}} = \frac{2\pi}{\Omega}\, \mathbf{s}_3 \times \mathbf{s}_1, \qquad \mathbf{b}_3^{\mathrm{sc}} = \frac{2\pi}{\Omega}\, \mathbf{s}_1 \times \mathbf{s}_2, \quad (2.122)$$

where $\Omega = \mathbf{s}_1 \cdot (\mathbf{s}_2 \times \mathbf{s}_3)$ is the volume of the supercell in real space. The Fourier transform $\mathbf{U_q}$ is therefore fully determined by the $\mathbf{G}^{\mathrm{sc}}$ vectors

$$\mathbf{U_q} \;=\; \mathbf{U_{G^{sc}}} \;=\; N_n^{-1/2} \sum_{I}^{N_n} \mathbf{U}_I\, e^{-i\mathbf{G}^{\mathrm{sc}}\cdot\mathbf{R}_I^0}, \quad (2.123)$$

where we have now written $\mathbf{U}_I = \mathbf{U}(\mathbf{R}_I^0)$ for short. In essence, Eq. (2.123) is equivalent to the intuitive statement that only plane waves are allowed which have periodicity according to the supercell geometry. A consequence of this fact is the restriction that not all $\mathbf{q}$ vectors will contribute to thermodynamic properties but only the set of $\mathbf{G}^{\mathrm{sc}}$ vectors. Due to the inverse relation of the real

---

[6]Note that, since the investigations in this work focus only on elementary crystals with one basis atom per primitive cell, we write all formulas regarding Fourier transforms in the corresponding reduced version, i.e., we do not include sums over basis atoms. Similar arguments will apply (in Sec. 2.3.3) to the mass scaling factors. General expressions can be found for instance in Ref. [68]. Note further that for the purpose of a convenient reading, we do not include the mass scaling factor and the eigenvectors of the dynamical matrix into the Fourier transforms in the present section. Both will be needed and thus included in Sec. 2.3.3. The important point is that the relations derived in this section still hold true after this inclusion (the mass is a mere scalar and the eigenvectors obey the necessary properties).

and reciprocal space, a larger supercell will produce a denser grid of $\mathbf{G}^{\mathrm{sc}}$ vectors. In experiment, the supercell corresponds in principle to the macroscopic crystal.[7] The plane waves contributing to experimental thermodynamic properties are therefore lying on a significantly denser grid as compared to the grids achievable theoretically [cf. Eq. (2.117)]. An interpolation scheme (based on a Fourier transform) can be applied to produce also theoretically a dense plane wave grid, i.e., to facilitate access to $\mathbf{q}$ vectors in between the $\mathbf{G}^{\mathrm{sc}}$ vectors. We will introduce this scheme in Sec. 2.4.1. It is nonetheless very important to carefully check the convergence of thermodynamic properties with the supercell size. The reason is that frequently significant deviations (see Sec. 3.4.3) can occur between the predicted interpolation and the true frequencies, if too few sampling points are used. The number of sampling points, however, correlates with the supercell size and we thus have to consider a new convergence parameter. The set of all convergence parameters increases therefore to: k sampling, plane wave cutoff E^{cut}, augmentation grid, and supercell size n^{sc}.

The reciprocal displacements $\mathbf{U}_{\mathbf{G}^{\mathrm{sc}}}$ and the corresponding $\mathbf{G}^{\mathrm{sc}}$ vectors have three important exact properties:

1) The $\mathbf{U}_{\mathbf{G}^{\mathrm{sc}}}$ obey a symmetry property which can be readily used to simplify the calculation of thermodynamic quantities. Let us consider

$$
\begin{aligned}
\mathbf{U}_{\mathbf{G}^{\mathrm{sc}}+\mathbf{G}} &= N_n^{-1/2} \sum_I^{N_n} \mathbf{U}_I \, e^{-i(\mathbf{G}^{\mathrm{sc}}+\mathbf{G})\cdot\mathbf{R}_I^0} \\
&= N_n^{-1/2} \sum_I^{N_n} \mathbf{U}_I \, e^{-i\mathbf{G}^{\mathrm{sc}}\cdot\mathbf{R}_I^0} \underbrace{e^{-i\mathbf{G}\cdot\mathbf{R}_I^0}}_{\substack{=1 \text{ due to} \\ \text{Eq. (2.77)}}} = \mathbf{U}_{\mathbf{G}^{\mathrm{sc}}},
\end{aligned}
\qquad (2.124)
$$

where $\mathbf{G}$ is a reciprocal lattice vector, Eq. (2.78), corresponding to the primitive cell, Eq. (2.76). Due to the construction of the supercell, Eqs. (2.114) to (2.116), the equilibrium positions $\mathbf{R}_I^0$ correspond to the lattice vectors $\mathbf{R}$ defined in Eq. (2.75) and therefore Eq. (2.77) can be applied to $e^{-i\mathbf{G}\cdot\mathbf{R}_I^0}$. Equation (2.124) states that the displacement $\mathbf{U}_{\mathbf{G}^{\mathrm{sc}}}$ has periodicity corresponding to the reciprocal lattice of the primitive cell. We therefore need to consider only displacements within the first Brillouin zone of the primitive lattice (prBZ). This applies likewise to all thermodynamic quantities. In particular, as shown in Sec. 2.3.3 the calculation of thermodynamic quantities will require a sum over $\mathbf{G}^{\mathrm{sc}}$ vectors and we can confine this sum to the prBZ. An example for the employed $\mathbf{G}^{\mathrm{sc}}$ meshes is given in Fig. 2.4.

2) For the case of elementary crystals with one atom per primitive cell as considered here, the number $N_{\mathbf{G}^{\mathrm{sc}}}$ of $\mathbf{G}^{\mathrm{sc}}$ vectors inside the prBZ equals the number N_n of atoms in the corresponding supercell. One way to see this is to calculate the ratio of the volume of the prBZ and the volume that each of the $\mathbf{G}^{\mathrm{sc}}$ vectors occupies:

$$
N_{\mathbf{G}^{\mathrm{sc}}} = \frac{\mathbf{b}_1 \cdot (\mathbf{b}_2 \times \mathbf{b}_3)}{\mathbf{b}_1^{\mathrm{sc}} \cdot (\mathbf{b}_2^{\mathrm{sc}} \times \mathbf{b}_3^{\mathrm{sc}})} = 4\,(n^{\mathrm{sc}})^3 = N_n.
\qquad (2.125)
$$

To obtain the second equality, we have used Eqs. (2.76), (2.79), (2.114), (2.115), and (2.122). The last equality follows from comparison with Eq. (2.117). In practical applications, one has to be cautious with $\mathbf{G}^{\mathrm{sc}}$ vectors which lie on the boundary of the prBZ. Such vectors should be taken only once into account as shown in Fig. 2.4.

---

[7]Strictly speaking, this is not fully correct since the boundary conditions are different. Those will be however negligible for the relevant scales.
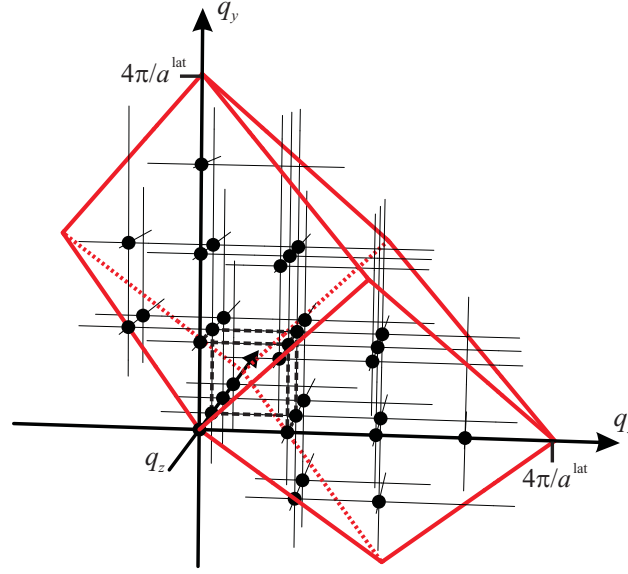
Figure 2.4: The mesh of $\mathbf{G}^{\mathrm{sc}}$ vectors (black dots) as defined by Eqs. (2.121) and (2.122) for a $2 \times 2 \times 2$ supercell, i.e., $n^{\mathrm{sc}} = 2$ in Eq. (2.114). Only $\mathbf{G}^{\mathrm{sc}}$ vectors lying inside the first primitive lattice Brillouin zone (prBZ; heavy red lines), Eq. (2.76), are shown. The supercell Brillouin zone (scBZ) is indicated by the heavy dashed lines. The reciprocal lattice vector is $\mathbf{q} = (q_x, q_y, q_z)$. The thin black lines are a guide to the eye. – Note that the scBZ defines a simple cubic mesh due to the cubic supercell, while the prBZ defines a base-centered-cubic lattice (the reciprocal lattice of fcc).

3) In general, the $\mathbf{U}_{\mathbf{G}^{\mathrm{sc}}}$ are complex variables. Taking however the complex conjugate of Eq. (2.123) and considering the fact that the real space displacements $\mathbf{U}_I$ are always real, we obtain

$$\mathbf{U}^*_{\mathbf{G}^{\mathrm{sc}}} = N_n^{-1/2} \sum_{I}^{N_n} \mathbf{U}_I \, e^{i\mathbf{G}^{\mathrm{sc}} \cdot \mathbf{R}_I^0} = \mathbf{U}_{-\mathbf{G}^{\mathrm{sc}}}, \qquad (2.126)$$

which means that the displacements at $\mathbf{G}^{\mathrm{sc}}$ and at $-\mathbf{G}^{\mathrm{sc}}$ are coupled to each other. This coupling can be understood also by considering a degrees-of-freedom argument: In real and in reciprocal space the number of degrees-of-freedom needs to be the same. If however the reciprocal displacements are complex, they have two degrees-of-freedom each while the real space displacements have only one. Therefore the coupling reduces the number of degrees-of-freedom in reciprocal space and ensures that it is equal to the number given in real space, which is the physically relevant one.

As a final step of the discussion of the supercell concept, we need to adapt the electronic system to the supercell geometry. We consider for that purpose the expansion of the electronic wave function in reciprocal space, Eq. (2.82), which now changes to:

$$\varphi_{\nu,\mathbf{k}}(\mathbf{r}) = e^{i\mathbf{k}\cdot\mathbf{r}} \sum_{\mathbf{G}^{\mathrm{sc}}}^{E^{\mathrm{cut}}} c_{\nu,\mathbf{k}+\mathbf{G}^{\mathrm{sc}}} \, e^{i\mathbf{G}^{\mathrm{sc}} \cdot \mathbf{r}} \quad \text{with} \quad \mathbf{k} \in \mathrm{scBZ}. \qquad (2.127)$$

The sum here runs over the supercell reciprocal vectors $\mathbf{G}^{\mathrm{sc}}$, which fulfill the condition Eq. (2.88), and $\mathbf{k}$ is now confined to the first Brillouin zone of the supercell lattice (scBZ), which is spanned by the vectors $\mathbf{b}_1^{\mathrm{sc}}$, $\mathbf{b}_2^{\mathrm{sc}}$, and $\mathbf{b}_3^{\mathrm{sc}}$ from Eq. (2.122). It is useful to compare Eq. (2.127) with the inverse

Fourier transform of the nuclei displacement given by:

$$\mathbf{U}_I = N_n^{-1/2} \sum_{\mathbf{G}^{\mathrm{sc}}}^{\mathrm{prBZ}} \mathbf{U}_{\mathbf{G}^{\mathrm{sc}}} \, e^{i\mathbf{G}^{\mathrm{sc}} \cdot \mathbf{R}_I^0}. \tag{2.128}$$

Here, according to Eq. (2.124) and the following discussion, the sum runs only over the prBZ. The distinction between the two Brillouin zones, prBZ and scBZ, is illustrated in Fig. 2.4. The comparison between Eqs. (2.127) and (2.128) should be performed with caution, since, as discussed in Sec. 2.3.1, the electronic and nuclei systems are treated on a different footing. Nonetheless, the comparison helps to reveal the role played by the $\mathbf{k}$ and $\mathbf{G}^{\mathrm{sc}}$ vectors:

1) The electronic wave function $\varphi_{\nu,\mathbf{k}}(\mathbf{r})$ depends on $\mathbf{k}$, i.e., on wave vectors from inside the scBZ, whereas $\mathbf{U}_I$ does not. The origin of the $\mathbf{k}$ dependence is that (Sec. 2.3.1) the electrons are free to move in the full crystal, i.e., also beyond the supercell. To describe this motion also plane waves are needed, which have wave vectors incommensurable with the supercell. The $\mathbf{k}$ vectors describe exactly such plane waves. In contrast, the nuclei are confined to their equilibrium positions and do not require a $\mathbf{k}$ dependence.

2) The sum over $\mathbf{G}^{\mathrm{sc}}$ vectors extends to E^{cut} in Eq. (2.127) and would need to go formally to infinity, whereas the sum in Eq. (2.128) is rigorously confined to the prBZ. In a sense, the prBZ defines a natural cutoff for the expansion of $\mathbf{U}_I$. The reason for this natural cutoff is that, again due to the confinement of the nuclei, the real space displacement of the nuclei is a function of the **discrete** equilibrium positions $\mathbf{R}_I^0$. Taking $\mathbf{G}^{\mathrm{sc}}$ vectors beyond the prBZ into account would only describe plane waves oscillating faster than the next nearest neighbor distance and would thus contain no new information. This fact was implicitly used above in Eq. (2.124). On the contrary, $\varphi_{\nu,\mathbf{k}}(\mathbf{r})$ depends on the **continuous** variable $\mathbf{r}$ and therefore all possible $\mathbf{G}^{\mathrm{sc}}$ vectors contain new information which could in principle be relevant.

The remaining equations from Sec. 2.1.7 need to be adapted to the supercell approach accordingly to Eq. (2.127) by changing $\mathbf{G} \to \mathbf{G}^{\mathrm{sc}}$ and by performing the k sampling over the scBZ. Additionally, we have to adjust the dependence of the electronic free energy as

$$F^{\mathrm{el}}(\{\mathbf{R}_I\}) \quad \to \quad F^{\mathrm{el}}(\{\mathbf{R}_I\}, \Omega), \tag{2.129}$$

with I running now only over the atoms inside the supercell. The dependence of F^{el} on the supercell volume Ω will turn out to be a crucial ingredient of the quasiharmonic approach. It will give rise to, e.g., the thermal expansion. With these preliminary considerations regarding the supercell concept, we can proceed with the formal introduction of the quasiharmonic approximation.

2.3.3 Quasiharmonic approximation

The central equation of the quasiharmonic approach[8] is a Taylor expansion of the electronic free energy F^{el} around the $T = 0$ K equilibrium nuclei positions $\{\mathbf{R}_I^0\}$:

$$F^{\mathrm{el}}(\{\mathbf{R}_I\}, \Omega, T) = F_0^{\mathrm{el}}(\Omega, T) + \frac{1}{2} \sum_{I,J}^{N_n} \sum_{\alpha,\beta}^{3} U_{I,\alpha} U_{J,\beta} \left[\frac{\partial^2 F^{\mathrm{el}}(\{\mathbf{R}_I\}, \Omega, T)}{\partial R_{I,\alpha} \partial R_{J,\beta}} \right]_{\{\mathbf{R}_I^0\}} + O(U^3). \tag{2.130}$$

---

[8]Note that the basic ideas underlying the quasiharmonic approximation are well known since already the beginning of the last century. A main contributor to the field of the theory of lattice dynamics was M. Born [69, 70]. A more recent discussion can be found for instance in Ref. [68].

Here, the zeroth order term is abbreviated as $F_0^{\text{el}}(\Omega, T) := F^{\text{el}}(\{\mathbf{R}_I^0\}, \Omega, T)$, α and β run over the three real space components of the vector $\mathbf{U}_I$, and $O(U^3)$ denotes terms of third and all higher orders in $\mathbf{U}_I$. We have further explicitly indicated the dependence of F^{el} on T, which enters through the Fermi-Dirac function, Eq. (2.65). The expansion of F^{el} does not contain the first order term

$$\sum_{I,\alpha} U_{I,\alpha} \left[\frac{\partial F^{\text{el}}(\{\mathbf{R}_I\}, \Omega, T)}{\partial R_{I,\alpha}} \right]_{\{\mathbf{R}_I^0\}}, \tag{2.131}$$

since, by definition of the equilibrium positions, it is identical to zero. We next define a key quantity of the quasiharmonic approximation, the dynamical matrix $\mathbf{D}$, with the components

$$D_{I\alpha, J\beta}(\Omega, T) := \frac{1}{M_I} \left[\frac{\partial^2 F^{\text{el}}(\{\mathbf{R}_I\}, \Omega, T)}{\partial R_{I,\alpha} \partial R_{J,\beta}} \right]_{\{\mathbf{R}_I^0\}}, \tag{2.132}$$

where the mass M_I of the nucleus I is included for later convenience. The quasiharmonic approximation is now introduced by neglecting the terms $O(U^3)$

$$F^{\text{el}}(\{\mathbf{R}_I\}, \Omega, T) \approx F_0^{\text{el}}(\Omega, T) + \underbrace{\frac{1}{2} \sum_{I,J}^{N_n} \sum_{\alpha,\beta}^{3} \frac{1}{M_I} U_{I,\alpha} U_{J,\beta} D_{I\alpha, J\beta}(\Omega, T)}_{=: \mathbf{U}\mathbf{D}(\Omega, T)\mathbf{U}/(2\mathbf{M})}, \tag{2.133}$$

where we have defined a short hand notation for future reference. The displacement vectors $\mathbf{U}$ and mass vector $\mathbf{M}$ comprise hereby the displacements and masses of all nuclei $\{\mathbf{U}_I\}$ and $\{M_I\}$ respectively. "Harmonic" refers to the inclusion of the second order term which will be subsequently transformed into a form similar to that of a harmonic oscillator. The term "quasi" emphasizes that the dynamical matrix is not constant, but depends on the supercell volume Ω. The next step is now to solve the effective nuclei Schrödinger equation, Eq. (2.110), based on the approximation Eq. (2.133), i.e., to solve the eigenvalue equation of the quasiharmonic Hamiltonian $\hat{H}^{\text{qh}}$

$$\hat{H}^{\text{qh}} \tilde{\Lambda}_\mu = \tilde{E}_\mu^{\text{qh}} \tilde{\Lambda}_\mu, \tag{2.134}$$

with eigenfunctions $\tilde{\Lambda}_\mu$ and eigenvalues $\tilde{E}_\mu^{\text{qh}}$ and with $\hat{H}^{\text{qh}}$ given by

$$\hat{H}^{\text{qh}}(\Omega, T) = -\sum_I^{N_n} \frac{\hbar^2}{2M_I} \nabla_I^2 + \hat{1} F_0^{\text{el}}(\Omega, T) + \frac{1}{2} \sum_{I,J}^{N_n} \sum_{\alpha,\beta}^{3} \frac{1}{M_I} \hat{U}_{I,\alpha} \hat{U}_{J,\beta} D_{I\alpha, J\beta}(\Omega, T), \tag{2.135}$$

where we have used the explicit form of the nuclei kinetic energy operator $\hat{T}^{\text{nuc}}(\{\mathbf{R}_I\})$, Eq. (2.8). It should be noted that the displacements $\mathbf{U}_I$ transform to operators $\hat{\mathbf{U}}_I$ when inserted into $\hat{H}^{\text{qh}}$ since they are functions of the nuclei positions. Further, due to the dependence of $\hat{H}^{\text{qh}}$ on Ω and T, the eigenfunctions and eigenvalues in Eq. (2.134) also require this dependence. As discussed in Sec. 2.3.1, we can use the correspondence principle to solve Eq. (2.134), since we by definition exclude quantum mechanical many-body effects (and since we have a well defined classical analogon to the quantum mechanical operators). We therefore transform the quantum mechanical quasiharmonic Hamilton operator, Eq. (2.135), into its classical version, the quasiharmonic Hamilton function H^{qh}, by the transformation rules

$$-i\hbar \nabla_I \rightarrow \mathbf{P}_I \qquad \text{and} \qquad \hat{\mathbf{U}}_I \rightarrow \mathbf{U}_I, \tag{2.136}$$

where $\mathbf{P}_I = \mathbf{P}(\mathbf{R}_I^0)$ is the classical momentum of nucleus I. Using Eq. (2.136), we obtain:

$$H^{\text{qh}}(\Omega, T) = \sum_I^{N_n} \sum_\alpha^3 \frac{1}{2M_I} P_{I,\alpha}^2 + F_0^{\text{el}}(\Omega, T) + \frac{1}{2} \sum_{I,J}^{N_n} \sum_{\alpha,\beta}^3 \frac{1}{M_I} U_{I,\alpha} U_{J,\beta} D_{I\alpha, J\beta}(\Omega, T). \quad (2.137)$$

The reason for changing into the classical description is that we can now Fourier expand $\mathbf{P}_I$ analogously to Eq. (2.128) for $\mathbf{U}_I$, which will allow to transform also H^{qh} into reciprocal space. The latter will turn out to be significantly more convenient than the real space representation Eq. (2.137). We need however to use for both a modified form:

$$\mathbf{U}_I = N_n^{-1/2} M_I^{-1/2} \sum_{\mathbf{G}^{\text{sc}}}^{\text{prBZ}} \sum_s^3 U_{\mathbf{G}^{\text{sc}}, s} \, e^{i\mathbf{G}^{\text{sc}} \cdot \mathbf{R}_I^0} \, \mathbf{w}_{\mathbf{G}^{\text{sc}}, s}, \quad (2.138)$$

$$\mathbf{P}_I = N_n^{-1/2} M_I^{1/2} \sum_{\mathbf{G}^{\text{sc}}}^{\text{prBZ}} \sum_s^3 P_{\mathbf{G}^{\text{sc}}, s} \, e^{i\mathbf{G}^{\text{sc}} \cdot \mathbf{R}_I^0} \, \mathbf{w}_{\mathbf{G}^{\text{sc}}, s}. \quad (2.139)$$

Here, the $\mathbf{P}_{\mathbf{G}^{\text{sc}}}$ are expansion coefficient corresponding to the momentum of a plane wave with vector $\mathbf{G}^{\text{sc}}$ and s runs over the three reciprocal components of the vectors $\mathbf{U}_{\mathbf{G}^{\text{sc}}}$ and $\mathbf{P}_{\mathbf{G}^{\text{sc}}}$ which are commonly called branches. As compared to the Fourier transforms utilized in Sec. 2.3.2, in particular Eq. (2.128), we have two changes: 1) The mass factors M_I have been included, which correspond however merely to scalars introduced for convenience. 2) The vectors $\mathbf{w}_{\mathbf{G}^{\text{sc}}, s}$, which correspond to eigenvectors of the **reciprocal** dynamical matrix [defined in Eq. (2.141)], have been introduced. This change is important and will be discussed below. First, using Eqs. (2.138) and (2.139) and anticipating Eqs. (2.144) and (2.145), we can rewrite Eq. (2.137) as [68]:

$$H^{\text{qh}}(\Omega, T) = \frac{1}{2} \sum_{\mathbf{G}^{\text{sc}}}^{\text{prBZ}} \sum_s^3 P_{\mathbf{G}^{\text{sc}}, s} P_{-\mathbf{G}^{\text{sc}}, s} + F_0^{\text{el}}(\Omega, T) +$$

$$+ N_n^{-1} \frac{1}{2} \sum_{\mathbf{G}^{\text{sc}}}^{\text{prBZ}} \sum_s^3 U_{\mathbf{G}^{\text{sc}}, s} U_{-\mathbf{G}^{\text{sc}}, s} \sum_{\alpha,\beta}^3 \sum_{I,J}^{N_n} D_{I\alpha, J\beta}(\Omega, T) \, e^{i\mathbf{G}^{\text{sc}} \cdot (\mathbf{R}_I^0 - \mathbf{R}_J^0)}. \quad (2.140)$$

We can now define the reciprocal dynamical matrix $\mathbf{D}_{\mathbf{G}^{\text{sc}}}$ as the Fourier transform of the real space dynamical matrix $\mathbf{D}$ with the following components:

$$D_{\mathbf{G}^{\text{sc}}, \alpha\beta}(\Omega, T) = N_n^{-1} \sum_{I,J}^{N_n} D_{I\alpha, J\beta}(\Omega, T) \, e^{i\mathbf{G}^{\text{sc}} \cdot (\mathbf{R}_I^0 - \mathbf{R}_J^0)}. \quad (2.141)$$

For each $\mathbf{G}^{\text{sc}}$, $\mathbf{D}_{\mathbf{G}^{\text{sc}}}$ is (in our study) a 3×3 matrix and has the important property of being Hermitian, which can be seen by writing:

$$\begin{aligned} (D_{\mathbf{G}^{\text{sc}}, \alpha\beta})^* &= N_n^{-1} \sum_{I,J}^{N_n} D_{I\alpha, J\beta} \, e^{-i\mathbf{G}^{\text{sc}} \cdot (\mathbf{R}_I^0 - \mathbf{R}_J^0)} \\ &= N_n^{-1} \sum_{I,J}^{N_n} D_{I\alpha, J\beta} \, e^{-i\mathbf{G}^{\text{sc}} \cdot (\mathbf{R}_J^0 - \mathbf{R}_I^0)} = D_{\mathbf{G}^{\text{sc}}, \alpha\beta}. \end{aligned} \quad (2.142)$$

To obtain the second line, we have interchanged the summation indices I and J and used the fact that $D_{I\alpha,J\beta} = D_{J\beta,I\alpha}$, since changing the order of differentiation in the defining equation, Eq. (2.132), does not affect the dynamical matrix. Any Hermitian matrix is diagonalizable and we can therefore write an eigenvalue equation for $\mathbf{D}_{\mathbf{G}^{\mathrm{sc}}}$:

$$\mathbf{D}_{\mathbf{G}^{\mathrm{sc}}}(\Omega, T)\, \mathbf{w}_{\mathbf{G}^{\mathrm{sc}};\,s} \;=\; [\omega_{\mathbf{G}^{\mathrm{sc}};\,s}(\Omega, T)]^2\, \mathbf{w}_{\mathbf{G}^{\mathrm{sc}};\,s}. \tag{2.143}$$

Here, $\mathbf{w}_{\mathbf{G}^{\mathrm{sc}};\,s}$ are the already introduced eigenvectors, which can be orthonormalized,

$$\mathbf{w}_{\mathbf{G}^{\mathrm{sc}};\,s} \cdot \mathbf{w}_{\mathbf{G}^{\mathrm{sc}};\,s'} \;=\; \delta_{s,s'}, \tag{2.144}$$

and which obey

$$\mathbf{w}_{-\mathbf{G}^{\mathrm{sc}};\,s} \;=\; \left(\mathbf{w}_{\mathbf{G}^{\mathrm{sc}};\,s}\right)^*, \tag{2.145}$$

due to $\mathbf{D}_{-\mathbf{G}^{\mathrm{sc}}} = (\mathbf{D}_{\mathbf{G}^{\mathrm{sc}}})^*$. Further in Eq. (2.143), $(\omega_{\mathbf{G}^{\mathrm{sc}};\,s})^2$ are the eigenvalues with the square included in order to make an identification of the $\omega_{\mathbf{G}^{\mathrm{sc}};\,s}$ with phonon frequencies (introduced below) possible. Using Eq. (2.143), we have $\sum_{\alpha,\beta}^{3} D_{\mathbf{G}^{\mathrm{sc}},\alpha\beta} = \sum_{s}^{3}(\omega_{\mathbf{G}^{\mathrm{sc}};\,s})^2$ and we thus obtain:

$$H^{\mathrm{qh}}(\Omega, T) \;=\; F_0^{\mathrm{el}}(\Omega, T) + \frac{1}{2} \sum_{\mathbf{G}^{\mathrm{sc}}}^{\mathrm{prBZ}} \sum_{s}^{3} \left\{ |P_{\mathbf{G}^{\mathrm{sc}};\,s}|^2 + [\omega_{\mathbf{G}^{\mathrm{sc}};\,s}(\Omega, T)]^2\, |U_{\mathbf{G}^{\mathrm{sc}};\,s}|^2 \right\}. \tag{2.146}$$

Here, we have also used the property Eq. (2.126) of the $\mathbf{U}_{\mathbf{G}^{\mathrm{sc}}}$, which translates accordingly to the $\mathbf{P}_{\mathbf{G}^{\mathrm{sc}}}$. Equation (2.146) is the reciprocal representation of H^{qh} we were intending to derive. The important difference to Eq. (2.137) is that the contributions from the different $\mathbf{G}^{\mathrm{sc}}$ vectors and different branches s do not couple to each other. In contrast, the real space representation, Eq. (2.137), has coupling contributions in the last term due to the real space dynamical matrix. At this point, it is appropriate to discuss the necessity to use, in Eqs. (2.138) and (2.139), a modified (and rather complicated) Fourier transform including the eigenvectors $\mathbf{w}_{\mathbf{G}^{\mathrm{sc}};\,s}$. The reason is that, if we used the "simple" Fourier transform Eq. (2.128), we would in general **not** achieve a decoupling of the different branches at a single $\mathbf{G}^{\mathrm{sc}}$ vector. In contrast, including $\mathbf{w}_{\mathbf{G}^{\mathrm{sc}};\,s}$ into the Fourier transform leads to a rotation of the reciprocal coordinates, $U_{\mathbf{G}^{\mathrm{sc}};\,s}$ and $P_{\mathbf{G}^{\mathrm{sc}};\,s}$, which in turn leads to their decoupling. In performing this rotation, one needs however to reconsider the relations derived in Sec. 2.3.2 and to check if they also apply to the "new" Fourier transforms Eqs. (2.138) and (2.139). This is indeed the case since, with Eqs. (2.144) and (2.145), the eigenvectors $\mathbf{w}_{\mathbf{G}^{\mathrm{sc}};\,s}$ obey the necessary conditions which were used in Sec. 2.3.2 for deriving these relations.

Equation (2.146) has a further important advantage: It has a form well known from the study of the harmonic oscillator, which is characterized by the eigenvalue equation:

$$\frac{1}{2}\left(\hat{p}^2 + \omega^2 \hat{u}^2\right)|n\rangle = E_n|n\rangle. \tag{2.147}$$

Here, $\hat{p}$, $\hat{u}$, and ω are respectively the momentum and displacement operator and the frequency of the oscillator. The eigenfunctions are denoted by $|n\rangle$. Their exact form does not concern us here and n serves merely as an index for enumerating them and identifying the corresponding eigenvalue E_n. We are only interested in the detailed form of the E_n which can be derived from the commutation relation

$$[\hat{u}, \hat{p}] \;=\; i\hbar \tag{2.148}$$

and is given by (e.g. Ref. [71])

$$E_n = \hbar\omega \left(n + \frac{1}{2} \right) \qquad \text{with} \qquad n = 0, 1, 2, \ldots, \infty, \tag{2.149}$$

i.e., the eigenvalues are discrete, not degenerate, bound from below, and extend to infinity in equidistant steps. In order to apply Eq. (2.147) to solving Eq. (2.146), we first transform $\mathbf{U}_{\mathbf{G}^{sc}}$ and $\mathbf{P}_{\mathbf{G}^{sc}}$ again to operators

$$\mathbf{U}_{\mathbf{G}^{sc}} \quad \rightarrow \quad \hat{U}_{\mathbf{G}^{sc}}, \qquad \mathbf{P}_{\mathbf{G}^{sc}} \quad \rightarrow \quad \hat{P}_{\mathbf{G}^{sc}}, \tag{2.150}$$

which are now required to obey the commutation relations:

$$[\hat{U}_{\mathbf{G}^{sc}, s}, \hat{P}_{\mathbf{G}^{sc\prime}, s\prime}] \quad = \quad -i\hbar \, \delta_{\mathbf{G}^{sc}, \mathbf{G}^{sc\prime}} \, \delta_{s, s\prime}, \tag{2.151}$$

$$[\hat{U}_{\mathbf{G}^{sc}, s}, \hat{U}_{\mathbf{G}^{sc\prime}, s\prime}] \quad = \quad [\hat{P}_{\mathbf{G}^{sc}, s}, \hat{P}_{\mathbf{G}^{sc\prime}, s\prime}] \; = \; 0. \tag{2.152}$$

The quantum mechanical quasiharmonic Hamiltonian in its reciprocal representation then reads

$$\hat{H}^{qh}(\Omega, T) \quad = \quad \hat{1}F_0^{el}(\Omega, T) \; + \; \frac{1}{2} \sum_{\mathbf{G}^{sc}}^{prBZ} \sum_s^3 \left\{ |\hat{P}_{\mathbf{G}^{sc}, s}|^2 \; + \; [\omega_{\mathbf{G}^{sc}, s}(\Omega, T)]^2 \, |\hat{U}_{\mathbf{G}^{sc}, s}|^2 \right\}$$

$$= \quad \hat{1}F_0^{el}(\Omega, T) \; + \; \frac{1}{2} \sum_i^{3N_n} \left\{ |\hat{P}_i|^2 \; + \; [\omega_i(\Omega, T)]^2 \, |\hat{U}_i|^2 \right\} \tag{2.153}$$

and its eigenvalue equation, Eq. (2.134), changes to a generalized version of Eq. (2.147)

$$\hat{H}^{qh} \, |\{n_i\}\rangle = \tilde{E}_{\{n_i\}}^{qh} \, |\{n_i\}\rangle, \tag{2.154}$$

with eigenfunctions $|\{n_i\}\rangle$ and eigenvalues $\tilde{E}_{\{n_i\}}^{qh}$ given by:

$$\tilde{E}_{\{n_i\}}^{qh}(\Omega, T) \; = \; F_0^{el}(\Omega, T) \; + \; \sum_i^{3N_n} \hbar\omega_i(\Omega, T) \left(n_i + \frac{1}{2} \right) \qquad \text{with} \qquad n_i = 0, 1, 2, \ldots, \infty. \tag{2.155}$$

Here, the index i is a short hand notation for both the $\mathbf{G}^{sc}$ vector and the branch index s. As shown in Eq. (2.125), there are N_n $\mathbf{G}^{sc}$ vectors in the prBZ and since to each correspond three branches, i runs over $3N_n$ values. The eigenfunctions $|\{n_i\}\rangle$ and eigenvalues $\tilde{E}_{\{n_i\}}^{qh}$ require a more complex notation than the ones in Eq. (2.147), since we have now an oscillator for each i and we therefore need the set $\{n_i\}$ of $3N_n$ indices for characterization. At this point, we can identify $\omega_i = \omega_{\mathbf{G}^{sc}, s}$ with a frequency corresponding to the oscillator at $\mathbf{G}^{sc}$ and s. These oscillators are reciprocal oscillators and the corresponding motion of the nuclei in real space is given by plane wave lattice vibrations. A crucial observation is that the amplitude of these lattice vibrations is quantized as a consequence of the discreteness of the eigenvalues $\tilde{E}_{\{n_i\}}^{qh}$, which by itself is originally rooted in the fundamental commutation relations, Eqs. (2.151) and (2.152). Such quantized plane wave lattice vibrations are referred to as phonons. The corresponding frequency is a measure of their quanta and is therefore called phonon frequency. Phonons can be viewed as a kind of particle, the so called quasi particle, since we can assign a definite momentum ($P_{\mathbf{G}^{sc}, s}$) and a definite position ($U_{\mathbf{G}^{sc}, s}$) to each phonon. Within the quasiharmonic approximation, phonons do not interact with each other with the consequence that if a phonon is once excited, it will always be present. Taking

higher order terms in the expansion in Eq. (2.130) into account (Sec. 2.3.5) switches on the phonon interaction, which can lead to destruction and creation of phonons.

As the final step of the quasiharmonic approach, we approximate the eigenvalues of the original effective nuclei Schrödinger equation, Eq. (2.110), with the eigenvalues of the quasiharmonic Hamiltonian

$$\tilde{E}_\mu^{\mathrm{nuc}} \approx \tilde{E}_{\{n_i\}}^{\mathrm{qh}}, \tag{2.156}$$

and apply Eq. (2.156) to Eq. (2.111) in order to evaluate an explicit expression for the free energy in terms of the frequencies $\omega_{\mathbf{G}^{\mathrm{sc}}, s}$:

$$
\begin{aligned}
F &\approx -k_{\mathrm{B}} T \ln \underbrace{\sum_{\{n_i\}} e^{-\beta \tilde{E}_{\{n_i\}}^{\mathrm{qh}}}}_{=: Z^{\mathrm{qh}}} \\
&= F_0^{\mathrm{el}}(\Omega, T) - k_{\mathrm{B}} T \ln \sum_{\{n_i\}} \exp\left[-\beta \sum_i^{3N_n} \hbar\omega_i(\Omega, T)\left(n_i + \frac{1}{2}\right)\right].
\end{aligned}
\tag{2.157}
$$

The outer sum runs here over all possible sets $\{n_i\}$ which can be constructed when each n_i can take the values $0, 1, 2, \ldots, \infty$. We have also defined the quasiharmonic partition function Z^{qh} which can be rewritten as:

$$Z^{\mathrm{qh}} = \sum_{\{n_i\}} \prod_i^{3N_n} e^{-\beta\hbar\omega_i(n_i+1/2)} = \prod_i^{3N_n} e^{-\beta\hbar\omega_i/2} \sum_{n=0}^{\infty} e^{-n\,\beta\hbar\omega_i} = \prod_i^{3N_n} e^{-\beta\hbar\omega_i/2}\left[1 - e^{-\beta\hbar\omega_i}\right]^{-1}. \tag{2.158}$$

To obtain the second equality, note that it is merely a generalization of

$$\sum_{n_1, n_2}^{\infty} n_1 n_2 = \left(\sum_{n_1}^{\infty} n_1\right)\left(\sum_{n_2}^{\infty} n_2\right), \tag{2.159}$$

whereas the last equality in Eq. (2.158) is obtained from the geometric series. Resubstituting Z^{qh} into Eq. (2.157), we finally obtain

$$F(\Omega, T) \approx F_0^{\mathrm{el}}(\Omega, T) + F^{\mathrm{qh}}(\Omega, T), \tag{2.160}$$

where we have defined the quasiharmonic free energy F^{qh} by

$$F^{\mathrm{qh}}(\Omega, T) := \underbrace{\sum_{\mathbf{G}^{\mathrm{sc}}}^{\mathrm{prBZ}'} \sum_s^3 \frac{1}{2}\hbar\omega_{\mathbf{G}^{\mathrm{sc}}, s}(\Omega, T)}_{=: E^{\mathrm{zp}}(\Omega; T) = \substack{\text{zero point}\\\text{energy}}} + \underbrace{T k_{\mathrm{B}} \sum_{\mathbf{G}^{\mathrm{sc}}}^{\mathrm{prBZ}'} \sum_s^3 \ln\left[1 - \exp\left\{-\beta\hbar\omega_{\mathbf{G}^{\mathrm{sc}}, s}(\Omega, T)\right\}\right]}_{=: S^{\mathrm{qh}}(\Omega, T) = \text{entropic contribution}},$$

$$\tag{2.161}$$

using again explicitly $\mathbf{G}^{\mathrm{sc}}$ and s instead of i. We have also changed the sum over the prBZ to a sum over prBZ′ which denotes that the $\mathbf{G}^{\mathrm{sc}} = \{0, 0, 0\}$ vector needs to excluded. This vector corresponds to a rigid shift of the full crystal and is unphysical since in a corresponding experimental setup the crystal is fixed in space. Note that including this degree of freedom would lead to a diverging F^{qh} since the corresponding frequencies are zero. The quasiharmonic free energy consists of a term

which does not explicitly depend on the temperature and which is referred to as the zero point energy, E^{zp}. Note however that $E^{\mathrm{zp}}(\Omega; T)$ depends implicitly on T through $\omega_{\mathbf{G}^{\mathrm{sc}} s}(T)$ (indicated by the semicolon). The second term in F^{qh} depends implicitly and explicitly on T and is referred to as the entropic contribution, TS^{qh}. Equations (2.160) and (2.161) are the key equations of the quasiharmonic approach. In order to show their computational requirements and compare their scaling behavior with the one of the original effective nuclei Schrödinger equation, Eqs. (2.110) and (2.112), we need to discuss the properties of the dynamical matrix and to show how to obtain it from a Kohn-Sham calculation. Before, let us add a brief comment on the statistical nature of the phonons.

Based on a similar derivation as the one applied above to obtain F^{qh}, one can derive an expression for the average occupation number f_{n_i} of the various phonon energy levels. It reads [68]

$$f_{n_i} \;=\; \left[e^{\beta \hbar \omega_i} - 1 \right]^{-1} \tag{2.162}$$

and it is called the Bose-Einstein function. In contrast to the Fermi-Dirac function, Eq. (2.65), it allows to occupy an energy level by an arbitrary number of phonons, i.e., phonons are bosons. An example Bose-Einstein function is plotted in Fig. 2.1.

2.3.4 Dynamical matrix

There are basically two distinct approaches to calculate the dynamical matrix. The first one is called the *direct force constant* method and it utilizes finite differences of forces to calculate the real space dynamical matrix $\mathbf{D}$. A part of the methodological work performed in the present study consisted of implementing the necessary routines allowing to employ this method and the results discussed in Chap. 4 are mainly based on the direct force constant method. We will therefore discuss it in detail in this section along with symmetry properties of the dynamical matrix. The second approach is the *linear response* method and it utilizes perturbation theory to calculate directly the reciprocal matrix $\mathbf{D}_{\mathbf{G}^{\mathrm{sc}}}$. It is discussed and compared with the direct force constant method in App. A.1.4.

The direct force constant approach [72] is based on an expression for the real space dynamical matrix in terms of forces acting on the nuclei which reads

$$D_{I\alpha, J\beta}(\Omega, T) \;=\; \frac{1}{M_I} \left[\frac{\partial^2 F^{\mathrm{el}}(\{\mathbf{R}_I\}, \Omega, T)}{\partial R_{I,\alpha} \partial R_{J,\beta}} \right]_{\{\mathbf{R}_I^0\}} = \; -\frac{1}{M_I} \left[\frac{\partial F_{I,\alpha}^{\mathrm{HF}}(\{\mathbf{R}_I\}, \Omega, T)}{\partial R_{J,\beta}} \right]_{\{\mathbf{R}_I^0\}}, \tag{2.163}$$

where we have defined the force $\mathbf{F}_{I,\alpha}^{\mathrm{HF}}$ on nucleus I in direction α by:

$$F_{I,\alpha}^{\mathrm{HF}}(\{\mathbf{R}_I\}, \Omega, T) \;=\; -\frac{\partial F^{\mathrm{el}}(\{\mathbf{R}_I\}, \Omega, T)}{\partial R_{I,\alpha}}. \tag{2.164}$$

The "HF" in the superscript is explained below. To show the advantage of formulating the dynamical matrix in terms of forces, note that the only quantities in the defining equation of $F^{\mathrm{el}}(\{\mathbf{R}_I\})$, Eq. (2.68), which explicitly depend on the nuclei coordinates $\{\mathbf{R}_I\}$ are $v(\mathbf{r})$ and V^{nuc} as can be seen from their definitions in Eqs. (2.49) and (2.50), respectively. The other quantities depend implicitly on the $\{\mathbf{R}_I\}$ since the charge density ρ depends on them through the self consistency cycle, Eq. (2.66). However, F^{el} is constructed such as to correspond to the minimum with respect to ρ and therefore this implicit dependence will not contribute to the derivative in Eq. (2.164). We

thus can write:

$$
\begin{aligned}
F_{I,\alpha}^{\mathrm{HF}}(\{\mathbf{R}_I\},\Omega,T) &= \int \rho(\mathbf{r},\Omega,T)\, \frac{\partial v(\mathbf{r},\{\mathbf{R}_I\},\Omega)}{\partial R_{I,\alpha}}\, d\mathbf{r} \;+\; \frac{\partial V^{\mathrm{nuc}}(\{\mathbf{R}_I\},\Omega)}{\partial R_{I,\alpha}} \\[2mm]
&= \int \rho(\mathbf{r},\Omega,T)\, \frac{Z_I e^2 (r_\alpha - R_{I,\alpha})}{4\pi\epsilon_0 |\mathbf{r}-\mathbf{R}_I|^3}\, d\mathbf{r} \;+\; \sum_{J\neq I}^{N_n} \frac{Z_I Z_J e^2 (R_{I,\alpha}-R_{J,\alpha})}{4\pi\epsilon_0 |\mathbf{R}_I-\mathbf{R}_J|^3}.
\end{aligned} \quad (2.165)
$$

Here, we have adjusted the dependence of ρ, $v(\mathbf{r})$, and V^{nuc} to correspond to the supercell approach (Ω dependence). Further, we have indicated the temperature dependence of ρ which enters through the electron occupation numbers f_i in its defining equation, Eq. (2.64). Equation (2.165) is a version of the Hellmann-Feynman theorem [73–75] and the forces are therefore referred to as Hellmann-Feynman (HF) forces. The key point of Eq. (2.165) is the second equality stating that the Hellmann-Feynman forces can be expressed analytically. This approach to obtain the forces should be contrasted with the other possibility which is a numerical finite difference approach

$$
F_{I,\alpha}^{\mathrm{HF}}(\{\mathbf{R}_I\},\Omega,T) = \frac{1}{\Delta R}\left[F^{\mathrm{el}}(R_{1,1},\ldots,R_{I,\alpha}+\Delta R,\ldots,R_{N_n,3},\Omega,T) - F^{\mathrm{el}}(\{\mathbf{R}_I\},\Omega,T)\right], \quad (2.166)
$$

with ΔR a suitably chosen displacement (typically in the range of $0.01a_0$). Equation (2.166) requires two separate Kohn-Sham calculations of F^{el}, with and without the displacement, each consisting of a full self consistency cycle Eq. (2.66). To calculate the forces on all N_n nuclei in all three spatial directions, we need $3N_n+1$ Kohn-Sham calculations. In contrast, utilizing the Hellmann-Feynman theorem, we need only 1 Kohn-Sham calculation at $\{\mathbf{R}_I\}$. The corresponding converged charge density ρ can then be employed in Eq. (2.165) to efficiently calculate the forces on all nuclei.

The Hellmann-Feynman theorem has been presented here in real space. It is however also fully applicable when the Kohn-Sham equations are given in terms of plane waves in reciprocal space, Eq. (2.86). The corresponding equations for the forces can be found for instance in Ref. [47]. In fact, the possibility to efficiently compute forces is a further advantage, additionally to the two mentioned at the beginning of Sec. 2.1.7, of the plane wave basis as compared for instance to an atomic like basis. The latter requires additional terms (so called Pulay forces [76]) which arise due to the explicit dependence of the basis on the nuclei coordinates.

For the calculation of the derivative of the forces in Eq. (2.163), we resort to the finite difference method:

$$
D_{I\alpha,J\beta}(\Omega,T) = -(M_I \Delta R)^{-1}\, F_{I,\alpha}^{\mathrm{HF}}(R_{1,1}^0,\ldots,R_{J,\beta}^0+\Delta R,\ldots,R_{N_n,3}^0,\Omega,T). \quad (2.167)
$$

We do not need to explicitly subtract $F_{I,\alpha}^{\mathrm{HF}}(\{\mathbf{R}_I^0\})$ in Eq. (2.167), since it is identical to zero due to the equilibrium nuclei positions. We hence have to perform $3N_n$ force calculations, i.e., according to the above discussion Kohn-Sham calculations, to obtain the full dynamical matrix $\mathbf{D}$ for a single supercell volume Ω. We will show in the following that this number can be reduced to one for the systems studied in the present work, if we employ translational and point symmetry arguments.

We first discuss translational symmetry. As a preliminary consideration, we point out the translational property of a supercell with all nuclei at their $T = 0$ K equilibrium positions $\{\mathbf{R}_I^0\}$. Due to the construction of the supercell, Eqs. (2.114) to (2.116), based on the conventional fcc unit cell, it is possible to translate the nuclei by a difference vector $\Delta\mathbf{R}_{I,J}^0 = \mathbf{R}_I^0 - \mathbf{R}_J^0$ where I and J can be any two nuclei out of the supercell. The resulting structure will match the original one exactly. We only need to take special care of the nuclei that move out of the supercell by mapping them back using the supercell vectors $\mathbf{s}_1$, $\mathbf{s}_2$, and $\mathbf{s}_3$ from Eq. (2.114). We write the translation of

nucleus K including the mapping as:

$$\text{mod}\big[\,\mathbf{R}_K^0 + \Delta\mathbf{R}_{I,J}^0,\ \{\mathbf{s}_i\}\big], \quad i = 1, 2, 3. \tag{2.168}$$

Let us now consider a calculation in which we displace a particular nucleus I into direction α:

$$\{R_{1,1}^0, \ldots, R_{I,\alpha}^0 + \Delta R, \ldots, R_{N_n,3}^0\} \quad \Rightarrow \quad \{\mathbf{F}^{\text{HF}}(\mathbf{R}_1), \ldots, \mathbf{F}^{\text{HF}}(\mathbf{R}_I), \ldots, \mathbf{F}^{\text{HF}}(\mathbf{R}_{N_n})\}. \tag{2.169}$$

We have indicted here that the displacement will create a force field, i.e., a force on each atom in the supercell. From the force field Eq. (2.169), we can construct the force field to the displacement of any other nucleus J in the same direction α,

$$\{R_{1,1}^0, \ldots, R_{J,\alpha}^0 + \Delta R, \ldots, R_{N_n,3}^0\} \tag{2.170}$$

without additional Kohn-Sham calculations by applying:

$$\Big\{\mathbf{F}^{\text{HF}}\left(\text{mod}\big[\,\mathbf{R}_1^0 + \Delta\mathbf{R}_{I,J}^0,\ \{\mathbf{s}_i\}\big]\right), \ldots, \mathbf{F}^{\text{HF}}\left(\text{mod}\big[\,\mathbf{R}_I^0 + \Delta\mathbf{R}_{I,J}^0,\ \{\mathbf{s}_i\}\big]\right), \ldots,$$

$$\ldots, \mathbf{F}^{\text{HF}}\left(\text{mod}\big[\,\mathbf{R}_J^0 + \Delta\mathbf{R}_{I,J}^0,\ \{\mathbf{s}_i\}\big]\right), \ldots, \mathbf{F}^{\text{HF}}\left(\text{mod}\big[\,\mathbf{R}_{N_n}^0 + \Delta\mathbf{R}_{I,J}^0,\ \{\mathbf{s}_i\}\big]\right)\Big\}. \tag{2.171}$$

Translational symmetry thus allows to reduce the computational effort from $3N_n$ to 3 calculations.

Let us now turn to point symmetry and consider first the symmetry properties of the perfect fcc crystal. There are 48 point symmetry operations (including mirror symmetries) which map the fcc crystal into itself. They can be represented by 3×3 matrices acting on Cartesian coordinates. Among them are

$$\mathbf{S}^{\text{xy}} = \begin{pmatrix} 0 & 1 & 0 \\ 1 & 0 & 0 \\ 0 & 0 & 1 \end{pmatrix} \quad \text{and} \quad \mathbf{S}^{\text{xz}} = \begin{pmatrix} 0 & 0 & 1 \\ 0 & 1 & 0 \\ 1 & 0 & 0 \end{pmatrix}, \tag{2.172}$$

which map the x axis onto the y axis and the x axis onto the z axis, respectively. We can use $\mathbf{S}^{\text{xy}}$ and $\mathbf{S}^{\text{xz}}$ to construct the force field corresponding to the displacement of nucleus I into direction $\beta = y$ and $\beta = z$ from a single Kohn-Sham calculation for I and $\alpha = x$. To do so, we have however to ensure that our supercell is compatible with both symmetry operations. To illustrate this, consider a supercell with:

$$\mathbf{s}_1 = (s_x, 0, 0), \quad \mathbf{s}_2 = (0, s_y, 0), \quad \mathbf{s}_3 = (0, 0, s_z). \tag{2.173}$$

If we displace nucleus I by ΔR along x, we obtain a pattern of displacements due to the image atoms. According to Eq. (2.118) [with $\mathbf{U} = (\Delta R, 0, 0)$] and using Eq. (2.173), this pattern reads

$$\mathbf{U}(\mathbf{R}_I^0 + n_1\mathbf{s}_1 + n_2\mathbf{s}_2 + n_3\mathbf{s}_3) = \begin{pmatrix} \Delta R \\ 0 \\ 0 \end{pmatrix} \left(\mathbf{R}_I^0 + \begin{pmatrix} n_1\,s_x \\ n_2\,s_y \\ n_3\,s_z \end{pmatrix} \right), \tag{2.174}$$

with n_1, n_2, and n_3 integers. Similarly, if we displace along y, we obtain:

$$\mathbf{U}(\mathbf{R}_I^0 + n_1\mathbf{s}_1 + n_2\mathbf{s}_2 + n_3\mathbf{s}_3) = \begin{pmatrix} 0 \\ \Delta R \\ 0 \end{pmatrix} \left(\mathbf{R}_I^0 + \begin{pmatrix} n_1\,s_x \\ n_2\,s_y \\ n_3\,s_z \end{pmatrix} \right). \tag{2.175}$$

The displacement patterns, Eqs. (2.174) and (2.175), can only be mapped onto each other using

$\mathbf{S}^{\mathrm{xy}}$, if $s_x = s_y$. This holds also true for the displacement along z and $\mathbf{S}^{\mathrm{xz}}$ and we therefore require $s_x = s_y = s_z$, i.e., a cubic supercell. In general, our supercell needs to be compatible with the symmetry operations that are to be used to map one displacement pattern onto the other. Based on appropriate supercells, we require only one Kohn-Sham calculation for

$$\{R_{1,1}^0, \ldots, R_{I,1}^0 + \Delta R, \ldots, R_{N_n,3}^0\} \quad \Rightarrow \quad \{\mathbf{F}^{\mathrm{HF}}(\mathbf{R}_1), \ldots, \mathbf{F}^{\mathrm{HF}}(\mathbf{R}_I), \ldots, \mathbf{F}^{\mathrm{HF}}(\mathbf{R}_{N_n})\}, \qquad (2.176)$$

from which we can construct the force field corresponding to

$$\{R_{1,1}^0, \ldots, R_{I,2}^0 + \Delta R, \ldots, R_{N_n,3}^0\} \qquad (2.177)$$

by using

$$\left\{ \mathbf{S}^{\mathrm{xy}} \cdot \mathbf{F}^{\mathrm{HF}} \left(\mathrm{mod}\left[\mathbf{S}^{\mathrm{xy}} \cdot \mathbf{R}_1^0, \{\mathbf{s}_i\} \right] \right), \ldots, \mathbf{S}^{\mathrm{xy}} \cdot \mathbf{F}^{\mathrm{HF}} \left(\mathrm{mod}\left[\mathbf{S}^{\mathrm{xy}} \cdot \mathbf{R}_I^0, \{\mathbf{s}_i\} \right] \right), \ldots, \right.$$

$$\left. \ldots, \mathbf{S}^{\mathrm{xy}} \cdot \mathbf{F}^{\mathrm{HF}} \left(\mathrm{mod}\left[\mathbf{S}^{\mathrm{xy}} \cdot \mathbf{R}_{N_n}^0, \{\mathbf{s}_i\} \right] \right) \right\} \quad (2.178)$$

and similarly for z and $\mathbf{S}^{\mathrm{xz}}$. Including both, translational and point symmetry operations, we can, for the elementary fcc crystals studied here, reduce the number of necessary Kohn-Sham calculations from $3N_n$ to 1 for each supercell volume Ω.

Finally in the discussion of the dynamical matrix, we need to comment on three important issues. First, the value for the displacement ΔR needed for the finite difference of the forces was introduced rather *ad hoc*. An appropriate displacement needs however to be derived from test calculations scanning various displacements. In general, if the displacement is too small, the forces will contain a significant amount of noise, while too large displacements will cause anharmonic contributions to be present. Both situations need to be avoided. We will address this issue in Sec. 3.4.4.1. Second, as described above, utilizing Hellmann-Feynman forces allows a significant reduction of the number of necessary Kohn-Sham calculations. However, the calculation of forces is rather sensitive with respect to convergence parameters (k sampling, E^{cut}, augmentation grid). It is therefore very important to carefully check the resulting thermodynamic properties with respect to the controllable errors. This issue will be addressed in Secs. 3.4.1 and 3.4.2. Third, to reduce the computational effort, the dynamical matrix $\mathbf{D}$ is typically approximated by:

$$D_{I\alpha,J\beta}(\Omega,T) = \frac{1}{M_I} \left[\frac{\partial^2 F^{\mathrm{el}}(\{\mathbf{R}_I\},\Omega,T)}{\partial R_{I,\alpha} \partial R_{J,\beta}} \right]_{\{\mathbf{R}_I^0\}} = -\frac{1}{M_I} \left[\frac{\partial F_{I,\alpha}^{\mathrm{HF}}(\{\mathbf{R}_I\},\Omega,T)}{\partial R_{J,\beta}} \right]_{\{\mathbf{R}_I^0\}} \approx \qquad (2.179)$$

$$\approx \frac{1}{M_I} \left[\frac{\partial^2 E_g^{\mathrm{el}}(\{\mathbf{R}_I\},\Omega)}{\partial R_{I,\alpha} \partial R_{J,\beta}} \right]_{\{\mathbf{R}_I^0\}} =: -\frac{1}{M_I} \left[\frac{\partial F_{I,\alpha}^{\mathrm{HF,0K}}(\{\mathbf{R}_I\},\Omega)}{\partial R_{J,\beta}} \right]_{\{\mathbf{R}_I^0\}} =: D_{I\alpha,J\beta}^{\mathrm{0K}}(\Omega).$$

Here, E_g^{el} is the $T = 0$ K ground state of the electronic Schrödinger equation, Eq. (2.16). The corresponding Hellmann-Feynman forces $\mathbf{F}^{\mathrm{HF,0K}}$ and the dynamical matrix $\mathbf{D}^{\mathrm{0K}}$ have been therefore marked with the "0K" superscript. Using $\mathbf{D}^{\mathrm{0K}}$, the full formalism leading to phonon frequencies and eventually to the quasiharmonic free energy can be applied as presented. It is however convenient to adopt also for the other quantities the notation:

$$\mathbf{D}_{\mathbf{G}^{\mathrm{sc}}} \to \mathbf{D}_{\mathbf{G}^{\mathrm{sc}}}^{\mathrm{0K}}, \quad \omega_{\mathbf{G}^{\mathrm{sc}},s} \to \omega_{\mathbf{G}^{\mathrm{sc}},s}^{\mathrm{0K}}, \quad E^{\mathrm{zp}} \to E^{\mathrm{zp,0K}}, \quad S^{\mathrm{qh}} \to S^{\mathrm{qh,0K}}, \quad \text{and} \quad F^{\mathrm{qh}} \to F^{\mathrm{qh,0K}}. \tag{2.180}$$

The $\mathbf{D}^{0K}$ approximation is performed in most applications of the quasiharmonic approach and its influence has not been assessed yet. In the present study, we will investigate the validity of this approximation in Sec. 4.2.

The discussion of the dynamical matrix and thus of the quasiharmonic approximation is now complete and we summarize the key equations and the flow of the main quantities. In this summary we use the $\mathbf{D}^{0K}$ approximation, while the full formalism based on $\mathbf{D}$ is developed in Sec. 3.3.4:

$$
\overbrace{}^{\substack{\text{HF forces from Kohn-Sham}\\\text{calculations for different }\Omega}}
$$

$$
\boxed{D^{0K}_{I\alpha,J\beta}(\Omega)} \;=\; -(M_I \Delta R)^{-1}\, F^{\mathrm{HF,0K}}_{I,\alpha}(R^0_{1,1},\dots,R^0_{J,\beta}+\Delta R,\dots,R^0_{N_n,3},\Omega) \tag{2.181}
$$

$$
\boxed{D^{0K}_{\mathbf{G}^{\mathrm{sc}},\,\alpha\beta}(\Omega)} \;=\; N_n^{-1}\sum_{I,J}^{N_n} \boxed{D^{0K}_{I\alpha,J\beta}(\Omega)}\, e^{i\mathbf{G}^{\mathrm{sc}}\cdot(\mathbf{R}^0_I-\mathbf{R}^0_J)} \tag{2.182}
$$

$$
\boxed{\mathbf{D}^{0K}_{\mathbf{G}^{\mathrm{sc}}}(\Omega)}\,\mathbf{w}_{\mathbf{G}^{\mathrm{sc}};\,s} \;=\; \boxed{(\omega^{0K}_{\mathbf{G}^{\mathrm{sc}};\,s})^2(\Omega)}\,\mathbf{w}_{\mathbf{G}^{\mathrm{sc}};\,s} \tag{2.183}
$$

$$
\overbrace{}^{\substack{\text{Kohn-Sham calculations}\\\text{for different }\Omega\text{ and }T}}
$$

$$
\boxed{F(\Omega,T)} \;\approx\; F^{\mathrm{el}}(\{\mathbf{R}^0_I\},\Omega,T) \;+\; \sum_{\mathbf{G}^{\mathrm{sc}}}^{\mathrm{prBZ}'}\sum_s^3 \left\{ \tfrac{1}{2}\hbar\,\boxed{\omega^{0K}_{\mathbf{G}^{\mathrm{sc}},s}(\Omega)} + k_{\mathrm{B}}T\ln\left[1-\exp\left\{-\beta\hbar\,\boxed{\omega^{0K}_{\mathbf{G}^{\mathrm{sc}},s}(\Omega)}\right\}\right]\right\}
$$

$$
\underbrace{} \;=\; F^{\mathrm{qh,0K}}(\Omega,T) = E^{\mathrm{zp,0K}}(\Omega)+TS^{\mathrm{qh,0K}}(\Omega) \tag{2.184}
$$

$$
\boxed{F(\Omega,T)}\,/N_n \;=\; F(V,T)\,. \tag{2.185}
$$
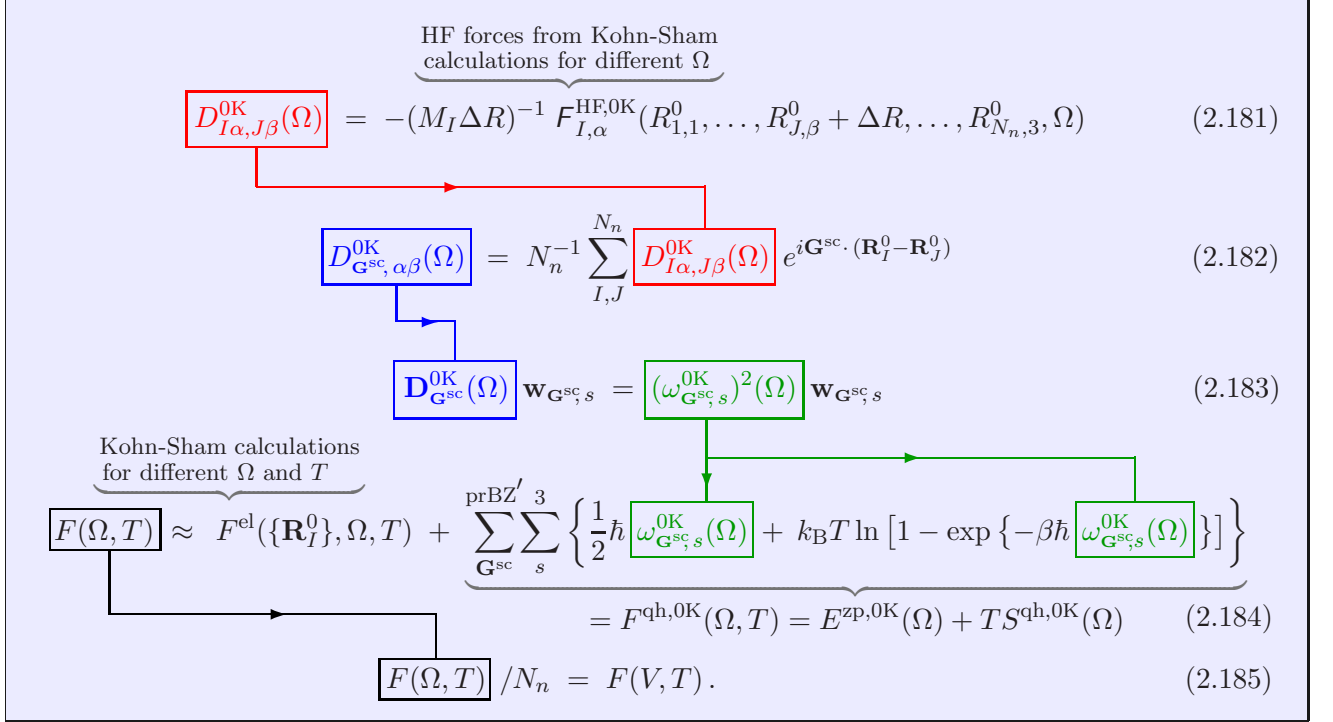
The free energy $F(\Omega,T)$ corresponds to a supercell with N_n atoms. Scaling by N_n therefore gives a per atom quantity $F(V,T)$ which corresponds to the free energy from Eq. (2.2). In our case, $F(V,T)$ is equivalent to the free energy per primitive unit cell with volume V from Eq. (2.80). We note that for reasons of a convenient discussion, we will hereafter also frequently change the notation for the forces, the dynamical matrix, the phonon frequencies, and the quasiharmonic free energy as

$$
\mathbf{F}^{\mathrm{HF,0K}}_I(\Omega) \;\to\; \mathbf{F}^{\mathrm{HF,0K}}_I(V),\quad \mathbf{D}^{0K}(\Omega)\to\mathbf{D}^{0K}(V),\quad \mathbf{D}^{0K}_{\mathbf{G}^{\mathrm{sc}}}(\Omega)\to\mathbf{D}^{0K}_{\mathbf{G}^{\mathrm{sc}}}(V),\quad \omega^{0K}_{\mathbf{G}^{\mathrm{sc}},s}(\Omega)\to\omega^{0K}_{\mathbf{G}^{\mathrm{sc}},s}(V)
$$

$$
E^{\mathrm{zp,0K}}(\Omega)/N_n \to E^{\mathrm{zp,0K}}(V),\quad S^{\mathrm{qh,0K}}(\Omega)/N_n \to S^{\mathrm{qh,0K}}(V),\quad\text{and}\quad F^{\mathrm{qh,0K}}(\Omega)/N_n \to F^{\mathrm{qh,0K}}(V), \tag{2.186}
$$

and analogously for the quantities without the "0K" superscript. In using the replacements in Eq. (2.186), it should be however remembered that to calculate these quantities (within the direct force constant method) a supercell is needed. In Eq. (2.184), we have changed F^{el}_0 back to its original definition $F^{\mathrm{el}}(\{\mathbf{R}^0_I\})$ and explicitly written its dependence on the temperature, which enters through the Fermi function, Eq. (2.65). To satisfy this dependence, we need to explicitly perform Kohn-Sham calculations at different temperatures. The practical approach will be presented in Sec. 3.3 and we note here only that ≈ 10 temperatures are sufficient. We also need to consider ≈ 10 different volumes for each temperature. For $F^{\mathrm{el}}(\{\mathbf{R}^0_I\})$, we can however use the fact that all atoms are in their $T=0$ K equilibrium positions which allows to use directly the one atomic primitive unit cell

with volume V. As noted above, the volume dependence of the Hellmann-Feynman forces $F_{I,\alpha}^{\mathrm{HF,0K}}$ needs to be computed using the supercell with volume Ω. Within the $T = 0$ K approximation of the dynamical matrix, Eq. (2.179), the $F_{I,\alpha}^{\mathrm{HF,0K}}$ are however temperature independent and one calculation at $T = 0$ K for each Ω suffices. The scaling $s^{\mathrm{qh,0K}}$ of the quasiharmonic approach within the $\mathbf{D}^{0\mathrm{K}}$ approximation therefore reads:

$$s^{\mathrm{qh,0K}} \;=\; N_V N_T \cdot \underbrace{s^{\mathrm{KS}}(a^{\mathrm{lat}}, E^{\mathrm{cut}}, N_k^{\mathrm{irr,pr}}, N_e^{\mathrm{pr}}, N^{\mathrm{it}})}_{\text{Kohn-Sham eq. for primitive cell}} \;+\; N_V \cdot \underbrace{s^{\mathrm{KS}}(a^{\mathrm{sc}}, E^{\mathrm{cut}}, N_k^{\mathrm{irr}}, N_e, N^{\mathrm{it}})}_{\text{Kohn-Sham eq. for supercell}}. \quad (2.187)$$

Here, N_V and N_T are the number of volume and temperature points respectively. We have further introduced $N_k^{\mathrm{irr,pr}} \approx N_n N_k^{\mathrm{irr,pr}}$ the number of irreducible $\mathbf{k}$ vectors inside the prBZ, $N_e^{\mathrm{pr}} = N_e/N_n$ the number of electrons in the prBZ, and $a^{\mathrm{sc}} = n^{\mathrm{sc}} a^{\mathrm{lat}}$. Equation (2.187) describes a readily accessible problem for present day computational resources. Its performance will be addressed in Sec. 4.1. In the following sections, we will present approaches that allow to go beyond the quasiharmonic approximation.

2.3.5 Beyond the quasiharmonic approximation

Two conceptually distinct routes exist to take the terms $O(U^3)$ in the expansion Eq. (2.130) into account:

1) *Classical statistical approaches*: The basic idea is to start with the general expression for the quantum mechanical free energy F and to replace it by its classical counterpart F^{clas}

$$F \;=\; -k_{\mathrm{B}} T \ln \sum_\mu \langle \tilde{\Lambda}_\mu | \exp \left\{ -\beta \left[-\sum_I^{N_n} \frac{\hbar^2}{2M_I} \nabla_I^2 + \hat{1} F^{\mathrm{el}}(\{\mathbf{R}_I\}) \right] \right\} | \tilde{\Lambda}_\mu \rangle \quad (2.188)$$

$$\Rightarrow \quad F^{\mathrm{clas}} \;=\; -k_{\mathrm{B}} T \ln \int d\mathbf{P}_I \int d\mathbf{R}_I \exp \left\{ -\beta \left[\sum_I^{N_n} \frac{1}{2M_I} |\mathbf{P}_I|^2 + F^{\mathrm{el}}(\{\mathbf{R}_I\}) \right] \right\} \Big/ (h^{3N_n} N_n!),$$
$$(2.189)$$

with the Planck constant $h = 2\pi\hbar$. The expression for F is obtained by multiplying Eq. (2.110) from left with $\tilde{\Lambda}_\mu^*$ and integrating over the nuclei coordinates, by inserting the result and Eq. (2.8) into Eq. (2.111), and by using Eq. (A.5). The expression for F^{clas} is obtained using the transformation rule for the momentum Eq. (2.136), by replacing the trace, Eq. (A.6), with an integral over the nuclei momenta and coordinates defined as in Eq. (A.8), and by scaling for consistency with $1/(h^{3N_n} N_n!)$ (see e.g. Ref. [77]). An advantage of Eq. (2.189) over Eq. (2.188) is that the term inside the exponential is diagonal in the nuclei coordinates, since $\mathbf{P}_I$ is a local operator in contrast to ∇_I, i.e., at each nucleus position $\mathbf{R}_I$, $\mathbf{P}_I$ has a definite value. Therefore, Eq. (2.189) needs not to be treated as a matrix equation and hence it scales as $s = (N_{\mathrm{mesh}}^3)^{N_n} \cdot s^{\mathrm{KS}}(a^{\mathrm{lat}}, E^{\mathrm{cut}}, N_k^{\mathrm{irr}}, N_e, N^{\mathrm{it}})$, i.e., the second term is removed as compared to the scaling of Eq. (2.188) given in Eq. (2.112). However, the prefactor $(N_{\mathrm{mesh}}^3)^{N_n}$ corresponding to the sampling of the nuclei phase space (i.e., the integral $\int d\mathbf{R}_I$) is still present and difficulty 1) from the discussion at the beginning of Sec. 2.3.1 still applies. [In fact, the prefactor doubles due to $\int d\mathbf{P}_I$; see however Eq. (2.190) below.] There are two complementary classes of methods to tackle this difficulty:

- *Monte Carlo methods* [78] are based on a stochastic/random sampling of the phase space.
- *Molecular dynamics simulations* [78] use deterministic equations of motion (e.g., Newton's equation of motion) to sample the phase space.

The advantages and disadvantages of both approaches are compared for instance in Ref. [79]. For our present purposes, we will employ a scheme based on a combination of both: The so called Langevin dynamics which extends the original molecular dynamics by a random element. This coupled approach has been implemented into the S/PHI/NX[9] code and extensively tested in a previous study [81]. It turns out to be a very efficient way to sample the phase space. We will discuss it in Sec. 2.3.6.

The discussion of the classical statistical approaches so far has been based on the free energy expression Eq. (2.189) which corresponds to a general definition of the free energy. In particular, evaluating Eq. (2.189) directly corresponds to calculating all terms in the expansion in Eq. (2.130). We would however like to benefit from the results obtained within the quasiharmonic approximation, which is, in comparison to the statistical methods, very efficient and contains already quantum mechanical effects, i.e., we would like to calculate only the $O(U^3)$ terms. The method which allows this is the so called thermodynamic integration discussed likewise in Sec. 2.3.6.

2) *Quantum mechanical perturbation theory*: The idea here is to explicitly include the $O(U^3)$ terms in the expansion Eq. (2.130) successively order by order. The solution of the quasiharmonic approximation, i.e., the system of non-interacting phonons, is fundamentally included as the unperturbed system which is subjected to quantum mechanical perturbation theory. The $O(U^3)$ terms correspond to interactions between phonons and can also lead to their creation or destruction. We will discuss this approach in Sec. 2.3.7.

Let us briefly contrast the two approaches with each other. Within the classical statistical approach all, i.e., infinitely many, orders of the expansion in Eq. (2.130) are taken into account, since the phase space is explicitly (numerically) sampled. Using quantum mechanical perturbation theory only the lowest and in practice typically only the third and fourth order terms are taken into account, since the corresponding calculations become rapidly infeasible. The quantum mechanical character of the system is however fully included as opposed to the classical approach. Another advantage is that with perturbation theory one obtains analytical formulas for thermodynamic properties which allows to efficiently study their temperature dependence. In contrast, within the statistical approach each temperature needs to be recalculated explicitly. It is difficult to *a priori* decide which approach is better suited, a combination being certainly desirable.

2.3.6 Thermodynamic integration based Langevin dynamics

The central idea of the thermodynamic integration[10] is to couple the full classical system, i.e., Eq. (2.189), to the **classical** quasiharmonic system, Eq. (2.146). The free energy that needs then to be sampled is effectively the difference free energy between these two systems, i.e., the terms $O(U^3)$ in Eq. (2.130). Since this difference is rather small, the corresponding sampling converges in

---

[9]The S/PHI/NX code [80] is developed at the Max-Planck-Institut für Eisenforschung, Düsseldorf, at which also the main part of the present work was performed. S/PHI/NX is an *ab initio* based multiscale library including, e.g., many features necessary for anharmonic calculations. The results presented in Sec. 4.3 were obtained using this package.

[10]In fact, thermodynamic integration is a more general scheme applicable to any two systems, one which is not directly solvable and one reference system which can be treated efficiently. The coupling of the two systems allows to solve also the original system.

reasonable numbers of sampling steps. This classical free energy for the $O(U^3)$ terms is eventually added to the quantum mechanical free energy of the quasiharmonic approximation, Eq. (2.160), resulting in the desired full free energy.

To introduce thermodynamic integration formally, we note first that in Eq. (2.189) the integral over the nuclei momenta can be carried out analytically giving [77, p. 63]

$$F^{\text{clas}} = -k_{\text{B}}T \ln \int d\mathbf{R}_I \, e^{-\beta F^{\text{el}}(\{\mathbf{R}_I\})} \big/ (\Lambda^{3N_n} N_n!), \tag{2.190}$$

where $\Lambda = h/\sqrt{2\pi M_I k_{\text{B}}T}$ is the de Broglie wavelength. Let us next define a coupled system with an electronic free energy F_λ^{el} given by

$$F_\lambda^{\text{el}}(\{\mathbf{R}_I\}, V) \;=\; (1-\lambda)\Big[F_0^{\text{el}}(V) \,+\, \mathbf{U}\mathbf{D}(V)\mathbf{U}/(2\mathbf{M})\Big] \,+\, \lambda F^{\text{el}}(\{\mathbf{R}_I\}, V), \tag{2.191}$$

where we have explicitly written the dependence on the volume V, used the shorthand notation from Eq. (2.133), and introduced a coupling parameter λ which can take the values $0\ldots1$. Equation (2.191) describes a linear coupling between the actual system of interest, given by F^{el}, and a system fully described by the (real space) dynamical matrix $\mathbf{D}$, i.e., by the second order approximation to Eq. (2.130). Next, we differentiate the classical free energy corresponding to F_λ^{el},

$$F_\lambda^{\text{clas}} = -k_{\text{B}}T \ln \int d\mathbf{R}_I \, e^{-\beta F_\lambda^{\text{el}}(\{\mathbf{R}_I\})} \big/ (\Lambda^{3N_n} N_n!) \;=:\; -k_{\text{B}}T \ln Z_\lambda, \tag{2.192}$$

where we have defined the classical partition function Z_λ of the coupled system, with respect to λ [the reason for this becoming apparent in Eq. (2.195) below]:

$$
\begin{aligned}
\frac{\partial F_\lambda^{\text{clas}}}{\partial \lambda} &= -k_{\text{B}}T Z_\lambda^{-1} \int d\mathbf{R}_I e^{-\beta F_\lambda^{\text{el}}(\{\mathbf{R}_I\})} \left[-\beta \frac{\partial F_\lambda^{\text{el}}}{\partial \lambda}\right] \big/ (\Lambda^{3N_n} N_n!) \\
&=: \left\langle \frac{\partial F_\lambda^{\text{el}}}{\partial \lambda} \right\rangle_{T,\lambda} \\
&= \left\langle F^{\text{el}}(\{\mathbf{R}_I\}, V) - F_0^{\text{el}}(V) - \mathbf{U}\mathbf{D}(V)\mathbf{U}/(2\mathbf{M}) \right\rangle_{T,\lambda}.
\end{aligned}
\tag{2.193}
$$

Here, we have defined the thermodynamic average $\langle.\rangle_{T,\lambda}$ at temperature T with respect to the λ coupled system, Eq. (2.191). An important point is that, under the ergodicity hypothesis [77], thermodynamic averages are equivalent to time averages, and the latter can be obtained directly from a molecular dynamics or in particular from a Langevin dynamics simulation. We will discuss this in more detail below. Assuming we know how to calculate $\langle.\rangle_{T,\lambda}$, we can obtain straightforwardly the difference ΔF^{clas} between the classical free energy of the system of interest, F^{clas}, and the classical quasiharmonic free energy $F^{\text{clas,qh}}$,

$$F^{\text{clas,qh}}(V,T) = -k_{\text{B}}T \ln \int d\mathbf{R}_I \, e^{-\beta\left[F_0^{\text{el}}(V) + \mathbf{U}\mathbf{D}(V)\mathbf{U}/(2\mathbf{M})\right]} \big/ (\Lambda^{3N_n} N_n!), \tag{2.194}$$

by integrating over λ from 0 to 1:

$$
\begin{aligned}
F^{\text{clas,ah}}(V,T) \;\;:=\;\; \Delta F^{\text{clas}}(V,T) &= F^{\text{clas}}(V,T) \,-\, F^{\text{clas,qh}}(V,T) \;= \tag{2.195} \\
&= \int_0^1 d\lambda \left\langle \frac{\partial F_\lambda^{\text{el}}}{\partial \lambda} \right\rangle_{T,\lambda} = \int_0^1 d\lambda \left\langle F^{\text{el}}(\{\mathbf{R}_I\}, V) - F_0^{\text{el}}(V) - \mathbf{U}\mathbf{D}(V)\mathbf{U}/(2\mathbf{M}) \right\rangle_{T,\lambda}.
\end{aligned}
$$

We have here defined $F^{\mathrm{clas,ah}}$ which is referred to as the explicitly anharmonic free energy. The full free energy F of the system is finally obtained by adding the classical $F^{\mathrm{clas,ah}}$ to the quantum mechanical quasiharmonic result, Eq. (2.160):

$$F(V,T) \approx F_0^{\mathrm{el}}(V,T) + F^{\mathrm{qh}}(V,T) + F^{\mathrm{clas,ah}}(V,T). \tag{2.196}$$

Equation (2.196) constitutes the final expression for the free energy of an elementary, non-magnetic perfect crystal. The extension to crystals with vacancies is discussed in Sec. 3.1 with the resulting free energy expression given in Eq. (3.35).

Let us now discuss how to calculate $\langle . \rangle_{T,\lambda}$ using molecular dynamics in the special form of Langevin dynamics. The Langevin scheme is discussed in detail in Ref. [81] and we therefore focus only on the main ideas and relevant parameters. The central equation of Langevin dynamics is an extended version of Newton's equation of motion, which we adapt here directly to the coupled system, Eq. (2.191),

$$\underbrace{M_I \frac{\partial^2 R_{I,\alpha}(t)}{\partial t^2} = \frac{-\partial F_\lambda^{\mathrm{el}}(\{\mathbf{R}_I(t)\})}{\partial R_{I,\alpha}}}_{\text{Newton's equation of motion}} \underbrace{- \zeta \frac{\partial R_{I,\alpha}(t)}{\partial t} + \mathsf{F}_{I,\alpha}^{\mathrm{rand}}(t)}_{\text{Additional Langevin term}}, \tag{2.197}$$

with $\alpha \in \{x,y,z\}$. In Eq. (2.197), the nuclei positions $\{\mathbf{R}_I\}$ are treated as functions of time t. Further, the additional Langevin term consists of a friction term $\zeta\, \partial\mathbf{R}_I/\partial t$, with the friction parameter ζ, and of a randomly generated force $\mathsf{F}_I^{\mathrm{rand}}$. Integrating Eq. (2.197) twice will generate a trajectory $\{\mathbf{R}_I\}_t$ through the phase space of the nuclei. Let us consider the time average $\langle . \rangle_{t,\lambda}$ of our quantity of interest, $\partial F_\lambda^{\mathrm{el}}/\partial\lambda$, over this trajectory given by

$$\left\langle \frac{\partial F_\lambda^{\mathrm{el}}}{\partial\lambda} \right\rangle_{t,\lambda} = \left(N^{\mathrm{LD}}\right)^{-1} \sum_i^{N^{\mathrm{LD}}} \frac{\partial}{\partial\lambda} F_\lambda^{\mathrm{el}}(\{\mathbf{R}_I\}_{t_i}), \tag{2.198}$$

with i running over the N^{LD} elements (also steps, structures, or configurations) of the Langevin dynamics (LD) phase space trajectory. Further in Eq. (2.198), $\{\mathbf{R}_I\}_{t_i}$ denotes the nuclei configuration at time t_i out of $\{\mathbf{R}_I\}_t$. The key point is now that this time average will equal the corresponding thermal average, i.e.,

$$\left\langle \frac{\partial F_\lambda^{\mathrm{el}}}{\partial\lambda} \right\rangle_{T,\lambda} = \left\langle \frac{\partial F_\lambda^{\mathrm{el}}}{\partial\lambda} \right\rangle_{t,\lambda}, \tag{2.199}$$

provided that the random force satisfies [81]

$$\left\langle \mathsf{F}_{I,\alpha}^{\mathrm{rand}}(t) \right\rangle_{t,\lambda} \equiv 0 \quad \text{and} \quad \left\langle (\mathsf{F}_{I,\alpha}^{\mathrm{rand}})^2(t) \right\rangle_{t,\lambda} \equiv 6\,\zeta N_n k_{\mathrm{B}} T \tag{2.200}$$

and N^{LD} is sufficiently large, which needs to be checked by convergence. Using Eq. (2.199) in Eq. (2.195), we can fully determine the anharmonic free energy $F^{\mathrm{clas,ah}}$. We will refer to the presented method, including thermodynamic integration and Langevin dynamics, as the thermodynamic integration based Langevin dynamics (TILD) method. We will discuss the scaling performance of the TILD method in Sec. 3.2.1. The discussion will serve as a direct motivation for the UP-TILD method, which will be derived later (Sec. 3.2.2) in order to significantly improve the performance of the TILD method. Before closing this section, we need however to comment on several important technical details of the TILD approach:

a) The correct choice of the friction parameter ζ is important for a Langevin dynamics simulation. If chosen inappropriately, $\langle \partial F_\lambda^{\mathrm{el}}/\partial\lambda \rangle_{t,\lambda}$ may converge to a wrong value. Moreover, the computational effort depends on the choice of ζ. (See Ref. [81] for further details.)

b) A method for integrating Eq. (2.197) needs to be chosen. A possible choice (also used in this study) is the van-Gunsteren-Berendsen scheme [82] which has been previously implemented into S/PHI/NX [80] and extensively tested [81]. This scheme is an advanced version of the Verlet algorithm [83] which is a very popular integration scheme in MD simulations [79]. The main idea of the Verlet algorithm is to expand the nuclei trajectory *twice* in time up to third order at each MD step. One expansion is performed forward in time and one backward. The reason for these two expansions is that adding them together removes the first and third order terms. The remaining terms correspond to the positions and accelerations of the nuclei, where the latter can be obtained from a finite difference of the forces, so that a closed set of equations is available. An advantage of the Verlet algorithm is that it is *symplectic*, which means in essence that it is stable over long time periods. The van-Gunsteren-Berendsen scheme has the additional feature that the finite time step used for the integration is only limited by the fastest oscillation of the system and not by stochastic fluctuations. A detailed description of this scheme can be found in Ref. [82].

c) Since Eq. (2.197) is integrated twice, we need to fix two integration constants, which are typically chosen to be the $T = 0$ K equilibrium nuclei positions $\{\mathbf{R}_I^0\}$ and additionally random start velocities. Such a choice is however far from the actual thermodynamic equilibrium and, to reach it, a significant number of molecular dynamics steps is needed. A possible solution (also employed in this study) is to use a pre-equilibration on the quasiharmonic reference potential (likewise implemented in S/PHI/NX). Since the quasiharmonic potential is given analytically this procedure requires negligible CPU time, but it brings the system very close to its actual equilibrium. The further equilibration requiring expensive Kohn-Sham calculations is then reduced to ≈ 20 equilibration steps. The molecular dynamics steps used to achieve equilibration have to be taken out when calculating the average Eq. (2.198).

d) A critical issue in using statistical methods is the correct estimate of the unavoidable statistical error, in order to provide a trustful interval for the calculated data. The estimation is a three step procedure:

   1) We need to consider the fact that adjacent molecular dynamics structures $\{\mathbf{R}_I\}_{t_i}$ will be strongly correlated as a consequence of the purely deterministic nature of the original Newton equation of motion. The contribution of correlated structures to the time average Eq. (2.198) is however effectively less than the one of uncorrelated/random structures. As a preliminary consideration to estimating the statistical error, we therefore need in a first place to determine the correlation time. For that purpose, we calculate the correlation coefficient [79]

$$C^{\mathrm{cor}}(t') = \frac{\displaystyle\sum_i^{N^{\mathrm{LD}}}\Big[\partial F_\lambda^{\mathrm{el}}(\{\mathbf{R}_I\}_{t_i})/\partial\lambda - \langle\partial F_\lambda^{\mathrm{el}}/\partial\lambda\rangle_{t,\lambda}\Big]\Big[\partial F_\lambda^{\mathrm{el}}(\{\mathbf{R}_I\}_{t_i+t'})/\partial\lambda - \langle\partial F_\lambda^{\mathrm{el}}/\partial\lambda\rangle_{t,\lambda}\Big]}{\displaystyle\sum_i^{N^{\mathrm{LD}}}\Big[\partial F_\lambda^{\mathrm{el}}(\{\mathbf{R}_I\}_{t_i})/\partial\lambda - \langle\partial F_\lambda^{\mathrm{el}}/\partial\lambda\rangle_{t,\lambda}\Big]^2},$$

(2.201)

which shows a steep change in its time dependence at the point when the molecular dynamics steps become uncorrelated [79].

2) In a next step, we divide the full trajectory $\{\mathbf{R}_I\}_t$ into N^{unc} segments each of the size of the correlation time. Out of each segment we take systematically a single structure and add it to a new set of uncorrelated (unc) structures. This procedure corresponds to the *stratified systematic sampling* [79].

3) Finally, we calculate the statistical error σ^{err} (cf. e.g. Fig. 4.13) from

$$\sigma^{\mathrm{err}} \;=\; \sqrt{\sigma^{\mathrm{var}}/N^{\mathrm{unc}}}, \tag{2.202}$$

where σ^{var} is the variance (var) given by

$$\sigma^{\mathrm{var}} \;=\; (N^{\mathrm{unc}} - 1)^{-1} \sum_{u}^{N^{\mathrm{unc}}} \left[\partial F_\lambda^{\mathrm{el}}(\{\mathbf{R}_I\}_{t_u})/\partial\lambda - \langle \partial F_\lambda^{\mathrm{el}}/\partial\lambda \rangle_{t,\lambda}^{\mathrm{unc}} \right]^2, \tag{2.203}$$

with the uncorrelated time average

$$\left\langle \frac{\partial F_\lambda^{\mathrm{el}}}{\partial\lambda} \right\rangle_{t,\lambda}^{\mathrm{unc}} \;=\; (N^{\mathrm{unc}})^{-1} \sum_{u}^{N^{\mathrm{unc}}} \frac{\partial}{\partial\lambda} F_\lambda^{\mathrm{el}}(\{\mathbf{R}_I\}_{t_u}), \tag{2.204}$$

and with the uncorrelated structures $\{\mathbf{R}_I\}_{t_u}$.

e) Due to their correlation, adjacent molecular dynamics configurations $\{\mathbf{R}_I\}_{t_i}$ are very similar. The similarity translates to the corresponding Kohn-Sham wave functions and it is therefore advantageous to use the converged Kohn-Sham wave function of the previous step as the initial wave function $\varphi_i^{\mathrm{start}}$ of the next self consistency cycle, Eq. (2.66). This reduces the number of iteration steps N^{it} needed to reach self consistency. In fact, an even better performance can be achieved by a wave function extrapolation. This feature is available in S/PHI/NX and was applied in the present work. The reduction (red) was $N^{\mathrm{it}} \approx 10 \;\rightarrow\; N^{\mathrm{it,red}} \approx 5$.

f) An efficient scheme to perform the λ integration in Eq. (2.195) is the generalized Simpson's rule [84].

2.3.7 Quantum mechanical perturbation theory

The quantum mechanical perturbative treatment of the higher order terms $O(U^3)$ in Eq. (2.130) proceeds along the following general lines. At first, we need to carefully decide which terms actually to include. The reason is that the contribution to materials properties does not increase monotonically order by order, but different orders can yield similar contributions. In fact, this situation occurs already for the third and fourth order term, which are known [68] to be equally important and which therefore need to be treated simultaneously. (This will become also apparent from our results in Sec. 4.4, Fig. 4.18.) Yet higher order terms yield a smaller contribution and are, in practice, typically not considered due to the large analytical and computational requirements. (We likewise follow this route.) Thus, the electronic free energy is expanded up to fourth order and then each term is transformed into a representation based on phonon coordinates, which are fully known/available from the diagonalization of the dynamical matrix (Sec. 2.3.3). Up to this stage, the procedure is rather straightforward and corresponds merely to a change of the basis.

This change is however needed, in order to provide a description based on a non-interacting second order term. For such a description, various highly involved methods and techniques have been developed (Green's functions methods [85], quantum field theoretical techniques [85], renormalization methods [68]), which eventually allow to derive expressions for the desired materials properties. For the particular case of nuclei vibrations, the operator renormalization method has been developed in detail in Ref. [68].

The basic idea of the operator renormalization method is to "design" modified/renormalized phonon operators which do **not** interact if higher order terms are included into the Hamiltonian. Note the important difference to the usual/original phonon operators (Sec. 2.3.3): The latter are non-interacting if the Hamiltonian consists solely of the second order term, whereas they start interacting if higher order terms are included. In contrast, the renormalized phonon operators would interact if the Hamiltonian consisted of the second term only, but they do not interact if the higher order terms are included. The actual construction procedure consists of setting the renormalized phonon operator equal to the original phonon operator plus a remainder. The remainder is then determined from a set of commutator relations for the higher order terms. Having calculated the renormalized phonon operator, the corresponding renormalized frequencies can be calculated straightforwardly since the new phonons do not interact. Eventually, phonon shifts (given below), anharmonic free energies, and the full set of thermodynamic properties can be calculated.

In the following, we give the key equations regarding the above discussed change of the basis, adjusted to the here investigated elementary materials. Concerning the operator renormalization method, we present only the final equations for the phonon shifts, which were applied for the calculations presented in Sec. 4.4, while details can be found in Ref. [68]. Let us thus expand F^{el} up to fourth order [using $F^{\mathrm{el}}(\Omega)/N_n \to F^{\mathrm{el}}(V)$ similarly as in Eq. (2.186)]

$$
\begin{aligned}
F^{\mathrm{el}}(\{\mathbf{R}_I\}, V) \;=\; \ldots \; &+ \frac{1}{3!} \sum_{I,J,K}^{N_n} \sum_{\alpha,\beta,\gamma}^{3} U_{I,\alpha} U_{J,\beta} U_{K,\gamma} \; \Phi^{\mathrm{3ord}}_{I\alpha,J\beta,K\gamma}(V) \\
&+ \frac{1}{4!} \sum_{I,J,K,L}^{N_n} \sum_{\alpha,\beta,\gamma,\delta}^{3} U_{I,\alpha} U_{J,\beta} U_{K,\gamma} U_{L,\delta} \; \Phi^{\mathrm{4ord}}_{I\alpha,J\beta,K\gamma,L\delta}(V) + O(U^5), \quad (2.205)
\end{aligned}
$$

with the dots denoting the lower order terms given in Eq. (2.130) and with the real space third order and fourth order tensors, Φ^{3ord} and Φ^{4ord}, with elements given by:

$$
\Phi^{\mathrm{3ord}}_{I\alpha,J\beta,K\gamma}(V) \;=\; \left[\frac{\partial^3 F^{\mathrm{el}}(\{\mathbf{R}_I\}, V)}{\partial R_{I,\alpha} \partial R_{J,\beta} \partial R_{K,\gamma}} \right]_{\{\mathbf{R}_I^0\}}, \qquad (2.206)
$$

$$
\Phi^{\mathrm{4ord}}_{I\alpha,J\beta,K\gamma,L\delta}(V) \;=\; \left[\frac{\partial^4 F^{\mathrm{el}}(\{\mathbf{R}_I\}, V)}{\partial R_{I,\alpha} \partial R_{J,\beta} \partial R_{K,\gamma} \partial R_{L,\delta}} \right]_{\{\mathbf{R}_I^0\}}. \qquad (2.207)
$$

Using the Fourier transform for the $\mathbf{U}_I$, Eq. (2.138), and the quasiharmonic result for the lower order terms, Eq. (2.153), we can rewrite Eq. (2.205) such that the full nuclei Hamiltonian from Eq. (2.110) can be transformed to

$$
\left\{ \hat{T}^{\mathrm{nuc}} + \hat{1} F^{\mathrm{el}} \right\} \;=\; \hat{H}^{\mathrm{qh}}(V) + \hat{H}^{\mathrm{3ord}}(V) + \hat{H}^{\mathrm{4ord}}(V) + O(U^5), \qquad (2.208)
$$

with

$$\hat{H}^{\text{3ord}}(V) = \sum_{\substack{\mathbf{G}^{\text{sc}},\mathbf{G}^{\text{sc}\prime}, \\ \mathbf{G}^{\text{sc}\prime\prime}}}^{\text{prBZ}} \sum_{s,s',s''}^{3} \Phi_{\mathbf{G}^{\text{sc}}s,\,\mathbf{G}^{\text{sc}\prime}s',\,\mathbf{G}^{\text{sc}\prime\prime}s''}^{\text{3ord}}(V)\ \hat{U}_{\mathbf{G}^{\text{sc}};s}\ \hat{U}_{\mathbf{G}^{\text{sc}\prime};s'}\ \hat{U}_{\mathbf{G}^{\text{sc}\prime\prime};s''}, \tag{2.209}$$

$$\hat{H}^{\text{4ord}}(V) = \sum_{\substack{\mathbf{G}^{\text{sc}},\mathbf{G}^{\text{sc}\prime}, \\ \mathbf{G}^{\text{sc}\prime\prime},\mathbf{G}^{\text{sc}\prime\prime\prime}}}^{\text{prBZ}} \sum_{\substack{s,s' \\ s'',s'''}}^{3} \Phi_{\mathbf{G}^{\text{sc}}s,\,\mathbf{G}^{\text{sc}\prime}s',\,\mathbf{G}^{\text{sc}\prime\prime}s'',\,\mathbf{G}^{\text{sc}\prime\prime\prime}s'''}^{\text{4ord}}(V)\ \hat{U}_{\mathbf{G}^{\text{sc}};s}\ \hat{U}_{\mathbf{G}^{\text{sc}\prime};s'}\ \hat{U}_{\mathbf{G}^{\text{sc}\prime\prime};s''}\ \hat{U}_{\mathbf{G}^{\text{sc}\prime\prime\prime};s'''}, \tag{2.210}$$

where the $\Phi_{\mathbf{G}^{\text{sc}}s,\,\mathbf{G}^{\text{sc}\prime}s',\,\mathbf{G}^{\text{sc}\prime\prime}s''}^{\text{3ord}}$ correspond to the elements of the Fourier transform of Φ^{3ord},

$$\Phi_{\mathbf{G}^{\text{sc}}s,\,\mathbf{G}^{\text{sc}\prime}s',\,\mathbf{G}^{\text{sc}\prime\prime}s''}^{\text{3ord}}(V) = \frac{1}{3!}\left(\frac{\hbar}{2N_n}\right)^{3/2}(M_I)^{-3/2}\left(\omega_{\mathbf{G}^{\text{sc}};s}(V)\,\omega_{\mathbf{G}^{\text{sc}\prime};s'}(V)\,\omega_{\mathbf{G}^{\text{sc}\prime\prime};s''}(V)\right)^{-1/2} + $$

$$+\sum_{I,J,K}^{N_n}\sum_{\alpha,\beta,\gamma}^{3}\Phi_{I\alpha,J\beta,K\gamma}^{\text{3ord}}(V)\,(w_{\mathbf{G}^{\text{sc}};s})_\alpha\left(w_{\mathbf{G}^{\text{sc}\prime};s'}\right)_\beta\left(w_{\mathbf{G}^{\text{sc}\prime\prime};s''}\right)_\gamma\,e^{i\mathbf{G}^{\text{sc}}\cdot\mathbf{R}_I^0}\,e^{i\mathbf{G}^{\text{sc}}\cdot\mathbf{R}_J^0}\,e^{i\mathbf{G}^{\text{sc}}\cdot\mathbf{R}_K^0}, \tag{2.211}$$

and where the $\Phi_{\mathbf{G}^{\text{sc}}s,\,\mathbf{G}^{\text{sc}\prime}s',\,\mathbf{G}^{\text{sc}\prime\prime}s'',\,\mathbf{G}^{\text{sc}\prime\prime\prime}s'''}^{\text{4ord}}$ correspond to the elements of the Fourier transform of Φ^{4ord}:

$$\Phi_{\mathbf{G}^{\text{sc}}s,\,\mathbf{G}^{\text{sc}\prime}s',\,\mathbf{G}^{\text{sc}\prime\prime}s'',\,\mathbf{G}^{\text{sc}\prime\prime\prime}s'''}^{\text{4ord}}(V) = \frac{1}{4!}\left(\frac{\hbar}{2N_n}\right)^{2}\frac{1}{M_I^2}\left(\omega_{\mathbf{G}^{\text{sc}};s}(V)\,\omega_{\mathbf{G}^{\text{sc}\prime};s'}(V)\,\omega_{\mathbf{G}^{\text{sc}\prime\prime};s''}(V)\,\omega_{\mathbf{G}^{\text{sc}\prime\prime\prime};s'''}(V)\right)^{-1/2}$$

$$+\sum_{I,J,K,L}^{N_n}\sum_{\alpha,\beta,\gamma,\delta}^{3}\Phi_{I\alpha,J\beta,K\gamma,L\delta}^{\text{4ord}}(V)\,(w_{\mathbf{G}^{\text{sc}};s})_\alpha\left(w_{\mathbf{G}^{\text{sc}\prime};s'}\right)_\beta\left(w_{\mathbf{G}^{\text{sc}\prime\prime};s''}\right)_\gamma\left(w_{\mathbf{G}^{\text{sc}\prime\prime\prime};s'''}\right)_\delta \times$$

$$\times\,e^{i\mathbf{G}^{\text{sc}}\cdot\mathbf{R}_I^0}\,e^{i\mathbf{G}^{\text{sc}}\cdot\mathbf{R}_J^0}\,e^{i\mathbf{G}^{\text{sc}}\cdot\mathbf{R}_K^0}\,e^{i\mathbf{G}^{\text{sc}}\cdot\mathbf{R}_L^0}. \tag{2.212}$$

In Eqs. (2.211) and (2.212), we have used the notation $(w_{\mathbf{G}^{\text{sc}};s})_\alpha$ for the real space component α of $\mathbf{w}_{\mathbf{G}^{\text{sc}};s}$. We stress again that, despite looking rather awkward, the preceding equations represent merely a change of the real space Hamiltonian into the reciprocal phonon basis. As described above, the operator renormalization method can be now applied to the reciprocal Hamiltonian Eq. (2.208) and, eventually, materials properties can be derived. We will be in particular interested in the quantum mechanical anharmonic phonon shift $\Delta\omega_{\mathbf{G}^{\text{sc}};s}^{\text{qm,ah}}(V,T)$ (an example temperature dependence shown in Fig. 2.1),

$$\Delta\omega_{\mathbf{G}^{\text{sc}};s}^{\text{qm,ah}}(V,T) = \Delta\omega_{\mathbf{G}^{\text{sc}};s}^{\text{3ord}}(V,T) + \Delta\omega_{\mathbf{G}^{\text{sc}};s}^{\text{4ord}}(V,T), \tag{2.213}$$

consisting of the third order, $\Delta\omega_{\mathbf{G}^{\text{sc}};s}^{\text{3ord}}$, and fourth order, $\Delta\omega_{\mathbf{G}^{\text{sc}};s}^{\text{4ord}}$, shifts given by [68]

$$\Delta\omega_{\mathbf{G}^{\text{sc}};s}^{\text{3ord}}(V,T) = -18\,\hbar^{-2}\sum_{\mathbf{G}^{\text{sc}\prime},\mathbf{G}^{\text{sc}\prime\prime}}^{\text{prBZ}'}\sum_{s',s''}^{3}|\Phi_{\mathbf{G}^{\text{sc}}s,\,\mathbf{G}^{\text{sc}\prime}s',\,\mathbf{G}^{\text{sc}\prime\prime}s'',\,\mathbf{G}^{\text{sc}\prime\prime\prime}s'''}^{\text{3ord}}(V)|^2\,f_{\mathbf{G}^{\text{sc}}s,\,\mathbf{G}^{\text{sc}\prime}s',\,\mathbf{G}^{\text{sc}\prime\prime}s'',\,\mathbf{G}^{\text{sc}\prime\prime\prime}s'''}^{\text{3ord}}(V,T), \tag{2.214}$$

$$\Delta\omega_{\mathbf{G}^{\text{sc}};s}^{\text{4ord}}(V,T) = 12\,\hbar^{-1}\sum_{\mathbf{G}^{\text{sc}\prime}}^{\text{prBZ}'}\sum_{s'}^{3}\Phi_{\mathbf{G}^{\text{sc}}s,\,-\mathbf{G}^{\text{sc}}s,\,\mathbf{G}^{\text{sc}\prime}s',\,-\mathbf{G}^{\text{sc}\prime}s'}^{\text{4ord}}(V)\,f_{\mathbf{G}^{\text{sc}\prime}s'}^{\text{4ord}}(V,T), \tag{2.215}$$

with

$$
\begin{aligned}
f^{\text{3ord}}_{\mathbf{G}^{\text{sc}}s,\,\mathbf{G}^{\text{sc}'}s',\,\mathbf{G}^{\text{sc}''}s'',\,\mathbf{G}^{\text{sc}'''}s'''}(V,T) \;=\; & \frac{-f_{\mathbf{G}^{\text{sc}'},s'} + f_{\mathbf{G}^{\text{sc}''},s''}}{\left(\omega_{\mathbf{G}^{\text{sc}},s} + \omega_{\mathbf{G}^{\text{sc}'},s'} - \omega_{\mathbf{G}^{\text{sc}''},s''}\right)_p} \;+\; \frac{f_{\mathbf{G}^{\text{sc}'},s'} + f_{\mathbf{G}^{\text{sc}''},s''} + 1}{\omega_{\mathbf{G}^{\text{sc}},s} + \omega_{\mathbf{G}^{\text{sc}'},s'} + \omega_{\mathbf{G}^{\text{sc}''},s''}} \\[2mm]
& + \frac{f_{\mathbf{G}^{\text{sc}'},s'} - f_{\mathbf{G}^{\text{sc}''},s''}}{\left(\omega_{\mathbf{G}^{\text{sc}},s} - \omega_{\mathbf{G}^{\text{sc}'},s'} + \omega_{\mathbf{G}^{\text{sc}''},s''}\right)_p} \;-\; \frac{f_{\mathbf{G}^{\text{sc}'},s'} + f_{\mathbf{G}^{\text{sc}''},s''} + 1}{\left(\omega_{\mathbf{G}^{\text{sc}},s} - \omega_{\mathbf{G}^{\text{sc}'},s'} - \omega_{\mathbf{G}^{\text{sc}''},s''}\right)_p},
\end{aligned}
$$
$$\tag{2.216}$$

$$
f^{\text{4ord}}_{\mathbf{G}^{\text{sc}'}s'}(V,T) \;=\; 2f_{\mathbf{G}^{\text{sc}'},s'} + 1, \tag{2.217}
$$

where $f_{\mathbf{G}^{\text{sc}'},s'}$ is the Bose-Einstein function [using a slightly different notation than in Eq. (2.162)]:

$$
f_{\mathbf{G}^{\text{sc}'},s'} \;=\; f_{\mathbf{G}^{\text{sc}'},s'}(V,T) \;=\; \left[\exp\left\{\beta\hbar\omega_{\mathbf{G}^{\text{sc}'},s'}(V)\right\} - 1\right]^{-1}, \quad \beta = (k_{\text{B}}T)^{-1}. \tag{2.218}
$$

Note that in Eqs. (2.216) and (2.217) all frequencies are volume dependent (but temperature independent). Further, prBZ' indicates the exclusion of the zero frequencies at Γ and $(.)_p$ denotes the principle value, which can be implemented using

$$
\frac{1}{(\omega)_p} \;=\; \frac{\omega}{\omega^2 + \gamma^2}, \tag{2.219}
$$

and which is simply a device to avoid divergences. For that purpose, the generic infinitesimal parameter γ needs to be finite but small [86].

In order to provide a better idea of the rather formal development, we sketch how one would proceed in practice in calculating the phonon shift $\Delta\omega^{\text{qm,ah}}_{\mathbf{G}^{\text{sc}}\!;s}$. We first fix the volume V and the supercell size. For the latter let us take a 2^3 supercell with 32 atoms. The major task is then to calculate the real space tensors Φ^{3ord} and Φ^{4ord}. For that purpose, we can apply the finite difference method similarly as in the case of the dynamical matrix. Due to the increased order, the equations become however more complex. For instance, to calculate a third order tensor element, we use:

$$
\begin{aligned}
\Phi^{\text{3ord}}_{I\alpha,J\beta,K\gamma} \;=\; \frac{1}{2\Delta R}\Bigg[& \frac{F^{\text{HF}}_{I,\alpha}(\,...\,R^0_{J,\beta}+\Delta R\,...\,R^0_{K,\gamma}+\Delta R\,...\,) \;-\; F^{\text{HF}}_{I,\alpha}(\,...\,R^0_{J,\beta}-\Delta R\,...\,R^0_{K,\gamma}+\Delta R\,...\,)}{2\Delta R} \\[2mm]
& - \frac{F^{\text{HF}}_{I,\alpha}(\,...\,R^0_{J,\beta}+\Delta R\,...\,R^0_{K,\gamma}-\Delta R\,...\,) \;-\; F^{\text{HF}}_{I,\alpha}(\,...\,R^0_{J,\beta}-\Delta R\,...\,R^0_{K,\gamma}-\Delta R\,...\,)}{2\Delta R} \Bigg].
\end{aligned}
$$
$$\tag{2.220}$$

The dots denote all the remaining $(3 \cdot 32 - 2)$ nuclei coordinates which correspond to the $T = 0$ K equilibrium positions. To calculate all Φ^{3ord} tensor elements for that supercell, we have to solve $(3 \cdot 32)^2$ equations of a type as Eq. (2.220). For each such equation, we need however four Kohn-Sham calculations so that we have in total $(4 \cdot 3 \cdot 32)^2 \approx 10^5$ calculations. For the full fourth order tensor, the number is $(8 \cdot 3 \cdot 32)^3 \approx 10^8$ and we stress that each calculation is a complete Kohn-Sham calculation in a 2^3 supercell (≈ 1 CPU hour for aluminum for instance). In order to make a calculation of $\Delta\omega^{\text{qm,ah}}_{\mathbf{G}^{\text{sc}}\!;s}$ nonetheless feasible, it is crucial to employ symmetry arguments: There are generic symmetries available in any tensor and related to the interchange of its indices, as a consequence of the arbitrariness of the order of differentiation in Eqs. (2.206) and (2.207). Other symmetries are of an intrinsic type and are related to the specific atomic structure. For the fcc structure, we can significantly reduce the number of calculations to $\approx 10^3$ (3. order) and $\approx 10^4$ (4. order) using

these arguments. Note however that the symmetry search routines become more complicated than for the dynamical matrix, since we have to compare pairs and triplets of displacements. Having computed $\Phi^{3\mathrm{ord}}$ and $\Phi^{4\mathrm{ord}}$, we perform the Fourier transforms Eqs. (2.211) and (2.212) which correspond merely to sums over the tensor elements dressed by the (quasi)harmonic quantities ($\omega_{\mathbf{G}^{\mathrm{sc}};s}$, $\mathbf{w}_{\mathbf{G}^{\mathrm{sc}};s}$) determined in Sec. 2.3.3 and by structural quantities ($\mathbf{G}^{\mathrm{sc}}$, $\mathbf{R}$). The Fourier transforms along with the (quasi)harmonic frequencies $\omega_{\mathbf{G}^{\mathrm{sc}};s}$ can then be used directly in Eqs. (2.214) and (2.215) to calculate the shift. The application of Eq. (2.214) is straightforward due to the simple dependence of $f^{4\mathrm{ord}}_{\mathbf{G}^{\mathrm{sc}\prime}s\prime}$, whereas the treatment of $f^{3\mathrm{ord}}_{\mathbf{G}^{\mathrm{sc}}s,\,\mathbf{G}^{\mathrm{sc}\prime}s\prime,\,\mathbf{G}^{\mathrm{sc}\prime\prime}s\prime\prime,\,\mathbf{G}^{\mathrm{sc}\prime\prime\prime}s\prime\prime\prime}$ in Eq. (2.214) is complicated by additional checks of the γ dependence. For our calculations, we found however that $\gamma = 0$ was always possible, since the available frequencies in the used supercells never fulfilled any of the conditions needed to yield a diverging $f^{3\mathrm{ord}}_{\mathbf{G}^{\mathrm{sc}}s,\,\mathbf{G}^{\mathrm{sc}\prime}s\prime,\,\mathbf{G}^{\mathrm{sc}\prime\prime}s\prime\prime,\,\mathbf{G}^{\mathrm{sc}\prime\prime\prime}s\prime\prime\prime}$.

We sketch also a different approach to obtain the phonon shift, which is particularly convenient if one is interested in $\Delta\omega^{\mathrm{qm,ah}}_{\mathbf{G}^{\mathrm{sc}};s}$ only for a single $\mathbf{G}^{\mathrm{sc}}$ and s. Note for that purpose that, if we use the approach described above, we always need to calculate the full real space tensors before we compute the Fourier transforms, since the latter depend on every real space tensor element. If it was possible to calculate the $\Phi^{3\mathrm{ord}}_{\mathbf{G}^{\mathrm{sc}}s,\,\mathbf{G}^{\mathrm{sc}\prime}s\prime,\,\mathbf{G}^{\mathrm{sc}\prime\prime}s\prime\prime}$ and $\Phi^{4\mathrm{ord}}_{\mathbf{G}^{\mathrm{sc}}s,\,\mathbf{G}^{\mathrm{sc}\prime}s\prime,\,\mathbf{G}^{\mathrm{sc}\prime\prime}s\prime\prime,\,\mathbf{G}^{\mathrm{sc}\prime\prime\prime}s\prime\prime\prime}$ directly, we could confine the calculations to the elements actually needed for a specific $\mathbf{G}^{\mathrm{sc}}$ and s in the sums Eqs. (2.214) and (2.214). This is particularly interesting for the fourth order shift which depends only on a small set of diagonal elements for $\mathbf{G}^{\mathrm{sc}}$, s, $\mathbf{G}^{\mathrm{sc}\prime}$, and $s\prime$. (This rather simple dependence arises due to various symmetry and conservation arguments; see Ref. [68].) A direct calculation of the Fourier elements is indeed possible. Instead of performing the finite difference in real space, we can employ it directly reciprocal space. This means that, rather displacing pairs and triplets of atoms, we now displace pairs and triplets of phonons, i.e., collective atomic displacements. The corresponding real space coordinates (needed for the actual calculation) can be obtained using the Fourier transform Eq. (2.138). There is however a complication occurring in performing the finite difference in reciprocal space: The Hellmann-Feynman theorem (Sec. 2.3.4) provides only forces on individual atoms. We therefore need to calculate the forces on the phonons numerically which increases the number of calculations by a factor of 2 as compared to the real space method.

2.4 From the free energy to materials properties

In the present section, we introduce the Fourier interpolation scheme allowing to obtain a continuous phonon dispersion and we collect the various formulas needed to obtain the investigated thermodynamic properties from the free energy surface.

2.4.1 Phonon dispersion

A phonon dispersion denotes the dependence of the phonon frequencies on the phonon wave vector $\mathbf{q}$ inside the prBZ. An example including also the volume dependence of the frequencies is shown in Fig. 2.1 for aluminum. Further results will be discussed extensively in Chap. 4. Typically, certain high symmetry directions are chosen for a convenient representation. For the fcc Brillouin zone, in particular, the following directions are used

$$\Gamma \rightarrow X,\ X\prime \rightarrow K \rightarrow \Gamma \rightarrow L, \tag{2.221}$$

with the coordinates (in units of $2\pi/a^{\mathrm{lat}}$):

$$\Gamma = (0,0,0), \quad X = (1,0,0), \quad X\prime = 2K/3, \quad K = (0.75, 0.75, 0), \quad L = (0.5, 0.5, 0.5). \tag{2.222}$$

Note that, due to point symmetry, the frequencies at X and X' are equivalent so that we can join the two points in plotting the dispersion. A difficulty in calculating phonon dispersions is the fact that the wave vectors $\mathbf{G}^{\mathrm{sc}}$, at which phonon frequencies are available according to Eq. (2.143), are rather sparse along the high symmetry directions for reasonable supercell sizes. In order to allow nonetheless a reasonable comparison to an experimental phonon dispersion, we apply a Fourier interpolation by replacing the Fourier transform of the dynamical matrix, Eq. (2.141), with

$$D_{\mathbf{q},\alpha\beta}(V) \;=\; N_n^{-1} \sum_{I,J}^{N_n} \sum_{k,l,m=0}^{1} \frac{A_{IJ,k1}\,A_{IJ,l2}\,A_{IJ,m3}}{\left(\sum_{s=1}^{3}\sum_{k=0}^{1} A_{IJ,ks}\right)} \, D_{I\alpha,J\beta}(V)\, e^{i\mathbf{q}\cdot\,[(\mathbf{R}_I^0 - \mathbf{R}_J^0) - k\mathbf{s}_1 - l\mathbf{s}_2 - m\mathbf{s}_3]}, \quad (2.223)$$

where the coefficients $A_{IJ,ks}$ are given by:

$$A_{IJ,ks} \;=\; \begin{cases} 1 & \text{for}\quad [k=0 \,\wedge\, (\mathbf{R}_I - \mathbf{R}_J)\cdot\mathbf{s}_s \leq 1/2)] \;\vee\; [k=1 \,\wedge\, (\mathbf{R}_I - \mathbf{R}_J)\cdot\mathbf{s}_s \geq 1/2)] \\ 0 & \text{for}\quad [k=0 \,\wedge\, (\mathbf{R}_I - \mathbf{R}_J)\cdot\mathbf{s}_s > 1/2)] \;\vee\; [k=1 \,\wedge\, (\mathbf{R}_I - \mathbf{R}_J)\cdot\mathbf{s}_s < 1/2)]. \end{cases} \quad (2.224)$$

In comparison to Eq. (2.141), the wave vector $\mathbf{q}$ in Eq. (2.223) is not limited to the $\mathbf{G}^{\mathrm{sc}}$ vectors corresponding to the considered supercell. It is rather allowed to take any value inside the prBZ. To guarantee that Eq. (2.223) yields a Hermitian matrix $\mathbf{D_q}$ if $\mathbf{q}$ does not fall on a $\mathbf{G}^{\mathrm{sc}}$ vector, the coefficients $A_{IJ,ks}$ and the modified exponential function had to be introduced. Effectively, the modification has two effects: 1) It "centers" the dynamical matrix. To explain this, it is sufficient to consider a fixed dynamical matrix element $D_{I\alpha,J\beta}$ with $\mathbf{R}_I = (x,0,0)$ and $\mathbf{R}_J = (0,0,0)$. For the supercell vectors used in this study [Eq. (2.114)], we then find that the phase factor of $D_{I\alpha,J\beta}$ is unchanged, i.e., as in Eq. (2.141), if $x \leq |\mathbf{s}_1|$. For the other case ($x \geq |\mathbf{s}_1|$), the exponent of the phase factor is modified to $[i\mathbf{q}\cdot(x - |\mathbf{s}_1|,0,0)]$, i.e., the corresponding atom is mapped such that it is always closest to the origin. This procedure corresponds in essence to centering the dynamical matrix. 2) Further, the modification maps atoms which lie on some border of the new centered cell onto each border and scales the corresponding dynamical matrix entries appropriately. The underlying idea to Eq. (2.223) has been given in Ref. [72], whereas the explicit expressions were derived in the present study. The phonon frequencies for arbitrary $\mathbf{q}$ can be now obtained by solving:

$$\mathbf{D}_{\mathbf{q},s}(V)\,\mathbf{w}_{\mathbf{q},s} \;=\; (\omega_{\mathbf{q},s})^2(V)\,\mathbf{w}_{\mathbf{q},s}. \quad (2.225)$$

Besides allowing to construct a phonon dispersion, the dense sampling of the frequencies can be also employed for the calculation of the quasiharmonic free energy. If we construct a mesh of $m \times m \times m$ points inside the prBZ the quasiharmonic free energy $F^{\mathrm{qh,m}}$ from this mesh is given by:

$$F^{\mathrm{qh,m}}(V,T) \;=\; \frac{1}{m^3} \sum_{\mathbf{q}}^{m^3} \sum_{s}^{3} \left\{ \frac{1}{2}\hbar\omega_{\mathbf{q},s}(V) \;+\; k_{\mathrm{B}}T \ln\left[1 - \exp\left\{-\beta\hbar\omega_{\mathbf{q},s}(V)\right\}\right] \right\}. \quad (2.226)$$

We have included here the scaling factor $1/m^3$ which makes $F^{\mathrm{qh,m}}$ a per atom quantity justifying the dependence on the atomic volume V.

2.4.2   Thermodynamic properties

In order to arrive at the thermodynamic quantities which can be compared directly to experiment, it is convenient to first derive an entropy surface $S(V,T)$, a pressure surface $P(V,T)$, an isochoric [isobaric] heat capacity surface $C_V(V,T)$ $[C_P(V,T)]$, and an adiabatic [isothermal] bulk modulus

surface $B_S(V,T)$ $[B_T(V,T)]$ from the free energy surface:

$$F(V,T) \tag{2.227}$$

$$S(V,T) = -\left[\frac{\partial F(V,T)}{\partial T}\right]_V \qquad\qquad P(V,T) = -\left[\frac{\partial F(V,T)}{\partial V}\right]_T \tag{2.228}$$

$$C_V(V,T) = T\left[\frac{\partial S(V,T)}{\partial T}\right]_V \quad C_P(V,T) = T\left[\frac{\partial S(V,T)}{\partial T}\right]_P \quad B_S(V,T) = -V\left[\frac{\partial P(V,T)}{\partial V}\right]_S \quad B_T(V,T) = -V\left[\frac{\partial P(V,T)}{\partial V}\right]_T$$

$$\tag{2.229}$$

The dashed lines indicate that the corresponding upper quantity enters the respective lower quantity by determining the direction of differentiation (cf. the subscript on the square brackets of the lower quantity). We stress that all quantities in Eqs. (2.227) to (2.229) are full V-T surfaces. Typically, in experiment these quantities are obtained at constant pressure and as a function of temperature. We can however obtain these quantities straightforwardly from the above surfaces. For that purpose, we define the thermal volume expansion $V_{P'}(T)$ at a constant pressure P' in an implicit way by using the pressure surface as:

$$P' = P(V_{P'}(T), T). \tag{2.230}$$

For the special case of $P' = 0$ Pa, we define the zero pressure equilibrium (eq) volume expansion $V^{\mathrm{eq}}(T)$ by

$$V^{\mathrm{eq}}(T) = V_{P'=0\mathrm{Pa}}(T) \tag{2.231}$$

and if additionally $T = 0$ K, we use:

$$V_0^{\mathrm{eq}} = V^{\mathrm{eq}}(T = 0\text{ K}). \tag{2.232}$$

From Eqs. (2.80) and (2.231), we obtain the thermal expansion of the $P = 0$ Pa equilibrium lattice constant $a^{\mathrm{lat,eq}}$:

$$a^{\mathrm{lat,eq}}(T) = [4V^{\mathrm{eq}}(T)]^{1/3} \qquad \text{and} \qquad a_0^{\mathrm{lat,eq}} = (4V_0^{\mathrm{eq}})^{1/3}. \tag{2.233}$$

We will be in particular interested in the relative expansion $\varepsilon^{\mathrm{eq}}(T)$ given by

$$\varepsilon(T) = \varepsilon^{\mathrm{eq}}(T) = \frac{1}{a_0^{\mathrm{lat,eq}}}\left[a^{\mathrm{lat,eq}}(T) - a_0^{\mathrm{lat,eq}}\right], \tag{2.234}$$

and the expansion coefficient $\alpha^{\mathrm{eq}}(T)$ given by:

$$\alpha(T) = \alpha^{\mathrm{eq}}(T) = \frac{1}{a^{\mathrm{lat,eq}}(T)}\frac{\partial a^{\mathrm{lat,eq}}(T)}{\partial T}. \tag{2.235}$$

In Eqs. (2.234) and (2.235), we have deliberately defined in a first step expressions with the "eq" superscript, in order to emphasize the correspondence to the zero pressure equilibrium lattice constant/volume. In principle, one can define the relative expansion and the expansion coefficient as well as all following quantities for any $V_{P'}$. As will be discussed in Sec. 4.1.2, we can however

safely neglect the pressure dependence for our purposes and we have thus introduced in a second step a simplified notation. Now, using $V^{\mathrm{eq}}(T)$ and the surfaces Eq. (2.229), we can define the usual representation for the isochoric and isobaric heat capacities by

$$C_V(T) \;=\; C_V^{\mathrm{eq}}(T) \;=\; C_V(V^{\mathrm{eq}}(T), T) \qquad \text{and} \qquad C_P(T) \;=\; C_P^{\mathrm{eq}}(T) \;=\; C_P(V^{\mathrm{eq}}(T), T), \tag{2.236}$$

and equivalently for the adiabatic and isothermal bulk modulus by:

$$B_S(T) \;=\; B_S^{\mathrm{eq}}(T) \;=\; B_S(V^{\mathrm{eq}}(T), T) \qquad \text{and} \qquad B_T(T) \;=\; B_T^{\mathrm{eq}}(T) \;=\; B_T(V^{\mathrm{eq}}(T), T). \tag{2.237}$$

There is an exact thermodynamic relation coupling the heat capacities and the bulk moduli [68]:

$$C_P/C_V \;=\; B_S/B_T. \tag{2.238}$$

We will use Eq. (2.238) to obtain B_S from B_T, C_P, and C_V, which is computationally more convenient than calculating the derivative of P with respect to V at a constant entropy S in Eq. (2.229). Further, we will use

$$B_{T,0} \;=\; B_T(T = 0\ \mathrm{K}), \tag{2.239}$$

and the pressure derivative of the isothermal bulk modulus:

$$B'_{T,0} \;=\; B'_T(T = 0\ \mathrm{K}), \qquad \text{with} \qquad B'_T(T) \;=\; \left[\frac{\partial B_T(V, T)}{\partial P} \right]_V. \tag{2.240}$$

It is important to distinguish the isochoric (i.e., *constant* volume) heat capacity from the *fixed* volume heat capacity C_{V_0} defined by:

$$C_{V_0}(T) \;=\; C_V(V_0^{\mathrm{eq}}, T) \quad \neq \quad C_V(V^{\mathrm{eq}}(T), T) \;=\; C_V(T). \tag{2.241}$$

Finally, the free energy F_P at zero pressure is given by:

$$F_P(T) \;=\; F_P^{\mathrm{eq}}(T) \;=\; F(V^{\mathrm{eq}}(T), T). \tag{2.242}$$

The determination of vacancy concentrations from $F(V, T)$ will be discussed in Sec. 3.1.

Chapter 3

Methodological developments

In this chapter, we discuss the main methodological developments that were obtained during the present work:

- In Sec. 3.1, we lift the restriction that the atoms are arranged on a perfect lattice and introduce an intuitive approach to treat point defects (cf. the discussion at the end of Sec. 2.3.1).

- We discuss in Sec. 3.2 the computational requirements of the TILD method (Sec. 2.3.6) and introduce an extension, the hierarchical coarse graining UP-TILD method, which reduces significantly the CPU time of the TILD method.

- In Sec. 3.3, we show how to compute the various parts of the free energy surface in practice, with a particular focus on the parametrization along V and T. We also reconsider in Sec. 3.3.4 the quasiharmonic approximation using the temperature dependent dynamical matrix.

- Finally, in Sec. 3.4, we address the four convergence parameters identified in Chap. 2: k sampling and plane wave cutoff E^{cut} (Sec. 2.1.7), the augmentation grid (Sec. 2.1.8), and the supercell size (Sec. 2.3.2). To this end, we present a method which enables efficient convergence checks.

3.1 An intuitive description/treatment of point defect formation

3.1.1 Motivation

With increasing temperature, the probability that atoms leave the vicinity of their $T = 0$ K equilibrium positions, $\{\mathbf{R}_I^0\}$, and that they start to penetrate through the lattice will likewise increase. For entropic reasons, this holds true even for otherwise ideal single crystalline materials as considered here. Thus, the translational symmetry of the crystal will be perturbed by the presence of thermally excited point defects. Due to the dominant role of the vacancies and to enable a convenient discussion, we will explain our approach for the treatment of point defects especially for vacancies. The key ideas and statements apply however in a similar manner to other types of point defects such as for instance self interstitials. The corresponding generalized expressions will be given in Sec. 3.1.4.

Two competing free energy contributions are commonly associated with the occurrence of vacancies:

1) *Creation/formation* free energy: In order to define this contribution, let us consider the free energy F^{p} of a perfect crystal, i.e., without vacancies, and the free energy F^{v} corresponding

to a crystal with one vacancy (single vacancy crystal). The formation free energy F^{f} of the vacancy is then generally defined as

$$F^{\mathrm{f}} = F^{\mathrm{v}} - F^{\mathrm{p}}, \tag{3.1}$$

with F^{v} and F^{p} obtained either at the same volume or the same pressure. In this general definition, it is implicitly assumed that the number of atoms in the perfect crystal and the crystal containing the vacancy is equal. For this to be true, the extra atom coming from the vacancy needs to be incorporated into the crystal at the energetically most favorable place, for instance at the surface. Defined in this way, F^{f} will – if we assume stable phases – always be **positive**, since the perfect crystal corresponds already to the most favorable configuration and therefore $F^{\mathrm{v}} > F^{\mathrm{p}}$. Put differently, considering F^{f} as the only contribution to vacancy formation, a vacancy would actually never occur.

2) *Configurational* free energy: Let us consider a crystal consisting of N atoms. If n is the number of vacancies then the number W of distinct ways ($\widehat{=}$ microstates) to arrange the vacancies in the crystal is given by [87]:

$$W = \frac{N(N-1)(N-2)\ldots(N-n+1)}{n!} = \frac{N!}{(N-n)!\,n!}. \tag{3.2}$$

Equation (3.2) corresponds to the classical or Boltzmann statistics. Classical statistics is applicable to point defect formation, since the atoms in a crystal are considered to be distinguishable as discussed in Sec. 2.3.1. The configurational free energy F^{c} is then given by [87]:

$$F^{\mathrm{c}} = -k_{\mathrm{B}}T \, \ln W. \tag{3.3}$$

Since the number of possible configurations W is always positive, F^{c} is always **negative** and will therefore favor vacancy formation.

Eventually, it will be the detailed balance between F^{f} and F^{c} which determines how many vacancies are created. Let us thus discuss the available approaches to calculate F^{f} and F^{c} within the framework of the so far developed formalisms.

There are basically two approaches to calculate the formation free energy within a periodic ansatz: the *rescaled volume* and the *constant pressure* approach. Within the *rescaled volume* (rv) approach the formation free energy is defined as [30]

$$F^{\mathrm{f,rv}}(\Omega^{\mathrm{p}}, T) = F^{\mathrm{v}}\left(\chi\Omega^{\mathrm{p}}, T; N^{\mathrm{v}}, n^{\mathrm{sc}}\right) - \chi\, F^{\mathrm{p}}(\Omega^{\mathrm{p}}, T; N^{\mathrm{v}}+1, n^{\mathrm{sc}}), \tag{3.4}$$

with the scaling factor $\chi = N^{\mathrm{v}}/(N^{\mathrm{v}}+1)$, with the number of atoms in the single vacancy crystal N^{v}, and with the volume of the perfect crystal Ω^{p}. Two calculations are needed in Eq. (3.4), one for a perfect crystal and one for a single vacancy crystal, both however in the same type of supercell. This is indicated by the dependence on the supercell size n^{sc} which fixes the supercell according to Eq. (2.114). The single vacancy supercell has one atom less than the perfect crystal supercell. To account for this, F^{p} needs to be rescaled by χ which is possible due to the extensivity of the perfect crystal free energy. It is however not apparent why the volume of the single vacancy cell needs to be rescaled as compared to the perfect supercell volume Ω^{p}. The new approach (derived in Sec. 3.1.2) will allow to obtain Eq. (3.4) as an approximation of a more general set of equations, with the volume scaling arising naturally [cf. Eq. (3.32)]. Within the second approach, the *constant*

pressure (cp) approach, the following definition of the formation free energy is commonly used:

$$F^{\text{f,cp}}(P,T) \;=\; \underbrace{F^{\text{v}}\left(\Omega_P^{\text{v}}, T; N^{\text{v}}, n^{\text{sc}}\right) - \chi F^{\text{p}}\left(\Omega_P^{\text{p}}, T; N^{\text{v}}+1, n^{\text{sc}}\right)}_{\text{Incomplete for } P > 0}. \tag{3.5}$$

Here, Ω_P^{v} (Ω_P^{p}) denotes the volume at which the single vacancy (perfect) supercell is at pressure P, Eq. 2.228. Defined in this way, $F^{\text{f,cp}}$ corresponds uniquely to the pressure P. However, we would like to express $F^{\text{f,cp}}$ as a function of volume to be consistent with the so far developed methodology with $F(\Omega, T)$ [$= N_n F(V,T)$; cf. Eq. (2.185)] being the central quantity. There exist at least two distinct possibilities to assign a volume dependence

$$F^{\text{f,cp}}(\Omega_P^{\text{v}}, T) = F^{\text{f,cp}}(P,T) \quad \text{and} \quad F^{\text{f,cp}}(\Omega_P^{\text{p}}, T) = F^{\text{f,cp}}(P,T), \tag{3.6}$$

since in general $\Omega_P^{\text{v}} \neq \Omega_P^{\text{p}}$. There is in fact another serious deficiency contained in Eq. (3.5). As indicated, it is incomplete for finite pressures, i.e., $P \neq 0$, since it misses a term proportional to P. Both issues, the assignment of the correct volume dependence and the missing pressure term will arise naturally as an approximation to our approach [cf. Eq. (3.26)]. This will, for instance, allow to straightforwardly explain the necessity for including the pressure term.

We stress the significance of the difficulties with Eqs. (3.4) and (3.5). For instance, Varotsos and Alexoupolous [88] discuss extensively the importance of distinguishing constant volume and constant pressure vacancy calculations, point out possible ambiguities, and develop a comprehensive set of equations. They also discuss the missing term in Eq. (3.5) and stress that it has been omitted often in literature. Their account is however not adapted to the periodic ansatz. The motivation in the present study was therefore to provide an accurate and straightforward approach that is compatible with the periodic boundary conditions as commonly employed in DFT calculations. Further, it should be more intuitive and general than the rescaled volume and constant pressure approaches which start directly by defining a formation free energy. Before introducing the new approach in the following section, we should briefly comment on two further aspects related to vacancy calculations.

The first comment refers to the configurational free energy F^{c}. It is generally obtained from Eq. (3.2) using Stirling's approximation and it reads [87]:

$$F^{\text{c}} \;\approx\; -k_{\text{B}}T[n - n\ln(n/N)]. \tag{3.7}$$

This approximation is well justified since n and N correspond to a macroscopic crystal and higher orders in Stirling's expansion will be negligible. We will therefore also apply Eq. (3.7) in the next section. Secondly, the treatment of vacancies presented here, starting with Eqs. (3.1) and (3.2), is only applicable to non-interacting vacancies. In principle, vacancies could agglomerate to form clusters such as for instance the so called divacancies. In aluminum however, which will be the focus of the vacancy calculations in Sec. 4.3.6, it has been shown that divacancies do not form [89]. Self interstitials are in general repulsive, i.e., do not form clusters, due to the associated tensile strain.

3.1.2 Volume optimized approach

The central quantity, which we are interested in, is the free energy $F(\Omega, T, n)$ of a macroscopic crystal at *fixed* volume Ω, temperature T, and containing n vacancies. In order to adapt our approach to the periodic ansatz, we introduce a large fictitious supercell with these properties and
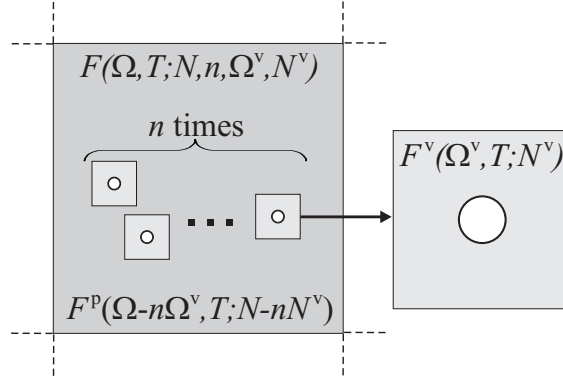
Figure 3.1: Schematic illustration of the concept of calculating the free energy $F(\Omega, T; N, n, \Omega^{\mathrm{v}}, N^{\mathrm{v}})$ of a periodic crystal with vacancies. The larger box represents a supercell of volume Ω at temperature T containing N atoms and n vacancies. A light-gray shaded box with a white circle represents a cell of volume Ω^{v}, containing N^{v} atoms, exactly one vacancy, and having the free energy $F^{\mathrm{v}}(\Omega^{\mathrm{v}}, T; N^{\mathrm{v}})$. The dark-gray shaded region represents the perfect crystal without vacancies, with volume $\Omega - n\Omega^{\mathrm{v}}$, $N - nN^{\mathrm{v}}$ atoms, and free energy $F^{\mathrm{p}}(\Omega - n\Omega^{\mathrm{v}}, T; N - nN^{\mathrm{v}})$. The dashed lines indicate periodic boundary conditions.

with N atoms to represent the macroscopic crystal (Fig. 3.1). Fictitious refers to the fact that an actual calculation of this supercell is not feasible. Beyond the supercell we have periodic boundary conditions as introduced in Sec. 2.3.2. As indicated in Fig. 3.1, we construct a cell/box around each vacancy which is large enough to cover its strain field and which we call the vacancy cell. The vacancy cell contains N^{v} atoms, has a volume of Ω^{v}, and a free energy $F^{\mathrm{v}} = F^{\mathrm{v}}(\Omega^{\mathrm{v}}, T; N^{\mathrm{v}})$. According to this construction, the crystal outside the vacancy cells can be described by a perfect crystal with a volume Ω^{p} and N^{p} atoms,

$$\Omega^{\mathrm{p}} = \Omega - n\Omega^{\mathrm{v}}, \tag{3.8}$$

$$N^{\mathrm{p}} = N - nN^{\mathrm{v}}, \tag{3.9}$$

and with a free energy $F^{\mathrm{p}} = F^{\mathrm{p}}(\Omega^{\mathrm{p}}, T; N^{\mathrm{p}})$. We can then write the free energy of the fictitious supercell as

$$F(\Omega, T; N, n, \Omega^{\mathrm{v}}, N^{\mathrm{v}}) = \underbrace{F^{\mathrm{p}}(\Omega^{\mathrm{p}}, T; N^{\mathrm{p}}) + nF^{\mathrm{v}}(\Omega^{\mathrm{v}}, T; N^{\mathrm{v}})}_{=:\ F^{\mathrm{ssc}}} + F^{\mathrm{c}}(N, n), \tag{3.10}$$

where we have defined F^{ssc} the free energy of a single specific configuration and where F^{c} is given by Eq. (3.7). Equation (3.10) and the definitions so far contain already the key conceptual ideas of our approach. We first state the most important one which is sufficient to understand the concept and, then, we comment on further aspects in more detail. The key idea is Eq. (3.8) which couples the volume of the perfect crystal and of the vacancy cells. Since in equilibrium the total free energy $F(\Omega, T, n)$ of the fictitious supercell needs to be minimal [Eq. (3.11) below], the volume of the perfect crystal and of the vacancy cells will adjust self-consistently, i.e., until the optimum volume for both is achieved when minimizing $F(\Omega, T, n)$. We thus refer to our approach a the volume optimized approach. The actual minimization procedure will depend on the free energy volume curves of the perfect crystal and of the vacancy cell. The resulting free energy $F(\Omega, T, n)$ is then the quantity that can be used to derive the thermodynamics of a crystal with vacancies.

To allow for a detailed understanding of the volume optimized method, we need to consider the

following aspects:

1) In writing Eq. (3.10), we need to take special care of vacancy configurations with overlapping vacancy cells. Such configurations need to be accounted for, since the term F^{ssc} must be consistent with F^{c} and the latter contains all possible configurations. For $nN^{\mathrm{v}} < N$, we can however always map overlapping onto non-overlapping configurations using the non-interacting vacancies assumption. This guarantees that Eq. (3.10) is applicable. The cases $nN^{\mathrm{v}} > N$ and $nN^{\mathrm{v}} = N$ are discussed in points 4) and 6).

2) When speaking about the strain field of a vacancy, we refer to perturbations which cannot be described by a change of the perfect crystal volume. The perfect crystal beyond the vacancy cell is allowed to adapt its volume to the presence of the vacancy as expressed by Eq. (3.8). Therefore, the effective influence range of the vacancy is not bound to the vacancy cell. In particular, the total free energy of the fictitious supercell is affected by the vacancy cell through the minimum free energy requirement with respect to Ω^{v}:

$$\partial F / \partial \Omega^{\mathrm{v}} \equiv 0. \tag{3.11}$$

3) By varying the temperature any number of vacancies n is possible. Consequently, the perfect crystal can have any number of atoms (given by $N - nN^{\mathrm{v}}$). This is not possible in pure geometrical terms due to the restriction by the supercell. We are however not explicitly interested in the specific geometrical arrangement. We only need the corresponding free energy of the perfect crystal F^{p} and this can be obtained for any number of atoms due to its extensivity property

$$F^{\mathrm{p}}(\Omega^{\mathrm{p}}, T; N^{\mathrm{p}}) / N^{\mathrm{p}} = F^{\mathrm{p}}(V^{\mathrm{p}}, T; 1) =: F^{\mathrm{p}}(V^{\mathrm{p}}, T), \tag{3.12}$$

with

$$V^{\mathrm{p}}(V, c) = \Omega^{\mathrm{p}} / N^{\mathrm{p}} = (V - c\Omega^{\mathrm{v}}) / (1 - cN^{\mathrm{v}}), \tag{3.13}$$

where we have defined the volume per atom $V = \Omega / N$ and the concentration of vacancies $c = n/N$. We can use Eq. (3.12) to rewrite Eq. (3.10). The resulting expression

$$\begin{aligned} F(\Omega, T; N, n, \Omega^{\mathrm{v}}, N^{\mathrm{v}}) / N &= (1 - cN^{\mathrm{v}}) F^{\mathrm{p}}(V^{\mathrm{p}}(V), T) + cF^{\mathrm{v}}(\Omega^{\mathrm{v}}, T; N^{\mathrm{v}}) + F^{\mathrm{c}}(c) \\ &=: F(V, T; c, \Omega^{\mathrm{v}}, N^{\mathrm{v}}) \end{aligned} \tag{3.14}$$

with

$$F^{\mathrm{c}}(c) = -ck_{\mathrm{B}}T(1 - \ln c), \tag{3.15}$$

is independent of N and defines the free energy per atom $F(V, T; c, \Omega^{\mathrm{v}}, N^{\mathrm{v}})$ of the full supercell consisting of the perfect crystal and n vacancy cells.

4) Let us consider the case $nN^{\mathrm{v}} > N$. The vacancy cells overlap necessarily in each configuration. Using the assumption of non-interacting vacancies, we can map each configuration on one which does not contain a perfect crystal part. We can then write the free energy of the fictitious cell as:

$$F(\Omega, T; N, n, \Omega^{\mathrm{v}}, N^{\mathrm{v}}) = nF^{\mathrm{v}}(\Omega^{\mathrm{v}}, T; N^{\mathrm{v}}) - F^{\mathrm{p}}(n\Omega^{\mathrm{v}} - \Omega, T; nN^{\mathrm{v}} - N) + F^{\mathrm{c}}(N, n). \tag{3.16}$$

The term $F^{\mathrm{p}}(n\Omega^{\mathrm{v}} - \Omega, T; nN^{\mathrm{v}} - N) = F^{\mathrm{p}}(-\Omega^{\mathrm{p}}, T; -N^{\mathrm{p}})$ needs to be subtracted, since in the overlap region each vacancy cell contributes a free energy containing the perfect crystal free

energy. Equation (3.16) can be rewritten using Eqs. (3.12) and (3.13) as

$$F(\Omega, T; N, n, \Omega^{\mathrm{v}}, N^{\mathrm{v}})/N = cF^{\mathrm{v}}(\Omega^{\mathrm{v}}, T; N^{\mathrm{v}}) - (cN^{\mathrm{v}} - 1)\, F^{\mathrm{p}}(V^{\mathrm{p}}, T) + F^{\mathrm{c}}(c), \qquad (3.17)$$

which is equivalent to Eq. (3.14) and thus equivalent to the $nN^{\mathrm{v}} < N$ case.

5) We can use the condition Eq. (3.11) and the general equilibrium condition with respect to the concentration of the vacancies,

$$\partial F/\partial c \equiv 0, \qquad (3.18)$$

to explicitly determine the equilibrium vacancy cell volume $\Omega^{\mathrm{v,eq}}$ and the equilibrium vacancy concentration c^{eq} so that

$$F(V, T) := F(V, T; c^{\mathrm{eq}}, \Omega^{\mathrm{v,eq}}, N^{\mathrm{v}}) = (1 - c^{\mathrm{eq}} N^{\mathrm{v}})\, F^{\mathrm{p}}(V^{\mathrm{p,eq}}, T) + c^{\mathrm{eq}} F^{\mathrm{v}}(\Omega^{\mathrm{v,eq}}, T; N^{\mathrm{v}}) + F^{\mathrm{c}}(c^{\mathrm{eq}}), \qquad (3.19)$$

with $V^{\mathrm{p,eq}} = (V - c^{\mathrm{eq}} \Omega^{\mathrm{v,eq}})/(1 - c^{\mathrm{eq}} N^{\mathrm{v}})$, which is the final free energy expression of our volume optimized approach (for $nN^{\mathrm{v}} < N$ and $nN^{\mathrm{v}} > N$). The remaining unknown quantity N^{v} is determined by the specific supercell used for the vacancy calculation and has to be checked for convergence.

6) At last, we need to consider the case $nN^{\mathrm{v}} = N$. For this particular value, the vacancy cells exactly fill the fictitious supercell. They further have a volume of $\Omega^{\mathrm{v}} = \Omega/n = N^{\mathrm{v}} V$ and we can use, instead of Eq. (3.10), the following expression for the free energy:

$$F(V, T) = cF^{\mathrm{v}}(N^{\mathrm{v}} V, T, N^{\mathrm{v}}) + F^{\mathrm{c}}(c). \qquad (3.20)$$

3.1.3 Derivation of the standard approaches from the new method

Let us first consider the constant pressure approach and show that the pressure inside the vacancy cells and inside the perfect crystal part equals the external pressure. Using Eq. (3.14) in Eq. (2.228), we have

$$P = -\frac{\partial F}{\partial V} = -(1 - cN^{\mathrm{v}})\frac{\partial F^{\mathrm{p}}}{\partial V^{\mathrm{p}}}\frac{\partial V^{\mathrm{p}}}{\partial V} = -\frac{\partial F^{\mathrm{p}}}{\partial V^{\mathrm{p}}} =: P^{\mathrm{p}}, \qquad (3.21)$$

where the last equality defines the pressure P^{p} of the perfect bulk subsystem. Equation (3.21) shows that P^{p} is equal to the externally applied pressure P. We next apply the equilibrium condition Eq. (3.11) to Eq. (3.14):

$$\frac{\partial F}{\partial \Omega^{\mathrm{v}}} = (1 - cN^{\mathrm{v}})\frac{\partial F^{\mathrm{p}}}{\partial V^{\mathrm{p}}}\frac{\partial V^{\mathrm{p}}}{\Omega^{\mathrm{v}}} + c\frac{\partial F^{\mathrm{v}}}{\partial \Omega^{\mathrm{v}}} = c\left(\frac{\partial F^{\mathrm{v}}}{\partial \Omega^{\mathrm{v}}} - \frac{\partial F^{\mathrm{p}}}{\partial V^{\mathrm{p}}}\right) \equiv 0. \qquad (3.22)$$

Defining $P^{\mathrm{v}} = -\partial F^{\mathrm{v}}/\partial \Omega^{\mathrm{v}}$, the pressure inside the vacancy cell, we therefore have for $c > 0$:

$$P^{\mathrm{v}} = P^{\mathrm{p}}. \qquad (3.23)$$

We next Taylor expand $F^{\mathrm{p}}(V^{\mathrm{p}}, T)$ in Eq. (3.14) around $c = 0$

$$
\begin{aligned}
F(V, T) &= (1 - cN^{\mathrm{v}})F^{\mathrm{p}}(V, T) + \frac{\partial F^{\mathrm{p}}(V)}{\partial V}(N^{\mathrm{v}} V - \Omega^{\mathrm{v}}) + O(c^2) + cF^{\mathrm{v}}(\Omega^{\mathrm{v}}, T; N^{\mathrm{v}}) + F^{\mathrm{c}}(c) \\
&= F^{\mathrm{p}}(V, T) + c\left[F^{\mathrm{v}}(\Omega^{\mathrm{v}}, T; N^{\mathrm{v}}) - N^{\mathrm{v}} F^{\mathrm{p}}(V, T) + Pv^{\mathrm{f}}\right] + O(c^2) + F^{\mathrm{c}}(c), \qquad (3.24)
\end{aligned}
$$

where we have defined the volume of vacancy formation:

$$v^{\mathrm{f}} \; = \; \Omega^{\mathrm{v}} - N^{\mathrm{v}}V. \tag{3.25}$$

Retaining only the terms linear in c and using the extensivity of F^{p}, we obtain the expression for the free energy within the constant pressure approach [88]

$$F(V_P, T) \; \approx \; F^{\mathrm{p}}(V_P, T) \; + \; c \underbrace{\left[F^{\mathrm{v}}(\Omega_P^{\mathrm{v}}, T; N^{\mathrm{v}}) - \chi F^{\mathrm{p}}(\Omega_P^{\mathrm{p}}, T; N^{\mathrm{v}}{+}1) + Pv_P^{\mathrm{f}} \right]}_{\text{Correct version of } F^{\mathrm{f,cp}}(\Omega_P^{\mathrm{p}}(V_P), T) \text{ from Eq. (3.5)}} \; + \; F^{\mathrm{c}}(c), \tag{3.26}$$

where $\Omega_P^{\mathrm{p}}(V_P) = (N^{\mathrm{v}}{+}1)V_P$, $v_P^{\mathrm{f}} = \Omega_P^{\mathrm{v}} - N^{\mathrm{v}}V_P$, and where the subscript on V and Ω^{v} indicates that both volumes correspond to the external pressure P. The term in the square brackets defines the correct version of the formation free energy at constant pressure. (An example for the temperature and volume dependence of the formation free energy of aluminum is given in Fig. 2.1.) In contrast to Eq. (3.5) it contains a term linear in P. Based on our derivation, we can straightforwardly analyze the necessity of this Pv^{f} term. It naturally arises from the Taylor expansion in Eq. (3.24) and needs to be taken into account since it is a part of the first order term. Equation (3.26) can be simplified by using the vacancy equilibrium condition Eq. (3.18)

$$\frac{\partial F}{\partial c} \; = \; F^{\mathrm{f,cp}}(V_P, T) + \frac{\partial F^{\mathrm{c}}}{\partial c} \; = \; F^{\mathrm{f,cp}}(V_P, T) + k_{\mathrm{B}}T - k_{\mathrm{B}}T(1 - \ln c) \; \equiv \; 0, \tag{3.27}$$

which gives the equilibrium vacancy concentration

$$c^{\mathrm{eq,cp}}(V_P, T) \; = \; \exp[-\beta F^{\mathrm{f,cp}}(V_P, T)], \tag{3.28}$$

and which allows to separate a vacancy contribution to the free energy F^{vac}

$$F(V_P, T) \; \approx \; F^{\mathrm{p}}(V_P, T) \; + \; F^{\mathrm{vac}}(V_P, T), \tag{3.29}$$

with:

$$F^{\mathrm{vac}}(V_P, T) \; = \; -k_{\mathrm{B}}T \, c^{\mathrm{eq,cp}}(V_P, T). \tag{3.30}$$

The rescaled volume approach can be obtained from Eq. (3.26) by realizing that:

$$\begin{aligned} F^{\mathrm{v}}(N^{\mathrm{v}}V_P, T; N^{\mathrm{v}}) \; &= \; F^{\mathrm{v}}(\Omega_P^{\mathrm{v}}, T; N^{\mathrm{v}}) \; + \; \frac{\partial F^{\mathrm{v}}}{\partial \Omega_P^{\mathrm{v}}} \, (N^{\mathrm{v}}V_P - \Omega_P^{\mathrm{v}}) \; + \; O([N^{\mathrm{v}}V_P - \Omega_P^{\mathrm{v}}]^2) \\ &= \; F^{\mathrm{v}}(\Omega_P^{\mathrm{v}}, T; N^{\mathrm{v}}) \; + \; Pv_P^{\mathrm{f}} \; + \; O([v_P^{\mathrm{f}}]^2). \end{aligned} \tag{3.31}$$

Therefore, to first order in v_P^{f}, we have

$$F(V, T) \; \approx \; F^{\mathrm{p}}(V, T) \; + \; c \underbrace{\left[F^{\mathrm{v}}(\chi \Omega^{\mathrm{p}}, T; N^{\mathrm{v}}) - \chi F^{\mathrm{p}}(\Omega^{\mathrm{p}}, T; N^{\mathrm{v}}{+}1) \right]}_{= \; F^{\mathrm{f,rv}}(\Omega^{\mathrm{p}}(V), T) \text{ from Eq. (3.4)}} \; + \; F^{\mathrm{c}}(c), \tag{3.32}$$

where $\Omega^{\mathrm{p}} = (N^{\mathrm{v}} + 1)V$ and where we have removed the pressure subscript for clarity. The quantity in square brackets is the formation free energy of the rescaled volume approach from Eq. (3.4). Similarly as for the constant pressure approach, we can derive

$$c^{\mathrm{eq,rv}}(V, T) \; = \; \exp[-\beta F^{\mathrm{f,rv}}(V, T)], \tag{3.33}$$

Table 3.1: Definitions of the various free energy (FE) contributions for the perfect and single vacancy supercell.

	perfect	vacancy
electronic FE for $T = 0\,\mathrm{K}$ equilibrium nuclei positions	$F_0^{\mathrm{p,el}}$	$F_0^{\mathrm{v,el}}$
quantum mechanical quasiharmonic FE	$F^{\mathrm{p,qh}}$	$F^{\mathrm{v,qh}}$
classical explicitly anharmonic FE	$F^{\mathrm{p,clas,ah}}$	$F^{\mathrm{v,clas,ah}}$

and thus finally:

$$F(V,T) \;\approx\; F^{\mathrm{p}}(V,T) \;-\; k_{\mathrm{B}}T\, c^{\mathrm{eq,rv}}(V,T). \tag{3.34}$$

We have thus obtained the two standard approaches as natural approximations of our general volume optimized method. In particular, we are now in a position to identify a hierarchy in the approximations: First, the constant pressure approach arises by terminating the Taylor series in the vacancy concentration in Eq. (3.24) after the first order term. The rescaled volume approach needs a further approximation by terminating the Taylor series in the volume of vacancy formation in Eq. (3.31) likewise after the first order term.

3.1.4 The final free energy expression and extension to other point defects

Let us rewrite for convenience the final free energy expression of the volume optimized approach, Eq. (3.19), in a more compact form:

$$F(V,T) \;=\; (1 - cN^{\mathrm{v}})\, F^{\mathrm{p}}\!\left(\frac{V - c\Omega^{\mathrm{v}}}{1 - cN^{\mathrm{v}}}, T\right) \;+\; cF^{\mathrm{v}}(\Omega^{\mathrm{v}}, T; N^{\mathrm{v}}) \;+\; F^{\mathrm{c}}(c). \tag{3.35}$$

We have omitted here for clarity the "eq" superscript as compared to Eq. (3.19), c and Ω^{v} are however implicitly assumed to correspond to their equilibrium values. For both supercells, the perfect and the single vacancy supercell, we need to perform separate calculations as given by Eq. (2.195):

$$F^{\mathrm{p}}(V,T) \;\approx\; F_0^{\mathrm{p,el}}(V,T) + F^{\mathrm{p,qh}}(V,T) + F^{\mathrm{p,clas,ah}}(V,T), \tag{3.36}$$

$$F^{\mathrm{v}}(\Omega^{\mathrm{v}}, T; N^{\mathrm{v}}) \;\approx\; F_0^{\mathrm{v,el}}(\Omega^{\mathrm{v}}, T; N^{\mathrm{v}}) + F^{\mathrm{v,qh}}(\Omega^{\mathrm{v}}, T; N^{\mathrm{v}}) + F^{\mathrm{v,clas,ah}}(\Omega^{\mathrm{v}}, T; N^{\mathrm{v}}). \tag{3.37}$$

The corresponding free energy contributions are defined in Tab. 3.1. The calculation procedure is the same, i.e., as discussed in Chap. 2, for both supercells except for a necessary modification of the quasiharmonic free energy computation for the vacancy supercell. The reason is the break of translational symmetry which obviates the use of Fourier transforms. We will discuss the necessary changes in Sec. 3.3.3. Equation (3.35) constitutes the most complete free energy expression used in the present work (in Sec. 4.3): The free energy of an elementary, non-magnetic crystal including vacancies.

The volume optimized approach can be easily generalized to other point defects, such as e.g.

self interstitials. In case of p different point defect types, Eq. (3.35) changes to:

$$F(V,T) \; = \; \left(1 - \sum_i^p c_i N_i\right) F^{\mathrm{p}}\left(\frac{V - \sum_i^p c_i \Omega_i}{1 - \sum_i^p c_i N_i}, T\right) \; + \; \sum_i^p c_i F_i(\Omega_i, T; N_i) \; + \; F_i^{\mathrm{c}}(c_i). \qquad (3.38)$$

Here, c_i, Ω_i, N_i, F_i, and F_i^{c} are the concentration, the point defect supercell volume, the number of atoms inside Ω_i, the free energy of the point defect supercell, and the configurational free energy of the ith point defect. Note that depending on the number of possible point defect places available in the crystal, F_i^{c} can be different for different defects. For each point defect supercell the free energy F_i is calculated similarly as in Eq. (3.37) for the vacancy supercell. Equation (3.38) corresponds to the free energy of an elementary, non-magnetic crystal including any type of point defects.

3.2   Accelerating DFT calculations of the anharmonic free energy: The UP-TILD method

3.2.1   Motivation

In order to motivate the necessity for a new method to calculate $F^{\mathrm{clas,ah}}$, let us briefly sketch the computational requirements of the two state-of-the-art approaches. Besides the TILD method, introduced in Sec. 2.3.6, we discuss an alternative approach which is solely based on molecular dynamics (MD) calculations. A comparison of these approaches will allow us to set up a certain hierarchy in the performance of the methods.

Let us thus consider calculating $F^{\mathrm{clas,ah}}$ employing conventional MD simulations. With this we mean that 1) we do not include the random Langevin term in Eq. (2.197) and that 2) we do not make use of the quasiharmonic reference potential, i.e., we use only the full electronic free energy $F^{\mathrm{el}}(\{\mathbf{R}_I\})$ in Eq. (2.191). We need to comment on both issues in more detail since either one prevents a direct computation of the free energy. As for 1), using the original Newton's equation of motion allows to calculate only system properties at constant energy (microcanonical ensemble). To enable a constant temperature calculation (canonical ensemble), as desired here, we need to couple it to a thermostat, such as for instance to the Nosé-Hoover thermostat [90, 91]. Such a thermostat, however, does not contain a random element as the Langevin term and the deterministic nature of the original Newton's equation of motion prevails. (Note that, in order to achieve a constant temperature, a fictitious degree-of-freedom is added to the equations of motion within the Nosé-Hoover scheme. The motion corresponding to this degree-of-freedom is however deterministic [78].) As for 2), a direct calculation of the free energy without a reference potential is not possible since the free energy is an entropic quantity [79]. This means that it depends on the phase space volume, i.e., the partition function [cf. e.g. Eq. (2.192)], and it therefore cannot be described by a time average like Eq. (2.198). (Note that within the thermodynamic integration such a description becomes possible by coupling the system to a reference.) We can however compute directly the inner energy from which the free energy can be obtained by integration with respect to T (see e.g. Ref. [92]).

Taking the above considerations into account, we performed anharmonic free energy calculations for a $2 \times 2 \times 2$ aluminum supercell (32 atoms) using for a first test the EAM method. To reach an accuracy of $\sigma^{\mathrm{err}} < 1$ meV/atom [cf. Eq. (2.202)], we needed $\approx 10^7$ MD steps. This is consistent with the number given in Ref. [93], where 10^6 MD steps were found to be sufficient for a 500 atoms supercell. (With an increasing number of atoms in the supercell, the spatial averaging improves reducing the number of MD steps. Specifically, the number of atoms in the supercell times the

number of MD steps is a constant, except for finite size effects.) In a second step, we have performed the same anharmonic free energy calculations employing the TILD method. It turns out that to reach $\sigma^{\mathrm{err}} < 1$ meV/atom, we need $\approx 10^4$ steps [including the λ integration in Eq. (2.195)]. Let us estimate the CPU requirements, if we were to perform these calculations using DFT. For that purpose, we anticipate the results from Sec. 3.4.4.3 that for a DFT converged[1] calculation in a $2 \times 2 \times 2$ aluminum supercell, we need a $4 \times 4 \times 4$ k sampling (2 048 kp·atom) and a plane wave cutoff $E^{\mathrm{cut}} = 14$ Ry. Such a calculation takes ≈ 1 CPU hour [2]. We thus have

$$\underbrace{\begin{array}{c} 10^7 \text{ CPU hours} \\ = 1\,000 \text{ CPU years} \end{array}}_{\text{original MD}} \quad \rightarrow \quad \underbrace{\begin{array}{c} 10^4 \text{ CPU hours} \\ = 1 \text{ CPU year} \end{array}}_{\text{TILD method}} \tag{3.39}$$

which makes clear that the TILD method shifts DFT based $F^{\mathrm{clas,ah}}$ calculations into a feasibility range. The given numbers are however for a single point on the $F^{\mathrm{clas,ah}}(V,T)$ surface. If we consider calculating the full surface (≈ 30 points) and take into account additional DFT convergence checks especially for the supercell size, such a study becomes computationally rather expensive.

As a final step in this section, let us explicitly write down the scaling behavior of the TILD method. Comparing Eq. (3.40) below with the scaling of the UP-TILD method will later provide an illustrative explanation of the essential features of the latter. The TILD method scaling s^{TILD} reads

$$s^{\mathrm{TILD}} \;=\; \textcolor{red}{N^{\mathrm{LD}}(V,T)}\; N_V N_T N_\lambda \cdot \underbrace{s^{\mathrm{KS}}(a^{\mathrm{sc}}, E^{\mathrm{cut,high}}, N_k^{\mathrm{high}}, N_e, N^{\mathrm{it,red}})}_{\text{Kohn-Sham eq. for supercell}}, \tag{3.40}$$

with N_λ the number of λ values needed for the integration in Eq. (2.195). The notation for the plane wave cutoff and the number of k points including the superscript "high" will be useful in the discussion of the UP-TILD method. We note that s^{qh} — the scaling of the calculation of the reference dynamical matrix $\mathbf{D}$ [cf. Eq. (2.191)] — is not explicitly included in s^{LD} since it is negligible as compared to the remaining terms which are due to solving the Langevin equations of motion, Eq. (2.197), N^{LD} times to generate the trajectory $\{\mathbf{R}_I\}_t$. Note that the latter calculation must be performed in the computationally expensive supercell [$a^{\mathrm{sc}} = n^{\mathrm{sc}} a^{\mathrm{lat}}$; cf. Eq. (2.187)] and that we cannot employ N_k^{irr} but we rather have to use N_k [cf. Eqs. (2.92) and (2.187)]. The reason is that the atoms are not fixed to their symmetric positions when performing MD runs and consequently also the symmetries for the k sampling are lost. Further, we have to compute a trajectory for N_V different volumes and N_T different temperatures, with $N_V N_T \approx 30$ as mentioned above. As pointed out in Sec. 2.3.5, the factor N_T is due to the fact that molecular/Langevin dynamics is a statistical approach and no analytical T dependence is produced as available using the perturbation approaches discussed in Sec. 2.3.7. The factor N_λ is not significant (for the present investigations on aluminum), since it can be reduced even to 1. The critical factor [marked red in Eq. (3.40)] is N^{LD} which corresponds to the above discussed $\approx 10^4$ Langevin dynamics steps needed to reach statistical convergence. In fact, N^{LD} is strongly dependent on the considered volume and temperature, which is due to the increased phase space available at larger volumes and temperatures. In contrast, it is rather independent of λ as a consequence of using the Langevin dynamics.

---

[1]Henceforth, it will be necessary to explicitly distinguish between DFT convergence (k sampling, plane wave cutoff, augmentation grid, and supercell size) and statistical convergence. Note also that the numbers given here refer to a pseudopotential calculation. Consequently, there is no augmentation grid present (cf. Sec. 2.1.8).

[2]As a reference, we take an AMD Opteron with a clock speed of 2.4 GHz.
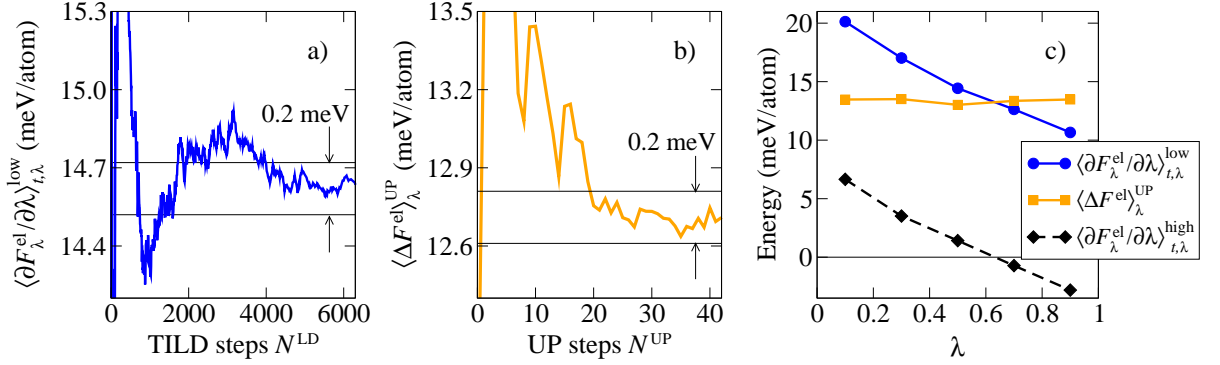
Figure 3.2: Illustration of the UP-TILD method for a 2^3 Al supercell at $V = 15.7\,\text{Å}^3$ and $T = 900\,\text{K}$. a) Statistical convergence of the time average $\langle \partial F_\lambda^{\text{el}}/\partial\lambda \rangle_{t,\lambda}^{\text{low}}$ as a function of the number of steps N^{LD} of the corresponding TILD run based on low converged DFT parameters. b) Statistical convergence of the upsampling average $\langle \Delta F^{\text{el}} \rangle_\lambda^{\text{UP}}$ [Eq.(3.42)] as a function of the number of uncorrelated TILD structures N^{UP} taken from the run in a). c) The λ dependence of the statistically converged quantities from a) and b) and their difference, which equals the time average $\langle \partial F_\lambda^{\text{el}}/\partial\lambda \rangle_{t,\lambda}^{\text{high}}$ for well converged DFT parameters according to Eq. (3.44).

3.2.2 Extending the TILD to the UP-TILD method

In order to overcome the difficulties with the computational requirements discussed in the previous section, we introduce the following extension of the TILD method which we refer to as the UP-TILD (UPsampled Thermodynamic Integration based Langevin Dynamics) method and which provides an efficient scheme to coarse grain the configuration space. The UP-TILD procedure can be structured into two main steps:

1) As a first step, we perform a "usual" TILD run as described in Sec. 2.3.6. The crucial point is now that instead of using well converged DFT parameters (cf. Sec. 3.2.1) we rather use a set of low converged parameters (specifically: 2^3 k mesh, 256 kp·atom, and 8 Ry plane wave cutoff). This reduces the time for a MD-step down to ≈ 120 s, i.e., a gain by a factor of ≈ 30 compared to the 1 hour calculation using highly converged DFT parameters. With this time reduction, the first run can be easily extended to several thousand steps in order to obtain the desired statistical accuracy. We denote the corresponding trajectory including N^{LD} structures and the time average as:

$$\begin{array}{ccccc} \text{TILD run with} & \longrightarrow & \{\mathbf{R}_I\}_t^{\text{low}} & \xrightarrow{\text{Eq. (2.198)}} & \left\langle \dfrac{\partial F_\lambda^{\text{el}}}{\partial\lambda} \right\rangle_{t,\lambda}^{\text{low}}. \\ \text{low parameters} & & & & \end{array} \qquad (3.41)$$

An example for the statistical convergence of $\langle \partial F_\lambda^{\text{el}}/\partial\lambda \rangle_{t,\lambda}^{\text{low}}$ is shown in Fig. 3.2a.

2) In a second step, we need to correct $\langle \partial F_\lambda^{\text{el}}/\partial\lambda \rangle_{t,\lambda}^{\text{low}}$ since we have a significant loss of accuracy due to the reduction of the DFT convergence parameters. We refer to this correction as the upsampling (UP). The upsampling itself can be divided into three steps:

    (a) We extract from $\{\mathbf{R}_I\}_t^{\text{low}}$ a set of N^{UP} uncorrelated structures $\{\mathbf{R}_I\}_{t_u}^{\text{low}}$ using Eq. (2.201).

(b) We then calculate the upsampling average $\left\langle \Delta F^{\mathrm{el}} \right\rangle_\lambda^{\mathrm{UP}}$ given by

$$\left\langle \Delta F^{\mathrm{el}} \right\rangle_\lambda^{\mathrm{UP}} = \left(N^{\mathrm{UP}} \right)^{-1} \sum_u^{N^{\mathrm{UP}}} \left[\Delta F^{\mathrm{el,low}}_{t_u} - \Delta F^{\mathrm{el,high}}_{t_u} \right], \tag{3.42}$$

with:

$$
\begin{aligned}
\Delta F^{\mathrm{el,low}}_{t_u} &= F^{\mathrm{el,low}}(\{\mathbf{R}_I\}^{\mathrm{low}}_{t_u}) - F^{\mathrm{el,low}}(\{\mathbf{R}^0_I\}), \\
\Delta F^{\mathrm{el,high}}_{t_u} &= F^{\mathrm{el,high}}(\{\mathbf{R}_I\}^{\mathrm{low}}_{t_u}) - F^{\mathrm{el,high}}(\{\mathbf{R}^0_I\}).
\end{aligned}
\tag{3.43}
$$

Here, $F^{\mathrm{el,low}}$ ($F^{\mathrm{el,high}}$) refers to the electronic free energy calculated using the low (high/well) converged set of DFT parameters. Note that the λ dependence of $\left\langle \Delta F^{\mathrm{el}} \right\rangle_\lambda^{\mathrm{UP}}$ is hidden in the trajectory $\{\mathbf{R}_I\}^{\mathrm{low}}_t$, which is additionally dependent on the volume and temperature. An example for the statistical convergence of $\left\langle \Delta F^{\mathrm{el}} \right\rangle_\lambda^{\mathrm{UP}}$ is shown in Fig. 3.2b and demonstrates the actual merit of the UP-TILD approach: The statistical convergence rate is improved by about two orders of magnitude compared to the original one for $\left\langle \partial F^{\mathrm{el}}_\lambda / \partial \lambda \right\rangle_{t,\lambda}$ keeping the number of the computationally expensive calculations $F^{\mathrm{el,high}}(\{\mathbf{R}_I\}^{\mathrm{low}}_{t_u})$ small. We typically obtain statistical convergence for $N^{\mathrm{UP}} < 100$.

(c) In the last step, the quantity of interest, the well DFT converged $\left\langle \partial F^{\mathrm{el}}_\lambda / \partial \lambda \right\rangle_{t,\lambda}^{\mathrm{high}}$, is obtained by:

$$\left\langle \partial F^{\mathrm{el}}_\lambda / \partial \lambda \right\rangle_{t,\lambda}^{\mathrm{high}} = \left\langle \partial F^{\mathrm{el}}_\lambda / \partial \lambda \right\rangle_{t,\lambda}^{\mathrm{low}} - \left\langle \Delta F^{\mathrm{el}} \right\rangle_\lambda^{\mathrm{UP}}. \tag{3.44}$$

An example for the upsampling at different λ values is shown in Fig. 3.2c. It demonstrates a further advantage of the UP-TILD method: The λ dependence of $\left\langle \Delta F^{\mathrm{el}} \right\rangle_\lambda^{\mathrm{UP}}$ becomes negligible. It is therefore a good approximation to neglect it completely and work with a single $\left\langle \Delta F^{\mathrm{el}} \right\rangle_\lambda^{\mathrm{UP}}$ at some fixed λ. (We typically use $\lambda = 0.5$.)

In order to verify that the UP-TILD approach is applicable to aluminum, our target material system (cf. Sec. 4.3), we calculated $\left\langle \partial F^{\mathrm{el}}_\lambda / \partial \lambda \right\rangle_{t,\lambda}^{\mathrm{high}}$ for some volumes directly and by means of Eq. (3.44). A representative set of our results is shown in Fig. 3.3. The figure illustrates the good performance of the method. The directly calculated values agree within the statistical uncertainty with the upsampled values and reproduce the volume dependence of $F^{\mathrm{clas,ah}}$ accurately. (The wiggles in the solid orange curve are due to statistical noise.) Moreover, Fig. 3.3 shows that it is indeed crucial to use the set of well converged DFT parameters, since the set of low converged DFT parameters yields both substantial deviations in the absolute values and an incorrect volume dependence.

A prerequisite for the UP-TILD approach to be applicable is that the phase spaces spanned by the set of low and high converged DFT parameters are sufficiently similar and that the difference can be described by a nearly constant energy shift. If the phase spaces differ significantly, the method will not be applicable. It should be also noted that the method cannot be applied to different supercell sizes since the corresponding phase spaces have different dimensions and a mapping onto each other is excluded by definition. In addition to computationally demanding explicit tests (Fig. 3.3), the performance of the UP-TILD method can be checked with two implicit criteria:

A) If the two phase spaces are similar, $\left\langle \Delta F^{\mathrm{el}} \right\rangle_\lambda^{\mathrm{UP}}$ is nearly independent of λ (Fig. 3.2c). Deviations from this independence can be thus used as a measure of the similarity of the phase spaces.

B) An alternative measure is the number of structures needed to obtain a statistically converged $\left\langle \Delta F^{\mathrm{el}} \right\rangle_\lambda^{\mathrm{UP}}$ for a single λ value.
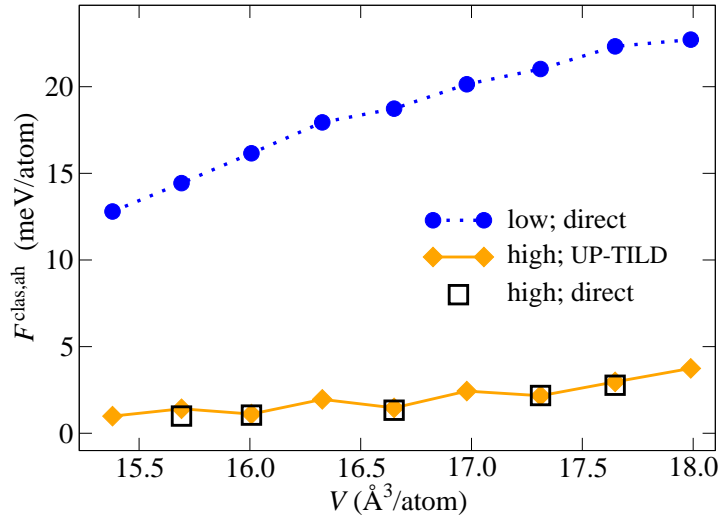
Figure 3.3: Classical anharmonic free energy $F^{\mathrm{clas,ah}}$ of aluminum at 900 K for the LDA functional and the 2^3 supercell as a function of the atomic volume V. Results for low and high converged DFT parameters are shown: low: 8 Ry, 256 kp·atom and high: 14 Ry, 2 048 kp·atom. Free energies obtained directly from a 'usual' TILD calculation are marked as 'direct', while 'UP-TILD' indicates that the UP-TILD method was employed.

3.2.3 Scaling performance of the UP-TILD method

The scaling s^{UP} of the UP-TILD method reads:

$$
s^{\mathrm{UP}} = N_V N_T \Big\{ \overbrace{N_\lambda N^{\mathrm{LD}}(V,T) \cdot s^{\mathrm{KS}}(a^{\mathrm{sc}}, E^{\mathrm{cut,low}}, N_k^{\mathrm{low}}, N_e, N^{\mathrm{it,red}})}^{\text{Step 1) TILD run with low parameters}}
$$
$$
+ \underbrace{N^{\mathrm{UP}}(V,T) \cdot s^{\mathrm{KS}}(a^{\mathrm{sc}}, E^{\mathrm{cut,high}}, N_k^{\mathrm{high}}, N_e, N^{\mathrm{it}})}_{\text{Step 2) Upsampling, } N^{\mathrm{UP}} \ll N^{\mathrm{LD}}} \Big\}.
$$

$$(3.45)$$

The first term in the curly brackets corresponds to step 1) and the second term to step 2) of the UP-TILD method. Let us compare Eq. (3.45) to Eq. (3.40). In Eq. (3.40), we find that the problematic factor N^{LD} ($\approx 10^4$) is coupled to the computationally expensive calculation based on the high converged DFT parameters $s^{\mathrm{KS}}(\ldots {}^{\mathrm{high}} \ldots)$. In contrast, in Eq. (3.45) N^{LD} and $s^{\mathrm{KS}}(\ldots {}^{\mathrm{high}} \ldots)$ appear only decoupled, which we have indicated by the different shading of the terms inside the curly brackets. Now, N^{LD} is coupled to the computationally inexpensive calculation $s^{\mathrm{KS}}(\ldots {}^{\mathrm{low}} \ldots)$, while $s^{\mathrm{KS}}(\ldots {}^{\mathrm{high}} \ldots)$ to the small factor N^{UP}. We need however to consider N^{it} iteration steps for the self consistency cycle, Eq. (2.66), since we cannot use the wave function extrapolation [point e) at the end of Sec. 2.3.6] for the uncorrelated structures of the upsampling. This increases the calculation time for $s^{\mathrm{KS}}(\ldots {}^{\mathrm{high}} \ldots)$ by a factor of 2 as compared to Eq. (3.40). We thus have

$$N^{\mathrm{LD}} \approx 10^4, \quad s^{\mathrm{KS}}(\ldots {}^{\mathrm{low}} \ldots) \approx 120\,\mathrm{sec}, \quad N^{\mathrm{UP}} \approx 100, \quad \text{and} \quad s^{\mathrm{KS}}(\ldots {}^{\mathrm{high}} \ldots) \approx 2\,\mathrm{h}, \quad (3.46)$$

and can estimate the CPU time requirements of the UP-TILD method to ≈ 20 days ($2 \times 2 \times 2$ aluminum supercell; cf. Sec. 3.2.1). Combining these estimations with Eq. (3.39) we thus have the

following hierarchy in the scaling performance of the three introduced methods:

$$\underbrace{\begin{array}{c} 10^7 \text{ CPU hours} \\ = 1\,000 \text{ CPU years} \end{array}}_{\text{original MD}} \rightarrow \underbrace{\begin{array}{c} 10^4 \text{ CPU hours} \\ = 1 \text{ CPU year} \end{array}}_{\text{TILD method}} \rightarrow \underbrace{\begin{array}{c} 500 \text{ CPU hours} \\ = 20 \text{ CPU days} \end{array}}_{\text{UP-TILD method}}. \tag{3.47}$$

3.2.4 Extensions of the UP-TILD method

We propose two extensions of the UP-TILD approach, the first one concerning the upgrade to a hierarchical scheme and the second one being an easy-to-use parallelization. Let us thus start with the hierarchical scheme which allows to further improve the convergence of the DFT calculations and/or to improve the statistical sampling. To illustrate this, consider a DFT convergence series with a set of values $\{x_1, x_2, x_3\}$ with successively increasing quality and computational expense: $x_1 < x_2 < x_3$. In a first step, we perform an efficient TILD simulation based on x_1 and we denote the corresponding low DFT converged time average as $\langle \partial F_\lambda^{\mathrm{el}}/\partial\lambda \rangle_{t,\lambda}^1$. In a second step, we calculate $\langle \Delta F^{\mathrm{el}} \rangle_\lambda^{\mathrm{UP},1\to2}$, the upsampling average of x_1 with respect to x_2, by:

$$\left\langle \Delta F^{\mathrm{el}} \right\rangle_\lambda^{\mathrm{UP},\,1\to2} = \left(N^{\mathrm{UP}}\right)^{-1} \sum_u^{N^{\mathrm{UP}}} (F_{t_u}^{\mathrm{el},x_1} - F_{t_u}^{\mathrm{el},x_2}). \tag{3.48}$$

Next, we calculate $\langle \Delta F^{\mathrm{el}} \rangle_\lambda^{\mathrm{UP},2\to3}$, the upsampling average of x_2 with respect to x_3, by:

$$\left\langle \Delta F^{\mathrm{el}} \right\rangle_\lambda^{\mathrm{UP},\,2\to3} = \left(N^{\mathrm{UP}\prime}\right)^{-1} \sum_u^{N^{\mathrm{UP}\prime}} (F_{t_u}^{\mathrm{el},x_2} - F_{t_u}^{\mathrm{el},x_3}). \tag{3.49}$$

This quantity converges statistically even faster than $\langle \Delta F^{\mathrm{el}} \rangle_\lambda^{\mathrm{UP},1\to2}$, i.e., $N^{\mathrm{UP}\prime} \ll N^{\mathrm{UP}}$, and therefore further reduces the expensive calculations corresponding to x_3. Note that in total only one MD run (for x_1) is necessary. To obtain finally the fully DFT converged time average $\langle \partial F_\lambda^{\mathrm{el}}/\partial\lambda \rangle_{t,\lambda}^3$, we replace Eq. (3.44) by:

$$\left\langle \partial F_\lambda^{\mathrm{el}}/\partial\lambda \right\rangle_{t,\lambda}^3 = \left\langle \partial F_\lambda^{\mathrm{el}}/\partial\lambda \right\rangle_{t,\lambda}^1 - \left\langle \Delta F^{\mathrm{el}} \right\rangle_\lambda^{\mathrm{UP},\,1\to2} - \left\langle \Delta F^{\mathrm{el}} \right\rangle_\lambda^{\mathrm{UP},\,2\to3}. \tag{3.50}$$

This scheme can be easily extended to higher hierarchies.

A straightforward application of the hierarchical UP-TILD approach is to a set of varying k samplings, plane wave cutoffs, and augmentation grids. We point out however a further very useful application. As stressed in Sec. 2.1.8, we have different possibilities to treat the high oscillations of the Kohn-Sham wave function close to the nuclei core with varying quality and efficiency. For instance for aluminum, we can assign $x_1 = \mathrm{pp}$ (pseudopotential) and $x_2 = \mathrm{PAW}$ (PAW method). Let us explicitly write down for future reference the corresponding upsampling average:

$$\left\langle \Delta F^{\mathrm{el}} \right\rangle_\lambda^{\mathrm{UP},\,\mathrm{pp}\to\mathrm{PAW}} = \left(N^{\mathrm{UP}}\right)^{-1} \sum_u^{N^{\mathrm{UP}}} (F_{t_u}^{\mathrm{el},\mathrm{pp}} - F_{t_u}^{\mathrm{el},\mathrm{PAW}}). \tag{3.51}$$

Note that due to Eq. (3.43) only energy differences enter the upsampling average but not the total

energies of the pseudo- or PAW potentials. We could also extend the convergence further by including x_3 = LAPW (LAPW method) and a corresponding upsampling average. Thus, the hierarchical UP-TILD method provides an extremely efficient way to check potential parametrizations not only for symmetric atomic structures but also for thermodynamically relevant structures.

Let us now turn to the issue of parallelization. We first point out that the second step of the UP-TILD method, the upsampling, is trivially parallelizable since each of the uncorrelated structures can be calculated independently of the others. In contrast, the first step, the low DFT converged TILD run, is naturally a sequential calculation, i.e., the various structures of the trajectory need to be calculated strictly one after the other. Even though the reduction of the DFT convergence parameters yields a strong CPU time reduction, the remaining times are in the order of CPU weeks and since a serial calculation is needed[3] this equals real time weeks. In many cases, it might be desirable to shorten the real time at the expense of using more CPUs and we therefore propose the following easy-to-use parallelization: Instead of performing a single TILD run, we perform in parallel N^{par} TILD runs. Denoting the trajectory of the jth run as $\{\mathbf{R}_I\}_{j,t}$, we then replace the time average Eq. (2.198) by:

$$\left\langle \frac{\partial F_\lambda^{\mathrm{el}}}{\partial \lambda} \right\rangle_{T/t,\lambda} = (N^{\mathrm{par}} N^{\mathrm{LD}})^{-1} \sum_j^{N^{\mathrm{par}}} \sum_i^{N^{\mathrm{LD}}} \frac{\partial}{\partial \lambda} F_\lambda^{\mathrm{el}}(\{\mathbf{R}_I\}_{j,t_i}). \tag{3.52}$$

Note that the sum over the different runs amounts to averaging over an ensemble of systems, i.e., to performing a thermodynamic average. We have thus changed the notation from $\langle . \rangle_t$ to $\langle . \rangle_{T/t}$. This scheme may be viewed as moving partially back to the original expression used to calculate the anharmonic free energy $F^{\mathrm{clas,ah}}$, Eq. (2.195). The remaining steps of the UP-TILD approach are performed as described so far. We stress however that such a parallelization crucially relies on an efficient equilibration scheme, as is the case in the present study [cf. point c) at the end of Sec. 2.3.6], since only configurations from trajectories after equilibration can be used in Eq. (3.52).

3.3 Integrated approach to thermodynamic quantities

Let us finally combine the various theoretical tools presented so far into a practicable integrated approach to calculate the free energy surface $F(V,T)$. To this end, we will be mainly concerned with finding appropriate parametrizations along V and T for the various contributions entering $F(V,T)$. For that purpose, we need to fix the temperature window of interest, which we take to be $T = 0\,\mathrm{K} \ldots T^{\mathrm{m}}$, where T^{m} is the melting temperature of the studied elements (cf. Fig. 4.1). The volume range is then determined by the equilibrium volume at $T = 0$ K, V_0^{eq} (cf. Tab. 4.1), and by the equilibrium volume at T^{m}, which is typically $\approx 1.1 V_0^{\mathrm{eq}}$ (cf. Fig. 4.4). The given parametrizations apply equally well to the free energy contributions of the perfect and single vacancy supercell [cf. Eq. (3.35)]. As pointed out in Sec. 3.1.4, we will however have to reconsider the calculation of the quasiharmonic free energy for the vacancy supercell (Sec. 3.3.3). As a measure of the quality of a parametrization we will frequently refer to the expansion coefficient α, Eq. 2.235, and to the specific heat C_P, Eq. 2.236. Being second derivatives of $F(V,T)$ both are extremely sensible to changes in the parametrizations. The specific numbers provided in the following are for aluminum[4].

---

[3]Serial refers here to the fact that the various MD structures need to calculated one after another. The calculation of a single structure can be parallelized in the usual manner for DFT calculations (for instance k point parallelization).

[4]As a reference for the relative values for α and C_P, we take the final quantities containing all contributions at the melting temperature of aluminum (934 K) and at zero pressure. LDA: $\alpha = 3.68 \cdot 10^{-5}$ K^{-1} and $C_P = 3.73\,k_{\mathrm{B}}$; GGA: $\alpha = 3.83 \cdot 10^{-5}$ K^{-1} and $C_P = 3.83\,k_{\mathrm{B}}$. See also Tab. 4.12.

3.3.1   Electronic free energy surface

Let us first focus on $F_0^{\mathrm{el}}(V,T)$, the electronic free energy for the $T = 0$ K equilibrium nuclei positions $\{\mathbf{R}_I^0\}$, with the temperature dependence entering via the Fermi-Dirac function, Eq. (2.65). The representation of $F_0^{\mathrm{el}}(V,T)$ becomes particularly convenient if it is divided into the temperature independent ground state energy $E_{g,0}^{\mathrm{el}}(V) := E_g^{\mathrm{el}}(\{\mathbf{R}_I^0\}, V, T)$ and a remaining part $\widetilde{F}_0^{\mathrm{el}}(V,T)$:

$$F_0^{\mathrm{el}}(V,T) \;=\; E_{g,0}^{\mathrm{el}}(V) + \widetilde{F}_0^{\mathrm{el}}(V,T). \tag{3.53}$$

The reason for this separation is that $\widetilde{F}_0^{\mathrm{el}}(V,T)$ can be accurately described with low order polynomials, while $E_{g,0}^{\mathrm{el}}(V)$ can be parametrized using standard equations-of-state (EOS). We studied three different EOSs: the Murnaghan [94], the third-order Birch-Murnaghan [95], and the Vinet [96] EOS. The latter has been found to describe theoretical and experimental data of various materials most accurately [97]. For the C_P of Al, we find negligible[5] differences between the three EOSs. For α, the Birch-Murnaghan and Vinet EOS yield a similar value which is, however, 1.9% larger than the one obtained with the Murnaghan EOS. We ascribe this to the improved nature of the Birch-Murnaghan and Vinet EOS. For the further analysis, we use the Vinet EOS which reads [96]

$$E_{g,0}^{\mathrm{el}}(V) \;=\; E_{g,0}^{\mathrm{el}}(V_0^{\mathrm{eq}}) \;+\; \frac{4B_{T,0}V_0^{\mathrm{eq}}}{(B_{T,0}'-1)^2} \;-\; \frac{V_0^{\mathrm{eq}}B_{T,0}}{(B_{T,0}'-1)^2} \left\{ 5 + 3B_{T,0}' \left[\left(\frac{V}{V_0^{\mathrm{eq}}}\right)^{1/3} - 1 \right] - 3\left(\frac{V}{V_0^{\mathrm{eq}}}\right)^{1/3} \right\}$$

$$\times \exp\left\{ -\frac{3}{2}\left(B_{T,0}'-1\right)\left[\left(\frac{V}{V_0^{\mathrm{eq}}}\right)^{1/3} - 1\right]\right\}, \tag{3.54}$$

with V_0^{eq}, $B_{T,0}$, and $B_{T,0}'$ defined in Eqs. (2.232), (2.239), and (2.240). We note that the choice of the EOS parametrization plays only a role if one is interested in highest accuracy results as needed e.g. in Sec. 4.3, while for "usual" applications this point is less crucial. On the other hand, an important point is that for a sensible parametrization of $E_{g,0}^{\mathrm{el}}(V)$ the volume range needs to be extended below V_0^{eq} to $\approx 0.9 V_0^{\mathrm{eq}}$, in contrast to the remaining free energy contributions. To obtain the surface $\widetilde{F}_0^{\mathrm{el}}(V,T)$, we calculate $\widetilde{F}_0^{\mathrm{el}}$ values on a mesh of ≈ 5 volume and ≈ 10 temperature points. The surface is then parametrized using a two dimensional fourth order polynomial as

$$\widetilde{F}_0^{\mathrm{el}}(V,T) \;=\; \sum_{i,j} a_{i,j} V^i T^j \quad \text{with} \quad i \geq 0,\; j \geq 1,\; \text{and}\; i+j \leq 4, \tag{3.55}$$

and with fitting coefficients $a_{i,j}$. The discrete set of $\widetilde{F}_0^{\mathrm{el}}$ values needed to perform the fit can be easily obtained via DFT: Only a small unit cell is required allowing for easy convergence and the resulting free energy surface is smooth. Inclusion of terms beyond the fourth order were found to provide no improvement to the fit.

3.3.2   Quasiharmonic free energy surface

The temperature dependence of the quasiharmonic free energy F^{qh} presents no additional challenge, due to the analytical dependence given in Eq. (2.161). In contrast, a sensible parametrization of F^{qh} along V turns out to be important. We critically test three approximations which are rather convenient, since for each it is practically sufficient to calculate F^{qh} only at two different volumes. The first two approximations begin in fact with a parametrization of the phonon frequencies:

---

[5]We call an error or effect negligible if it is below 1% for α and below 0.5% for C_P (cf. footnote on previous page).
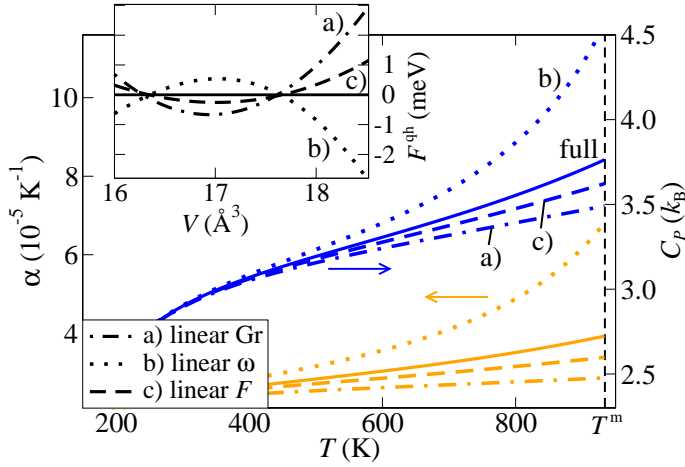
Figure 3.4: Quasiharmonic expansion coefficient α and heat capacity C_P of Al. The solid lines show fully converged quantities. The dot-dashed [dotted/dashed] lines represent quantities based on a) the linear Grüneisen (Gr) [b) the linear frequency ω/ c) the linear free energy F] approximation [see Eqs. (3.56) to (3.58) respectively for details]. The inset shows the corresponding quasiharmonic free energies F^{qh} (per atom) at 900 K referenced to the fully converged F^{qh}. The curves correspond to GGA results. LDA results show the same behavior. The vertical thin dashed line marks the melting temperature T^{m}.

a) The volume dependence is parametrized using the linear Grüneisen approximation [68]

$$-\frac{V}{\omega_{\mathbf{q},s}(V)}\frac{\partial\omega_{\mathbf{q},s}(V)}{\partial V} = \gamma_{\mathbf{q},s} = \text{const}, \tag{3.56}$$

with the Grüneisen constant $\gamma_{\mathbf{q},s}$. Solving for $\omega_{\mathbf{q},s}(V)$ yields $\omega_{\mathbf{q},s}(V) = a_{\mathbf{q},s}V^{-\gamma_{\mathbf{q},s}}$, with an integration constant $a_{\mathbf{q},s}$.

b) The frequencies are assumed to depend linearly on the volume:

$$\partial\omega_{\mathbf{q},s}/\partial V = c_{\mathbf{q},s} = \text{const}. \tag{3.57}$$

c) The free energy is assumed to depend linearly on the volume:

$$\partial F^{\text{qh}}/\partial V = c = \text{const}. \tag{3.58}$$

Assumption c) is not equivalent to b), since the F^{qh} dependence on $\omega_{\mathbf{q},s}$ is strongly non-linear.

Based on highly converged DFT free energies (cf. Sec. 3.4) for several (seven) volumes, we are in the position to check the validity/performance of each of these approximations. The volume dependence of these free energies is fitted to a polynomial of third order:

$$F^{\text{qh}}(V,T) = \sum_{i=0}^{3} a_i(T)V^i. \tag{3.59}$$

Extending the polynomial to higher orders yields only negligible changes in the thermodynamic properties. Figure 3.4 shows the comparison with respect to the target quantities α and C_P. As can be seen, applying approximation b) yields dramatically wrong α and C_P values at temperatures close to the melting point T^{m}. At T^{m}, they are overestimated by 74% and 21%, respectively. In contrast, approximation a) yields a strong underestimation, -27% for α and -7% for C_P. The best approximation is c) yielding an underestimation of -14% for α and -4% for C_P. However, the remaining error is still significant when considering the small contributions beyond the quasi-harmonic approximation (compare to Tab. 4.12) and could, in particular, have a strong influence on the determination of anharmonic contributions.[6] A correct treatment of the volume dependence

---

[6]Note that this situation would occur, if we used a harmonic, i.e., fixed volume, dynamical matrix as a reference for our anharmonic calculations. In order to obtain the volume dependence of the anharmonic contribution, we would

of the quasiharmonic free energy surface is therefore crucial.

We note a further important point: In Fig. 3.4, we included the volume dependence of the free energy (at 900 K; inset) which results from each of the approximations. The differences in the free energies between the various approximations are in the range of a few meV/atom, which might be considered as relatively small. Nonetheless, these small differences lead to the strong differences in the expansion coefficient and heat capacity. This is a very important observation and we will return to it in Sec. 3.4.2 where we consider the error propagation in DFT thermodynamics.

3.3.3 Quasiharmonic free energy for point defects

The break of translational symmetry due to the creation of a point defect has two consequences: 1) The Fourier transforms Eqs. (2.138) and (2.139) and the following transformations leading to the eigenvalue equation, Eq. (2.143), and to the fundamental phonon frequencies determining the quasiharmonic free energy, Eq. (2.161), cannot be applied. 2) The symmetry considerations regarding the real space dynamical matrix $\mathbf{D}$ as discussed in Sec. 2.3.4 need to be modified.

The first issue can be solved rather straightforwardly. In fact, we do not need to change into Fourier space to obtain the frequencies. We have used this procedure in Sec. 2.3.3 deliberately for two reasons: First, it allows an interpretation of the eigenvalues of the dynamical matrix in terms of phonon frequencies. Second, it allows easily to extend the formalism to arbitrary wave vectors $\mathbf{q}$ as performed in Sec. 2.4.1. Let us now however use a more direct approach which can be applied also to defect supercells and which consists of solving the eigenvalue equation of the **real space** dynamical matrix $\mathbf{D}$:

$$\mathbf{D}(V)\,\mathbf{w}_i \;=\; \omega_i^2(V)\,\mathbf{w}_i. \tag{3.60}$$

The dynamical matrix $\mathbf{D}$ is in our case a $3N_n \times 3N_n$ matrix and we thus have $3N_n$ eigenvectors $\mathbf{w}_i$ each of size $3N_n$ and $3N_n$ eigenvalues ω_i^2. For a perfect crystal, the ω_i match exactly the frequencies $\omega_{\mathbf{G}^{\mathrm{sc}};s}$. (Note that there are N_n $\mathbf{G}^{\mathrm{sc}}$ vectors and for each s runs over 3 branches so that we have also in reciprocal space $3N_n$ frequencies $\omega_{\mathbf{G}^{\mathrm{sc}};s}$ as needed to conserve the degrees of freedom.) We can therefore use directly the ω_i to obtain the quasiharmonic free energy, Eq. (2.161), now as

$$F^{\mathrm{qh}}(V) \;=\; \frac{1}{3N_n} \sum_i^{3N_n-3} \left\{ \frac{1}{2}\hbar\omega_i(V) \,+\, k_{\mathrm{B}}T \ln\left[1 - e^{-\beta\hbar\omega_i(V)} \right] \right\}, \tag{3.61}$$

again omitting the 3 zero frequencies. We need to take special care in using Eq. (3.61) in combination with a quasiharmonic free energy obtained from a dense Fourier interpolated mesh, Eq. (2.226). To explain this consider calculating the free energy of a crystal with vacancies using Eq. (3.35). To calculate $F^{\mathrm{v,qh}}$, we are forced to use Eq. (3.61) due to the above discussed symmetry break. For $F^{\mathrm{p,qh}}$, we might want to use $F^{\mathrm{p,qh,m}}$, i.e., the Fourier interpolated version Eq. (2.226), in order to improve the description at lower temperatures. This leads however to a shift in the perfect crystal free energy with respect to $F^{\mathrm{v,qh}}$ and produces an incorrect coupling between the perfect crystal and vacancy supercell in Eq. (3.35). To nonetheless profit from the good performance of Eq. (2.226) at low temperatures, we introduce the following correction scheme:

$$F(V,T) \;=\; \widetilde{F}(V,T) - F^{\mathrm{p,qh}}(V,T) + F^{\mathrm{p,qh,m}}(V,T). \tag{3.62}$$

Here, $\widetilde{F}$ is the free energy obtained from Eq. (3.35) using $F^{\mathrm{p,qh}}$ and $F^{\mathrm{v,qh}}$, which are all obtained

---

then need to subtract F^{qh}. If $F^{\mathrm{qh}}(V)$ was incorrectly parametrized, we could easily obtain large errors in $F^{\mathrm{clas,ah}}(V)$, in fact even leading to a wrong sign.

from Eq. (3.61). [For $F^{\mathrm{p,qh}}$, also the equivalent expression Eq. (2.161) can be used.] Subsequently, $F^{\mathrm{p,qh}}$ is subtracted and $F^{\mathrm{p,qh,m}}$ calculated on a well converged mesh is added.

To perform vacancy calculations in practice, it is often indispensable to apply a generalized version of the described correction scheme:

$$F(V,T) \;=\; \widetilde{F}(V,T) - F^{\mathrm{p}}(V,T) + F^{\mathrm{p,best}}(V,T). \tag{3.63}$$

Here, $\widetilde{F}$ refers to a free energy calculated using consistent parameters (e.g., k sampling, plane wave cutoff, augmentation grid) for the perfect bulk, F^{p}, and the vacancy supercell, F^{v}, in Eq. (3.35). Further, $F^{\mathrm{p,best}}$ is the perfect crystal free energy calculated using the best convergence parameters. The correction is important for the final thermodynamic quantities (e.g., Fig. 4.17) but does not affect vacancy related properties such as the concentration (e.g., Fig. 4.15), since the latter are obtained directly from $\widetilde{F}$.

Let us now discuss the second of the above issues concerning the symmetries of the real space dynamical matrix. As derived in Sec. 2.3.4, translational and point symmetries allow to reduce the number of Kohn-Sham calculations needed to fully fill the perfect crystal dynamical matrix to one. For point defects, this number increases significantly. The matrices Eq. (2.172) can however still be used to map some of the displacements and corresponding force fields onto each other by the rules given in Sec. 2.3.4. This applies in particular to displacements in the same atomic shell around the point defect.

3.3.4 Extension to a temperature dependent dynamical matrix

Let us now abandon the approximation performed in Eq. (2.179) and consider the temperature dependent dynamical matrix. The quasiharmonic formalism, Eqs. (2.181) to (2.185), changes to:

$$\underbrace{D_{I\alpha,J\beta}(\Omega, T^{\mathrm{el}})}_{} \;=\; -(M_I \Delta R)^{-1}\, \overbrace{F^{\mathrm{HF}}_{I,\alpha}(R^0_{1,1},\dots,R^0_{J,\beta}+\Delta R,\dots,R^0_{N_n,3},\Omega,T^{\mathrm{el}})}^{\text{HF forces from Kohn-Sham calculations for different } \Omega \text{ and } T^{\mathrm{el}}} \tag{3.64}$$

$$D_{\mathbf{G}^{\mathrm{sc}},\alpha\beta}(\Omega,T^{\mathrm{el}}) \;=\; N_n^{-1}\sum_{I,J}^{N_n} D_{I\alpha,J\beta}(\Omega,T^{\mathrm{el}})\, e^{i\mathbf{G}^{\mathrm{sc}}\cdot(\mathbf{R}^0_I - \mathbf{R}^0_J)} \tag{3.65}$$

$$\mathbf{D}_{\mathbf{G}^{\mathrm{sc}}}(\Omega,T^{\mathrm{el}})\, \mathbf{w}_{\mathbf{G}^{\mathrm{sc}},s} \;=\; (\omega_{\mathbf{G}^{\mathrm{sc}},s})^2(\Omega,T^{\mathrm{el}})\, \mathbf{w}_{\mathbf{G}^{\mathrm{sc}},s} \tag{3.66}$$

$$\underbrace{F^{\mathrm{el}}_0(\Omega,T^{\mathrm{el}})}_{\substack{\text{Kohn-Sham calculations}\\\text{for different } \Omega \text{ and } T^{\mathrm{el}}}} + \underbrace{\sum_{\mathbf{G}^{\mathrm{sc}}}^{\mathrm{prBZ}'}\sum_s^3 \left\{ \frac{\hbar}{2}\,\omega_{\mathbf{G}^{\mathrm{sc}},s}(\Omega,T^{\mathrm{el}}) + k_{\mathrm{B}}T^{\mathrm{nuc}}\ln\left[1-\exp\left\{-\beta\hbar\,\omega_{\mathbf{G}^{\mathrm{sc}},s}(\Omega,T^{\mathrm{el}})\right\}\right]\right\}}_{=\; F^{\mathrm{qh}}(\Omega,T^{\mathrm{nuc}},T^{\mathrm{el}})} \tag{3.67}$$

$$\approx\; F(\Omega,T^{\mathrm{el}},T^{\mathrm{nuc}}) \;\;\rightarrow\;\; T^{\mathrm{el}}=T^{\mathrm{nuc}}=T \;\;\rightarrow\;\; F(\Omega,T)\,/N_n \;=\; F(V,T). \tag{3.68}$$

Compared to Eqs. (2.181) to (2.185), we have performed the following changes. The Hellmann-Feynman forces $\mathbf{F}^{\mathrm{HF}}_I$ are now calculated from the electronic free energy $F^{\mathrm{el}}(\{\mathbf{R}_I\})$. The latter is

temperature dependent through the Fermi-Dirac function, Eq. (2.65), and this renders also the forces temperature dependent. We have denoted the corresponding temperature by T^{el} and we will refer to it as the electronic temperature. This enables a distinction with the nuclei temperature T^{nuc}, which explicitly enters the quasiharmonic free energy, and it will prove convenient for the following discussion and the subsequent parametrization. The dependence of $\mathbf{F}_I^{\mathrm{HF}}$ on T^{el} carries over to the real space dynamical matrix $\mathbf{D}$, the reciprocal dynamical matrix $\mathbf{D}_{\mathbf{G}^{\mathrm{sc}}}$, and the phonon frequencies $\omega_{\mathbf{G}^{\mathrm{sc}}s}$, on which we have thus dropped the "0K" superscript. The quasiharmonic free energy F^{qh} likewise depends implicitly on T^{el}, besides its explicit dependence on T^{nuc}. As indicated, at the end of a calculation the electronic and nuclei temperature need to be set equal to the actual external temperature T. The difference in the free energy resulting from Eqs. (3.64) to (3.68) as compared to the free energy resulting from Eqs. (2.181) to (2.185) is fully contained in the quasiharmonic free energy and we therefore write:

$$\Delta F^{\mathrm{qh}}(\Omega, T) \quad \leftarrow \quad \Delta F^{\mathrm{qh}}(\Omega, T^{\mathrm{nuc}}, T^{\mathrm{el}}) \;=\; F^{\mathrm{qh}}(\Omega, T^{\mathrm{nuc}}, T^{\mathrm{el}}) - F^{\mathrm{qh,0K}}(\Omega, T^{\mathrm{nuc}}). \tag{3.69}$$

It will proof useful (Sec. 4.2) to investigate also derived thermodynamic properties by separating their temperature dependence as $(T) \to (T^{\mathrm{el}}, T^{\mathrm{nuc}})$. In particular, we will be interested in the temperature dependencies of the isobaric heat capacity C_P and the free energy F_P, for which we consider:

$$F^{\mathrm{qh}}(\Omega, T^{\mathrm{nuc}}; T^{\mathrm{el}}) \quad \to \quad \begin{cases} C_P(T^{\mathrm{nuc}}; T^{\mathrm{el}}), \\ F_P(T^{\mathrm{nuc}}; T^{\mathrm{el}}). \end{cases} \tag{3.70}$$

As indicated by the semicolon, C_P and F_P are calculated from a quasiharmonic free energy surface at a fixed T^{el}. Equation (3.70) should be contrasted with the fully consistent approach, i.e., the one required to obtain the final thermodynamic properties:

$$F^{\mathrm{qh}}(\Omega, T) \;=\; F^{\mathrm{qh}}(\Omega, T^{\mathrm{nuc}} = T, T^{\mathrm{el}} = T) \quad \to \quad \begin{cases} C_P(T), \\ F_P(T). \end{cases} \tag{3.71}$$

An important point is that, while we have

$$F_P(T) \;=\; F_P(T^{\mathrm{nuc}} = T; T^{\mathrm{el}} = T), \tag{3.72}$$

the heat capacity does not obey this relation in general:

$$C_P(T) \;\neq\; C_P(T^{\mathrm{nuc}} = T; T^{\mathrm{el}} = T). \tag{3.73}$$

The reason for this inequality is the fact that C_P is a derivative quantity thus depending on the curvature of the quasiharmonic free energy surface, which is different for $F^{\mathrm{qh}}(\Omega, T^{\mathrm{nuc}}; T^{\mathrm{el}})$ and $F^{\mathrm{qh}}(\Omega, T)$. This issue will become more clear in Sec. 4.2.

A calculation required to obtain $\Delta F^{\mathrm{qh}}(\Omega, T)$ scales as:

$$s^{\mathrm{qh}} \;=\; N_V N_T \cdot \underbrace{s^{\mathrm{KS}}(a^{\mathrm{lat}}, E^{\mathrm{cut}}, N_k^{\mathrm{irr,pr}}, N_e^{\mathrm{pr}}, N^{\mathrm{it}})}_{\text{Kohn-Sham eq. for primitive cell}} + N_V N_T \cdot \underbrace{s^{\mathrm{KS}}(a^{\mathrm{sc}}, E^{\mathrm{cut}}, N_k^{\mathrm{irr}}, N_e, N^{\mathrm{it}})}_{\text{Kohn-Sham eq. for supercell}}. \tag{3.74}$$

Comparing Eq. (3.74) to Eq. (2.187), we see that the number of Kohn-Sham calculations for the supercell increases as compared to the $T = 0$ K dynamical matrix formalism, since we need to account for the temperature dependence of the Hellmann-Feynman forces.

In practice, we found the following scheme to be particularly convenient to calculate $\Delta F^{\mathrm{qh}}(\Omega, T)$. For a fixed volume we determine $\mathbf{D}$ on a mesh of 5 different T^{el}. Using the standard procedure we calculate the corresponding frequencies so that we have a set of frequencies for each of the 5 different T^{el}. We then fit

$$\omega_{\mathbf{G}^{\mathrm{sc}}, s}(T^{\mathrm{el}}) \; = \; a_{\mathbf{G}^{\mathrm{sc}}, s} + c_{\mathbf{G}^{\mathrm{sc}}, s}(T^{\mathrm{el}})^2 + d_{\mathbf{G}^{\mathrm{sc}}, s}(T^{\mathrm{el}})^3, \tag{3.75}$$

to the set of frequencies separately for each $\mathbf{G}^{\mathrm{sc}}$ vector and branch s. The T^{el} and T^{nuc} dependencies are calculated using the standard expression:

$$F^{\mathrm{qh}}(T^{\mathrm{nuc}}, T^{\mathrm{el}}) \; = \; \sum_{\mathbf{G}^{\mathrm{sc}}}^{\mathrm{prBZ}'} \sum_{s}^{3} \left\{ \frac{\hbar}{2} \, \omega_{\mathbf{G}^{\mathrm{sc}}, s}(T^{\mathrm{el}}) \; + \; k_{\mathrm{B}} T^{\mathrm{nuc}} \ln \left[1 - \exp \left\{ -\beta \hbar \, \omega_{\mathbf{G}^{\mathrm{sc}}, s}(T^{\mathrm{el}}) \right\} \right] \right\}. \tag{3.76}$$

The volume dependence is treated as described in Sec. 3.3.2 and $\Delta F^{\mathrm{qh}}(\Omega, T)$ is eventually determined from Eq. (3.69).

3.3.5   Anharmonic free energy surface

Before discussing the critical volume and temperature parametrization of the anharmonic free energy surface $F^{\mathrm{clas,ah}}(V, T)$, let us reconsider the equations of the TILD approach in view of the results of the previous section. The electronic free energy of the coupled system F_λ^{el}, Eq. (2.191), depends in fact on the electronic temperature T^{el}

$$F_\lambda^{\mathrm{el}}(\{\mathbf{R}_I\}, T^{\mathrm{el}}) \; = \; (1 - \lambda) \left[F_0^{\mathrm{el}}(T^{\mathrm{el}}) \; + \; \mathbf{U} \mathbf{D}(T^{\mathrm{el}}) \mathbf{U}/(2\mathbf{M}) \right] \; + \; \lambda F^{\mathrm{el}}(\{\mathbf{R}_I\}, T^{\mathrm{el}}), \tag{3.77}$$

(neglecting now the volume dependence) and this carries over to the partition function, Eq. (2.192), which is additionally explicitly depending on the nuclei temperature T^{nuc}:

$$Z_\lambda(T^{\mathrm{el}}, T^{\mathrm{nuc}}) \; = \; \int d\mathbf{R}_I \, e^{-F_\lambda^{\mathrm{el}}(\{\mathbf{R}_I\}, T^{\mathrm{el}})/(k_{\mathrm{B}} T^{\mathrm{nuc}})} \Big/ (\Lambda^{3N_n} N_n!). \tag{3.78}$$

The final equation for the anharmonic free energy, Eq. (2.195), reads then

$$\begin{aligned} F^{\mathrm{clas,ah}} \; = \; & \int_0^1 d\lambda \, Z_\lambda^{-1}(T^{\mathrm{el}}, T^{\mathrm{nuc}}) \, (\Lambda^{3N_n} N_n!)^{-1} \\[4pt] & \times \int d\mathbf{R}_I \, e^{-F_\lambda^{\mathrm{el}}(\{\mathbf{R}_I\}, T^{\mathrm{el}})/(k_{\mathrm{B}} T^{\mathrm{nuc}})} \Big[F^{\mathrm{el}}(\{\mathbf{R}_I\}, T^{\mathrm{el}}) - F_0^{\mathrm{el}}(T^{\mathrm{el}}) \; - \; \mathbf{U} \mathbf{D}(T^{\mathrm{el}}) \mathbf{U}/(2\mathbf{M}) \Big], \end{aligned} \tag{3.79}$$

where we have used the original definition of the thermal average, Eq. (2.193), and where we have explicitly stated each temperature dependence. The electronic temperature T^{el} enters through the Fermi-Dirac function, Eq. (2.65), while the nuclei temperature T^{nuc} enters through the Langevin dynamics in particular through Eq. (2.200). We note that the reference for the thermodynamic integration can be chosen arbitrarily and we therefore could remove the temperature dependence of the dynamical matrix by replacing $\mathbf{D}(T^{\mathrm{el}}) \rightarrow \mathbf{D}^{\mathrm{0K}}$. The other temperature dependencies need however to be respected and, since $T = T^{\mathrm{el}} = T^{\mathrm{nuc}}$ must be fulfilled at the end of a calculation, we have in principle to perform the molecular dynamics simulations at a T^{nuc} which corresponds to the T^{el} used to determine $F^{\mathrm{el}}(\{\mathbf{R}_I\})$. Previous studies ignored this subtle dependence. Using

the UP-TILD method, we are for the first time able to investigate the actual influence of T^{el} on $F^{clas,ah}$ (Sec. 4.3.5).

Let us now discuss the V and T parametrization of $F^{clas,ah}$ which turns out to be a critical point in calculating derivative quantities such as α or C_P. The problem has three aspects:

a) A technical one: Even though tools are available to sample the phase space effectively (e.g., the UP-TILD method), reducing the statistical error σ^{err}, Eq. (2.202), to much less than 1 meV/atom quickly becomes computationally prohibitive, especially for high temperatures. Thus, in practice, the anharmonic free energy surface will contain non-negligible statistical noise.

b) A physical one: Despite the statistical noise, we can clearly identify that the temperature dependence of the surface contains higher order contributions at least up to the cubic term (see Figs. 4.13b and 4.16). Moreover, our results also suggest that V-T coupling terms have non-negligible contributions.

c) A fundamental one: In contrast to the temperature dependence of the quasiharmonic free energy [Eq. (2.184)], no analytical equation for the full anharmonic free energy, i.e., containing all orders in the expansion Eq. (2.130), is known.

Due to the lack of an analytical expression, it looks tempting to use a polynomial series to expand $F^{clas,ah}(V,T)$. Based on the discussion above and extensive convergence checks, it became clear that this is critically hindered by an interplay of a) and b): In order to take higher orders into account, we need a sufficiently large polynomial basis. However, increasing the polynomial basis, the parametrization becomes unphysical due to the statistical noise in the data used for the fit. We will therefore derive in Sec. 4.3.4 a conceptually different and physically motivated approach which solves this problem.

3.4 Towards highly accurate DFT free energies

In Chap. 2, we have discussed the origin of the key convergence parameters in DFT based thermo-dynamic calculations (k sampling, plane wave cutoff, augmentation grid, and supercell size). In this section, we will address the actual convergence behavior of thermodynamic properties (specifically α and F_P) for the studied elements (cf. Tab. 4.1). We focus hereby on some issues (Secs. 3.4.1 to 3.4.3), which we found to be particularly important and which we therefore discuss in detail. In Sec. 3.4.4, we eventually give an overview and a brief discussion of the full list of DFT parameters, on which the results presented in Chap. 4 are based, including also the statistical issues for the anharmonicity calculations.

3.4.1 Efficient convergence: Decoupling procedure and a supercell size based technique

A quantity, we identified to be crucial in achieving a high accuracy in thermodynamic calculations, is the size of the grid used to calculate the augmentation charges (henceforth labeled **augGrid**) within the PAW method. (The augmentation charges correspond to ρ^{aug} from Sec. 2.1.8.) To allow a proper investigation of the augGrid, it is important to separate the dependence of the augGrid from the grid used to store the wave function and charge density coefficients (henceforth labeled **basicGrid**), which is determined by the plane wave cutoff. [This dependence is typically introduced for simplicity, since then only a single parameter (the cutoff) needs to be controlled.]
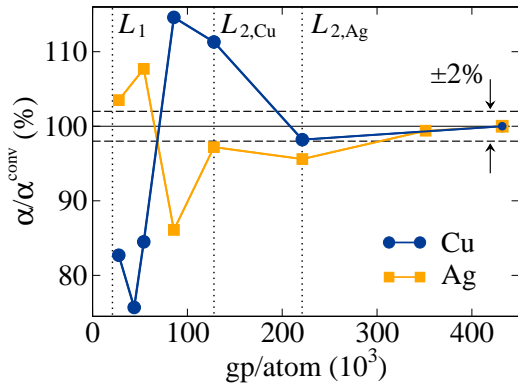
Figure 3.5: Convergence of the expansion coefficient α with respect to the augGrid size (see text) in terms of grid points per atom (gp/atom) for Cu and Ag. The values are scaled with respect to α^{conv} which corresponds to $432 \cdot 10^3$ gp/atom. The lines L_1 (similar for Cu and Ag on this scale) and $L_{2,\mathrm{Cu/Ag}}$ correspond to grid sizes being 8 and 64 times larger than the basic grid at a converged cutoff (see Tab. 3.2). The values were obtained using a 3^3 supercell and a k mesh of $7 \cdot 10^3$ kp·atom.

To account for this, we performed the augGrid convergence tests by keeping the well converged cutoffs from Tab. 3.2 fixed.

The influence of the augGrid size on the expansion coefficient α is demonstrated in Fig. 3.5 for two elements with hard, i.e. strongly localized, augmentation charges, Cu and Ag. The example of Cu shows that working with an augGrid 8 times larger than the basicGrid[7] (line L_1 in Fig. 3.5) results in a -24.3% error in α. [Note that we determine the error at a specific augGrid value by the maximum deviation detected before convergence, i.e., in this case the error is given by the second augGrid value ($44 \cdot 10^3$) and not by the first ($28 \cdot 10^3$; line L_1).] Even by making the augGrid 64 times larger than the basicGrid[8] (line L_2 in Fig. 3.5), the error is still 11.3%. In the case of Ag, the larger equilibrium lattice constant yields a larger basicGrid. For this case, an augGrid 64 times larger than the basicGrid reduces the error in γ to -4.4%.

In order to fully reveal the significance of these results for the augGrid convergence, let us return to the above discussed (artificial) correlation with the plane wave cutoff. Consider that we were using the standard coupled procedure for checking convergence, i.e., having the plane wave cutoff (basicGrid) as the only parameter and the augGrid determined automatically. As a consequence, we would find that extremely large cutoffs are necessary to reduce the errors and to obtain reasonable thermodynamic quantities. For instance, to obtain an error $<2\%$, we would need a cutoff >500 eV (in contrast to the converged cutoff of 290 eV) even when using an extra high precision calculation (cf. footnote 8). Since however the computational requirements increase much more rapidly with the size of the basicGrid than with the size of the augGrid, such a convergence test would be in fact not even feasible. It is therefore crucial to realize that actually only the augGrid causes the the slow convergence rather than the basicGrid and that a decoupled treatment makes calculations much more feasible.

The decoupled treatment is however only the first step, since, even if we apply this procedure, a direct calculation of the augGrid convergence rate employing a well converged supercell size for all investigated elements is still computationally very expensive. Using, for instance, a 3^3 supercell would require more than $10,000$ CPU-hours (AMD Opteron with a clock speed of 2.4 GHz). In order to tackle this challenge, we introduce in a second step a scaling procedure, which allows an efficient and accurate determination of the convergence rate. The key idea of this approach is as follows: Let us assume a general physical target quantity, say g, and two convergence parameters c_1 and c_2. We are interested in the convergence rate of g with respect to c_1 at a converged value

---

[7] In VASP [46] (the software package used for the PAW calculations presented in this work), such an augGrid size is achieved for a high precision calculation (flag: PREC=HIGH).

[8] This corresponds in VASP to a high precision calculation with an additional support grid (flag: AD-DGRID=TRUE).
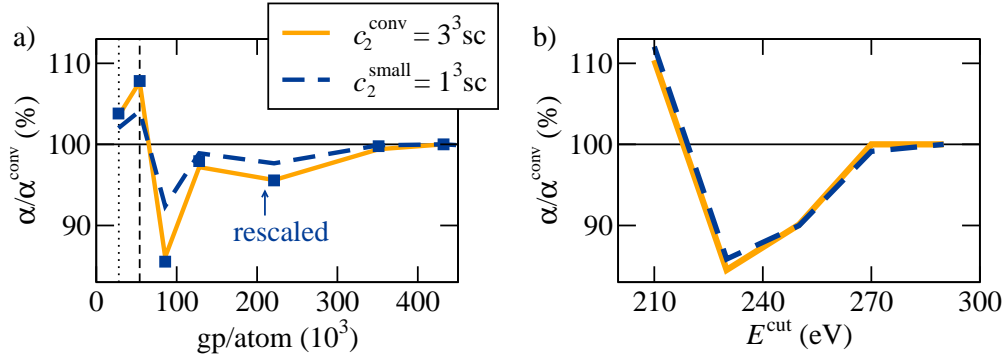
Figure 3.6: Illustration of the supercell size based convergence technique. a) AugGrid convergence of the expansion coefficient α for Ag for the 1^3 and 3^3 supercell (sc). The blue squares show the convergence of the 1^3 sc after rescaling it using Eq. (3.80) with $s = 2$. The dotted (dashed) line indicates $c_1^a = 28 \cdot 10^3$ ($c_1^b = 54 \cdot 10^3$) gp/atom. b) Similar to a), but with the plane wave energy cutoff E^{cut} as the convergence parameter and with a scaling parameter of 1.

of $c_2 = c_2^{\text{conv}}$, i.e. $g(c_1, c_2^{\text{conv}})$. For most cases, computing $g(c_1, c_2^{\text{conv}})$ directly is highly expensive. However, we have found that in many cases the following approximation can be utilized to obtain an accurate description of $g(c_1, c_2^{\text{conv}})$:

$$g(c_1, c_2^{\text{conv}}) \approx g(c_1^a, c_2^{\text{conv}}) + s\,\Delta g, \tag{3.80}$$

$$\Delta g = g(c_1, c_2^{\text{small}}) - g(c_1^a, c_2^{\text{small}}).$$

Here, s is a linear scaling parameter defined as

$$s = \frac{g(c_1^b, c_2^{\text{conv}}) - g(c_1^a, c_2^{\text{conv}})}{g(c_1^b, c_2^{\text{small}}) - g(c_1^a, c_2^{\text{small}})} \tag{3.81}$$

and c_1^a, c_1^b ($c_1^a \neq c_1^b$), and c_2^{small} are fixed (but not fully converged) parameters. The idea is then to study in a first step the convergence of $g(c_1, c_2^{\text{small}})$ in detail. Therefore, c_2^{small} is chosen such as to provide a computationally inexpensive calculation. In a second step, the scaling parameter s is calculated by performing only two (expensive) calculations for c_2^{conv}: $g(c_1^a, c_2^{\text{conv}})$ and $g(c_1^b, c_2^{\text{conv}})$. Based on these data, $g(c_1, c_2^{\text{conv}})$ is approximated by Eq. (3.80).

To be more specific, let us consider g to be the expansion coefficient α, c_1 to be the augGrid size, and c_2 to be the supercell size. Further, c_2^{small} corresponds to a 1^3 and c_2^{conv} to a 3^3 supercell. We set $c_1^a = 28 \cdot 10^3$ gp/atom and $c_1^b = 54 \cdot 10^3$ gp/atom. The resulting scaling parameter is $s \approx 2$, which means that the changes in the convergence dependence of α are two times larger for c_2^{conv} than for c_2^{small}. Using s we can thus extrapolate the changes for c_2^{small} to the ones for c_2^{conv}. As a representative example, Fig. 3.6a shows the results we obtained for Ag. As can be seen, the computed values closely follow the scaling relation according to Eq. (3.80). Thus, to obtain a densely sampled convergence dependence for large supercells only two expensive calculations are needed and a gain in computational efficiency of at least one order of magnitude can be easily achieved. We also studied, how the scaling parameter depends on the chemical species and the supercell size. Our results show a small chemical dependence ($< 10\%$). The supercell size dependence shows a significant scaling parameter but only when increasing a 1^3 to a 2^3 supercell. We further verified that the same approach can be applied to determine the plane wave cutoff convergence of large supercells (Fig. 3.6b). For this case, a scaling parameter generally close to 1 is found. For the k
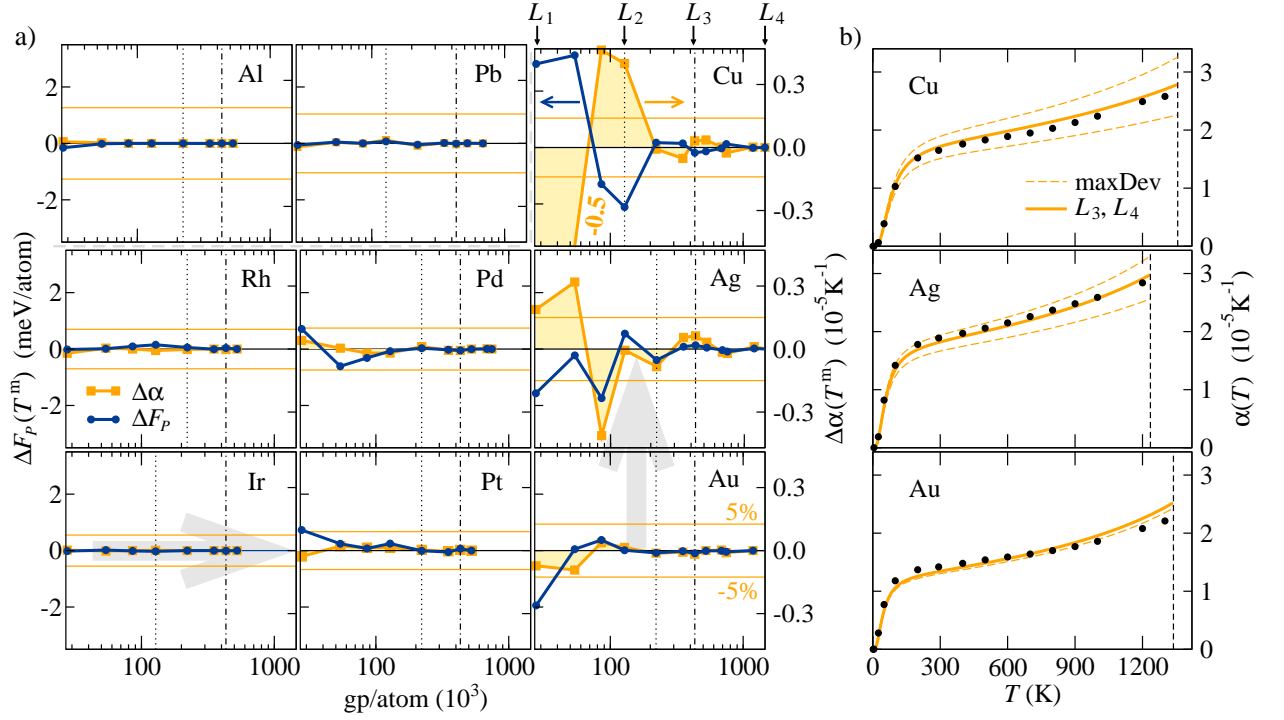
Figure 3.7: Illustration of the influence of the augGrid on thermodynamic properties (GGA). a) AugGrid convergence (logarithmic scale) of the expansion coefficient α and the isobaric free energy F_P for all investigated elements at the melting temperature T^{m}. The presented values, $\Delta\alpha$ and ΔF_P, are referenced with respect to the corresponding quantities with the highest employed augGrid. Line L_1 $[L_2]$ (falls together with the left y-axis [dotted line]) corresponds to an augGrid at a converged cutoff for a standard [extra] high precision calculation (cf. footnote 7 [8]). Line L_3 (dot-dashed line) corresponds to the augGrid size used in the present study (Sec. 4.1). For the noble metals, Cu, Ag, and Au, line L_4 indicates the highest considered augGrid. The orange solid horizontal lines indicate the 5% error for α. The values were obtained using a k mesh of $7 \cdot 10^3$ kp·atom and a 1^3 supercell. The scaling procedure [Eq. (3.80)] was used to rescale the values to correspond to large supercells. The gray arrows emphasize the chemical trend for the size of the error among the transition metals. Al and Pb are separated to distinguish them from the transition metals. b) The temperature dependence of α for the noble metals. The solid lines represent the converged quantities $[L_3$ and L_4 in a)] and the dashed lines correspond to the maximum deviation (maxDev) from a). Note that for the purpose of a convenient representation, the curves corresponding to the mixed approach (Fig. 4.5b) are shown.

sampling, starting from a 1^3 supercell [parameter c_2^{small} in Eq. (3.80)] is not sufficient to guarantee a reasonable approximation, we rather need to apply a 2^3 supercell. The reason is the fact that using a 2^3 supercell guarantees k meshes which are commensurable to the converged 4^3 supercell. The scaling parameter is ≈ 1.

The convergence rate of α and F_P with respect to the augGrid size is summarized in Fig. 3.7a for all studied metals. (For the critical elements, we had in fact to extend the range of the augGrid size to even larger values than shown in Fig. 3.5.) An inspection of Fig. 3.7a shows that the convergence rate correlates inversely with the hardness (localization) of the augmentation charge of the specific element: Among the transition metals, α and F_P converge slower when filling up the d shell and when reducing the atomic radius (indicated by the gray arrows). Thus, Cu, having the hardest augmentation charge, is the most sensitive element in the present study. In contrast, Al and Pb, where only s and p electrons form the chemical bonds, exhibit a relatively low dependence on the augGrid. In Fig. 3.7b, the explicit influence of an unconverged augGrid mesh is shown for the expansion coefficient of the critical elements. We stress here again that such a situation (i.e.,

the uncertainty given by the dashed lines) would occur for a standard high precision calculation (see footnote 7). To avoid the error, we used for the final calculations (Sec. 4.1) the augGrid size of $432 \cdot 10^3$ gp/atom (L_3), which yields a coefficient similar to that originating from the highest augGrid size used in our convergence tests (L_4) (solid lines in Fig. 3.7b).

3.4.2 Error propagation in thermodynamic calculations

A further convergence parameter, which we found to be crucial in predicting thermodynamic properties of metals with very high accuracy, is the k sampling of the electronic dispersion. The difficulties with the k sampling become particularly apparent, if we are interested in calculating $F^{\mathrm{qh,0K}}$ as intended in Sec. 4.1. To obtain $F^{\mathrm{qh,0K}}$, we need to compute the dynamical matrix from an electronic free energy surface corresponding to $T = 0$ K, i.e., the electronic ground state. The associated Fermi-Dirac function shows at this temperature a sharp change at the Fermi energy [μ in Eq. (2.65)], which causes the sums over the **k** vectors [e.g., Eq. (2.87)] to converge extremely slowly. A first necessary step to tackle this difficulty is the replacement of the Fermi-Dirac function by an artificial electron occupation function as given for instance by the Methfessel-Paxton scheme [98]. In this scheme, an artificial temperature T^{art} controlling the electron occupation numbers is introduced. Increasing T^{art} improves the k sampling convergence, but the forces on the atoms still correspond to the (desired) $T = 0$ K electronic ground state. However, to guarantee the latter, one needs to ensure that the artificial electronic entropy term associated with T^{art} does not exceed 1 meV/atom [99]. We thus used the Methfessel-Paxton scheme based on a sufficiently low artificial temperature of $k_{\mathrm{B}}T^{\mathrm{art}} = 0.1$ eV for the convergence checks presented in this section and for the final calculations (Sec. 4.1).

Despite the usage of T^{art}, a careful convergence study of the k sampling is important to assess the introduced error in the final quantities. To account for this aspect, we investigated in detail the convergence behavior for all elements, similarly as for the augmentation grid. Concerning the presentation of the results, we follow however a different route now, in order to reveal an important property of errors in thermodynamic calculations. Let us thus start with discussing the errors in α and F_P at a fixed absolute temperature (400 K; see Fig. 3.8), in contrast to the augGrid where we looked directly at the melting temperature T^{m}, i.e., at a varying absolute temperature (cf. Tab. 4.1). Figure 3.8 reveals the important fact that we have a different group of critical elements than found for the augGrid: Al and Pb exhibit a strikingly worse convergence behavior for α (note the logarithmic scale) as compared to the transition metals. For instance for Al, the convergence of α shows even at the largest considered k mesh ($190 \cdot 10^3$ kp·atom) a significant gradient. For Pb, the smallest considered k sampling $2 \cdot 10^3$ kp·atom yields an error in α as large as -25% ($0.7 \cdot 10^{-5} \mathrm{K}^{-1}$). For the free energy F_P of Al and Pb, we find instead a comparable (or slightly worse) convergence behavior as for the transition metals.

Let us now, in a second step, extend the discussion from $T = 400$ K to $T = T^{\mathrm{m}}$ focusing first on F_P. For that purpose, we use in Fig. 3.9a a different representation of the errors than in Fig. 3.8: For each element, we extract only the (absolute) error in F_P, denoted by F_P^{err}, corresponding to the k sampling marked by the vertical dot-dashed line in Fig. 3.8 (the k samplings actually used in Sec. 4.1). We then plot this error versus the melting temperature T^{m} of the respective element. The result is given by the dashed line in Fig. 3.9a. We see that all elements have a comparable F_P^{err} of ≈ 1 meV/atom in accordance with the conclusion drawn from Fig. 3.8. The similar procedure is applied to obtain F_P^{err} at T^{m} and the result is given by the solid line in Fig. 3.9a. For this temperature, we find a significantly different behavior of F_P^{err}: It increases (in average) strongly with the melting temperature, in fact showing even a linear dependence. As a consequence, the elements with a high melting temperature have likewise a high error in F_P at T^{m}.
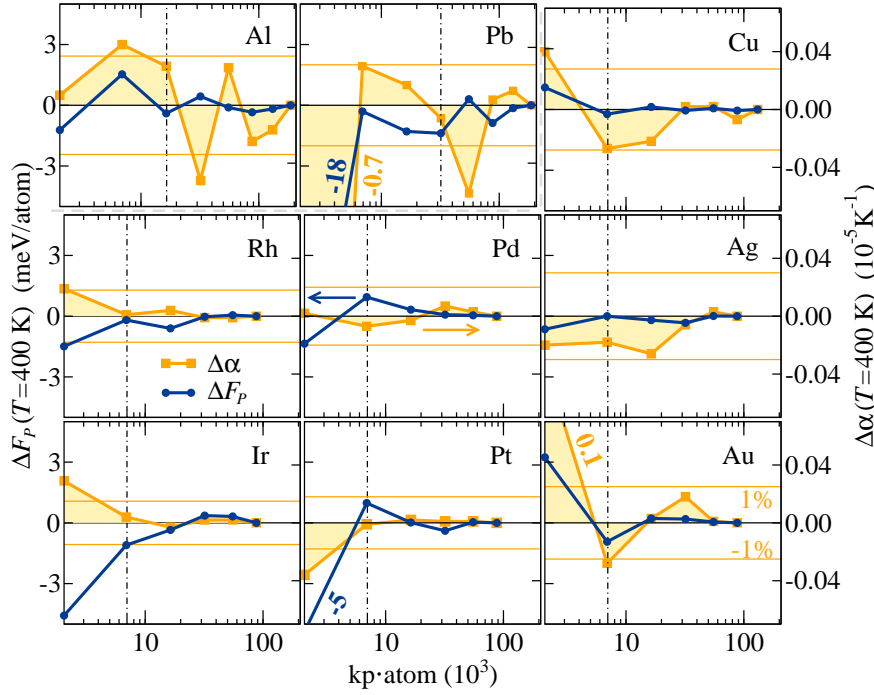
Figure 3.8: k sampling convergence of the expansion coefficient α and the free energy F_P for all studied elements at $T = 400$ K. The x-axis starts at the smallest investigated k mesh of $2 \cdot 10^3$ kp·atom and the vertical dot-dashed line indicates k meshes used for the calculations presented in Sec. 4.1. Additionally, the 1% error of α is shown by the orange solid horizontal lines. The values were obtained using the plane wave cutoffs from Tab. 3.2, an augGrid size of $432 \cdot 10^3$ kp·atom, and a 2^3 supercell.
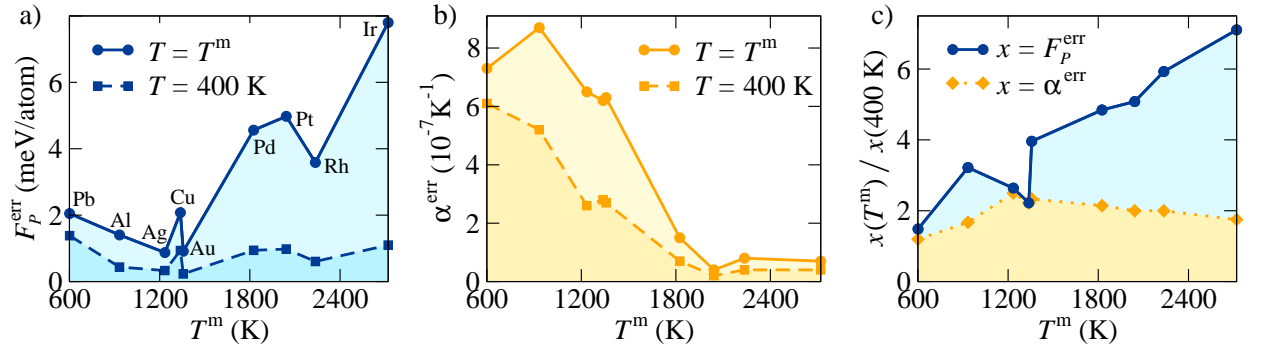
Figure 3.9: Illustration of error propagation in DFT thermodynamic calculations. a) The magnitude of the error in the free energy, F_P^{err} (=largest deviation before convergence), at the k samplings marked with the vertical dot-dashed lines in Fig. 3.8 plotted versus the melting temperature T^{m} of the respective element. The error is obtained at $T = 400$ K (dashed line; corresponding to the values in Fig. 3.8) and at $T = T^{\mathrm{m}}$. b) As a) but for the error in the expansion coefficient α^{err}. c) Ratio of the curves in a) (solid line) and b) (dotted line).
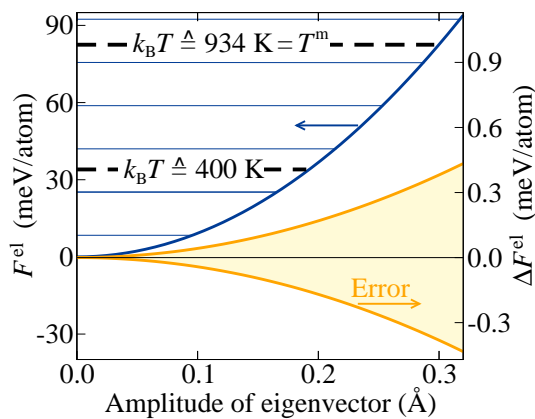

Figure 3.10: Origin of the T dependence of F_P^{err} from Fig. 3.9a. The thick blue solid line shows the electronic free energy F^{el} along the transversal eigenvector at the L point for aluminum (2^3 supercell). The thin blue horizontal lines indicate some of the corresponding phonon energy levels. The thick dashed horizontal lines show the energies corresponding to 400 K and the melting temperature of Al. The orange solid lines show how the difference ΔF^{el} between two F^{el} curves ($7 \cdot 10^3$ and $16 \cdot 10^3$ kp·atom) increases with the displacement (referenced such that, at each T, the mean value of both energies is set to zero). All energies are based on the quasiharmonic approximation.

In order to understand the increase of F_P^{err} with temperature, it is in fact sufficient to consider only a single element and to perform an analysis of its electronic free energy F^{el}. This issue is illustrated in Fig. 3.10 for aluminum. The thick blue solid line shows the electronic free energy along an eigenvector of the dynamical matrix and the horizontal solid lines indicate some of the corresponding phonon energy levels. Further, the thick dashed horizontal lines represent the two temperatures of interest. From Fig. 3.10, it becomes apparent that, with increasing temperature, the spatial extension of the phonon displacements also increases. On the other hand, with increasing spatial displacement, the error in F^{el} increases in a strong non-linear fashion (orange solid lines). Therefore, higher energy/temperature phonons are stronger affected by an error in F^{el} than lower energy ones. This will in turn affect the quasiharmonic free energy – the main contribution to F_P – much stronger at high temperatures than at lower ones.

Let us now return to the discussion of α and analyze how the error in this quantity propagates with temperature. We recall that, based on Fig. 3.8, we have identified Al and Pb as the metals with the slowest convergence rate for α at $T = 400\,\text{K}$. The corresponding error α^{err} is now visualized in Fig. 3.9b (dashed line) using again the alternative representation. Based on the results obtained for F_P^{err} and the knowledge from Sec. 3.3.2 that small changes in F_P (a few meV/atom) can have a significant effect on α, we might expect that the trend for α^{err} changes significantly at T^{m}. In particular, we expect that α^{err} of the high melting metals (Rh, Ir) will increase stronger than for Al and Pb. Figure 3.9b and more clearly Fig. 3.9c show however that this is not the case: The ratio $\alpha^{\text{err}}(T^{\text{m}})/\alpha(400\,\text{K})$ is nearly constant for the various elements, in contrast to the linearly increasing ratio for F_P^{err}. This means that the originally (at 400 K) largest errors for Al and Pb are still the largest at T^{m}.

In order to understand this behavior, we need to carefully analyze the type of the errors assessed in this section and in Sec. 3.3.2: 1) The error F_P^{err} (this section) refers to the difference between two F_P curves (for instance for two k samplings) at some temperature (here, either 400 K or T^{m}) when both curves are set equal at 0 K (absolute free energies are physically not relevant). The important point is that from the knowledge of F_P^{err} alone, we can only conclude that, at some fixed temperature, the two corresponding free energy surfaces $F(V,T)$ are shifted by a constant. We have however no information about the local V and T dependence of the two $F(V,T)$ surfaces. 2) In contrast, the error assessed in Sec. 3.3.2 (in particular, inset of Fig. 3.4) refers directly to differences in the local V and T dependence. To distinguish the two types of errors, let us call 1) a global error and 2) a local error. Next, we need to recall that the expansion coefficient α depends on the local structure of $F(V,T)$ (Sec. 2.4.2). Thus, α (and other thermodynamic properties) will be much stronger affected by a local error in the free energy than by a global one and this explains that the results of this section are in fact not in contradiction to Sec. 3.3.2. Let us summarize this finding schematically by

Global error in $F(V,T)$ Local error in $F(V,T)$

Small effect   Large effect

Derived thermodynamic properties
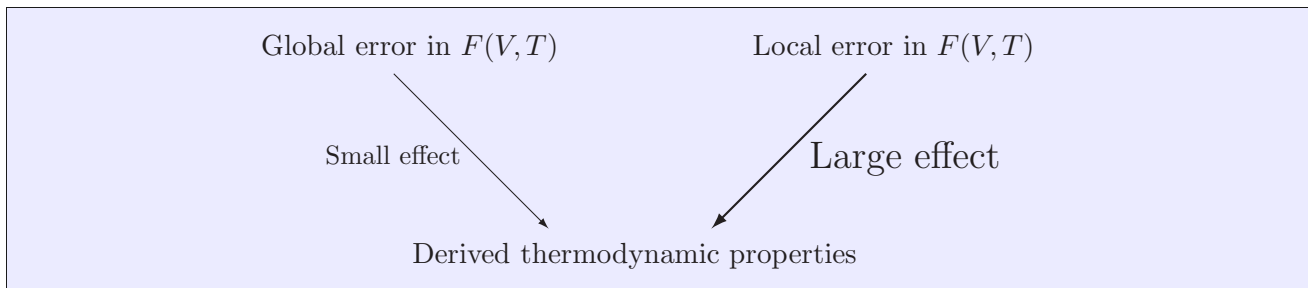
and by the key message: To estimate the error in derived thermodynamic quantities, it is not sufficient to know the magnitude of the error in $F(V,T)$, we also need to know the nature of the latter.
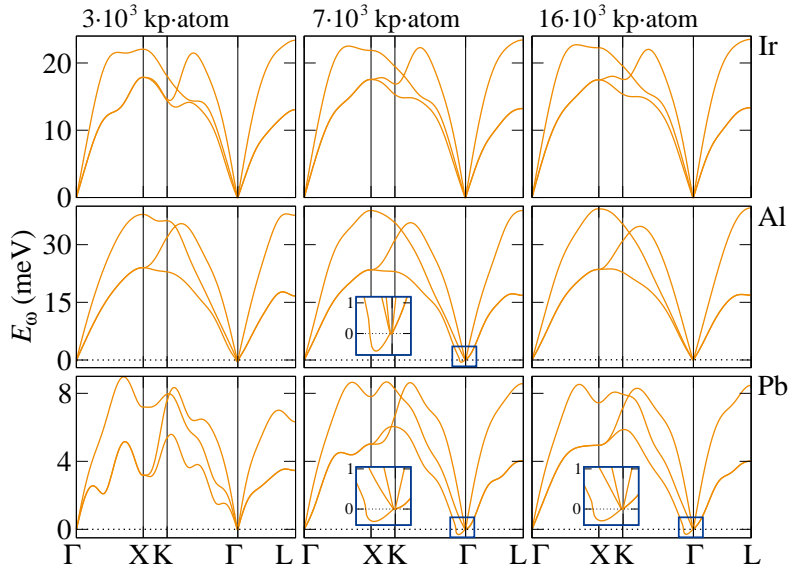
Figure 3.11: k sampling convergence of the phonon dispersion $\omega_{\mathbf{q},s}$ [$E_\omega = h\nu = h\omega/(2\pi)$ with h the Planck constant] along some high symmetry directions for Ir, Al, and Pb for the 4^3 supercell and the GGA functional. The insets enlarge the unphysical phonon instabilities (imaginary frequencies; see text).

3.4.3   The origin of unphysical imaginary frequencies and their treatment

In addition to the study of the convergence of the averaged quantities, α and F_P, discussed in Secs. 3.4.1 and 3.4.2, it is necessary to analyze the convergence of the phonon dispersion $\omega_{\mathbf{q},s}$. This analysis is important for two reasons: 1) The first concerns our interest to evaluate the theoretical phonon dispersion directly and thus the comparison with experiment (Sec. 4.1.3). If we, knew that α and F_P are well converged, we could not directly conclude that this applies similarly to $\omega_{\mathbf{q},s}$, since errors in the latter might cancel in average [Eq. (2.226)] and thus not be visible in α and F_P. 2) The second reason is the convergence rate for α and F_P. Suppose that we found it to be very slow and that, as a consequence, we needed to employ computationally expensive convergence parameters to obtain a good accuracy. However, this slow convergence rate might be caused by only a small fraction of the phonon frequencies (for instance imaginary frequencies introduced below) and a careful analysis and treatment might allow to use computationally less expensive parameters.

With these aspects in mind, we calculated the convergence behavior of $\omega_{\mathbf{q},s}$ for all parameters and studied elements. Let us first focus on the k sampling and further on three representative cases shown in Fig. 3.11 for a detailed discussion. Among the transition metals, the dispersion of Ir shows the slowest convergence. Nevertheless, the convergence is still rapid and no qualitative changes are observed. In contrast to all transition metals, the convergence of Al and Pb is more complex: For some k meshes an anomalous behavior appears in the vicinity of the Γ point (indicated by the squares in Fig. 3.11). In these regions, the phonon frequencies are imaginary. (For convenience, the imaginary frequencies are shown as negative frequencies in Fig. 3.11.) In principle, the presence of imaginary frequencies indicates that the structure is unstable against deformations along the associated phonon wave vector. Put differently, this means that the structure corresponds to a saddle point on the electronic free energy surface rather than to a minimum. The imaginary frequencies found for some k samplings are, however, not related to a genuine structural instability, but are unphysical and caused by not fully converged parameters. In the case of Al, the instability occurring at $7 \cdot 10^3$ kp·atom can be removed by enlarging the k sampling to $16 \cdot 10^3$ kp·atom. For Pb, the instability is more persistent and occurs even for large samplings ($16 \cdot 10^3$ kp·atom). To ensure that the instability is not caused by a too small k sampling, we further increased the k sampling ($55 \cdot 10^3$ kp·atom; not shown in Fig. 3.11), but found no changes in the phonon dispersion.

In order to show that the instability of Pb is indeed fictitious, the remaining critical convergence
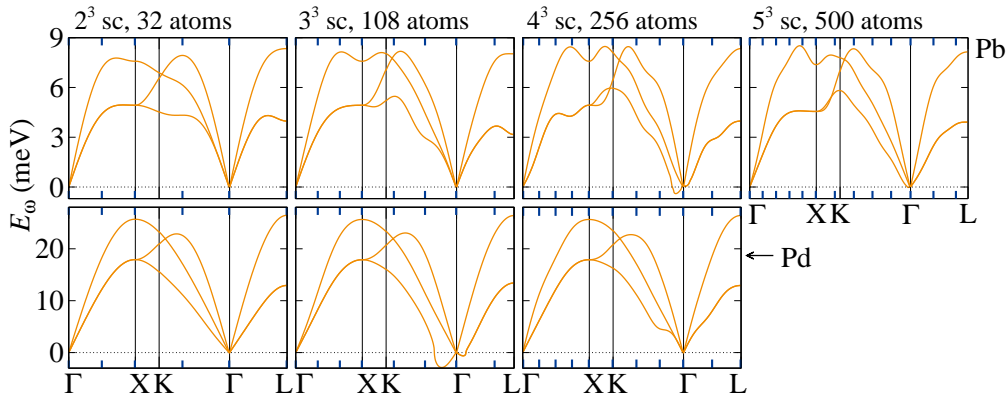
Figure 3.12: Supercell (sc) size convergence of the phonon dispersion for Pb and Pd. The k mesh size was $32 \cdot 10^3$ kp·atom for the 5^3 supercell of Pb and $7 \cdot 10^3$ kp·atom for the other supercells (Pb and Pd). Exact wave vectors $\mathbf{G}^{sc}$ are marked by dark blue ticks.

parameter, the supercell size, needs to be considered. To this end, we calculated the dependence of the phonon dispersion on the supercell size for the various elements. The dispersion of Pb is by far the most sensitive in this respect. In fact, while a 4^3 supercell was sufficient to obtain convergence for the other elements, we had to extend the investigations to a 5^3 supercell (500 atoms) for Pb. Figure 3.12 illustrates the dependence of the Pb dispersion on the supercell size. There are no phonon instabilities for a 2^3 and 3^3 supercell. Increasing the size to 4^3, an instability occurs in the vicinity of the Γ point in the direction Γ to K. This is the supercell size that was employed for the above discussed k sampling convergence. One can now see that increasing the supercell size further to 5^3 almost completely removes the imaginary frequencies. We expect a complete disappearance of the imaginary frequencies when going to even larger supercells, since previous calculations based on the linear response method [100] and experiment [101] report no instability.

Let us discuss a second illustrative example for the influence of the supercell size: the phonon dispersion of Pd shown in Fig. 3.12. We find that, except for the vicinity of the Γ point, the dispersion of all supercells shows a very smooth sinusoidal and thus simple dependence along the wave vector as found for elements in which the nearest neighbor interactions dominate (cf. the discussion for Cu, Ag, and Au in Sec. 4.1.3). In fact, due to the overall "well-behaved" phonon dispersion without any instabilities found for the 2^3 supercell, one might be easily mislead and consider this supercell size as the converged one. (Note that this dispersion is different from the one for Pb for the same cell size, since the latter shows already departures from the simple dependence and the influence of longer ranged interactions.) However, increasing the supercell size to 3^3, a small instability occurs in the vicinity of the Γ point along the L direction and a larger one along the K direction. The instability disappears again for the 4^3 supercell.

A closer inspection of this feature reveals that there is an intricate interplay between the sampling of the phonon Brillouin zone and the occurrence of anomalies in the phonon dispersion as a consequence of long range interactions. To explain this we need to recall the procedure (and its limits) used to obtain a dense phonon dispersion along the high symmetry directions. Originally, phonon frequencies are only available at the N_n (=number of atoms) exact wave vectors which are fully captured by the used supercell (denoted $\mathbf{G}^{sc}$ in Sec. 2.3). Since using only the $\mathbf{G}^{sc}$ vectors would yield a very coarse sampling for reasonable supercell sizes (cf. the dark blue ticks in Fig. 3.12), we introduced in Sec. 2.4.1 the Fourier interpolation scheme which allows to obtain an arbitrarily dense sampling. The important point now is the fact that the Fourier interpolation
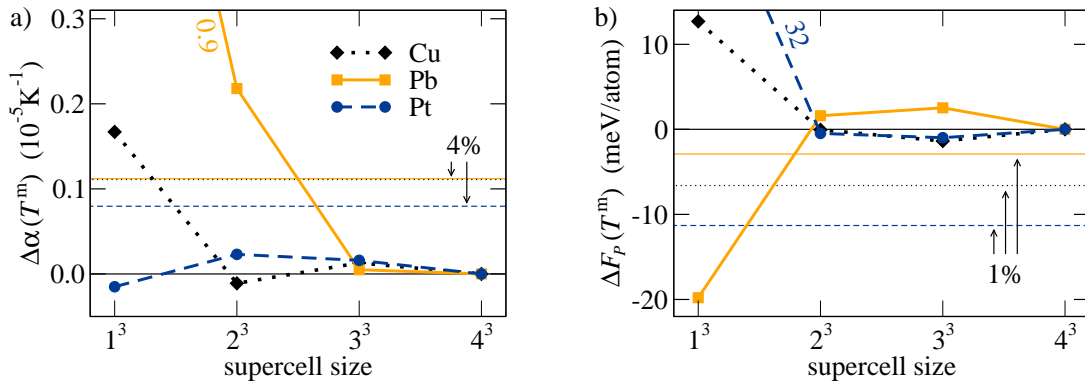
Figure 3.13: Supercell size convergence of the expansion coefficient α and the isobaric free energy F_P for Cu, Pb, and Pd at the melting temperature T^{m}. The shown values, $\Delta\alpha$ and ΔF_P, are referenced with respect to the 4^3 supercell. The used k-point and augGrid mesh were consistently for all supercell sizes $7 \cdot 10^3$ kp·atom and $432 \cdot 10^3$ gp/atom, respectively.

corresponds to a sinus-like basis and that the number of basis functions actually included in the interpolation is determined by the number of available $\mathbf{G}^{\mathrm{sc}}$ vectors, i.e., with increasing supercell size also the number of basis functions increases. If only small supercell sizes are accessible the Fourier interpolation is therefore best suited for describing sinusoidally shaped dispersions as found, for instance, for the 2^3 supercell of Pd. The "true" phonon dispersion of Pd shows however strong deviations from this simple dependence in the vicinity of the Γ point along the K direction. The reason is an experimentally verified [101] anomaly, which will be discussed in more detail in Sec. 4.1.3 (cf. Fig. 4.3). Based on this discussion, we can explain the observed dependence of the Pd phonon dispersion on the supercell size (Fig. 3.12) as follows: For the 2^3 supercell, the number of included Fourier basis functions is so small that none of them matches the highly oscillatory dependence (along the wave vector) which is needed to describe the sharp changes of the anomaly. Put differently, all basis functions available in the 2^3 supercell are orthogonal to each of the basis functions which would be necessary to describe the shape of the anomaly. The situation changes for the 3^3 supercell, where one (fast oscillating) basis function, which is captured by the supercell, is also needed to describe the anomaly. Since this is however only a single basis function it cannot reproduce the anomaly properly. In fact, it strongly overshoots the dependence causing the observed "dip" with imaginary frequencies. For the 4^3 supercell, further basis functions with a yet faster oscillatory dependence are included and they are able to improve the description of the anomaly significantly even removing the imaginary frequencies.

The occurrence of imaginary frequencies due to insufficient convergence requires special care when calculating thermodynamic quantities. A possible approach would be to calculate the thermodynamic quantities exclusively for highly converged parameters, for which the unphysical instabilities are fully absent. However, even in the presence of these instabilities sufficiently converged thermodynamic quantities can be obtained by neglecting all imaginary frequencies when calculating the quasiharmonic free energy according to Eq. (2.226). We found this choice/approximation to have little effect on the free energy and derived quantities in most cases, since the phase space around the Γ point is negligible compared to the full Brillouin zone. An example of how well this approach works is given in Fig. 3.13, where the convergence of α and F_P for Cu, Pb, and Pd is shown. Pb and Pd, for which imaginary frequencies are present (for the 4^3 and 3^3 supercell, respectively), show a similarly good convergence behavior as Cu without such frequencies, thus indicating that the neglect of unphysical imaginary frequencies is a reasonable approximation.

Table 3.2: Details for the PAW calculations of $F^{\mathrm{qh},0\mathrm{K}}$; E^{cut} is the plane wave cutoff, "augGrid" the augmentation grid in grid points (gp) per atom, and $\mathbf{D}$ the dynamical matrix; see also text.

	Pb	Al	Cu	Ag	Pd	Rh	Au	Pt	Ir
supercell	5^3				4^3				
atoms	500				256				
E^{cut} (eV)	150	250	290		270			250	
augGrid (10^3 gp/atom)					432				
k density (10^3 kp·atom)	32	16			7				
k mesh for supercell	4^3	4^3			3^3				
electron occupation				Methfessel-Paxton, 0.1 eV					
displacement for $\mathbf{D}$				0.01 a_0					
q mesh for primitive BZ				16^3					

3.4.4   Computational details

3.4.4.1   Details for Sec. 4.1, Systematic study

For the LAPW+lo reference calculations (Sec. 4.1.2), we used the WIEN2K code [102]. The muffin tin (mt) radius[9] R^{mt} $[= \sqrt[3]{3\Omega_I/(4\pi)}]$ was held constant when varying the volume of the crystal V. For each element, R^{mt} was adjusted such that the spheres were nearly touching at the smallest V. The resulting sphere radii are ranging from $2.3\,a_0$ to $2.5\,a_0$. A 24^3 k mesh ($= 6 \cdot 10^3$ kp·atom) was used for Al, a 20^3 k mesh ($= 8 \cdot 10^3$ kp·atom) for Pb, and an 18^3 k mesh ($= 14 \cdot 10^3$ kp·atom) for the other elements. The product $R^{\mathrm{mt}}K^{\mathrm{max}}$ was set to 10, where K^{max} ($= \sqrt{2m_e E^{\mathrm{cut}}/\hbar^2}$) corresponds to the magnitude of the largest reciprocal electronic wave vector. [In LAPW+lo calculations, it is more convenient to specify $R^{\mathrm{mt}}K^{\mathrm{max}}$ rather than K^{max} (or E^{cut}) as a consequence of the matching condition between plane waves and atomic orbitals at the sphere surface [49].] The maximum ℓ^{max} value for the waves inside the atomic spheres [similar to the number of expansion coefficients in Eq. (2.96) within the PAW method] was set to $\ell^{\mathrm{max}} = 12$. The WIEN2K code employs an additional plane wave cutoff G^{max} for the Fourier expansion of the charge density, which we set to $G^{\mathrm{max}} = 14\,a_0^{-1}$. Relativistic effects were included fully within the atomic spheres and using the scalar relativistic approximation in the valence region.

The PAW calculations were performed using the VASP [46] code and the potentials provided with this package [53]. To calculate $F_0^{\mathrm{el}}(T)$, we used the finite temperature formulation of DFT [26] (cf. Sec. 2.1.4). The electronic dispersion was sampled using the Monkhorst-Pack scheme [103] and a k mesh of 32^3 ($= 33 \cdot 10^3$ kp·atom). The details for the calculations of $F^{\mathrm{qh},0\mathrm{K}}$ are compiled in Tab. 3.2. The convergence issues of the DFT related parameters have been discussed in Secs. 3.4.1 to 3.4.3. For the calculation of the dynamical matrix, we used the direct force constant method (cf. Sec. 2.3.4). We studied displacements (for the finite difference of the forces) in the range of $0.0005\,a_0$ to $0.1\,a_0$ for all elements. We find, in general, that the thermodynamic properties are rather insensitive (examples given in Fig. 3.14) with respect to a variation in the displacement. In

---

[9]We use the notation customary in the corresponding literature (e.g., Ref. [49]) and give in brackets reference to our notation from Secs. 2.1.7 and 2.1.8.
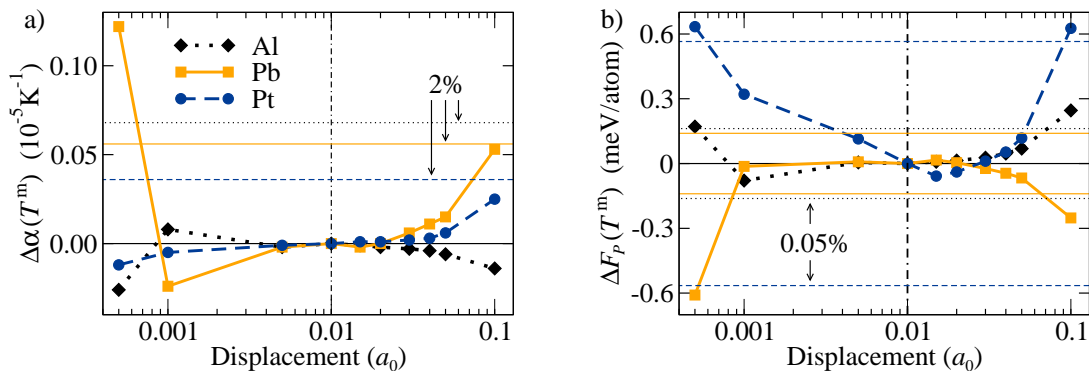
Figure 3.14: Dependence of a) the expansion coefficient α and b) the isobaric free energy F_P on the displacement used to calculate the dynamical matrix (a_0 =Bohr radius) for Al, Pb, and Pd at the respective melting temperature T^{m}. The shown values, $\Delta\alpha$ and ΔF_P, are referenced with respect to α and F_P at 0.01 a_0 (marked by the vertical dot-dashed line) and the horizontal lines mark the relative values with respect to these quantities. A k sampling of $7 \cdot 10^3$ kp·atom and a 1^3 supercell size were used for the calculation.

particular, we observe a plateau in the region close to 0.01 a_0 which indicates the harmonic region, while at smaller and larger values numerical noise and anharmonic effects, respectively, become visible (departure from the constant dependence). Therefore, a value of 0.01 a_0 was employed for the calculations in Sec. 4.1. For the sampling of the phonon dispersion, we used likewise the Monkhorst-Pack scheme [103] and a well converged q mesh of 16^3.

3.4.4.2 Details for Secs. 4.2 and 4.3.5, Temperature dependent dynamical matrix

In order to simulate the T dependence of the dynamical matrix, the artificial electron occupation function (Methfessel-Paxton scheme) was replaced by the physical Fermi-Dirac distribution. The associated difficulty is that, predominantly at lower temperatures, the k sampling convergence becomes significantly worse. We therefore investigated even larger k samplings (up to $187 \cdot 10^3$ kp·atom for Al and up to $131 \cdot 10^3$ kp·atom for Rh) than in Sec. 3.4.2. The results for the target quantity, C_P, are summarized in Fig. 3.15. For Rh, we obtain a reasonable convergence, whereas for Al (light blue solid lines) we have a remaining scatter even though utilizing denser samplings. In principle, the resulting accuracy for the C_P contribution in Al would be sufficient for most purposes, since the uncertainty of $\pm 0.1 k_{\mathrm{B}}$ ($\pm 2.6\%$ of the full heat capacity) is rather small. In Sec. 4.3, we will however reveal that the contributions due to other excitation mechanisms are similarly small and it would be therefore desirable to narrow the uncertainty in this contribution further.

For that purpose, we studied the influence of the T dependent dynamical matrix using also the linear response method (a complementary method to the direct forces constant method) as implemented in the ABINIT code [104–107]. To utilize the ABINIT code we replaced the PAW description of the core electrons by the pseudopotential description employing exactly the same pseudopotential as in Sec. 4.3. See therefore the discussion in the following subsection. We calculated phonons (and eigenvectors) at wave vectors corresponding to a 2^3 supercell and Fourier transformed this mesh into its real space representation. Using Eq. (2.223), the real space representation was back transformed onto a dense (16^3) mesh in reciprocal space. We find that a faster convergence rate is obtained with the linear response method (dark blue solid lines in Fig. 3.15; note the smaller k meshes), which allowed us to estimate slightly lower bounds for the thermodynamic properties of Al (see Tab. 4.3). All details regarding the final calculations of the T dependent dynamical matrix (presented in Secs. 4.2 and 4.3.5) are compiled in Tab. 3.3.
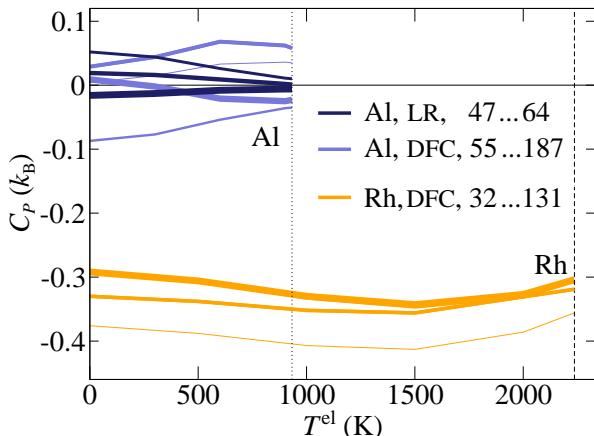
Figure 3.15: k sampling convergence of the C_P contribution due to a T dependent dynamical matrix for Rh and Al at the respective melting temperature. The representation is equivalent to Fig. 4.10a, but referenced here with respect to the consistently calculated heat capacity $C_P(T = T^{\mathrm{m}})$ for a convenient visualization of the results for both elements. "DFC" denotes direct force constant method (PAW calculations) and "LR" linear response (the latter only for Al and utilizing pseudopotentials). The numbers in the legend give the range of investigated k samplings in 10^3 kp·atom. The thickness of the lines increases with increasing k sampling. The vertical lines denote the melting temperatures of the elements.

Table 3.3: Parameters for the calculations of the influence of the T dependent dynamical matrix presented in Sec. 4.2 (Rh) and in Sec. 4.3.5 (Al). "pp", "DFC", and "LR" denote the pseudopotential, the direct force constant, and the linear response method, respectively. See text and Tab. 3.2 for further details (e.g., units of augGrid and k sampling).

	code	core	**D** method	supercell	E^{cut} (eV)	augGrid	k density	q mesh
Rh	VASP	PAW	DFC ($0.01\,a_0$)	2^3	270	$432 \cdot 10^3$	$131 \cdot 10^3$	16^3
Al	ABINIT	pp	LR	$\widehat{=}2^3$	191 (14 Ry)	—	$64 \cdot 10^3$	16^3

3.4.4.3 Details for Sec. 4.3, Anharmonicity and vacancies

The calculations of the full excitation spectrum of aluminum, presented in Sec. 4.3, were performed using the norm-conserving pseudopotential formalism. We were able to construct[10] accurate pseudopotentials reproducing well the PAW results at a lower converged cutoff: 191 eV (14 Ry) vs. 250 eV (18 Ry). The actual quality of our pseudopotentials will be assessed in Sec. 4.3.2 using the PAW based thermodynamic results from Sec. 4.1 as a reference. Besides speeding up the calculations due to the lower cutoff, the pseudopotential formalism allowed us to utilize the S/PHI/NX code [80], which has various features implemented supporting anharmonicity calculations (see Secs. 2.3.5 and 2.3.6). Details regarding the pseudopotential calculations of the various free energy contributions are listed in Tab. 3.4. In the following, we discuss briefly the most important technical aspects.

For the quasiharmonic contribution of the perfect crystal $F^{\mathrm{p,qh}}$, we employed the linear response method (using the ABINIT code and identical pseudopotentials as for S/PHI/NX) as described in the previous subsection, in order to profit from the faster k sampling convergence. This method allowed us also to calculate frequencies on a q mesh corresponding to a 4^3 supercell, while still employing high k samplings (for the electronic dispersion). Further, we used a rather high cutoff for $F^{\mathrm{p,qh}}$, to provide a well defined reference for the anharmonic contribution $F^{\mathrm{p,clas,ah}}$. This turned out to be important due to the small magnitude of the latter. For the calculation of $F^{\mathrm{p,clas,ah}}$ itself, we employed the UP-TILD method as discussed in Sec. 3.2. The necessary Langevin dynamics

---

[10]We generated the Al pseudopotentials using the FHI98PP code [56] and the Hamann construction scheme [108]. The $3s$ and $3p$ electrons were treated as valence electrons. Cutoff radii of 1.25 and 1.40 Bohr radius were used for the s and d components of the GGA pseudopotential. The remaining p component and all the components of the LDA pseudopotential were constructed using the default cutoff radii of FHI98PP. The d component was used as a local orbital.

Table 3.4: The used plane wave cutoffs E^{cut}, k densities, and some further information for the pseudopotential (pp) calculations of the free energy contributions entering Eqs. (4.9) to (4.11). Note that $F_0^{\mathrm{p,el}}$ and $F_0^{\mathrm{v,el}}$ have been separated according to Eq. (3.53). Example k meshes corresponding to a one atom unit cell (k mesh 1 atom) are also given. Further: ζ=friction parameter, dt=time step; see also text for details.

		code		sc	E^{cut} (Ry)	k mesh (kp·atom)	k density 1 atom	comments
perfect	$E_{g,0}^{\mathrm{p,el}}$	ABINIT	identical pp	—	14	$186,624$	57^3	
	$\widetilde{F}_0^{\mathrm{p,el}}$	ABINIT		—	14	$3,014,284$	144^3	
	$F^{\mathrm{p,qh}}$	ABINIT		4^3	34	$46,656$	36^3	linear response
	$F^{\mathrm{p,clas,ah}}$	S/PHI/NX		2^3	14	$2,048$	13^3	λ=0.5, ζ=0.01, dt=10 fs
vacancy	$E_{g,0}^{\mathrm{v,el}}$	ABINIT	identical pp	3^3	14	$186,624$	57^3	
	$\widetilde{F}_0^{\mathrm{v,el}}$	ABINIT		2^3	14	$186,624$	57^3	
	$F^{\mathrm{v,qh}}$	S/PHI/NX		2^3	14	$6,912$	19^3	direct force const., $\pm 0.01\, a_0$
	$F^{\mathrm{v,clas,ah}}$	S/PHI/NX		2^3	14	$2,048$	13^3	λ=0.5, ζ=0.01, dt=10 fs

simulations were performed using a corresponding implementation in S/PHI/NX [81]. We used a friction parameter $\zeta = 0.01$ and a time step $dt = 10$ fs for the MD simulations. The number of MD steps was adjusted to the specific volume, temperature, and supercell size, such as to achieve a statistical error of less than 1 meV/atom. Our largest simulations consisted of $\approx 10\,000$ MD steps. For investigating the convergence behavior of $F^{\mathrm{p,clas,ah}}$ with respect to the plane wave cutoff and k mesh, we applied the hierarchical UP-TILD method as discussed in Sec. 3.2.4. We performed the convergence checks for a set of selected volumes and, in particular, high temperatures (i.e., close to the melting point), which is important to achieve a high accuracy. The corresponding atomic configurations represent the most distorted structures, which in turn are the most sensitive with respect to the convergence parameters. As for the volume, at least two points have to be investigated to obtain the influence on the thermodynamic properties. Based on these considerations, we find that a cutoff of 14 Ry and a k sampling of $2,048$ kp·atom are sufficient. It is interesting to compare these values to the converged parameters for the quasiharmonic contribution (34 Ry and $46,656$ kp·atom; see Tab. 3.4): The anharmonic contribution converges considerably faster than the quasiharmonic one. The reason is that the anharmonic contribution is based directly on the energy, whereas the quasiharmonic one relates to the second derivative in the potential energy surface.

We investigated the λ dependence [Eq. (2.195)] in detail for the perfect bulk and vacancy calculations by studying λ values at extreme conditions, such as temperatures close to the melting point, sufficiently large volumes, and λ values close to 0 and 1. Specifically, we computed a dense set of λ values at 900 K, for a small and a large volume for both the perfect bulk and the vacancy cell. The results, shown in Fig. 3.16a, reveal that the perfect bulk and the vacancy cell show nearly the same λ dependencies. Moreover, we see, even at this high temperature, only negligible deviations from linearity for the smaller volume. For the larger volume, deviations are found for λ values close to 0 and 1, which partially compensate each other. The consequence of the increase in the number of λ values in the integration in Eq. (2.195) is shown in Fig. 3.16b. For the larger volume, the free energy obtained from an integration based on the dense λ sampling (λ set2 in Fig. 3.16b) is 0.9 meV/atom higher than one based on $\lambda = 0.5$ only. Since the free energy at the smaller volume does not change upon inclusion of more λ values, we observe in total a small positive shift in the
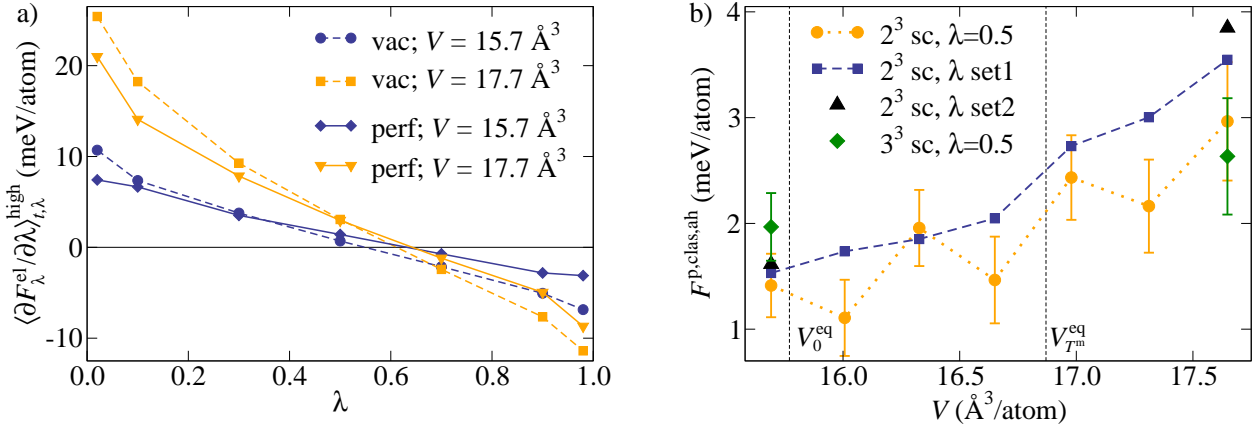
Figure 3.16: Results for the convergence tests of the anharmonic contribution in aluminum. a) λ dependence of the ensemble average $\langle \partial F_\lambda^{\mathrm{el}}/\partial\lambda \rangle_{t,\lambda}^{\mathrm{high}}$ for the perfect (perf) and vacancy (vac) supercell for a small and a large volume each. The results were obtained for a 2^3 supercell, the LDA-functional, and a temperature of 900 K. The statistical error $\sigma^{\mathrm{err}} \approx 0.5$ meV/atom, Eq. (2.202), is of a similar size as the symbols indicating the calculated values. The solid and dashed lines are guides to the eye. b) Explicitly anharmonic free energy $F^{\mathrm{p,clas,ah}}$ at 900 K for the LDA functional. Results for the 2^3 and 3^3 supercell (sc) and for three different λ samplings, $\lambda = 0.5$, λ set1= $\{0.1, 0.3, 0.5, 0.7, 0.9\}$, and λ set2=set1+$\{0.02, 0.98\}$, used for the integration in Eq. (2.195), are shown. The symbols represent the calculated values, the corresponding vertical lines show the statistical error, and the dashed and dotted lines in-between are a guide for the eye. The vertical black dashed lines indicate the 0 K (including zero-point vibrations) and the melting temperature equilibrium volumes of LDA, V_0^{eq} and $V_{T^{\mathrm{m}}}^{\mathrm{eq}}$, respectively.

slope of the $F^{\mathrm{p,clas,ah}}(V)$ curve. This shift decreases α by -1.6% and C_P by -0.6% (cf. footnote 4 on page 77). These changes are opposite to the changes (2.1% for α and 0.8% for C_P) caused by the negative shift of the slope of $F^{\mathrm{p,clas,ah}}(V)$, which occurs when the supercell size is increased from 2^3 to 3^3 (see Fig. 3.16b). For the calculations in Sec. 4.3, we used the 2^3 supercell at $\lambda = 0.5$.

The influence of the vacancies was taken into account using the volume optimized approach (Sec. 3.1). To calculate $\widetilde{F}_0^{\mathrm{v,el}}$, we employed a 2^3 supercell using the same volumes, temperatures, and parametrization as for $\widetilde{F}_0^{\mathrm{p,el}}$. (Note that the details regarding the parametrization of the various free energy contributions have been discussed in Sec. 3.3.) As for the k sampling, we investigated three meshes: 14^3 ($87,808$ kp·atom), 16^3 ($131,072$ kp·atom), and 18^3 ($186,624$ kp·atom). We find that the electronic term yields negligible (cf. footnote 5 on page 78) contribution to α and C_P for all k meshes. To calculate $F^{\mathrm{v,qh}}$, we used the direct force constant method using a positive and negative displacement of ± 0.01 Bohr radius to obtain the Hellmann-Feynman forces. We investigated a 2^3 supercell with two different k meshes, 5^3 ($= 4,000$ kp·atom) and 6^3 ($= 6,912$ kp·atom), and a 3^3 supercell with a 3^3 k mesh ($= 2,916$ kp·atom). We find negligible differences between all three calculations for α and C_P. Note that, as discussed in Sec. 3.3.3, the calculation of the quasiharmonic free energy contributions, $F^{\mathrm{p,qh}}$ and $F^{\mathrm{v,qh}}$, requires special attention to ensure a consistent treatment of the vacancy supercell with the corresponding bulk part. To account for this, we employed the correction scheme Eq. (3.62) for the supercell and Eq. (3.63) for the plane wave cutoff. The anharmonic free energy of the vacancy supercell $F^{\mathrm{v,clas,ah}}$ was treated in exactly the same manner as the perfect crystal counterpart. In particular, we ensured the applicability of the UP-TILD procedure to the vacancy cell by calculating two free energy points at 900 K for different volumes directly. Further, we tested the supercell size convergence by increasing the supercell from 2^3 to 3^3 and found also here only negligible effects.

3.4.4.4 Details for Sec. 4.4, Quantum mechanical anharmonicity

The quantum mechanical phonon shift of aluminum (third and fourth order) was investigated for the longitudinal phonon branch at the L point in a 2^3 supercell. We further fixed the volume to $a^{\mathrm{lat}} = 4.054$ Å (low temperature equilibrium lattice constant). The tensors were calculated as derivatives from the $T = 0$ K electronic potential energy surface. For the third order shift, we calculated the real space tensor using the finite difference method (displacement 0.01 Bohr radius) for the Hellmann-Feynman forces (cf. Sec. 2.3.7). We implemented a search routine to determine all symmetry equivalent pairs of displacements and reduced the actual Kohn-Sham calculations to the irreducible part of the tensor (reduction $\approx 10^5 \rightarrow 10^3$). We then Fourier transformed the real space tensor using the phonon basis as determined from the (quasi)harmonic calculations for aluminum presented in Sec. 4.1. The phonon shift was eventually calculated from the expressions derived in Ref. [68] using the operator renormalization method [cf. also Eq. (2.214)]. In our calculations, we did not experience difficulties with divergences so that we could set the generic infinitesimal parameter for determining the principle value [γ in Eq. (2.219)] to 0. The fourth order term was treated directly in reciprocal space by performing the finite difference in the phonon basis (using energies rather than forces). The used DFT related parameters were: LDA, PAW method, $E^{\mathrm{cut}} = 250$ eV, $131 \cdot 10^3$ kp·atom, Methfessel-Paxton [98] occupation with 0.1 eV. For the critical parameter, the k sampling, we investigated three different meshes 12^3 ($= 55 \cdot 10^3$ kp·atom), 14^3 ($= 88 \cdot 10^3$ kp·atom), and 16^3 ($= 131 \cdot 10^3$ kp·atom) for the fourth order tensor, which is the more sensitive one being a higher order derivative. We find a variation in the fourth order shift of only 0.2 meV at the melting temperature among these k meshes (cf. Fig. 4.18).

Chapter 4

Results: Selected topics

In this chapter, the key results of the thesis are discussed:

- Section 4.1 presents a systematic study of the two dominating free energy contributions, F_0^{el} and $F^{\mathrm{qh,0K}}$, for the full range of fcc metals and for an extensive set of thermodynamic quantities. Based on the highly converged DFT results (Sec. 3.4), we are able to address the quality of two popular xc functionals (cf. Sec. 2.1.6) in predicting thermodynamic properties.

- For two representative elements, Rh and Al, we extend in Sec. 4.2 the quasiharmonic description to the T dependent dynamical matrix formalism. The corresponding phonon shift, its influence on $F^{\mathrm{qh,0K}} \to F^{\mathrm{qh}}$, and on derived thermodynamic properties are investigated.

- For Al, the set of physical excitation mechanisms is further extended (Sec. 4.3) by including the *classical* anharmonic and vacancy contribution, which becomes feasible by employing our new point defect formalism (Sec. 3.1) and the UP-TILD method (Sec. 3.2). With these calculations, we are able to tackle a long standing debate about the dominating contributions beyond the quasiharmonic approximation to the high temperature heat capacity of aluminum.

- In Sec. 4.4, the anharmonic contribution in aluminum is investigated using a complementary method: *quantum mechanical* perturbation theory. This approach allows to validate the classical results of Sec. 4.3 at low temperatures.

- Finally (Sec. 4.5), the highly accurate DFT results for aluminum are used as a reference to evaluate the quality of three state-of-the-art EAM parametrizations in predicting thermodynamic properties. We investigate the question whether the hierarchy found in the complexity of the construction procedures of the EAM potentials correlates with their predictive power.

4.1 Assessing DFT accuracy in predicting thermodynamic properties of metals

4.1.1 Motivation

Throughout Sec. 4.1, we focus on the dominant free energy contributions which are given by Eqs. (2.184) and (3.53):

$$F(V,T) = F_0^{\mathrm{el}}(V,T) + F^{\mathrm{qh,0K}}(V,T) = E_{g,0}^{\mathrm{el}}(V) + \widetilde{F}_0^{\mathrm{el}}(V,T) + E^{\mathrm{zp,0K}}(V) + TS^{\mathrm{qh,0K}}(V). \quad (4.1)$$

This free energy expression includes the quasiharmonic approximation, Eq. (2.133), and the $\mathbf{D}^{0K}$ approximation, Eq. (2.179). In order to classify the corresponding calculations correctly, we need to comment on two important issues with respect to previous studies:

Figure 4.1: Part of the periodic table showing in gray the investigated elements. In each field the upper left number gives the atomic mass in atomic units. Below the electron configuration, the atomic number and symbol, and the element name are shown. The values are from Ref. [113]. For the investigated elements, the melting point in Kelvin is additionally given (bold number in upper right corner; Ref. [14]).

1) The $\mathbf{D}^{0K}$ approximation is not an approximation which is only performed in the present work. It has been implicitly assumed in previous studies, without however being explicitly mentioned. With respect to our main goal of providing a complete *ab initio* description of elementary non-magnetic metals, we have discussed the full necessary formalism (including for instance the FEBO derivation; Sec. 2.1.3) and are, therefore, now in the position to check the validity of approximations made in previous studies.

2) DFT calculations of $F^{qh,0K}$, in particular for elementary materials, are nowadays standard and several studies are available (see e.g., Refs. [109–111] and further references provided in the following sections). The key points that distinguish and motivate this study in comparison to previous ones are:

   - A *systematic* study of an extensive set of materials properties up to the melting point for a *large number* of materials with the same crystal structure. In contrast, previous *ab initio* studies mostly concentrated on one or two elements and a few properties. We have in particular chosen all metals which are non-magnetic and crystallize in the fcc structure (cf. Fig. 4.1). Such a systematic approach allows to investigate for instance chemical trends. A comparable systematic study is the pioneering work of Moruzzi et al. [112], who investigated fcc and bcc metals combining LDA and a Debye treatment of the lattice dynamics. The essential difference, however, is that in our study we replace the empirical Debye treatment by a fully consistent *ab initio* approach.

   - *Highly converged* results with respect to k sampling, plane wave cutoff, augmentation grid, and supercell size and the *assessment* of the remaining error provided in Sec. 3.4. As discussed further in Sec. 3.4, these DFT parameters become critical when considering the quasiharmonic approximation particularly at high temperatures.

   - The study of all elements and properties using the *two complementary xc functionals*: LDA and GGA-PBE. In combination with the well controlled numerical convergence, this approach allows to analyze the performance of these functionals.

The calculations presented in Sec. 4.1 were performed using the PAW method with the quality of the PAW potentials assessed in Secs. 4.1.2 and 4.1.4. The used DFT convergence parameters are compiled in Sec. 3.4.4.1 (in particular Tab. 3.2).

4.1.2 Electronic free energy and zero-point vibrations at $T = 0$ K

At $T\!=\!0$ K, two free energy contributions are present: $E^{\mathrm{el}}_{g,0}(V)$ and $E^{\mathrm{zp,0K}}(V)$. The dominant term is the electronic ground state energy $E^{\mathrm{el}}_{g,0}(V)$, which is thus discussed first. We calculated $E^{\mathrm{el}}_{g,0}(V)$ for all elements and fitted the Vinet equation of state, Eq. (3.54), to the results. Parameters for the equilibrium lattice constant, bulk modulus, and its derivative are listed in Tab. 4.1. The additional superscript "e" emphasizes the exclusion of zero-point vibrations, $E^{\mathrm{zp,0K}}(V)$, at this stage. Table 4.1 contains also the results of our LAPW+lo reference calculations (cf. Sec. 3.4.4) for $E^{\mathrm{el}}_{g,0}(V)$. In general, a remarkably good agreement between the PAW and LAPW+lo results is found. For the transition elements, the PAW lattice constant (bulk modulus) is consistently 0.1% (-2.2%) larger (smaller) than the corresponding LAPW+lo prediction. This is true for LDA and GGA. For Al and Pb, we find for both functionals a slightly smaller (larger) PAW lattice constant (bulk modulus). These results indicate that the approximations intrinsically connected to the used PAW potentials (cf. Sec. 2.1.8), i.e.,

- finite number of basis and projector functions,

- frozen core approximation,

- scalar relativistic effects only implicitly included,

are justified and that the PAW potentials can be employed for the further calculations of thermodynamic properties. It would be however desirable to find out the explicit influence of these differences between PAW and LAPW+lo on thermodynamic quantities. Corresponding tests are presented in Sec. 4.1.4.

For simplicity, experimental data being extrapolated to $T = 0$ K are frequently directly compared with *ab initio* $E^{\mathrm{el}}_{g,0}(V)$ values without taking zero-point vibrations into account. However, the experimental data correspond to the free energy $F(V, T\!=\!0\,\mathrm{K})$ and thus contain a contribution due to zero-point vibrations. To estimate the error related to their neglect, we fitted in a second step $F(V, T\!=\!0\,\mathrm{K}) = E^{\mathrm{el}}_{g,0}(V) + E^{\mathrm{zp,0K}}(V)$ to the Vinet equation of state. The results indexed with a superscript "i" are also given in Tab. 4.1. They show that the inclusion of zero-point vibrations has only a minor effect on the lattice constant. The average increase is ≈ 0.1%. In contrast, for the bulk modulus the effect is significantly stronger (reduction of ≈ 2%). In particular, the Al GGA-bulk modulus softens considerably by about 4%. The change in the equilibrium properties can be directly understood by an analysis of $E^{\mathrm{zp,0K}}(V)$. Note first that the value of $E^{\mathrm{zp,0K}}$ at a^{lat}, which we find to be in average 25 meV/atom, affects only the absolute free energy. To account for the change in the lattice constant, the linear term in the volume dependence of $E^{\mathrm{zp,0K}}$ must be included. For the considered elements, the magnitude of the phonon frequencies decreases with volume (cf. Fig. 4.9) which in turn yields a decreasing zero point energy. The consequence is a modified energy-volume dependence with an equilibrium volume shifted to larger lattice constants. The bulk modulus is indirectly affected by the linear term in $E^{\mathrm{zp,0K}}$ since it softens with increasing volume. Inclusion of the second order term has also an explicit effect on $B_{T,0}$, since the latter is a second order derivative. For all considered elements, both effects, the implicit and explicit, lead to a softening of $B_{T,0}$.

An additional effect included in the experimental data are ambient pressure conditions (100 kPa), whereas theoretically zero pressure conditions are more straightforward to assess. To test the importance of pressure we performed corresponding calculations. The results show that the effect of pressure on the lattice constant and bulk modulus is systematically more than an order of magnitude smaller than the changes due to zero-point vibrations. They show further that the ambient

pressure conditions are also irrelevant for the study of materials properties at higher temperatures. We therefore concentrate here and in the remainder of Chap. 4 only on values obtained at 0 Pa.

The comparison between experiment and theory shows that LDA/GGA under-/overestimates the experimental value of the lattice constant $a_0^{\mathrm{lat,eq}}$ and over(under)estimates the value of the bulk modulus $B_{T,0}$. This behavior is a well established trend observed in numerous previous studies. For the set of metals investigated in this study, we find that LDA underestimates $a_0^{\mathrm{lat,eq}}$ on average by -0.7% and GGA overestimates it on average by 1.8%. The error in $B_{T,0}$, being a second derivative of $F(V,T)$, is much larger in magnitude (LDA-average: 11.6%, GGA-average: -13.7%) and is inversely correlated to the error in $a_0^{\mathrm{lat,eq}}$ (Fig. 4.2). The inverse relation can be explained by the volume dependence of the total energy [Eq. (3.54)] causing a monotonous decrease of $B_{T,0}$ with increasing volume. Particularly for GGA, an increase of the error with the number of d-electrons among the $4d$ and $5d$ transition metals is apparent.

4.1.3 Phonon dispersion

In order to allow an accurate and consistent comparison between experimental and theoretical phonon dispersions, the latter have to be computed at the experimental temperature. The temperature enters the calculation of $\omega_{\mathbf{q},s}$ at three distinct points depending on the considered approximation:

1) Using the quasiharmonic approximation, Eq. (2.133), and the $\mathbf{D}^{0\mathrm{K}}$ approximation, Eq. (2.179), the phonon frequencies $\omega_{\mathbf{q},s}$ are volume dependent, but not explicitly temperature dependent. For the zero pressure condition as considered here, they will be a function of the temperature dependent equilibrium volume $V^{\mathrm{eq}}(T)$, Eq. (2.231), and thus have an implicit temperature dependence:

$$\omega_{\mathbf{q},s} = \omega_{\mathbf{q},s}(V^{\mathrm{eq}}(T)). \tag{4.2}$$

2) As discussed in Sec. 3.3.4, going beyond the $\mathbf{D}^{0\mathrm{K}}$ approximation, the phonon frequencies become dependent on the electronic temperature T^{el} due to the dependence of the dynamical matrix $\mathbf{D}$ on T^{el}. We therefore have an explicit temperature dependence:

$$\omega_{\mathbf{q},s} = \omega_{\mathbf{q},s}(T^{\mathrm{el}}). \tag{4.3}$$

3) Finally, as discussed in Sec. 2.3.5, going beyond the quasiharmonic approximation leads to interaction among phonons (their creation and annihilation), which also causes a temperature dependent frequency shift. In particular, performing molecular/Langevin dynamics (Secs. 2.3.6 and 3.3.5) the frequency shift will explicitly depend on the electronic temperature T^{el} and the nuclei temperature T^{nuc} which both determine the nuclei motion [cf. Eqs. (3.77) to (3.79)]:

$$\omega_{\mathbf{q},s} = \omega_{\mathbf{q},s}(T^{\mathrm{el}}, T^{\mathrm{nuc}}). \tag{4.4}$$

[Note that at the end of a calculation $T^{\mathrm{el}} = T^{\mathrm{nuc}} = T$ must be set, cf. Eq. (3.68) and the following discussion.]

The most dominant contribution to the temperature dependence of $\omega_{\mathbf{q},s}$ is given by Eq. (4.2). This temperature dependence is fully included in the phonon dispersion results presented in this section. The dependencies given by Eqs. (4.3) and (4.4) will be considered in Secs. 4.2 and 4.4, respectively, for a smaller set of elements. Our results based on Eq. (4.2) for both xc functionals, LDA and GGA, are shown in Fig. 4.3a.
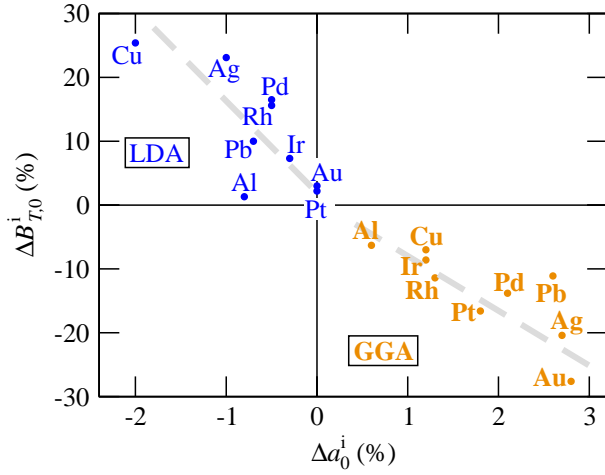
Figure 4.2: Correlation between the deviation from experiment for the lattice constants Δa_0^i and the bulk moduli $\Delta B_{T,0}^i$ (Tab. 4.1). All quantities contain the influence of zero-point vibrations. The dashed lines are a guide for the eye and emphasize the linear trend for each functional.

Table 4.1: Results for the equilibrium lattice constant $a_0^{\text{lat,eq}}$, bulk modulus $B_{T,0}$, and its derivative $B_{T,0}'$ (cf. Sec. 2.4.2) for the projector-augmented wave (PAW) and the LAPW+lo method. For aluminum, the pseudopotential (pp) results (cf. Sec. 4.3) and the EAM results (cf. Sec. 4.5) are also included. The EAM parametrizations are Mei-Davenport (MD) [62], Zope-Mishin (ZM) [63], and Ercolessi-Adams (EA) [64]. The superscript "e" ("i") indicates whether zero-point vibrations are excluded (included). The deviation from experiment is labeled Δa_0^i and $\Delta B_{T,0}^i$. LAPW+lo values marked with an asterisk are estimated values obtained using the (relative) zero-point contributions from the PAW results. All experimental lattice constants are taken from Ref. [14] ($T = 5$ K). The experimental bulk moduli are taken from Ref. [68] (low temperature values) for Al, Pb, Cu, Ag, Au and from Ref. [114] (Pd, $T \to 0$ K), Ref. [115] (Rh, $T \to 0$ K), and Ref. [116] (Pt, Ir, $T \to 0$ K). The available experimental $B_{T,0}'$ are taken from Ref. [117] (collection of experimental $T \to 0$ K data).

| | LDA | | | **Al** | GGA | | | | EAM | |
	LAPW	PAW	pp	Exp.	LAPW	PAW	pp	ZM	MD	EA
$a_0^{\text{lat,eq,e}}$(Å)	3.986	3.985	3.968		4.043	4.041	4.050	4.050	4.049	4.032
$a_0^{\text{lat,eq,i}}$(Å)	3.999*	3.998	3.981	4.032	4.056*	4.054	4.063	4.059	4.063	4.042
Δa_0^i(%)	-0.8*	-0.8	-1.3		0.6*	0.6	0.8	0.7	0.8	0.2
$B_{T,0}^e$(GPa)	83	84	82		77	78	75	79	76	82
$B_{T,0}^i$(GPa)	79*	80	78	79	74*	75	72	77	73	80
$\Delta B_{T,0}^i$(%)	0.0*	1.3	-1.2		-6.3*	-5.0	-8.9	-2.5	-7.6	1.3
$B_{T,0}'$	4.5	4.6	4.6	4.7	4.7	4.7	4.6	4.3	4.1	4.8

| | **Pb** | | | | | **Cu** | | | | |
| | LDA | | Exp. | GGA | | LDA | | Exp. | GGA | |
	LAPW	PAW		LAPW	PAW	LAPW	PAW		LAPW	PAW
$a_0^{\text{lat,eq,e}}$(Å)	4.881	4.875		5.047	5.030	3.522	3.524		3.638	3.637
$a_0^{\text{lat,eq,i}}$(Å)	4.885*	4.879	4.905	5.052*	5.034	3.529*	3.530	3.602	3.645*	3.644
Δa_0^i(%)	-0.4*	-0.5		3.0*	2.6	-2.0*	-2.0		1.2*	1.2
$B_{T,0}^e$(GPa)	52	53		39	40	188	183		141	136
$B_{T,0}^i$(GPa)	51*	52	49	39*	40	183*	178	142	137*	132
$\Delta B_{T,0}^i$(%)	13.2*	15.6		-13.5*	-11.1	28.5*	25.4		-3.4*	-7.0
$B_{T,0}'$	4.7	5.0	5.5	4.2	5.6	5.1	5.1	5.3	5.1	5.1

Continued.

Table 4.1 (continued).

	Ag LDA LAPW	Ag LDA PAW	Ag Exp.	Ag GGA LAPW	Ag GGA PAW	Au LDA LAPW	Au LDA PAW	Au Exp.	Au GGA LAPW	Au GGA PAW
$a_0^{\mathrm{lat,eq,e}}$(Å)	4.008	4.016		4.152	4.165	4.054	4.062		4.163	4.174
$a_0^{\mathrm{lat,eq,i}}$(Å)	4.014*	4.022	4.061	4.159*	4.172	4.057*	4.066	4.065	4.167*	4.179
Δa_0^{i}(%)	-1.2*	-1.0		2.4*	2.7	-0.2*	0.0		2.5*	2.8
$B_{T,0}^{\mathrm{e}}$(GPa)	140	136		91	88	193	189		139	134
$B_{T,0}^{\mathrm{i}}$(GPa)	137*	133	109	89*	86	190*	186	180	136*	131
$\Delta B_{T,0}^{\mathrm{i}}$(%)	26.8*	23.1		-17.6*	-20.4	5.1*	2.8		-25.0*	-27.6
$B'_{T,0}$	5.8	5.7	5.9	5.8	5.9	5.9	5.8	5.9	6.0	6.0

	Rh LDA LAPW	Rh LDA PAW	Rh Exp.	Rh GGA LAPW	Rh GGA PAW	Pd LDA LAPW	Pd LDA PAW	Pd Exp.	Pd GGA LAPW	Pd GGA PAW
$a_0^{\mathrm{lat,eq,e}}$(Å)	3.762	3.767		3.839	3.842	3.847	3.854		3.949	3.954
$a_0^{\mathrm{lat,eq,i}}$(Å)	3.766*	3.770	3.798	3.844*	3.847	3.851*	3.858	3.879	3.954*	3.959
Δa_0^{i}(%)	-0.8*	-0.7		1.2*	1.3	-0.7*	-0.5		1.9*	2.1
$B_{T,0}^{\mathrm{e}}$(GPa)	321	313		260	252	230	223		169	165
$B_{T,0}^{\mathrm{i}}$(GPa)	316*	308	269	255*	248	226*	219	195	166*	162
$\Delta B_{T,0}^{\mathrm{i}}$(%)	12.8*	10.0		-8.8*	-11.4	20.2*	16.5		-11.5*	-13.8
$B'_{T,0}$	5.3	5.2		5.4	5.3	5.7	5.5		5.7	5.7

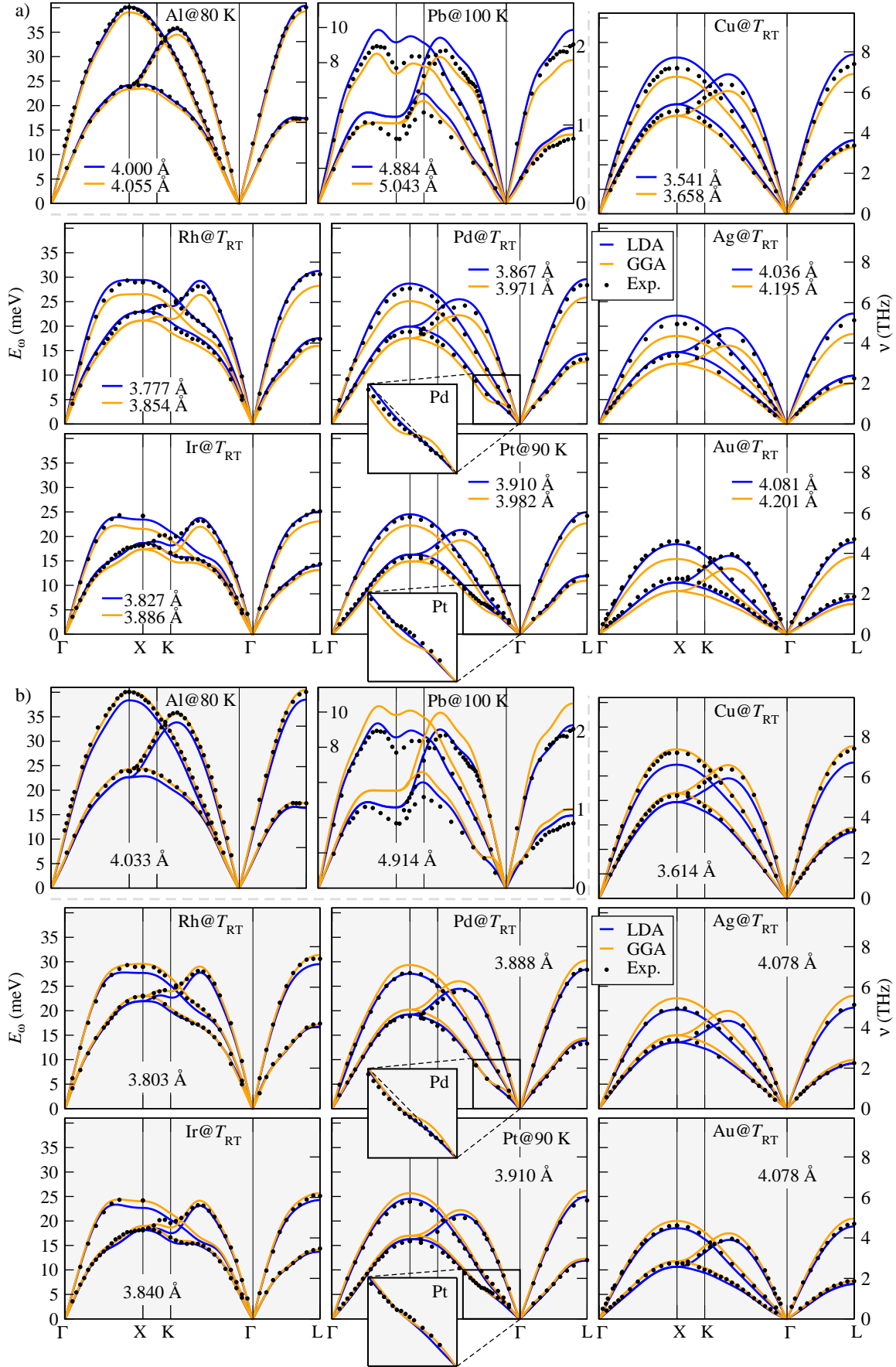|	Ir LDA LAPW	Ir LDA PAW	Ir Exp.	Ir GGA LAPW	Ir GGA PAW	Pt LDA LAPW	Pt LDA PAW	Pt Exp.	Pt GGA LAPW	Pt GGA PAW
$a_0^{\mathrm{lat,eq,e}}$(Å)	3.819	3.819		3.879	3.877	3.900	3.906		3.976	3.977
$a_0^{\mathrm{lat,eq,i}}$(Å)	3.822*	3.821	3.835	3.882*	3.880	3.903*	3.909	3.909	3.978*	3.980
Δa_0^{i}(%)	-0.3*	-0.3		1.2*	1.2	-0.2*	0.0		1.8*	1.8
$B_{T,0}^{\mathrm{e}}$(GPa)	406	401		349	342	308	301		246	245
$B_{T,0}^{\mathrm{i}}$(GPa)	402*	397	366	345*	338	304*	297	288	243*	242
$\Delta B_{T,0}^{\mathrm{i}}$(%)	8.7*	7.3		-6.8*	-8.6	4.7*	2.4		-16.3*	-16.6
$B'_{T,0}$	5.2	5.1		5.2	5.2	5.5	5.5		5.4	5.6

Figure 4.3: Phonon dispersions $\omega_{\mathbf{q},s}$ [$E_\omega = h\nu = h\omega/(2\pi)$ with h the Planck constant] along high symmetry directions. The insets in the Pd and Pt phonon dispersions magnify the Kohn anomalies (see text; the dashed line is a guide for the eye). A 5^3 supercell was used for Pb and a 4^3 supercell for all other elements (see Sec. 3.4 for further details). The experimental values are taken from Ref. [118] for Rh, from Ref. [119] for Ir, and from Ref. [101] for all other elements. Al and Pb are slightly separated to emphasize the periodic table correspondence of the other elements and the dispersion of Pb is rescaled to visualize it properly. a) Calculated at the DFT obtained equilibrium lattice constant (given in the legends) for the given temperature (T_{RT} =room temperature). b) Calculated at the experimental lattice constant (see Sec. 4.1.8). The gray shading is included to allow a convenient distinction to a).

Generally, both functionals show a good agreement with experimental data. LDA, yielding larger phonon frequencies than GGA, overestimates the experimental data in most cases, while GGA underestimates it. A systematic trend we observe is that one can estimate from the comparison of different xc functionals approximate error bars for the theoretical calculations with respect to experimental data. Small deviations between LDA and GGA, as e.g. for Al, thus indicate small error bars and hence a high predictive power, while larger deviations as for Ag or Au indicate lower prediction accuracy.

The phonon dispersion of Cu, Ag, and Au is comparatively "simple" and can be described accurately already with nearest neighbor interactions. The dispersion of these elements has been the subject of previous theoretical studies (Cu [120–123], Ag [124], and Au [125, 126]). For Ag and Au, however, only the LDA formalism has been used in these investigations. The available data from the literature is in good agreement with our results. The remaining elements exhibit more complex phonon dispersions. Anomalies, i.e., deviations from the "simple" dependence, are caused by interactions of the phonons with the electronic Fermi surface. To resolve these anomalies in the phonon dispersion, force constants including long range inter-atomic interactions need to be captured, i.e., large supercells as used in the present study are crucial. As pointed out in Ref. [118], the dispersion relations of these elements "constitute a severe test for any theoretical treatment".

We first focus on Pd and Pt. The anomalies in the vicinity of the Γ point (enlarged in the insets of Fig. 4.3a) have been attributed to virtual Kohn transitions [101]. Figure 4.3a shows that these Kohn anomalies are strong for the GGA calculated dispersions, whereas the LDA dispersions show almost no deviation from linearity. In order to identify why LDA behaves differently, we repeated the calculations of the phonon dispersion at the same (experimental) lattice constant for LDA and GGA (cf. Fig. 4.3b). For Pt, both functionals yield a comparable anomaly under these conditions. We therefore conclude that, for Pt, the xc functional dependence is mainly related to an effect of the atomic structure on the Fermi surface rather than due to changes in the Fermi surface caused by LDA/GGA. For Pd however, this argument does not hold, since calculating the phonon dispersion at the same lattice constant yields a stronger pronounced anomaly for GGA than for LDA. Previous theoretical studies on Pd [120, 127] based on the linear response method have not reported the anomaly. However, in a recent theoretical study [128] on the electron-phonon coupling in Pd, the anomaly has been resolved and correlated to a distinct peak in the phonon line widths.

The phonon dispersion of Rh and Ir shows anomalies in almost all branches. These pronounced anomalies originate from sharp peak-like features (caused by the d-states) in the electronic Fermi surface. Both elements have been the subject of only a few experimental and theoretical (LDA) investigations [118, 119, 129]. Our LDA phonon dispersions agree well with the LDA results from Refs. [129] and [119], where a sophisticated supercell approach has been employed. In particular, the approach was based on calculations for various supercells (also non-cubic), which were then combined using an interpolation scheme to generate a phonon dispersion including the information from all supercells. This procedure allowed to include also long-ranged force constants.

The phonon dispersion of Al has been in the focus of numerous studies [109, 120, 121, 126, 130]. It is, at first glance, similar to the phonon dispersion of Cu, Ag, and Au. However, a detailed inspection reveals anomalies for most branches. This is consistent with theoretical findings in Ref. [68]. Our results for the LDA and GGA phonon dispersion of Al in Fig. 4.3 accurately reproduce these anomalies. It is noteworthy that a 4^3 supercell is the minimum cell size to resolve these anomalies.

Pb exhibits the most complex phonon dispersion among the investigated elements. This "complexity" became already apparent in Sec. 3.4.3 when inspecting the convergence with respect to the supercell size. The theoretical dispersions computed for a large 5^3 supercell (500 atoms) reproduce
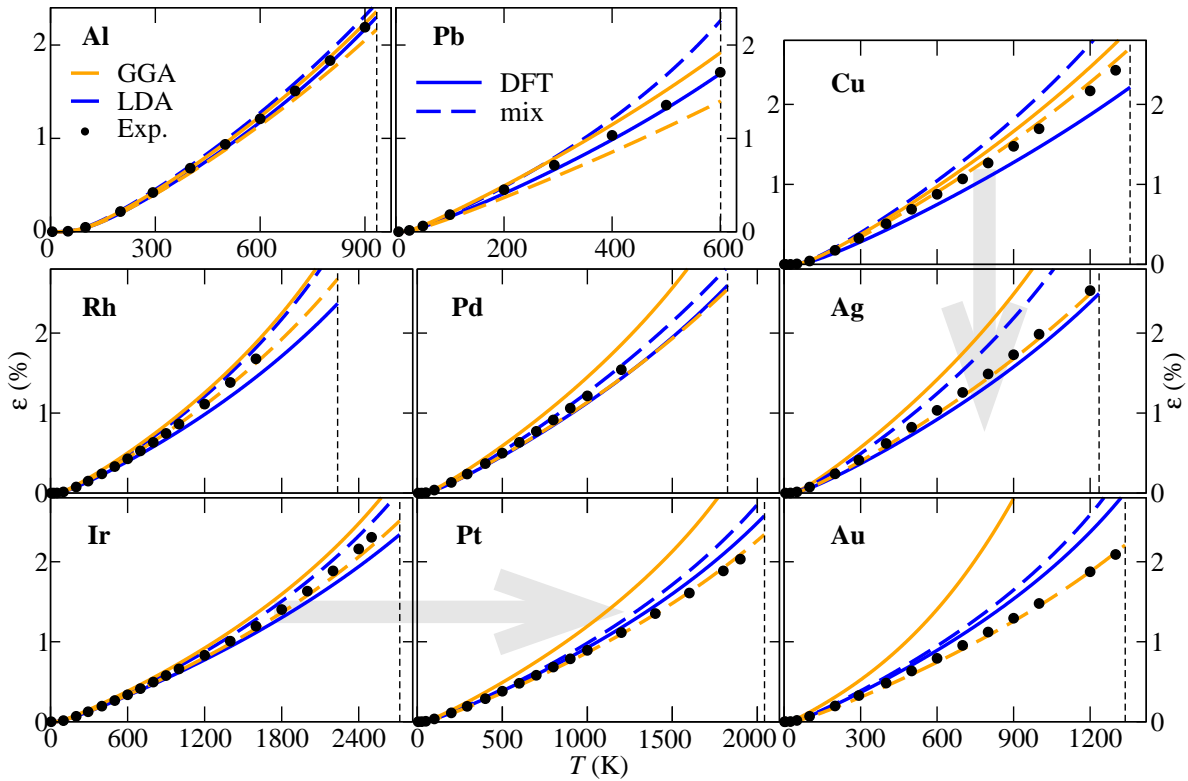
Figure 4.4: Linear thermal expansion ε, Eq. (2.234), as a function of temperature T. The solid lines indicate results obtained fully from DFT (LDA/GGA). The dashed lines correspond to the mixed approach as discussed in Sec. 4.1.8. The gray shaded arrows show the direction of increasing error among the transition elements (see text). The melting temperature is indicated for each element (cf. Fig. 4.1) by the vertical dashed line. The experimental data are taken from Ref. [14].

reasonably the experiment. The LDA results for Pb agree well with a previous LDA linear response study [100], which naturally includes long range force constants. A study performed subsequent to our investigations [131] could even further improve the description of the Pb phonon dispersion by including spin-orbit coupling effects. It would be interesting to investigate if spin-orbit coupling also affects the thermodynamic properties of Pb. (In Ref. [131] only the phonon dispersion has been calculated due to the enormous computational requirements associated with spin-orbit coupling.) In fact, we will return to this issue in Sec. 4.1.8 as a possible explanation for the observed behavior of the thermodynamic properties of Pb.

4.1.4   Thermal expansion

The results for the thermal expansion ε and the expansion coefficient α are shown in Figs. 4.4 (solid lines) and 4.5a. (Note that the lower parts of Figs. 4.5 to 4.8 will only be discussed in Sec. 4.1.8.) Let us first return to the evaluation of the PAW potentials as discussed in Sec. 4.1.2. We focus on the expansion coefficient, since it is the most sensitive thermodynamic quantity. To estimate the PAW parametrization error, the following procedure is applied: In Eq. (4.1), the LAPW+lo results (Tab. 4.1) are used for the description of the $T = 0$ K energy surface $E_{g,0}^{\mathrm{el}}(V)$, while the remaining contributions are obtained from PAW. The resulting expansion coefficient for GGA is shown in Fig. 4.5a (dot-dashed lines) and should be compared with the orange solid line. We find for all elements only a small effect strongly supporting the argument that the employed PAW potentials
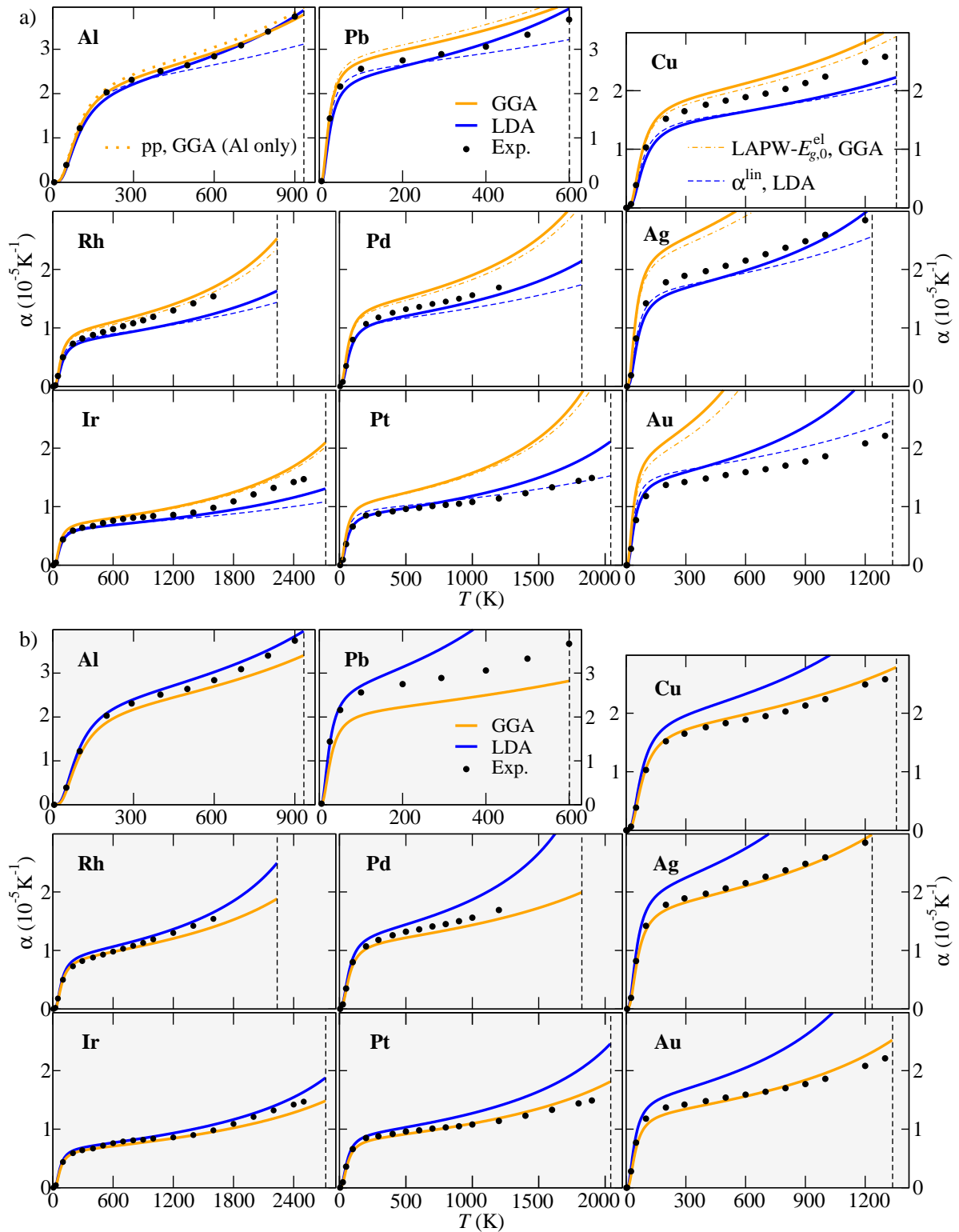
Figure 4.5: Thermal expansion coefficient α, Eq. (2.235). The melting temperature is indicated for each element (cf. Fig. 4.1) by the vertical dashed line. The experimental data are taken from Ref. [14]. a) The LDA and GGA α (solid lines) are calculated fully from DFT. Additionally, α^{lin} the expansion coefficient based on the linear approximation Eq. (3.58), the expansion coefficient calculated from a free energy surface with $E_{g,0}^{\text{el}}(V)$ from LAPW+lo (see text), and the pseudopotential (pp) result for the Al α (not discussed until Sec. 4.3.2) are shown (dashed, dot-dashed, and dotted lines). b) The LDA and GGA α are calculated using the mixed approach as discussed in Sec. 4.1.8. The gray shading is included to allow a convenient distinction to a). This applies likewise to Figs. 4.6b to 4.8b in the following.

are indeed reliable for thermodynamic calculations.

We now turn to the comparison of our DFT results for ε and α with experiment. In performing this comparison, one should keep in mind that both are differential quantities, which might mask errors in the absolute values of the lattice constants (listed in Tab. 4.1). Figures 4.4 and 4.5a reveal on average a better agreement for the LDA than for the GGA results with GGA predicting a too large expansion. The deviation between the GGA results and experiment shows a chemical trend among the transition metals which is indicated in Fig. 4.4 by the gray arrows. Filling up the d-shell and increasing the atomic radius enlarges the error. The two most prominent examples are Ag and Au, where in particular the GGA α shows a significant deviation from experiment.

In general, we find for both, ε and α, that most experimental data lie in between the LDA and GGA results. The probability for this to occur is however not as high as found for the phonon dispersion which is most apparent for α (Fig. 4.5). For instance, while the experimental phonon dispersion of Pt is enclosed by the LDA and GGA results, the expansion coefficient of Pt fulfills this only up to a certain temperature. Above this temperature both the LDA α and the GGA α increase much faster than the experimental data. We attribute this to the fact that the expansion coefficient is highly sensitive with respect to the free energy surface and that small changes in $F(V,T)$ significantly affect α in particular at high temperatures. To support this we have included in Fig. 4.5, the LDA expansion coefficient α^{lin} which was calculated from a free energy surface based on the linear approximation Eq. (3.58) (dashed lines). The curves for α^{lin} are to be compared with the fully converged LDA α (blue solid lines) based on the interpolation Eq. (3.59), which includes additionally higher order terms as compared to Eq. (3.58). The corresponding change in $F(V,T)$ is below 1 meV/atom. To see this, compare the dashed line with the zero line in the inset in Fig. 3.4. This free energy is for Al, the situation however does not change significantly for the other elements. In contrast, the change when going from α^{lin} to the converged α is very strong in particular at high temperatures. In fact, the difference between α^{lin} and α shows the same chemical trend as the deviation from experiment and is thus again most pronounced for Au. The discrepancy between the fully converged DFT results and experimental data will be investigated further in Sec. 4.1.8, where we present an approach allowing to detect which free energy contribution actually causes these large deviations.

Previous *ab initio* studies on the thermal expansion of metals are rare. For the elements investigated here, we have found LDA studies for Al [109, 110], Cu [122], and Ag [124]. In Ref. [122], a combined LDA and GGA study of thermodynamic properties for Cu has been performed. These data are in good agreement with our corresponding LDA/GGA data. However, the influence of the second order term on α has been neglected. For instance in Ref. [109], the presented expansion coefficient shows only a linear behavior at temperatures above 300 K and not the steeper increase as we observe upon inclusion of the second order term.

4.1.5   Heat capacity

The results for the heat capacity at constant pressure C_P and constant volume C_V are shown in Fig. 4.6a in comparison with experimental data. We focus first on C_P which is the experimentally measured quantity. Similar conclusions as in the previous section for the thermal expansion can be drawn: LDA yields an (astonishingly) good agreement with experiment and the GGA error shows the same chemical trend as in the case of the expansion coefficient. Hence, the largest deviations are again found for the noble metals Ag and Au. We note that our heat capacity results compare well with available previous calculations (Cu [122], Ag [124]).

Our approach allows to directly determine the electronic contributions, C_P^{el}, to the heat capacity (dot-dashed lines in Fig. 4.6a). For Al, Pb, Cu, Ag, and Au the electrons make only a small
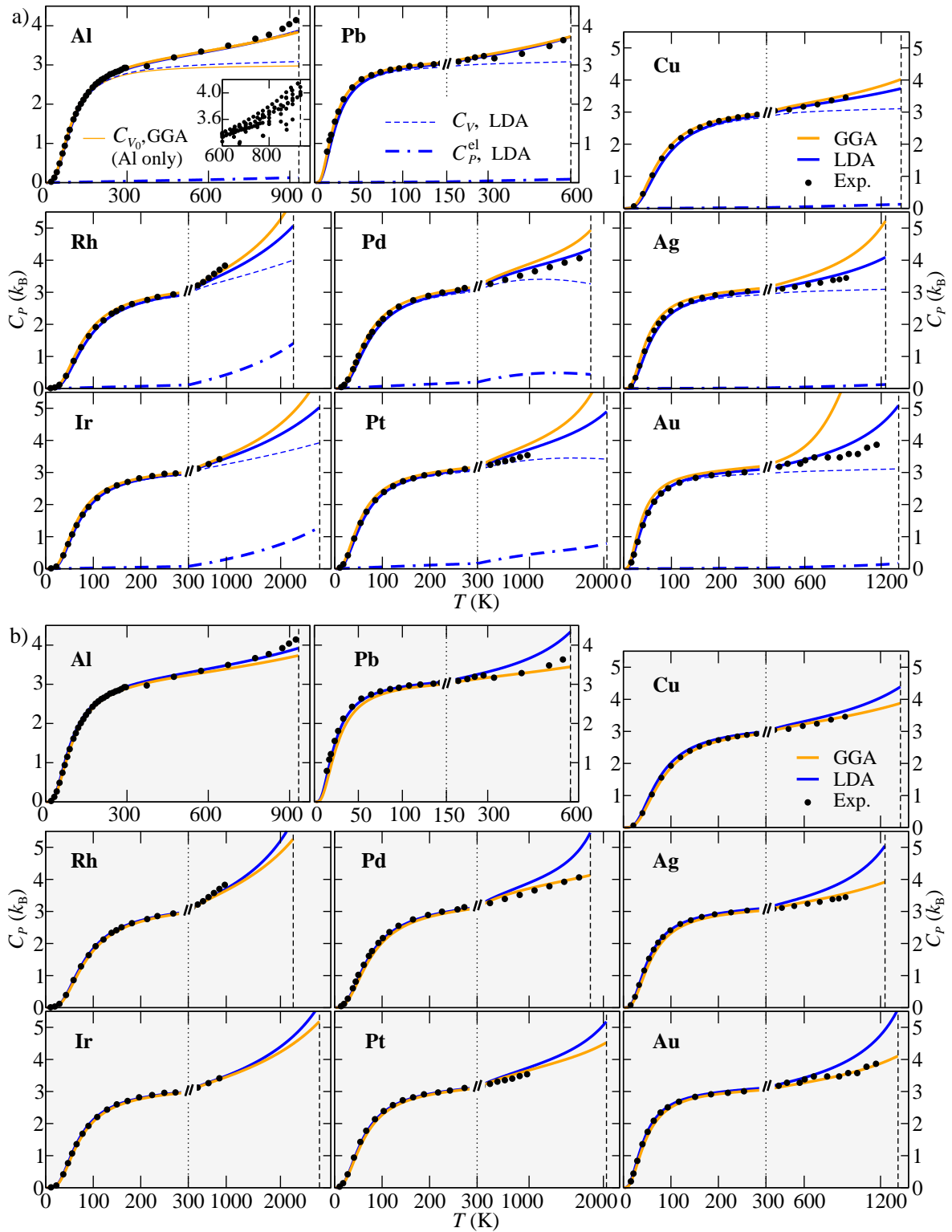
Figure 4.6: Isobaric heat capacity C_P, Eq. (2.236), at $P = 0$ Pa as a function of temperature T in units of the Boltzmann constant k_B. The temperature axis is split by the vertical dotted line into two parts to allow a convenient representation. The melting temperature is indicated for each element (cf. Fig. 4.1) by the vertical dashed line. The experimental data are taken from Ref. [132]. a) The LDA and GGA C_P (solid lines) are calculated fully from DFT. Additionally, the constant volume heat capacity C_V, Eq. (2.236), for LDA (dashed lines), the electronic contribution, C_P^{el}, to the LDA heat capacity (dot-dashed lines), and the GGA fixed volume heat capacity C_{V_0} [Eq. (2.241)] for Al discussed in Sec. 4.3.1 (thin solid line) are shown. The inset for Al is a zoom into the high temperature region visualizing the experimental scatter which will be also discussed in Sec. 4.3.1. The additional experimental references are given in Fig. 4.17. b) The LDA and GGA C_P are calculated using the mixed approach as discussed in Sec. 4.1.8.

contribution to the heat capacity over the full temperature range up to the melting point. For instance at 900 K, the contribution for Al, Cu, Ag, and Au is $\sim 0.1\,k_{\mathrm{B}}$ and $\sim 0.2\,k_{\mathrm{B}}$ for Pb. For Pb, however, already at $600\,\mathrm{K}$ the melting point is reached. The contribution at $600\,\mathrm{K}$ is $\sim 0.1\,k_{\mathrm{B}}$. This order of magnitude agrees for instance with findings in Ref. [122] (for Cu) and Ref. [124] (for Ag). In contrast to these elements, C_P^{el} becomes significant for Pd, Pt, Rh ($\sim 0.4\,k_{\mathrm{B}}$ at $900\,\mathrm{K}$), and Ir ($\sim 0.3\,k_{\mathrm{B}}$ at $900\,\mathrm{K}$). For Pd, Pt, Rh, and Ir, the origin of the significant electronic contribution are large electronic entropy effects due to a high electronic density of states near the Fermi level caused by partially occupied d states (d states peak). Results for the electronic density of states of Pd, Pt, Rh, and Ir can be found for instance in Ref. [133]. Particularly interesting in this respect is a comparison of the temperature dependence of C_P^{el} (dot-dashed lines in Fig. 4.6a). For Pd, C_P^{el} increases up to $\approx 0.5k_{\mathrm{B}}$ at $1000\,\mathrm{K}$ and decreases above this temperature until it reaches $\approx 0.4k_{\mathrm{B}}$ at the melting temperature (1827 K). This indicates that the d states peak has been filled at least up to its half and that excitations of further electrons become energetically unfavorable. For Pt, we find a linearly increasing C_P^{el} up to its melting point. For Ir and in particular for Rh, the electronic contribution increases even stronger than linearly up to the melting point. This indicates that half filling of the d states peak is not reached before melting for Rh and Ir.

Another noteworthy feature is observed for Al, for which the DFT calculated C_P for both xc functionals agrees excellently with experiment up to $\approx 70\%$ of the melting temperature. For higher temperatures, the experimental heat capacity increases stronger than the theoretical prediction. The possible origins of these deviations will be investigated in detail in Sec. 4.3. In focusing on this temperature region, we will also have to discuss in more detail the up to now problematic experimental/theoretical situation.

Let us turn to the heat capacity at constant volume C_V. It falls together with C_P in the low temperature region (up to ≈ 300 K), whereas it significantly deviates from the latter at higher temperatures. The reason for the faster increase of C_P is directly correlated to the strong increase of the expansion coefficient at high temperatures (Fig. 4.5a): C_P is obtained from the derivative of the entropy with respect to temperature, Eq. (2.229). The important point is that this derivative needs to be calculated at constant pressure, i.e., in the direction of the thermal expansion on the entropy surface $S(V, T)$. Thus, the behavior of the thermal expansion/expansion coefficient will directly affect the behavior of C_P and easily enable values of above $4k_{\mathrm{B}}$ for this quantity. In contrast, the derivative needed to calculate C_V is obtained from $S(V, T)$ in the direction of the temperature axis and the maximum contribution that can be obtained from the quasiharmonic entropy surface is only $3k_{\mathrm{B}}$ (Dulong-Petit rule). The reason why also C_V can go beyond the classical limit of $3k_{\mathrm{B}}$, particularly visible for Rh and Ir, is the contribution of the electrons. Their influence modifies the curvature of the entropy surface and thus also C_V. Note however that we have in general $3k_{\mathrm{B}} + C_P^{\mathrm{el}} \neq C_V$. This inequality can be again explained by considering the direction of differentiation: C_P^{el} corresponds to the electronic contribution obtained from a derivative in the direction of the thermal expansion. The electronic contribution contained in C_V corresponds to a derivative in the direction of the temperature axis.

4.1.6   Bulk modulus

In experiment, the adiabatic bulk modulus B_S is typically measured, while in theory the isothermal bulk modulus B_T [cf. Eqs. (2.229) and (2.237)] is more straightforward to assess. The two bulk moduli coincide however only at $T = 0$ K, whereas at higher temperatures B_S and B_T deviate strongly as exemplified for the GGA bulk modulus of Al in Fig. 4.7a. To allow for an unbiased comparison, we therefore computed the full temperature dependence of B_S from Eq. (2.238) for all elements. In Fig. 4.7a, we display however only the temperature interval up to $300\,\mathrm{K}$ (except for

Pt), due to the missing experimental data for comparison at higher temperatures.

In comparing with the available experimental data, we find a similar behavior as observed already for the thermal expansion and the heat capacity. Compare for instance B_S and α along the column Cu, Ag, Au: For Cu, GGA yields a better B_S and a (slightly) better α. For Ag, LDA yields a good description of both, B_S and α, while GGA starts deviating. For Au finally, GGA deviates strongly, whereas LDA clearly shows a better agreement with experiment. It is important to point out that in order to achieve such a consistent comparison between theory and experiment for ε, α, C_P, and B_S, the inclusion of the second order term in the parametrization of $F^{\mathrm{qh},0\mathrm{K}}$ (cf. the corresponding discussion for α^{lin} in Sec. 4.1.4) when calculating B_S is crucial. To show this, Fig. 4.7 contains also B_S^{lin} (dashed lines), i.e., the LDA adiabatic bulk modulus resulting from a calculation based on the approximation Eq. (3.58). The curves for B_S^{lin} deviate strongly from the fully converged LDA B_S resulting from Eq. (3.59) (blue solid lines) and they would not allow to derive a reasonable description of the bulk modulus.

4.1.7 Free energy

We finally come to the free energy at constant (zero) pressure F_P. The results are shown in Fig. 4.8a in comparison with values obtained from the CALPHAD approach [7]. For the elementary materials considered here, CALPHAD interpolates calorimetrically measured free energies as a function of temperature. In order to compare our DFT free energies $F_P^{\mathrm{DFT}}(T)$ to the CALPHAD free energies $F_P^{\mathrm{CAL}}(T)$, we shift both using:

$$
\begin{align}
\widetilde{F}_P^{\mathrm{DFT}}(T) &= F_P^{\mathrm{DFT}}(T) - F_P^{\mathrm{DFT}}(T^{\mathrm{ref}}), \tag{4.5}\\
\widetilde{F}_P^{\mathrm{CAL}}(T) &= F_P^{\mathrm{CAL}}(T) - F_P^{\mathrm{CAL}}(T^{\mathrm{ref}}). \tag{4.6}
\end{align}
$$

We follow the CALPHAD approach and chose a finite temperature as the reference ($T^{\mathrm{ref}} = 200$ K). The reason to use a temperature different from 0 K is the lack of accurate experimental data at low temperatures, which causes the CALPHAD free energies to diverge in this region. To allow for a convenient comparison, we included also the difference free energy ΔF_P,

$$
\Delta F_P(T) = \widetilde{F}_P^{\mathrm{CAL}}(T) - \widetilde{F}_P^{\mathrm{DFT}}(T), \tag{4.7}
$$

for both xc functionals in Fig. 4.8a.

The results for the free energy follow closely the trends found for the thermal expansion, the heat capacity, and the bulk modulus. In general, the LDA results are in good agreement with the CALPHAD data, whereas the GGA error exhibits the same chemical trend among the transition metals: Filling up the d shell and increasing the atomic radius, the GGA deviation from experiment increases and cumulates again in significant errors for Pt, Ag, and Au. In fact, for Au we find that the contribution from the second order term in Eq. (3.59) (cf. the discussion for α^{lin} and B_S^{lin} in the preceding sections) is so strong that the (GGA) free energy starts to diverge at ≈ 1000 K. This is the reason why we have cut the corresponding curve at this temperature. The divergence occurs consistently also for the thermodynamic quantities discussed so far, it however did not become apparent yet due to the chosen scale in Figs. 4.4 to 4.7.

At this stage, we want to highlight the *consistent agreement* between the DFT results and experiment (i.e., the same qualitative and quantitative trends) observed for **all** thermodynamic quantities: ε, α, C_P, B_S, and F_P. This is remarkable, since in experiment – in contrast to the theoretical description where all quantities are rigorously connected due to their derivation from the free energy surface – largely different setups and techniques are employed. To be more specific,
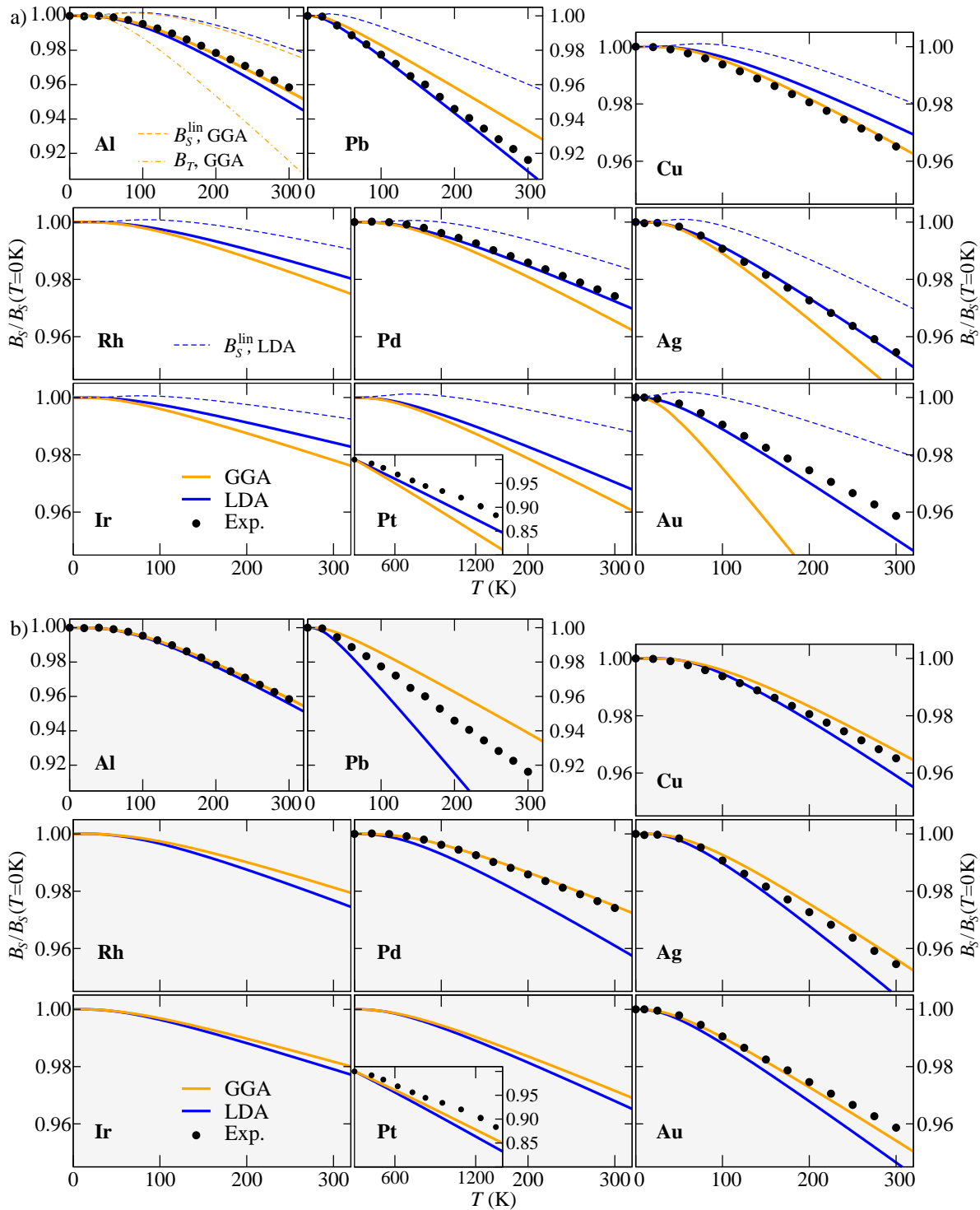
Figure 4.7: Relative adiabatic bulk modulus B_S, Eq. (2.237), at $P = 0$ Pa as a function of temperature T up to 300 K. The bulk modulus is scaled with respect to its $T = 0$ K value as given in Tab. 4.1. The inset shows the high temperature region for Pt. The experimental data are taken from Ref. [15] (Al), Ref. [134] (Pb), Ref. [135] (Cu), Ref. [136] (Ag, Au), Ref. [137] (Pd), and Ref. [138] (Pt). a) The LDA and GGA B_S (solid lines) are calculated fully from DFT. Additionally, B_S^{lin} the adiabatic bulk modulus based on the linear approximation Eq. (3.58) for LDA (all elements; blue dashed lines) and GGA (Al only; orange dashed line) and the isothermal bulk modulus B_T for GGA Al (orange dot-dashed line) are shown. b) The LDA and GGA B_S are calculated using the mixed approach as discussed in Sec. 4.1.8.
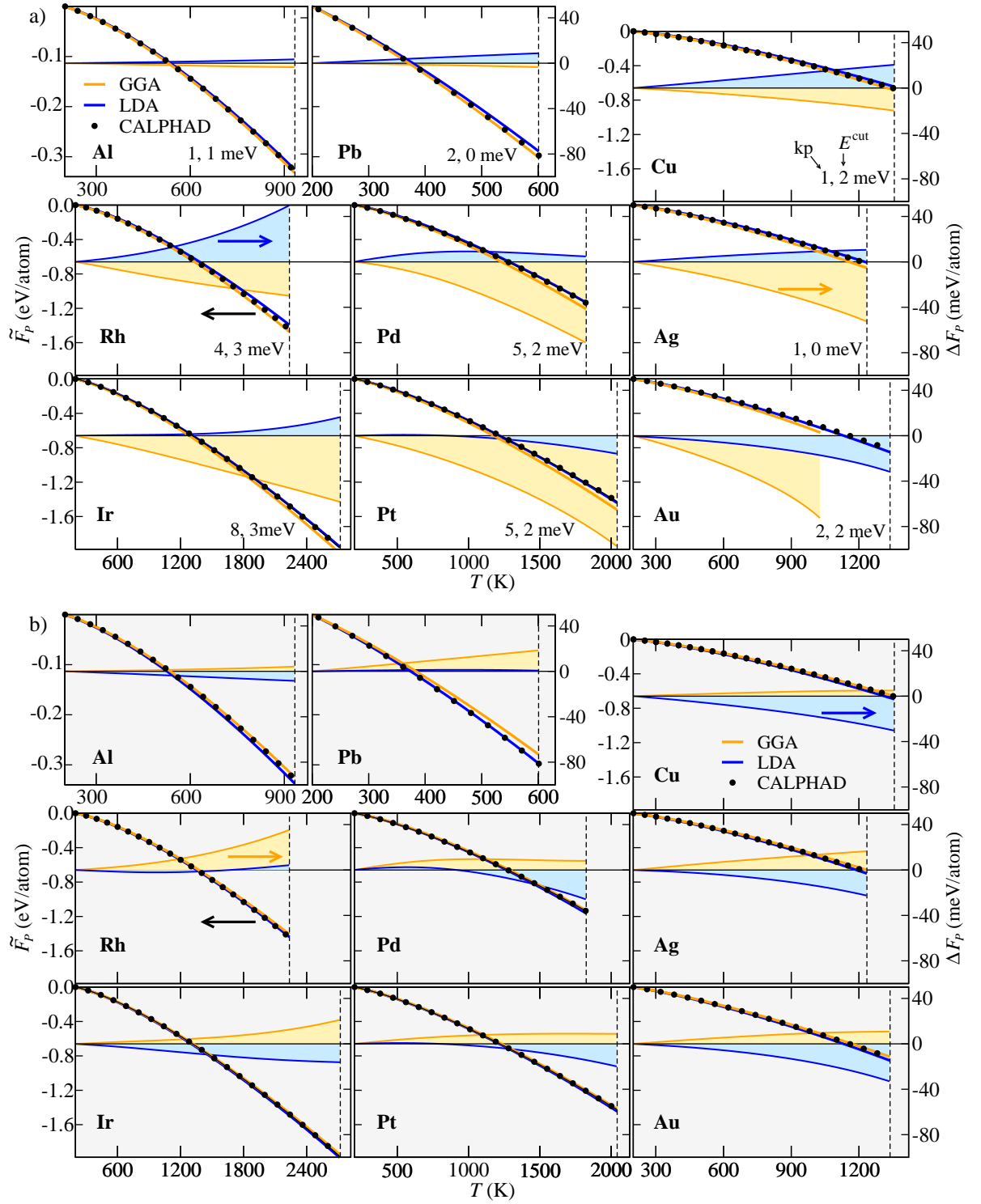
Figure 4.8: Free energy F_P at $P = 0$ Pa as a function of temperature T in comparison with values obtained with the CALPHAD method [7] (using THERMOCALC version Q [139] and the "PURE4-SGTE Pure Elements Database"). On the left axis, the free energies $\widetilde{F}_P$ shifted according to Eq. (4.5) and on the right axis, the difference free energy ΔF_P according to Eq. (4.7) are shown. The curves for ΔF_P are shaded as a guide for the eyes. The melting temperature is indicated for each element (cf. Fig. 4.1) by the vertical dashed line. a) The LDA and GGA free energies are calculated fully from DFT. Additionally, for each element the error (in meV/atom ≈ 0.023 kcal/mol) in F_P at the corresponding melting temperature based on the convergence tests in Sec. 3.4 is given. The first number refers to the error from the k sampling (kp) and the second to the error due to the plane wave cutoff E^{cut}. The error due to the augmentation grid is consistently zero and thus not shown. The incomplete curve for the GGA ΔF_P is discussed in the text. b) The LDA and GGA F_P are calculated using the mixed approach as discussed in Sec. 4.1.8.

ε and α are typically measured simultaneously and F_P is mostly derived from C_P measurements. Nonetheless, we still have three distinct classes of quantities measured in separate experimental setups all leading to a consistent picture when compared to the DFT results:

1) Thermal expansion ε and its coefficient α.

2) Isobaric heat capacity C_P and free energy F_P.

3) Adiabatic bulk modulus B_S.

Consistent agreement between experiment and DFT results for a large set of metals.

The question which arises now is: Can one employ these systematic results in order to determine the source of the – for some elements substantial – error in the theoretical data, in particular for the GGA results? We address this question in the following section.

4.1.8   Comparison between theory and experiment: Mixed approach

It remains an aim of our study to use the consistent and systematic trends observed so far, in order to derive strategies for an improved materials description. In this context, it is interesting to take also the $T = 0$ K DFT parameters and their deviation from experiment into account. It is a remarkable fact that the largest error observed in F_P, which is caused by the divergence in the GGA description of Au, coincides with the largest deviation from experiment at $T = 0$ K (see Fig. 4.2/Tab. 4.1). Vice versa, the small errors in the GGA $T = 0$ K quantities for Al (but also for Cu, Ir, and Rh) are consistent with relatively small errors in the respective free energies. Note further that GGA gives systematically a too low free energy, whereas the free energy from LDA is almost always too high. This behavior, which in a similar fashion is also seen in the derived thermodynamic quantities, is likewise correlated to the observed trends for the $T = 0$ K data (Fig. 4.2).

In order to quantitatively analyze the influence of the errors in the $T = 0$ K parameters, different approaches have to be employed depending on the considered quantity. For the phonon dispersion, the DFT calculated equilibrium lattice constant (Sec. 4.1.3) can be simply replaced by the experimental lattice constant at the given temperature [121, 140, 141]. Figure 4.3b shows the effect for all elements. The difference between the LDA and GGA results is systematically reduced and thus the mean deviation from experiment decreases slightly. This effect is most prominent for GGA. A further interesting consequence is that replacing the fully theoretical lattice constant by the experimental one changes the qualitative behavior of LDA and GGA: While in Fig. 4.3a (theoretical lattice constant) the LDA/GGA curves give rise to an upper/lower bound of the experimental data, in Fig. 4.3b (experimental lattice constant) the opposite behavior is found. The same trend has earlier been reported for a small subset of the here investigated systems, Al [121] and Cu [121, 122].

In order to estimate how the error in the $T = 0$ K quantities affects thermodynamic properties, the following approach is introduced: In a first step, we use the experimental values for $a_0^{\text{lat,eq}}$, $B_{T,0}$, and B'_{T0} as given in Tab. 4.1 in order to construct the exact (experimental) free energy volume curve $F^{\text{exp}}(V, T = 0\,\text{K})$ from the Vinet equation of state, Eq. (3.54). For elements, where no experimental data are available for $B'_{T,0}$, we use the average of the LDA and GGA value given in Tab. 4.1. In a second step, we use F^{exp} to derive a mixed experimental-theoretical free energy surface F^{mix} by:

$$F^{\text{mix}}(V,T) \; = \; F^{\text{exp}}(V, T = 0\,\text{K}) + \widetilde{F}_0^{\text{el}}(V,T) + TS^{\text{qh,0K}}(V). \tag{4.8}$$

Note that F^{exp} contains already the influence of zero-point vibrations and is therefore not additionally included in Eq. (4.8). Finally, in a third step, $F^{\text{mix}}(V,T)$ is used to derive all thermodynamic

properties. In the following, we call this approach of combining the experimental free energy F^{exp} with the fully *ab initio* calculated thermal energy contribution $\widetilde{F}_0^{\text{el}} + TS^{\text{qh,0K}}$ the mixed approach.

We applied the mixed approach to ε, α, C_P, B_S, and F_P [Figs. 4.4 (dashed lines), 4.5b, 4.6b, 4.7b, and 4.8b, respectively]. In general, i.e., for all elements and all quantities, the same effect as observed for the phonon dispersion is found: The mixed approach flips the results for LDA and GGA, i.e., if GGA predicted a lower magnitude of a quantity than LDA using the fully DFT based approach, it predicts a higher magnitude using the mixed approach. As for the agreement with experiment, the following changes due to the mixed approach are observed:

- For the transition elements, one needs to distinguish between LDA and GGA:

  - For LDA, the agreement with experiment mostly **worsens** upon the application of the mixed approach. (One exception is the F_P of Rh for which it improves.)

  - In contrast, the GGA agreement with experiment generally and substantially **improves**. This becomes most evident for Au, where the fully DFT based GGA free energy F_P diverges (cf. Sec. 4.1.7). The mixed approach does not only allow to obtain F_P up to the melting temperature, but it also provides an outstanding agreement with experiment.

- Applying the mixed approach to Al only negligibly affects the agreement with experiment, since the original $T = 0$ K quantities are already in good agreement with experiment.

- In the case of Pb, the mixed approach strongly decreases the agreement with experiment for both LDA and GGA for almost all quantities.

We have thus identified the main source of the error in the GGA description of thermodynamic properties of transition metals: It originates from the errors already inherent in the description of the $T = 0$ K energy surface. This is an important statement and it implies that the entropic contributions can be predicted with a high accuracy. The situation is different for LDA. Here, we have already a good description of the thermodynamics of the transition metals using the fully DFT based approach, while the mixed approach worsens the description. This leads to the conclusion that, for LDA, we have a cancellation of the errors in the $T = 0$ K and entropic quantities. Improving only one yields a decrease in the accuracy of the combined quantity. In summary, fully DFT based calculations yield a better description for LDA, whereas the mixed approach is more suitable for GGA.

This conclusion holds also for Al which can be viewed as a special case with negligible error. However, as pointed out above, the results for Pb show a considerably different behavior. As a possible explanation, we refer to the discussion of the phonon dispersion of Pb at the end of Sec. 4.1.3. In Ref. [131], it was found that spin-orbit coupling (not included in our study) improves the description of the phonon dispersion of Pb. We can therefore only speculate that the thermodynamic properties are also affected by spin-orbit coupling and that including them would yield a description consistent with the results for the transition elements.

4.2 Beyond the conventional scheme: Temperature dependent dynamical matrix

Let us now extend the calculations presented in Sec. 4.1 beyond the $\mathbf{D}^{\text{0K}}$ approximation. For that purpose, the explicit dependence of the dynamical matrix $\mathbf{D}$ on the electronic temperature T^{el} is included as discussed in Sec. 3.3.4. This extension leads to an explicit temperature dependence of

the phonon frequencies [Eq. (4.3)], modifies therefore the quasiharmonic free energy (see Sec. 3.3.4), and consequently also the resulting thermodynamic properties. Out of the nine elements studied in Sec. 4.1, we focus now on two representative elements: aluminum and rhodium, which stand for the elements with a small and with a large electronic contribution, respectively (cf. Fig. 4.6a).

We first discuss rhodium and in particular its LDA phonon frequencies shown in Fig. 4.9. To allow a convenient representation, the T^{el} dependence of the frequencies at four representative $\mathbf{q}$ vectors/branches (marked with the arrows in Fig. 4.9a) is displayed in Fig. 4.9b. We find that most frequencies decrease with T^{el} and only a few ($\approx 10\%$) show the opposite behavior as for the $2/3\,\mathrm{K_T}$ point. The predominant decrease of the frequencies can be traced back to a decrease of the force constants with increasing T^{el}. It can be thus concluded that the influence of electrons softens the inter-atomic force constants at higher temperatures. The magnitude of the change in the frequencies is in the range of 1 meV at the melting temperature (2236K), which might be considered as relatively small ($3\% \ldots 5\%$) when compared to the absolute values (Fig. 4.9a). One needs however to use a different reference for a sensible comparison, which is the implicit temperature dependence of the phonon frequencies caused by the thermal expansion $V^{\mathrm{eq}}(T)$. Figure 4.9c shows this comparison for two $\mathbf{q}$ vectors. Here, indeed a different situation is found: The magnitude of the shift caused by the T^{el} dependence is $\approx 25\%$ of the shift due to the implicit temperature dependence, i.e., due to *quasi*harmonicity. Since however the latter is an important contribution to thermodynamic properties, a decisive questions is: To what extent do the electronic phonon shifts affect thermodynamic properties?

In order to answer this question it is useful to consider first thermodynamic quantities obtained from a quasiharmonic free energy surface at fixed T^{el} as discussed in Sec. 3.3.4. An example is given in Fig. 4.10a, which shows the $C_P(T^{\mathrm{nuc}};T^{\mathrm{el}})$ dependence on the (respectively fixed) value for T^{el} (thick solid lines). The nuclei temperature T^{nuc} is set to T^{m} since this yields the largest contribution and visualizes the effect best. We find that LDA and GGA yield a slightly different qualitative temperature dependence, but the overall change in $C_P(T^{\mathrm{nuc}};T^{\mathrm{el}})$ when going from $T^{\mathrm{el}} = 0\,\mathrm{K}$ to $T^{\mathrm{el}}=T^{\mathrm{m}}$ is for both similarly small ($< 0.05\,k_{\mathrm{B}}$). Let us now, in a second step, contrast this result with the influence of T^{el} on the consistently calculated $C_P(T)$, Eq. (3.71). For that case, the effect is considerably stronger [dots marked with $C_P(T=T^{\mathrm{m}}) - C_P(T^{\mathrm{nuc}}=T^{\mathrm{m}};T^{\mathrm{el}}=0\,\mathrm{K})$ in Fig. 4.10a]: The contribution is $0.29\,k_{\mathrm{B}}$, i.e., 6 times larger.

To explain this rather unintuitive feature, the temperature dependence of the isobaric free energy F_P as shown in Fig. 4.10b needs to be considered. The dashed lines visualize the T^{nuc} dependence of $F_P(T^{\mathrm{nuc}};T^{\mathrm{el}})$ for four different T^{el} values. The heat capacity $C_P(T^{\mathrm{nuc}};T^{\mathrm{el}})$ (thick solid lines in Fig. 4.10a) corresponds roughly to the second derivative along F_P with respect to temperature. (This is not exactly true since the first derivative should be done at constant volume and not pressure, but the essential conclusions are still the same.) The fully consistent $C_P(T)$ corresponds instead to the second derivative of the consistently calculated $F_P(T)$ (thick solid line in Fig. 4.10b). The latter is however constructed by choosing at a certain T^{nuc} the $F_P(T^{\mathrm{nuc}};T^{\mathrm{el}})$ surface for which $T^{\mathrm{nuc}} = T^{\mathrm{el}}$ as illustrated by the filled circles in Fig. 4.10b. This leads to a considerably different curvature and consequently to a different second derivative. We stress the importance of this result: In order to fully include the influence of the T^{el} dependence of the dynamical matrix on derivative thermodynamic quantities, it is not sufficient to calculate the dynamical matrix and hence the quasiharmonic free energy at a single, possibly sufficiently high T^{el}. It is rather necessary to calculate several $\mathbf{D}(T^{\mathrm{el}})$ and to obtain the consistent quasiharmonic free energy $F^{\mathrm{qh}}(\Omega, T^{\mathrm{nuc}}=T;T^{\mathrm{el}}=T)$ as discussed in Sec. 3.3.4.

Taking the fully consistently calculated $C_P(T)$ into account, let us investigate its influence on the final heat capacity and compare it to the other contributions, in particular to the *quasi*harmonic
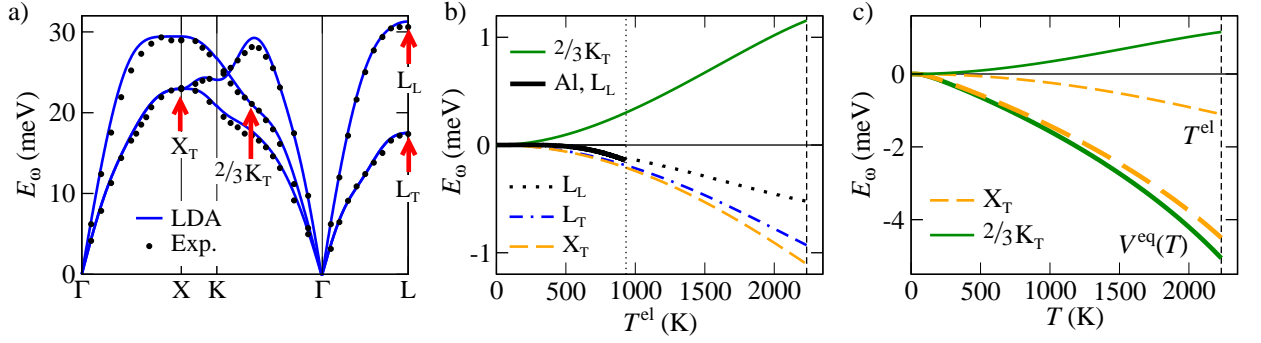
Figure 4.9: Illustration of the influence of temperature on the phonon frequencies of rhodium. The plotted results are for LDA. The GGA dependencies show a similar behavior. a) Quasiharmonic phonon dispersion of rhodium (as in Fig. 4.3). The $\mathbf{q}$ vectors and branches, to which the phonon shifts shown in b) and c) correspond to, are marked with the arrows. The subscripts stand for transversal (T) and longitudinal (L) modes. b) Phonon shifts for rhodium due to the influence of the electronic temperature T^{el} [Eq. (4.3)] at the $\mathbf{q}$ vectors marked in a). Additionally, the shift for aluminum at L_L is shown (black solid line). The dashed (dotted) vertical line corresponds to the melting temperature of rhodium (aluminum). c) Comparison between the temperature dependence shown in b) (thin lines, marked with T^{el}) and the implicit temperature dependence of the phonon frequencies due to the thermal expansion [Eq. (4.2); thick lines, marked with $V^{\mathrm{eq}}(T)$] for two $\mathbf{q}$ vectors.
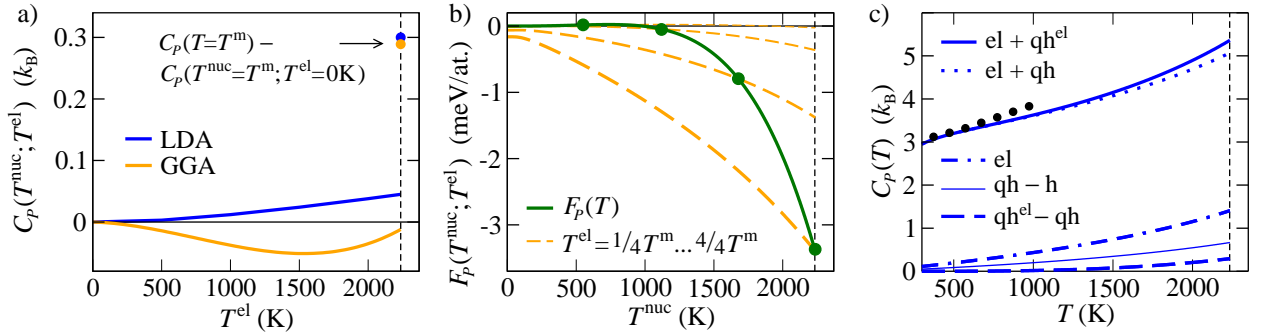

Figure 4.10: Illustration of the influence of the T^{el} dependent phonon shift on thermodynamic properties of rhodium. The dashed vertical line corresponds to the melting temperature of rhodium. a) The dependence of the isobaric heat capacity $C_P(T^{\mathrm{nuc}}; T^{\mathrm{el}})$ from Eq. (3.70) on T^{el} with $T^{\mathrm{nuc}} = T^{\mathrm{m}}$. The curves are referenced with respect to $C_P(T^{\mathrm{nuc}} = T^{\mathrm{m}}; T^{\mathrm{el}} = 0K)$. Additionally, the consistently calculated $C_P(T)$ [Eq. (3.71)] at T^{m}, similarly referenced, is shown. b) The dependence of the isobaric free energy $F_P(T^{\mathrm{nuc}}; T^{\mathrm{el}})$ from Eq. (3.70) on T^{nuc} for four different electronic temperatures (dashed lines): $T^{\mathrm{el}} = 1/4\,T^{\mathrm{m}}$, $2/4\,T^{\mathrm{m}}$, $3/4\,T^{\mathrm{m}}$, and $4/4\,T^{\mathrm{m}}$. The thickness of the lines increases with temperature. Additionally, the consistently calculated free energy $F_P(T)$ (solid line) from Eq. (3.71) is included and the dots indicate the crossing points between $F_P(T)$ and the other curves, which exactly fall together with the fixed T^{el} temperatures of $F_P(T^{\mathrm{nuc}}; T^{\mathrm{el}})$. All curves are referenced with respect to $F_P(T^{\mathrm{nuc}}; T^{\mathrm{el}} = 0\,\mathrm{K})$ and correspond to the LDA functional c) Consistently calculated isobaric heat capacity C_P for the LDA functional in comparison with experiment (black dots; Ref. [132]). The thick solid line corresponds to C_P including electronic (el) and quasiharmonic contributions based on a temperature dependent dynamical matrix (qh$^{\mathrm{el}}$). The dotted line corresponds to a C_P based on the electronic and quasiharmonic (qh) contribution but within the $\mathbf{D}^{\mathrm{0K}}$ approximation [Eq. (2.179)]. The pure electronic contribution is indicated by the dot-dashed line, the quasiharmonic minus the harmonic (h) contribution by the thin solid line, and qh$^{\mathrm{el}}$−qh by the dashed line.

Table 4.2: The contribution of the various mechanisms to the heat capacity of rhodium at T^{m}. "Full" denotes C_P including all mechanisms and the other notation is as in Fig. 4.10c.

	full	h	el	qh$-$h	qh$^{\mathrm{el}}-$qh
$C_P(k_{\mathrm{B}})$	5.36	2.99	1.41	0.67	0.29
$C_P(\%)$	100	56	26	13	5

one. For that purpose, Fig. 4.10c shows the high temperature heat capacity of rhodium. Indeed, the contribution to C_P caused by the T^{el} dependent phonon shift (dashed line) is $\approx 1/2$ of the contribution originating from the thermal expansion, which corresponds to the quasiharmonic minus the harmonic contribution (thin solid line). Using the total heat capacity (thick solid line) as a reference, the contribution due to the T^{el} dependent phonon shift is in the range of 5%. A quantitative comparison of the influence of the various investigated mechanisms is given in Tab. 4.2.

We now turn to aluminum. For its phonon frequencies, we find that most of them show a shift with a magnitude < 0.05 meV at T^{m} (934 K). This is $< 5\%$ of the shift observed for Rh at its melting temperature of 2236 K. An interesting finding is the fact that if considering both elements at the same absolute temperature, say 934 K, the shift for Al is considerably closer in size to that for Rh. This is illustrated in Fig. 4.9b for the L_{L} point. It should however not be expected that, by (artificially) extending the melting temperature of Al, we would achieve the same order of magnitude as for Rh also at higher temperatures. The phonon shift sensibly depends on the electronic density of states and this is significantly different for Al and Rh. In fact, we find for some Al phonon shifts a curvature indicating that the magnitude of the shift will remain constant or maybe even decrease with temperature, in contrast to the linearly increasing magnitude for Rh. The T^{el} dependent phonon shift of Al will be contrasted with the thermal expansion caused shift in Sec. 4.4, where we will be able to compare both also to the shift caused by anharmonicity. The influence of the T^{el} dependent dynamical matrix on the thermodynamics of Al will be discussed in Sec. 4.3.5 together with the results for the anharmonic and vacancy contribution.

4.3   Beyond the quasiharmonic approximation: Anharmonicity and vacancies in Al

4.3.1   Motivation

The fact that, at elevated temperatures, the heat capacity C_P of metals strongly deviates from the harmonic prediction — i.e., the heat capacity at fixed volume C_{V_0} (cf. thin solid line in Fig. 4.6a for Al) — is well known. Indeed, this was pointed out almost 90 years ago in a seminal work by Born and Brody [142]. In this and in many subsequent studies, various mechanisms such as the thermal expansion, the occurrence of anharmonicity, the electronic degrees of freedom [142], or the formation of vacancies [143] have been proposed to explain the non-linear increase. *Ab initio* methods as those used to obtain our results (Sec. 4.1) allow to accurately determine the contribution of two of the proposed mechanisms (Fig. 4.6): the thermal expansion which is captured by the quasiharmonic approximation and the electronic degrees of freedom captured by the temperature dependent DFT approach. However, the *subtle* balance between further contributions, such as explicit anharmonicity and vacancies, has not yet been resolved in the literature even for the simple elementary metals as considered in the present study [144].

Let us focus on aluminum which is a prototypical example. It has been studied intensively in the past decades due to its industrial importance (light weight, corrosion resistance) and the availability of single crystals. Measuring the high temperature heat capacity, however, turns out to be a challenge and despite numerous measurements using various techniques the obtained data scatter largely as shown in the inset of Fig. 4.6a and in Fig. 4.17a below. A quantitative assessment of the subtle influences to the free energy/heat capacity has therefore been considerably hampered. Selected examples of the corresponding literature shall illustrate this fact: Initially, the contribution to the high temperature heat capacity due to thermally activated vacancies was believed to exceed the anharmonic contribution and to cause a non-linear temperature dependence [143]. In 1968, Brooks and Bingham [145] measured the heat capacity of aluminum using dynamic adiabatic calorimetry. Reducing the experimental heat capacity from constant pressure to fixed volume and employing a Debye model, the authors interpreted the non-linear increase in their experimental data as arising mainly from explicit anharmonicity. In 1985, Ditmars et al. [13] measured the enthalpy of aluminum by means of isothermal phase-change calorimetry and Shukla et al. [146] calculated from these results the isobaric heat capacity. Shukla et al. then employed the same reduction scheme as Brooks and Bingham [145] to obtain the fixed volume heat capacity. In a subsequent theoretical analysis, they went beyond the Brooks and Bingham approach [145] by employing empirical potentials rather than a simple Debye model to calculate the fixed volume heat capacity. The comparison of the experimental and theoretical data suggested that, in contrast to the original work by Brooks and Bingham [145], the vacancy contribution dominates the anharmonicity. More recently, in 2004, Forsblom et al. [93] calculated the explicit anharmonicity contribution to the fixed volume heat capacity employing the embedded atom method (EAM; see Sec. 2.2). Their results show, in contrast to the study in Ref. [146], that the contribution due to explicit anharmonicity can well be of a magnitude similar to the one obtained for the vacancy contribution from Ref. [146]. The precise value could not be assessed, since it varied significantly between the used potential parametrizations.[1]

In order to resolve the ongoing controversy and to identify the key mechanisms, two critical issues have to be addressed: a) First, all previous theoretical studies have been restricted to fixed volume calculations, i.e., only C_{V_0} was assessed. This restriction constitutes a serious limitation, since it requires the use of the above mentioned reduction scheme [93, 145, 146] in order to compare to experimental data at constant pressure. This reduction involves model assumptions and experimental input parameters such as the temperature dependent bulk modulus, thermal expansion, and the thermal expansion coefficient. Such an approach is therefore a potential source for uncontrolled errors/error cancellation. b) Second, all previous studies were based on a simple Debye model or on empirical potentials, with Forsblom et al. [93] employing the most sophisticated empirical method, the EAM approach. In Sec. 4.5, we will be able to judge **explicitly** whether the EAM method is suitable for determining the subtle influence of high temperature mechanisms by comparing to the *ab initio* results presented in the following. At this stage, we can only judge **implicitly** from the EAM results of Forsblom et al. [93], which indicate that the presently available empirical potentials might indeed fail in this respect due to the scatter between predictions from different potentials.[1]

The aim of the investigations presented in Sec. 4.3 is to overcome both limitations. For that purpose, we consider the complete volume and temperature dependent free energy surface of aluminum including vacancies and anharmonicity. As discussed in Sec. 2.4, the explicitly calculated volume

---

[1]Forsblom et al. [93] employed three potential parametrizations and obtained at the melting temperature an anharmonic contribution to the fixed volume heat capacity of 0.06 k_{B}, 0.03 k_{B}, and −0.05 k_{B} (cf. Fig. 2 in Ref. [93]; k_{B}: Boltzmann constant). Shukla et al. [146] estimated a vacancy contribution to the fixed volume heat capacity of 0.08 k_{B} at the melting point [cf. Eq. (15) and Fig. 4 in Ref. [146] and our discussion in Sec. 4.3.6]

dependence provides access to properties at constant pressure which corresponds to the typical experimental condition. The DFT approach allows on the other hand for an unbiased parameter-free derivation of the desired quantities, in contrast to the difficulties occurring for the empirical approaches. In fact, our DFT results will eventually provide a test-bed to evaluate the EAM potentials *a posteriori* (Sec. 4.5). Specifically, we computed $F(V,T)$ using the volume optimized approach and the UP-TILD method according to Eqs. (3.35) to (3.37),

$$\boxed{F^{\mathrm{p}}(V,T) = F_0^{\mathrm{p,el}}(V,T) + F^{\mathrm{p,qh}}(V,T) + F^{\mathrm{p,clas,ah}}(V,T)} \tag{4.9}$$

$$F(V,T) = (1-cN^{\mathrm{v}})\, F^{\mathrm{p}}\left(\frac{V-c\Omega^{\mathrm{v}}}{1-cN^{\mathrm{v}}},T\right) + cF^{\mathrm{v}}(\Omega^{\mathrm{v}},T;N^{\mathrm{v}}) + F^{\mathrm{c}}(c), \tag{4.10}$$

$$\boxed{F^{\mathrm{v}}(\Omega^{\mathrm{v}},T;N^{\mathrm{v}}) = F_0^{\mathrm{v,el}}(\Omega^{\mathrm{v}},T;N^{\mathrm{v}}) + F^{\mathrm{v,qh}}(\Omega^{\mathrm{v}},T;N^{\mathrm{v}}) + F^{\mathrm{v,clas,ah}}(\Omega^{\mathrm{v}},T;N^{\mathrm{v}})} \tag{4.11}$$

the various free energy contributions being defined in Tab. 3.1 and the remaining quantities in Sec. 3.1.2. Further, following the philosophy developed in Sec. 4.1 all free energy contributions were calculated using both xc functionals: LDA and GGA-PBE. To allow a convenient discussion, we focus in the following on: C_P, α, and F_P. The heat capacity is the main quantity of interest. The expansion coefficient is equally sensitive as C_P, experimentally however more accurately accessible, which will allow a cross check of our results (cf. Sec. 4.3.7). The free energy is included to show the fact that small absolute F_P values can have significant effects on derived properties (cf. the curves for the vacancies in Fig. 4.12 below).

4.3.2 Pseudopotential evaluation

The technical aspects of the calculations in the present section, Sec. 4.3, were discussed in detail in Sec. 3.4. It was also pointed out why it is advantageous to employ the pseudopotential rather than the PAW method in the case of aluminum DFT calculations as considered here. However, due to missing reference data, the actual evaluation of the used pseudopotential remained an open issue. Now, that the validated PAW results from Sec. 4.1 are available, we are in a position to fill this gap. The evaluation is split into four steps:

1) Let us first consider the $T = 0\,\mathrm{K}$ results given in Tab. 4.1. We could in principle compare directly to the LAPW+lo results here. For consistency with the following steps, the differences to the PAW results are given instead. For both pseudopotentials, LDA and GGA, a rather good agreement is found: The lattice constant is under(over)estimated only by -0.4% (0.2%) for LDA (GGA). The bulk modulus deviates by -2.4% (-3.8%) for LDA (GGA).

2) A more severe test concerns thermodynamic quantities. To perform this test, we calculate the electronic and quasiharmonic free energy contributions entering Eq. (4.1) using the pseudopotential method, derive the thermodynamic quantities, and compare with the corresponding PAW results (Figs. 4.4 to 4.8). Note that this test differs from the evaluation of the PAW method against the LAPW+lo method (Sec. 4.1.4) where only a single term from Eq. (4.1) was considered. Here, the pseudopotential result falls together with the PAW result on the given scales, except for α, the most sensitive quantity (Fig. 4.5). We therefore mentioned/displayed the pseudopotential (pp) result only in Fig. 4.5. For the quantities of interest here and focusing on the GGA results at T^{m}, we find that the α (C_P) computed using the pseudopotential

method overestimates the PAW result by 4.8% (1.4%) or $0.18 \cdot 10^{-5}$ K^{-1} ($0.07 k_{\mathrm{B}}$). For F_P, an underestimation of 0.9% or 3 meV/atom is found.

3) It is necessary to determine the source of the errors given in 2). For that purpose, we perform a pseudopotential calculation exchanging $E_{g,0}^{\mathrm{el}}(V)$ [Eq. (4.1)] by the corresponding PAW data, i.e., the $T = 0$ K errors given in 1) are removed. We then find that for instance the error in α for GGA at T^{m} [from 2)] reduces from 4.8% to 1.2%. This means that 3/4 of the error in the thermodynamic properties given in 2) are caused by the $T = 0$ K errors given in 1). In a similar manner, the errors arising from $F^{\mathrm{qh,0K}}$ and $\widetilde{F}^{\mathrm{el}}$ were separated out and the error in $\widetilde{F}_0^{\mathrm{el}}$ was found to be negligible as compared to $F^{\mathrm{qh,0K}}$. Thus, the remaining 1/4 of the errors in the thermodynamic properties is coming from the quasiharmonic free energy $F^{\mathrm{qh,0K}}$.

4) It would be desirable to extend the tests performed in 2) beyond a comparison to quasiharmonic properties for the following reason: The quasiharmonic free energy is obtained from the dynamical matrix (Sec. 2.3.3) which depends on the local electronic free energy surface in the vicinity of the $T = 0$ K equilibrium nuclei positions. The atomic structures determining the anharmonic free energy, the quantity of major interest in the following sections, will however typically correspond to structures far from equilibrium. A direct evaluation of these structures by performing an extra PAW molecular dynamics run would be computationally rather expensive. The extension of the UP-TILD method discussed in Sec. 3.2.4 provides here an efficient alternative. We thus calculated $\left\langle \Delta F^{\mathrm{el}} \right\rangle_\lambda^{\mathrm{UP,\,pp \to PAW}}$, Eq. (3.51), and find also for this test that the pseudopotential and PAW results agree very well: $\left\langle \Delta F^{\mathrm{el}} \right\rangle_\lambda^{\mathrm{UP,\,pp \to PAW}} \approx 0.5$meV/atom (at 900 K and $\lambda = 0.5$).

The *technical* results of the tests given in points 1) to 4) have a very important consequence for the *physical* results discussed in Secs. 4.3.3 to 4.3.7: The $T = 0$ K energy (3/4) and quasiharmonic free energy (1/4) have been found to be the dominating sources for the errors of the pseudopotential properties while the remaining free energy contributions have been identified to yield far smaller errors. This is important since the absolute values of these "remaining" contributions will turn out to be very small compared to the quasiharmonic contribution (see Fig. 4.11 below). Based on the tests presented here, we have thus ensured that the small absolute numbers of the "remaining" contributions are reliable. In contrast, the final curves based on all free energy contributions (Fig. 4.17 below) do contain the errors given in 2). The corresponding error bars are therefore included in these figures.

4.3.3   Explicit anharmonicity: Direct *ab initio* calculations

A key result of the calculations presented in Sec. 4.3 is that the dominating contribution to thermodynamic properties of aluminum is contained in the quasiharmonic description of the perfect crystal. All remaining contributions can be considered as small perturbations on top of the quasiharmonic result. This is demonstrated schematically in Fig. 4.11, while Fig. 4.12 contains a more detailed description and Tab. 4.3 gives actual numbers at the melting point. In this and the following section, we concentrate on discussing the results for explicit anharmonicity, for the influence of T^{el} on the nuclei motion (quasi- and anharmonic; Sec. 4.3.5), and vacancies (Sec. 4.3.6), since the electronic and quasiharmonic contribution were intensively treated in Sec. 4.1. In Sec. 4.3.7, all contributions are combined and the resulting thermodynamic properties are compared to experiment.

Let us thus focus on the classical anharmonic free energy of the perfect crystal. Previous *ab initio* studies of the anharmonic free energy are rather scarce [130, 147]. One exception is the work by Večadlo and Alfè [130], who determined the melting curve of aluminum under extreme
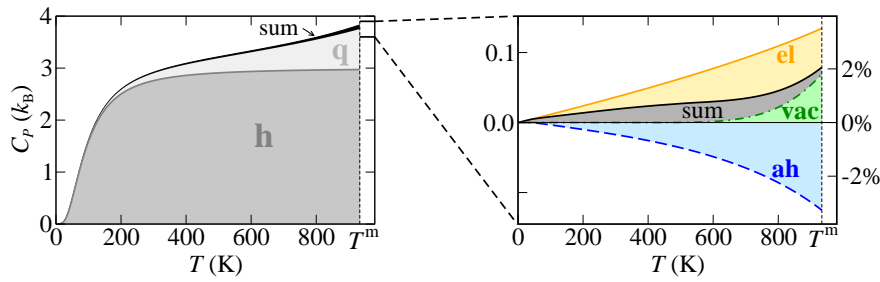
Figure 4.11: Illustration of the dominant role played by the quasiharmonic (qh=q+h) contribution for the example of the heat capacity. The right diagram magnifies the "smaller" contributions. See Fig. 4.12/Tab. 4.3 below for further details.
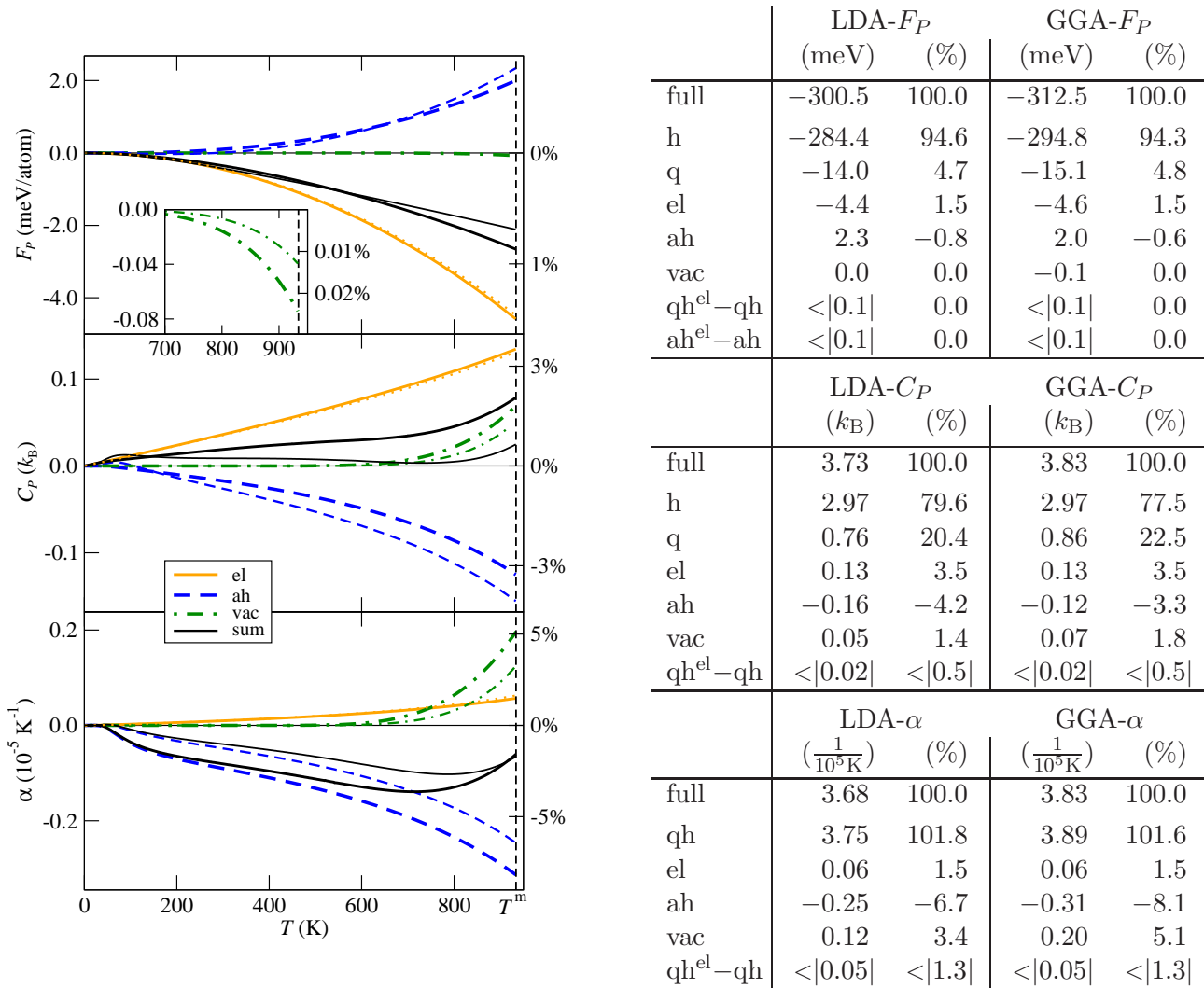

| | LDA-F_P | | GGA-F_P | |
	(meV)	(%)	(meV)	(%)
full	−300.5	100.0	−312.5	100.0
h	−284.4	94.6	−294.8	94.3
q	−14.0	4.7	−15.1	4.8
el	−4.4	1.5	−4.6	1.5
ah	2.3	−0.8	2.0	−0.6
vac	0.0	0.0	−0.1	0.0
qh^{el}−qh	<|0.1|	0.0	<|0.1|	0.0
ah^{el}−ah	<|0.1|	0.0	<|0.1|	0.0

| | LDA-C_P | | GGA-C_P | |
	(k_B)	(%)	(k_B)	(%)
full	3.73	100.0	3.83	100.0
h	2.97	79.6	2.97	77.5
q	0.76	20.4	0.86	22.5
el	0.13	3.5	0.13	3.5
ah	−0.16	−4.2	−0.12	−3.3
vac	0.05	1.4	0.07	1.8
qh^{el}−qh	<|0.02|	<|0.5|	<|0.02|	<|0.5|

| | LDA-α | | GGA-α | |
	($\frac{1}{10^5 K}$)	(%)	($\frac{1}{10^5 K}$)	(%)
full	3.68	100.0	3.83	100.0
qh	3.75	101.8	3.89	101.6
el	0.06	1.5	0.06	1.5
ah	−0.25	−6.7	−0.31	−8.1
vac	0.12	3.4	0.20	5.1
qh^{el}−qh	<|0.05|	<|1.3|	<|0.05|	<|1.3|

Figure 4.12/Table 4.3: Influence of the various investigated excitation mechanisms on the free energy F_P, the heat capacity C_P, and the expansion coefficient α of aluminum.

Figure 4.12: The electronic (el), anharmonic (ah), vacancy (vac) contribution and their sum. Thick lines show GGA results. LDA results are either shown as thin lines or coincide with the GGA result. The dotted lines show the el contribution from a PAW calculation (all other results are for pseudopotentials). The right axes are scaled with respect to the 'full' GGA values at the melting temperature T^m (indicated by the vertical dashed line) given in Tab. 4.3. The inset shows an enlargement of the vacancy contribution to F_P at high temperatures.

Table 4.3: The quasiharmonic contribution (qh) is split for F_P and C_P into its harmonic (h) and "quasi" (q) part, i.e., the thermal expansion. The contribution due to inclusion of the T^{el} dependence in the dynamical matrix is indicated by "qh^{el}−qh". The effect of including the T^{el} dependence in the anharmonic contributions is indicated by "ah^{el}−ah" (F_P only).
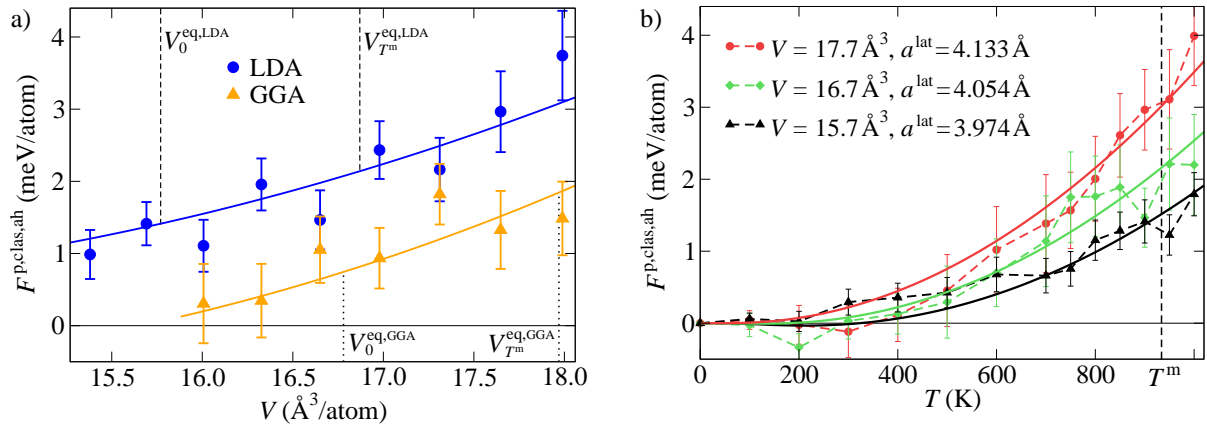
Figure 4.13: Explicitly anharmonic free energy for the perfect crystal $F^{\mathrm{p,clas,ah}}$ of aluminum. The calculated values are represented by the dots/diamonds/triangles. At each point the statistical error σ^{err}, Eq. (2.202), is represented by the vertical solid lines. The solid lines are fits using the analytical model (see Sec. 4.3.4). a) Volume dependence of $F^{\mathrm{p,clas,ah}}$ at 900 K for both investigated functionals. The vertical dashed (dotted) lines indicate the 0 K (including zero-point vibrations) and the melting temperature T^{m} equilibrium volumes of LDA (GGA), $V_0^{\mathrm{eq,LDA}}$ ($V_0^{\mathrm{eq,GGA}}$) and $V_{T^{\mathrm{m}}}^{\mathrm{eq,LDA}}$ ($V_{T^{\mathrm{m}}}^{\mathrm{eq,GGA}}$), respectively. b) Temperature dependence of $F^{\mathrm{p,clas,ah}}$ at three different volumes for the LDA functional. The dashed lines in-between are a guide for the eye. GGA results show the same qualitative dependence. The melting temperature T^{m} is indicated by the vertical dashed line.

temperatures and pressures. The temperature and pressure region investigated in their work is very different from ours so that the corresponding anharmonic free energies cannot be used here.

A representative set of our results for $F^{\mathrm{p,clas,ah}}$ is shown in Fig. 4.13. Despite considerable statistical errors, the figures provide some clear trends: First we note that $F^{\mathrm{p,clas,ah}}$ is positive in the whole region except for a small low temperature regime, which is likely due to statistical noise. The absolute values close to the melting temperature are ≈ 2 meV, which is about two orders of magnitude smaller than $F^{\mathrm{p,qh}}$. The volume dependence is positive with a small positive curvature. The temperature dependence has a curvature which goes beyond second order. The results for LDA and GGA are qualitatively similar. Comparing relative $F^{\mathrm{p,clas,ah}}$ values, i.e., referenced to the corresponding equilibrium volume, LDA and GGA results differ by an almost constant shift. At 900 K, this shift is ≈ 0.5 meV (see Fig. 4.13a).

The anharmonic contribution to the free energy has a significant influence on α and C_P as compared to the electronic contributions. Figure 4.12 shows that α is shifted downwards by $\approx -7\%$ and C_P by $\approx -3.5\%$. In fact, the negative anharmonic contribution to C_P cancels the positive contribution from electronic excitations over a large temperature range yielding a close to zero net contribution. For α, the anharmonic contribution is much stronger (roughly a factor of 5) compared to the electronic one yielding a net decrease of the expansion coefficient. An important conclusion from these results is that explicit anharmonicity cannot be considered as the origin of the non-linear increase, which applies to both the expansion coefficient and the heat capacity. In fact, even the sign is opposite to the one previously assumed [145]: For both quantities, anharmonicity results in a reduction rather than in an increase at high temperatures.

A major source of this unexpected behavior lies in the increase of $F^{\mathrm{p,clas,ah}}$ with increasing volume. To verify this statement, we artificially forced $F^{\mathrm{p,clas,ah}}(V,T)$ in a separate calculation to

be volume independent: $F^{\text{fix}}(V, T) = F^{\text{p,clas,ah}}(V(T{=}0\,\text{K}), T)$. Note that the explicit temperature dependence is fully included. Replacing the full anharmonic free energy by F^{fix} makes the anharmonic contribution to α practically disappear, while the anharmonic contribution to C_P is reduced by $\approx 60\%$.

4.3.4   Explicit anharmonicity: Introduction of an analytical model

In order to resolve the physical origin of the positive volume dependence, we developed an approximate analytical model. The key idea is to replace the full phonon spectrum by a single effective frequency and describe anharmonicity by its renormalization. Within this model (mod), the anharmonic free energy $F^{\text{ah,mod}}$ is expressed as:

$$F^{\text{ah,mod}}(V, T) = \widetilde{F}^{\text{qh}}(T; \overline{\omega}^{\text{qh}}(V) + \overline{\omega}^{\text{ah}}) - \widetilde{F}^{\text{qh}}(T; \overline{\omega}^{\text{qh}}(V)). \tag{4.12}$$

Here, $\overline{\omega}^{\text{qh}}$ is an effective/averaged quasiharmonic frequency, $\overline{\omega}^{\text{ah}}$ the renormalization shift due to anharmonicity, and $\widetilde{F}^{\text{qh}}(T; \overline{\omega})$ is obtained from an adapted version of Eq. (2.161):

$$\widetilde{F}^{\text{qh}}(T; \overline{\omega}) = k_{\text{B}} T \ln\left[1 - \exp\left(-\frac{\hbar\overline{\omega}}{k_{\text{B}}T}\right)\right]. \tag{4.13}$$

To obtain $\overline{\omega}^{\text{qh}}$, we use our computed quasiharmonic phonon frequencies $\omega_{\mathbf{G}^{\text{sc}}, s}$. In particular, we calculate the average [cf. Eqs. (2.125) and (2.161)]:

$$\overline{\omega}^{\text{qh}}(V) = (3N_n)^{-1} \sum_{\mathbf{G}^{\text{sc}}}^{N_n} \sum_{s}^{3} \omega_{\mathbf{G}^{\text{sc}}, s}(V). \tag{4.14}$$

Figure 4.14b (black solid line) shows the volume dependence of $\overline{\omega}^{\text{qh}}$. The anharmonic shift $\overline{\omega}^{\text{ah}}$ in Eq. (4.12) accounts for the anharmonic free energy. Tests based on our *ab initio* data showed that, in order to capture the essential qualitative features, it is sufficient to assume $\overline{\omega}^{\text{ah}}$ to be volume independent. The magnitude of this volume independent shift is used as a free parameter to fit to the *ab initio* data and to explore the physics embodied in the model. The resulting anharmonic free energy for three different $\overline{\omega}^{\text{ah}}$ is shown in Fig. 4.14c. If we assume a negative shift, $F^{\text{ah,mod}}$ is negative and shows a negative volume dependence. Thus, to reproduce the positive anharmonic free energy observed in the *ab initio* results, the renormalization shift must be positive, i.e., the renormalized phonons must be blue-shifted in average. By introducing a linear volume and temperature dependence[2] in $\overline{\omega}^{\text{ah}}$ also a good quantitative description of the full volume and temperature dependence of the anharmonic free energy surface is achieved. The quality of this approach is shown in Fig. 4.13 (solid lines). It was also successfully employed for the parametrization of the corresponding vacancy contribution (Fig. 4.16).

   The key result we obtain from this analysis is that the vibrational free energy and hence the major part of the thermodynamics of aluminum at high temperatures, up to the melting point, can be well described by renormalized phonon frequencies. Compared to the quasiharmonic frequencies, the renormalized frequencies are in average energetically harder (blue-shifted), but exhibit a similar volume dependence.

---

[2]We use $\hbar\overline{\omega}^{\text{ah}} = a + bT + cV$ and obtain the following fitting parameters: LDA: $a = -2.6$ meV, $b = 9.9 \cdot 10^{-4}$ meV/K, $c = 0.15$ meV/Å^3 and GGA: $a = -4.5$ meV, $b = 3.1 \cdot 10^{-4}$ meV/K, $c = 0.27$ meV/Å^3.
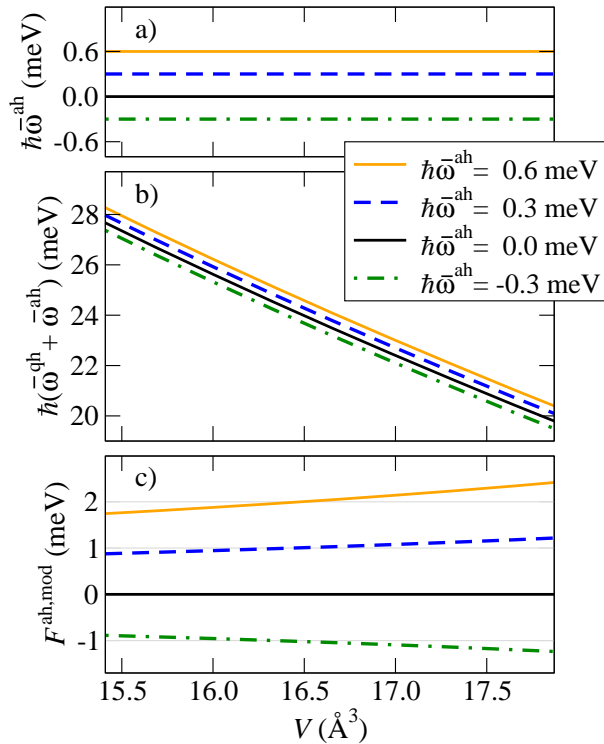
Figure 4.14: Illustration of the analytical model (see text) describing the origin of the anharmonic free energy: a) Volume independent anharmonic frequency $\overline{\omega}^{\mathrm{ah}}$. b) Effective frequency resulting from the sum of the quasiharmonic frequency $\overline{\omega}^{\mathrm{qh}}$ and $\overline{\omega}^{\mathrm{ah}}$. c) Model anharmonic free energy $F^{\mathrm{ah,mod}}$ at the melting temperature as obtained from Eq. (4.12) and the frequencies from b).

4.3.5   Influence of the electronic temperature on the nuclei motion

The influence of the T^{el} dependent dynamical matrix on the thermodynamics of Al was much more challenging to obtain than the one for Rh which has been discussed in Sec. 4.2. The reason for this difficulty is the small absolute size of this influence and the extremely sensitive dependence of the thermodynamic properties of Al on the electronic k sampling. Based on the convergence checks performed in Sec. 3.4, we were however able to estimate rather low limiting bounds, which are listed in Tab. 4.12. For instance for C_P, we find that the T^{el} dependent phonon shift yields a change with a magnitude below $0.02\,k_{\mathrm{B}}$ at T^{m}. This result corresponds already to the consistently calculated $C_P(T)$ (cf. the discussion in Sec. 4.2 for Rh). Compared to the corresponding contribution for Rh ($0.3\,k_{\mathrm{B}}$), this is rather low. Using however the contribution of the vacancies to the C_P of Al ($0.05\,k_{\mathrm{B}}$) as a reference, we are in the same order of magnitude and the influence of the electronic phonon shift is thus not negligible. A further reduction of the uncertainty in this contribution would however exceed sensible computational times at present. For this study, we therefore use the estimated limits as error bounds in the final thermodynamic properties (Fig. 4.17).

In Sec. 3.3.5, we have discussed that, similarly as the dynamical matrix, also the higher order contributions, i.e., explicit anharmonicity, depend on the electronic temperature. To determine the corresponding contribution, we used a further advantage of the hierarchical UP-TILD method: We can apply the method not only to a set of varying convergence parameters as discussed in Sec. 3.2.4, but also to a set of varying physical parameters as for instance various electronic temperatures. We thus calculated the change in the anharmonic free energy upon varying the electronic temperature and find it to be $\approx 50\%$ of the change caused by the T^{el} dependence of the dynamical matrix. The exact contribution cannot however be singled out due to the above discussed scatter in the T^{el} dependence of the dynamical matrix. The reason is that the T^{el} dependent dynamical matrix constitutes the correct reference potential which should be used to obtain the T^{el} dependence of the anharmonic shift [see Eq. (3.79)].

4.3.6   Vacancies: Electronic, quasiharmonic, and anharmonic excitations

In this section, we discuss the second mechanism proposed as a source for the non-linear increase in the experimental heat capacity of aluminum: The thermal formation of vacancies. In advance, we comment on self interstitials and show that this other possible type of thermally activated point defects can be excluded as a potential candidate for explaining the non-linear increase.

In aluminum (fcc crystal), two self interstitial sites are available: the tetrahedral and octahedral. The octahedral site is known [148] to be energetically preferred and its formation energy has been calculated from *ab initio* giving $E^{\mathrm{f}} = 3.4$ eV [148]. This is considerably higher than for vacancies (cf. Tab. 4.4 below) and would indeed yield only negligible self interstitial concentrations. However, inspecting Ref. [148], we found that a rather small supercell (16 atoms) and k sampling (1024k·atom) were used. Both values are critical since a self interstitial requires larger supercells than the vacancy due to its stronger strain field (cf. with the vacancy supercells in Sec. 3.4.4.3) and since our results show that Al is one of the most sensitive elements with respect to the k sampling (Fig. 3.8). We therefore investigated in detail the influence of these parameters in a separate study [149] and found indeed a different converged formation energy of $E^{\mathrm{f}} = 2.8$eV. Even more interestingly, an additional phonon analysis revealed that the octahedral site is in fact meta stable, i.e., a saddle point on the energy surface. Following the relaxation path resulted in a new self interstitial configuration with a different symmetry: two Al atoms sharing an interstitial site (dumbbell geometry). Our finding is consistent with empirical knowledge about self interstitials in fcc metals [150]. As a consequence, for thermodynamic properties, the dumbbell configuration needs to be considered instead of the original octahedral site due to its energetical preference. The actual decrease to $E^{\mathrm{f}} = 2.5$ eV does however not change the conclusion that self interstitials in Al do not yield a noticeable contribution to thermodynamic properties as we explicitly verified by using Eq. (3.38).

As for the vacancies, monovacancies are believed to be dominating, while the influence of divacancies has been found to be negligible due to a negative (repulsive) binding energy [89]. Starting with the seminal work by Gillan [30], monovacancies in aluminum have been studied extensively in the past by *ab initio* techniques [89, 148, 151–153]. However, the focus has been mainly on $T = 0$ K properties. Finite temperature effects, except for the configurational entropy, have not been included. One exception is a combined study [89] where the $T = 0$ K energetics and the harmonic contribution have been determined by DFT, while the remaining finite temperature effects have been obtained by employing empirical potentials (referred to as the ai/ep-approach in the following).

Our results for the full [i.e., including all free energy terms in Eqs. (4.9) and (4.11)] contribution of the vacancies to F_P, α, and C_P are shown in Fig. 4.12. The contribution to F_P is negative and rather small, ≈ -0.1 meV/atom at T^{m}, i.e., well below 0.1% of the quasiharmonic reference. Surprisingly, despite the small free energy contribution due to vacancies, they substantially contribute to α and C_P in the temperature window from ≈ 700 K up to T^{m}. This effect is related to the strong non-linear decrease of this contribution with temperature. For both quantities, α and C_P, the anharmonic contribution is positive and amounts to $\approx 5\%$ and $\approx 2\%$ of the quasiharmonic reference at T^{m}, respectively.

With the fully *ab initio* calculated results at hand, we have a reference against which the performance/accuracy of previously suggested empirical approaches for estimating the effect of vacancies can be tested. One such empirical estimation [146] starts from the following expression for the vacancy contribution to the vacancy heat capacity C_P^{vac}:

$$C_P^{\mathrm{vac}} = \left(\frac{E^{\mathrm{f}}}{k_{\mathrm{B}}T} \right)^2 \exp\left(-\frac{E^{\mathrm{f}} - TS^{\mathrm{f}}}{k_{\mathrm{B}}T} \right) . \qquad (4.15)$$

Table 4.4: The formation energy E^{f} and entropy of formation S^{f} for various approaches and combinations of the free energy contributions used for the calculation of vacancy properties of aluminum. ai/ep indicates values for the coupled *ab initio*-empirical potentials approach from Ref. [89]. The further values (also the experimental) are obtained by fitting the vacancy concentrations over the temperature range given in Fig. 4.15 to the function $\exp[-(E^{\text{f}} - TS^{\text{f}})/k_{\text{B}}T]$. The notation is as in Fig. 4.15.

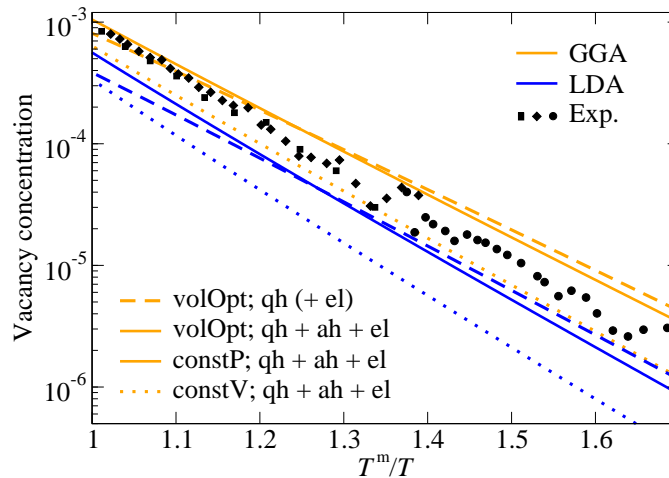|	E^{f} (eV)		S^{f} (k_{B})	
	LDA	GGA	LDA	GGA
volOpt; qh	0.65	0.58	0.2	0.1
volOpt; qh + el	0.65	0.58	0.2	0.1
volOpt; qh + ah + el	0.78	0.68	2.2	1.5
constP; qh + ah + el	0.78	0.68	2.2	1.5
constV; qh + ah + el	0.85	0.75	2.5	1.9
ai/ep [89]	0.78	0.61	1.6	1.3
experiment	0.75		2.4	

Figure 4.15: Equilibrium vacancy concentration of aluminum as a function of the inverse temperature multiplied by the melting temperature T^{m}. Results for the two investigated exchange-correlation functionals, LDA and GGA, are shown. The solid lines correspond to a volume optimized (volOpt) calculation, Eq. (3.35), with all free energy terms included in Eqs. (3.36) and (3.37). They also correspond to a calculation based on the constant pressure (constP) approach, Eq. (3.29), including all free energy contributions, since the results for the volOpt and constP approach fall together on the given scale. The dashed lines correspond to a volume optimized calculation excluding the anharmonic free energy $F^{\text{clas,ah}}$, in Eqs. (3.36) and (3.37). The dashed lines also correspond to a volume optimized calculation excluding the anharmonic, $F^{\text{clas,ah}}$, and electronic, $\widetilde{F}_0^{\text{el}}$, (indicated by the parentheses enclosing the electronic contribution in the legend), terms in Eqs. (3.36) and (3.37) [see also Eq. (3.53)]. The dotted lines correspond to a calculation based on the constant volume (constV) approach, Eq. (3.34), and including all free energy terms. The squares indicate experimental values from Ref. [154] (differential dilatometry). The diamonds/circles indicate experimental values from Ref. [155] (differential dilatometry/positron annihilation).
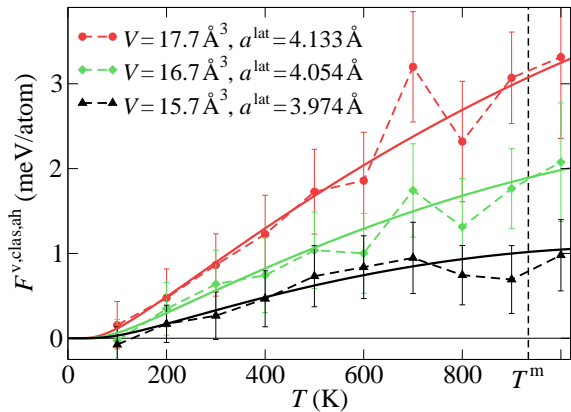
Figure 4.16: Temperature dependence of the explicitly anharmonic free energy $F^{\mathrm{v,clas,ah}}$ for the vacancy cell of aluminum at three different volumes for the LDA functional. The dots/diamonds/triangles represent the calculated values. At each point the statistical error σ^{err}, Eq. (2.202), is represented by the vertical solid lines. The dashed lines in-between are a guide for the eye and the solid lines are fits using the analytical model (see Sec 4.3.4). GGA results show the same qualitative dependence. The melting temperature T^{m} is given by the vertical dashed line.

Here, E^{f} is the formation energy, which was set in Ref. [146] to the experimental value 0.66 eV from Ref. [156]. Further, the entropy of formation S^{f} was estimated to be $1.4\,k_{\mathrm{B}}$ based on experimental heat capacity data and empirical potential calculations of the heat capacity excluding vacancy contributions. Using these values, the authors of Ref. [146] estimated an increase in C_P of $0.08\,k_{\mathrm{B}}$ at T^{m} due to vacancies. This approximate value based on experimental input is in surprisingly good agreement with our explicitly calculated values of $0.05\,k_{\mathrm{B}}$ for LDA and $0.08\,k_{\mathrm{B}}$ for GGA.

We finally turn to the comparison with the ai/ep-approach, discuss the validity of the constant volume/pressure approach, and analyze the influence of the various free energy contributions to the vacancy concentration. Figure 4.15 summarizes the corresponding results. A comparison with experiment (squares, diamonds, and dots) shows overall a good agreement: Using the full approach, i.e., the volume optimized formalism including all free energy contributions, LDA and GGA are very close to experiment and form a lower and upper bound, in consistence with our results for other thermodynamic properties in Sec. 4.1. Further, it becomes apparent that the constant pressure approach is a very good approximation to the volume optimized formalism, whereas the constant volume approach yields significantly lower concentrations. To enable a comparison with the ai/ep approach and to allow a quantitative analysis of the influence of the various free energy contributions, we deduced from the temperature dependence of the vacancy concentrations the formation energy E^{f} and entropy S^{f}. The data compiled in Tab. 4.4 show a good agreement of our full approach with the ai/ep approach [93]. With respect to the influence of the free energy contributions Tab. 4.4 reveals: The electronic contribution is negligible. In contrast, the anharmonic contribution to the vacancies has a large influence on the entropy of formation increasing it from $0.2\,k_{\mathrm{B}}$ ($0.1\,k_{\mathrm{B}}$) to $2.2\,k_{\mathrm{B}}$ ($1.5\,k_{\mathrm{B}}$) for LDA (GGA). This strong influence can be traced back to the temperature dependence of the explicitly anharmonic free energy surface for the vacancy cell. From Fig. 4.16, it becomes apparent that the anharmonic free energy is concave at higher temperatures in contrast to the convex temperature dependence of the perfect crystal anharmonic free energy (Fig. 4.13b). The corresponding difference favors the creation of vacancies.

4.3.7   Comparison between theory and experiment

So far, the terms entering Eqs. (4.9) to (4.11) have been discussed separately. Now, we construct the full free energy surface $F(V,T)$ including all excitations, calculate the final thermodynamic quantities, and compare with experiment focusing on α and C_P. In contrast to the comparisons performed in Secs. 4.1.4 and 4.1.5, we are now interested in small effects in the high temperature region which is thus shown magnified (Fig. 4.17). The low temperature region is also magnified to illustrate the different experimental situations in the two extreme temperature regimes. Further,

to allow an unbiased comparison, an extensive set of experimental data is included. Let us start with C_P.

Figure 4.17a shows a very good agreement between theory and experiment for the low temperature heat capacity, where experimental scatter is negligible. In the temperature region up to ≈ 600 K, the majority of the experimental data agree well with our *ab initio* results. Above 600 K, there is large experimental scatter making a fair comparison with the *ab initio* values difficult. A general trend is that almost all experiments performed later than 1950 (solid squares in Fig. 4.17a) show a steeper increase towards the melting temperature making the *ab initio* data a lower bound. Based on the presently available experimental measurements, a final conclusion whether the remaining small deviation ($\approx 0.2\,k_{\mathrm{B}}$ at T^{m}) is due to the limited accuracy of presently available exchange-correlation functionals or due to errors in experiment is not possible. The fact that the *ab initio* results form a lower bound to the scattered experimental data suggests that there are additional sources for the heat capacity in the experimental measurements, however of varying influence. Possible sources are imperfections within the sample such as dislocations, grain boundaries, impurities, etc. Systematic deviations can also be caused by the experimental setup, such as for instance the sample holder. In particular, the cubic dependence of the radiant heat-exchange coefficient on the temperature is an experimental challenge [168].

In contrast to the heat capacity, which is experimentally difficult to measure and shows large scatter in the data, the temperature dependence of the thermal expansion coefficient requires the determination of inter-atomic distances which can be obtained by X-ray measurements with high precision. The experimental together with our *ab initio* data are shown in Fig. 4.17b. The *ab initio* values agree with the experimental data over the full temperature range up to the melting temperature T^{m}. Even details such as the curvature of α at high temperatures are well reproduced. It is important to note that only the combined interplay of the electronic, quasiharmonic, anharmonic, and vacancy contribution (black solid lines in Fig. 4.12) provides this agreement. Particularly important for the steep increase close to the melting temperature is the strongly non-linear increase due to vacancy formation.

4.4 Quantum mechanical treatment of the anharmonic contribution

In Sec. 4.1.3, we have pointed out that there are two distinct *explicit* temperature dependencies of the phonon frequencies, given by Eqs. (4.3) and (4.4), and in Sec. 4.2 we have presented our results for the latter dependency. The first one, which is caused by phonon-phonon interactions, is implicitly contained in the anharmonicity calculations presented in Sec. 4.3.3. Its influence on the thermodynamic properties is therefore also implicitly included and this actually allowed us to perform the final comparison with experimental data already in Sec. 4.3.7. As discussed in detail in Sec. 2.3.5, it is nonetheless desirable to study the phonon shift due to phonon-phonon interaction explicitly with a complementary method, i.e., with perturbation theory. The main reason is the fact that the anharmonic calculations based on molecular dynamics are purely classical, while the perturbation theory as presented in Sec. 2.3.7 fully contains quantum mechanical effects. Corresponding calculations are however computationally extremely expensive and in order to render the calculations presented in this section feasible, we focused on a single $\mathbf{q}$ vector and branch of the phonon dispersion ($\mathrm{L_L}$ point; see Fig. 4.18) at constant volume. The choice of the $\mathrm{L_L}$ was motivated by the fact that a previous model potential study [176] (discussed in detail below) found the largest shift for this $\mathbf{q}$ vector.

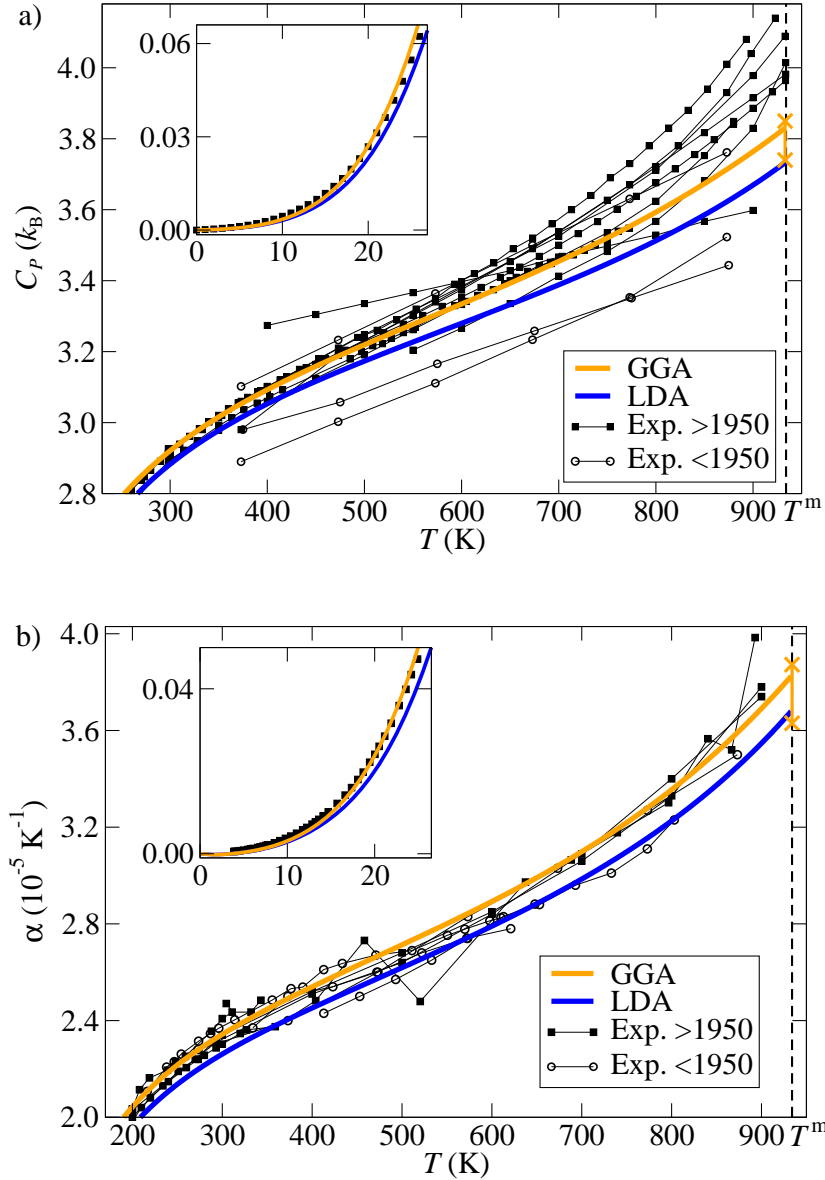The results for the third and fourth order phonon shift are presented in Fig. 4.18. It becomes

Figure 4.17: a) Heat capacity C_P and b) thermal expansion coefficient α including all investigated excitation mechanisms compared to experiment. The melting temperature T^m is given by the vertical dashed line. At T^m, the crosses indicate the sum of the estimated pseudopotential error (Sec. 4.3.2) and the uncertainty due to the (qh^{el}-qh) contribution (Sec. 4.2) for the GGA. The LDA error is $\approx 1/2$ of the GGA error. Experimental data older than 1950 are indicated by the open circles (Refs. [157–159] for C_P and [160–163] for α). The remaining experimental results are indicated by the filled squares (Refs. [13, 143, 145, 164–169] and [14, 170–174]). The inset shows the low temperature region with experimental data from Refs. [13] and [175].
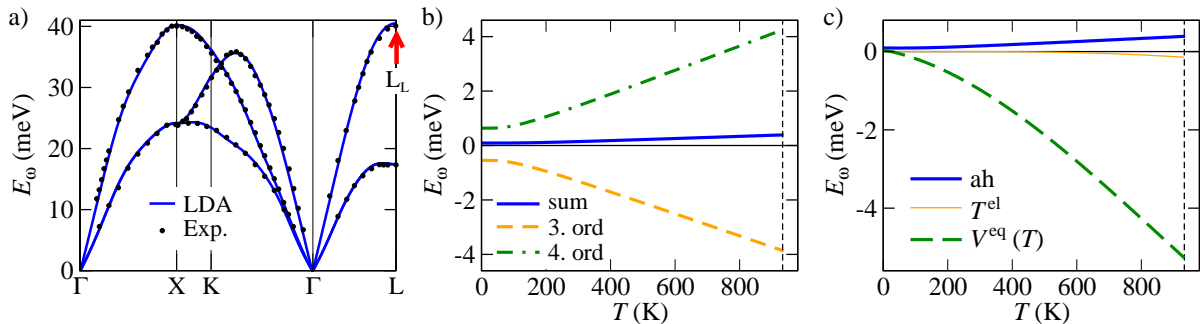
Figure 4.18: a) Quasiharmonic phonon dispersion of aluminum as in Fig. 4.3. The **q** vector and branch at which the anharmonic shift was calculated [b) and c)] is marked with the arrow. b) The third and fourth order contribution to the quantum mechanical anharmonic shift. c) Comparison between the various temperature dependencies of the phonon frequencies: the anharmonic (ah) shift corresponding to the sum from b), the T^{el} dependent shift discussed in Sec. 4.2, and the shift due to the thermal expansion $V^{\mathrm{eq}}(T)$.

apparent that if we consider each order separately (Fig. 4.18b), we have a strong phonon shift which has a magnitude similar to the shift caused by the thermal expansion $V^{\mathrm{eq}}(T)$ (Fig. 4.18c). The third order leads to a negative shift and the fourth order to a positive one so that in total both contributions tend to cancel each other. This effect of cancellation is known [86] and, as mentioned above, it has been also calculated for aluminum [176]. In order to facilitate this rather early (1990) study of the phonon shift, the author in Ref. [176] employed a force constant harmonic model potential with pairwise and first neighbor three body interactions. (Note that the pairwise interaction is harmonic but taking many body effects into account can still lead to anharmonicity.) The provided values of -0.80 and 0.95 meV for the third and fourth order shift at room temperature agree astonishingly well with our values of -1.30 and 1.44 meV. In order to explain this good agreement, we need to consider how the model potential was constructed: The force constants were fitted to experimental frequencies and to higher order elastic constants [176]. The such obtained model potential thus implicitly contains a large pool of experimental information. In particular, the fit to the highest order elastic constants yields information closely related to the anharmonic phonon shifts. Based on these considerations, we can in fact consider the comparison with the results from the model potential calculation as an indirect comparison with experimental data.

The influence of quantum mechanics is visible in the low temperature region (to ≈ 200 K) of both orders. Classically, each of the shifts would start at 0 meV and increase linearly with temperature. Quantum mechanically, we have at $T = 0$ K an energy shift of ≈ 0.5 meV and a parabolic temperature dependence. This energy shift is a direct consequence of the zero-point vibrations: Due to these vibrations the atoms explore already at $T = 0$ K the electronic free energy surface in the vicinity of their classical equilibrium positions. The (small) contribution of the anharmonic terms in this region manifests itself as the $T = 0$ K shift of the anharmonic frequencies. Above ≈ 200 K, the temperature dependence of the anharmonic phonon shifts changes into a linear, classical dependence. Considering the physically relevant sum of both orders the quantum mechanical influence cancels largely and a classical picture can be applied even at lower temperatures. It can be thus concluded that for the high temperature region which was of interest in Sec. 4.3.1, quantum mechanical effects are not important.

We can draw another important conclusion from the results of this section, which nicely supports the physical idea behind our model used to parametrize the anharmonic free energy surface (Sec. 4.3.4). We found that the model is able to describe the directly calculated results for $F^{\mathrm{clas,ah}}$

accurately, if we assume a positive shift in the (artificial) renormalization frequency $\overline{\omega}^{\mathrm{ah}}$. This frequency however corresponds to the sum of the contribution of the third and fourth order obtained here explicitly and it indeed shows a positive shift with temperature. In fact, even quantitatively a good agreement can be observed: To obtain the correct magnitude of ≈ 1 meV/atom in the anharmonic free energy at 900 K (Fig. 4.13), a renormalization frequency of $\overline{\omega}^{\mathrm{ah}} \approx 0.5$ meV is needed (cf. Fig. 4.14). This agrees with the results for the directly calculated anharmonic phonon shift (cf. Fig. 4.18c at 900 K).

4.5   Achievable accuracy with empirical approaches: EAM vs. DFT

In this final section of Chap. 4, our aim is to employ the highly accurate DFT results of Secs. 4.1 and 4.3, in order to evaluate the performance of the embedded atom method (EAM) in predicting thermodynamic properties of metals, in particular of aluminum. The EAM approach was motivated in Sec. 2.2 by the fact that EAM potentials allow to tackle system sizes and simulation times orders of magnitude larger than addressable using DFT. Based on the discussions that followed Sec. 2.2, particularly concerning the DFT calculation of anharmonic contributions, we can now remotivate the EAM approach very specifically: Despite advanced techniques, like for instance the UP-TILD method, the DFT calculation of anharmonic contributions in aluminum took many months of CPU time. In contrast, using EAM potentials the CPU time consumption was in the order of minutes.

We choose the following three commonly employed EAM potentials: the parametrizations of Mei-Davenport [62], Zope-Mishin [63], and Ercolessi-Adams [64]. A particular motivation for this choice is that the construction procedures for these potentials follow a certain hierarchy in their complexity. This issue is illustrated in Tab. 4.5. The Mei-Davenport potential employs 13 fitting parameters and only a rather small set of $T = 0$ K reference data. The Zope-Mishin potential has the same number of parameters, but in addition to the reference data used for the Mei-Davenport potential, further $T = 0$ K *ab initio* results are employed. Finally, the Ercolessi-Adams potential is the most elaborated, since it uses not only a large set of $T = 0$ K data, but also information about structures relevant at higher temperatures. Additionally, it is based on significantly more fitting parameters which should increase its flexibility. Based on this choice of potentials, we will be able to address the question whether the quality of the thermodynamic results correlates with the complexity of the construction procedure.

The $T = 0$ K properties for the three potentials are shown in Tab. 4.1 (page 104). The deviation from experimental values is small and in the range of the deviation for the *ab initio* results. This is however not surprising since these quantities enter directly the potential optimization (information about the bulk modulus is contained in the elastic constants). Let us thus turn to more advanced tests and discuss first the EAM phonon dispersions, which are shown in Fig. 4.19 in comparison with DFT and experiment. Figure 4.19 reveals the significantly different performance of the EAM potentials. The Mei-Davenport potential considerably underestimates the longitudinal branches by ≈ 5 meV. The Zope-Mishin and Ercolessi-Adams potentials agree better with DFT/experiment, with the first one slightly overestimating and the latter underestimating the DFT/experimental dispersion. An important point concerns the dependence of the phonon dispersion on the **q** vector. As discussed in Sec. 4.1.3, the phonon dispersion of aluminum is rich of Kohn-anomalies which distinguish it from a "simple" dispersion as found for instance for Cu. While these anomalies are accurately described by DFT, none of the EAM potentials can reproduce them (cf. e.g. the low energy branches along Γ to K and Γ to L). We note that all EAM dispersions are calculated in the same, sufficiently large supercell (4^3) as used for the DFT calculations. The reason for the lack of

Table 4.5: Illustration of the increasing level of complexity in the construction procedure of the Mei-Davenport (MD) [62], Zope-Mishin (ZM) [63], and Ercolessi-Adams (EA) [64] EAM parametrizations. Shown are the pair potential v^{pair}, the atomic charge density ρ^{at}, and the embedding energy f^{emb}. The explicitly given functions contain only significant fitting parameters (p_1, p_2, p_3) occurring in the exponents. The implicit determination of f^{emb} (for ZM) is based on matching to a universal equation-of-state proposed in Ref. [117]. Further, n^{fit} gives the number of fitting parameters and the last column the quantities used as a reference for the fitting procedure: a^{lat}=lattice constant, E^{coh}=cohesive energy, E^{f}=vacancy formation energy, c/a=ratio of the lattice vector lengths in hcp, E^{stack}=stacking fault energy, E^{surf}=surface energy, and $E(V)$=energy volume dependence. The $T = 0$ K reference data are obtained from experiment or from *ab initio* [for $E(V)$ for instance]. For the fitting of the Ercolessi-Adams potential also structures from a molecular dynamics (MD) run have been used.

	$v^{\text{pair}}(r)$	$\rho^{\text{at}}(r)$	$f^{\text{emb}}(\rho)$	n^{fit}	Reference for fitting
MD	$r\,e^{-r}$	$\sum_{i=0}^{5} r^{-i}$	complex expansion in $(\ln \rho)$	13	$T{=}0\,$K: a^{lat}, E^{coh}, E^{f} elastic constants
ZM	$r^{-p_1}{-}r^{-p_2}$	$r^{p_3}e^{-r}[1{+}e^{-r}]$	implicit using universal EOS	13	$T{=}0\,$K: a^{lat}, E^{coh}, E^{f}, c/a, elastic constants, $E(V)$: bcc, fcc, sc, hcp
EA	| |	cubic splines through a set of fitting points	| |	40	$T{=}0\,$K: a^{lat}, E^{coh}, E^{f}, E^{stack}, elastic constants, E^{surf} $T{>}0\,$K: 85 MD structures

Kohn anomalies is the fact that they are due to a complex interplay between the phonons and the electronic Fermi surface and this interplay is not captured by the EAM parametrizations.

The performance of the EAM potentials in predicting quasiharmonic thermodynamic properties is displayed in Fig. 4.20. To allow for an unbiased comparison, we use here the purely quasiharmonic DFT results as a reference, which means that they are obtained from a free energy surface with the $\widetilde{F}_0^{\text{el}}$ term excluded from Eq. (4.1). Averaged over the various properties, we find that the Ercolessi-Adams potential yields the best performance. For instance, the heat capacity (Fig. 4.20c) or the free energy (Fig. 4.20f) of this potential agree reasonably well with the DFT data. However, the thermal expansion and consequently also the expansion coefficient (Figs. 4.20a and b) strongly underestimate the DFT results. The situation is even more critical for the other two EAM potentials which dramatically under (Zope-Mishin) and overestimate (Mei-Davenport) the DFT thermal expansions. This shortcoming of the EAM potentials can be traced back to a wrong description of the volume dependence of the quasiharmonic free energy. Further, we observe an interesting feature for the low temperature heat capacity enlarged in the inset of Fig. 4.20c. Here, the Ercolessi-Adams and Zope-Mishin potentials agree well with the quasiharmonic DFT result [solid black line], which is a consequence of the fact that the long wavelength limit is well described by these potentials (Fig. 4.19). There is however a small discrepancy with the experimental data. The reason is the missing electronic contribution as shown by the dotted curve, which is the DFT result containing this additional contribution (i.e., the $\widetilde{F}_0^{\text{el}}$ term being included in the calculation). The inability to describe electronic contributions to the free energy is a general drawback of the EAM approach.

We now turn to the discussion of the subtle influences of explicit anharmonicity and vacancies summarized and compared to the DFT results from Sec. 4.3 in Fig. 4.21 and Tab. 4.6. Figure 4.21a

shows the volume dependence of the anharmonic free energy of the perfect crystal $F^{\mathrm{p,clas,ah}}$ which was identified in Sec. 4.3.3 to be important for deriving thermodynamic quantities. It reveals that the Zope-Mishin potential yields not only a qualitatively wrong volume dependence (decreasing with volume instead of increasing), but also a negative sign for the $F^{\mathrm{p,clas,ah}}$ values instead of the correct positive one. The negative sign can be explained by the qualitatively incorrect description of the temperature dependence of $F^{\mathrm{p,clas,ah}}$ by the Zope-Mishin potential as illustrated in Fig. 4.21b. The wrong description of both the volume and temperature dependence of $F^{\mathrm{p,clas,ah}}$ cumulates in a qualitatively wrong prediction of the anharmonic contribution to the heat capacity (Fig. 4.21c). The situation is significantly better for the other two EAM potentials which describe $F^{\mathrm{p,clas,ah}}(V, T)$ qualitatively well. The resulting anharmonic contribution to C_P is in reasonable agreement with DFT for the Ercolessi-Adams potential, while it is too large in magnitude for the Mei-Davenport potential. For the vacancy concentrations shown in Fig. 4.21d, we find that all EAM parametrizations yield a similar result which is also in reasonable agreement with DFT/experiment. A more quantitative analysis (Tab. 4.6) reveals however that the entropy of vacancy formation (equal to the slope of the curves in Fig. 4.21d) is correctly predicted only by the Mei-Davenport potential.

The final thermodynamic quantities based on all possible excitation mechanisms, i.e., quasiharmonic, anharmonic, and vacancies for the EAM potentials and electronic excitations additionally for DFT, are represented by the heat capacity in Fig. 4.21e and the expansion coefficient in Fig. 4.21f. For the heat capacity of the Zope-Mishin and Mei-Davenport potential, we observe an interesting situation: Whereas the purely quasiharmonic heat capacity (Fig. 4.20c) significantly deviates from the quasiharmonic DFT heat capacity, the situation for the heat capacity including all excitation mechanisms (Fig. 4.21e) is considerably improved. The latter is mainly a consequence of the strong (but incorrect) contribution due to anharmonicity (Fig. 4.21c). Thus, the errors in the two separately incorrectly predicted contributions (quasiharmonic and anharmonic) cancel each other to yield a reasonable result in their sum. For the Ercolessi-Adams potential, we find a different situation: We have a reasonable description of the separate heat capacity contributions, whereas the resulting full heat capacity shows the worst agreement with DFT/experiment out of the three EAM potentials. This might be surprising at first sight, but the following two reasons explain this behavior: First, both the quasiharmonic and anharmonic heat capacity are slightly lower than the corresponding DFT result, i.e., show a deviation with the same sign. This accumulates in a larger deviation in the resulting heat capacity. Second, the DFT result contains additionally the electronic contribution which pushes the heat capacity slightly upwards (cf. Fig. 4.12).

The anharmonic contribution to the expansion coefficient (not shown in Fig. 4.21) is qualitatively similar to the anharmonic heat capacity (Fig. 4.21c). However, the anharmonic contributions for the Zope-Mishin and Mei-Davenport potential are not strong enough to fully cancel the wrong quasiharmonic prediction of the expansion coefficient (Fig. 4.20b) as observed for the heat capacity. For the Ercolessi-Adams potential anharmonicity pushes the expansion coefficient down, increasing the disagreement with DFT/experiment. In fact, while we have identified this potential as giving the best quasiharmonic properties, it is now (i.e., for the full excitation spectrum) the worst EAM parametrization.

Let us comment on a rather technical issue, which however illustrates well a further important difficulty of EAM potentials in combination with volume dependent thermodynamic properties. In our calculations, we experienced frequently that the originally provided EAM potentials showed an unphysical, singular behavior at higher but still relevant volumes. An example is given in Fig. 4.21a for the case of the volume dependence of $F^{\mathrm{p,clas,ah}}$ for the Ercolessi-Adams potential. The filled squares indicate the actually calculated values which show a kink at a certain volume. We found also a similar behavior for the Mei-Davenport potential. For the latter, we could remove the
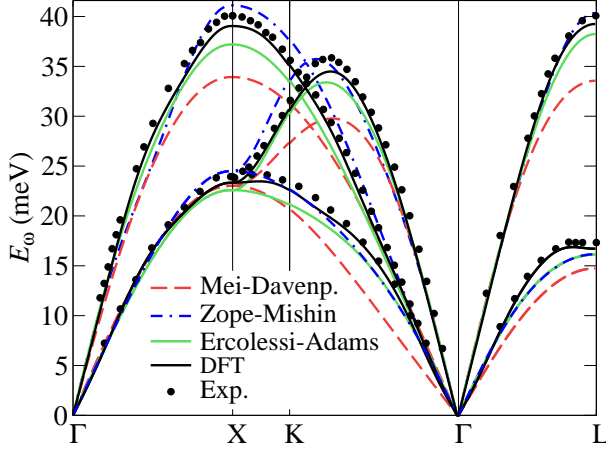
Figure 4.19: Phonon dispersion $\omega_{\mathbf{q},s}$ [$E_\omega = h\omega/(2\pi)$] of aluminum for the three investigated EAM parametrizations Mei-Davenport [62], Zope-Mishin [63], and Ercolessi-Adams [64] in comparison with DFT (GGA, PAW) data and experiment. A 4^3 supercell (256 atoms) was consistently used for all theoretical dispersions. Experimental values are from Ref. [101].
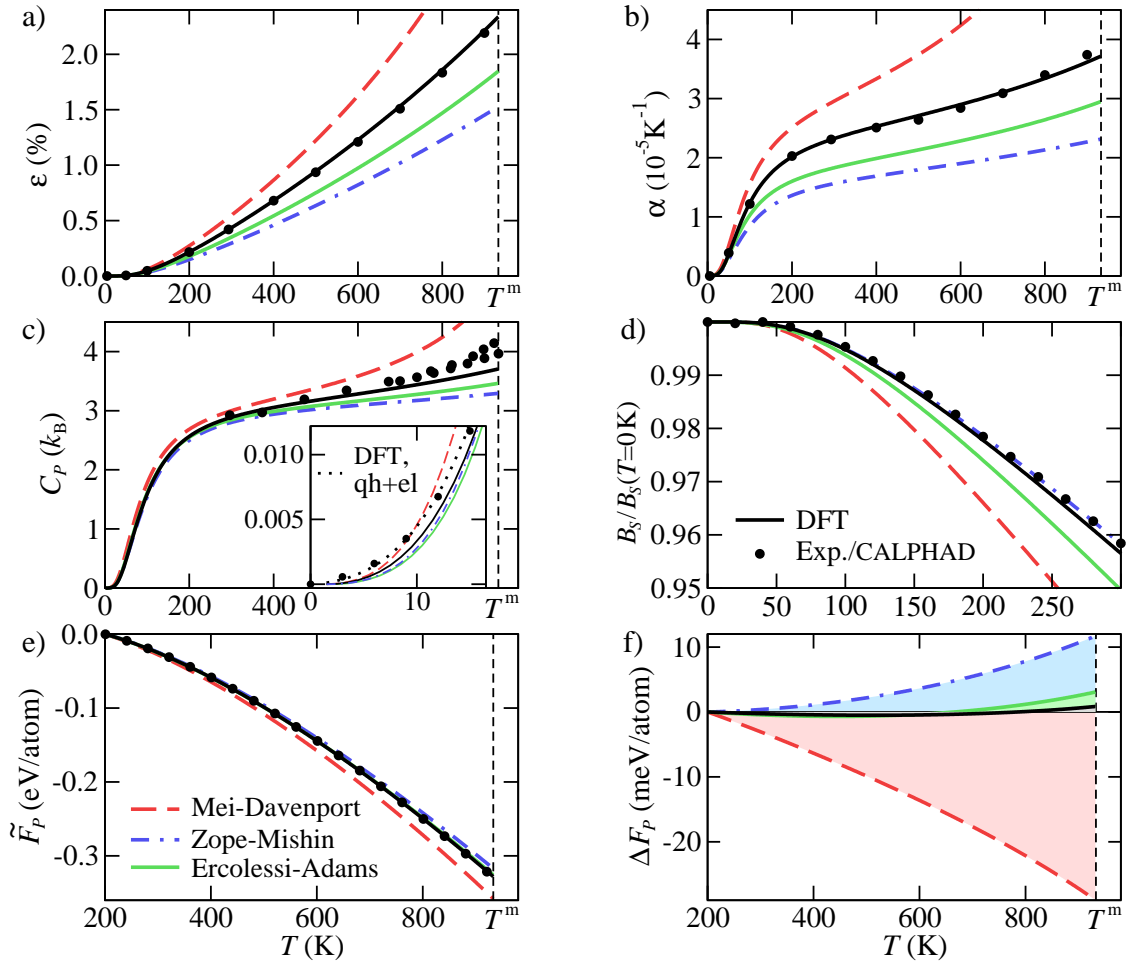

Figure 4.20: Quasiharmonic thermodynamic properties of aluminum for the three investigated EAM parametrizations (see Fig. 4.19 for references) in comparison with DFT (GGA, PAW) and experiment/CALPHAD. The DFT values do not contain the electronic contribution [except for the dotted curve in the inset in c)]. Experimental references are the same as in Figs. 4.4 to 4.8. a) Linear thermal expansion ε, Eq. (4.8). b) Expansion coefficient α, Eq. (2.235). c) Isobaric heat capacity C_P, Eq. (2.236). The inset shows the low temperature region. d) Adiabatic bulk modulus B_S, Eq. (2.237). e) Isobaric free energy $\widetilde{F}_P$, Eq. (2.242), shifted according to Eq. (4.5) for DFT and CALPHAD and similarly for the EAM potentials. f) The difference ΔF_P according to Eq. (4.7) for DFT and similarly for the EAM potentials.

Table 4.6: The formation energy E^{f} and entropy of formation S^{f} of a vacancy in aluminum for the investigated EAM potentials (cf. Fig. 4.19) in comparison with DFT (GGA, pseudopotential) and experiment. The values (also the experimental) are obtained by fitting the vacancy concentrations over the temperature range given in Fig. 4.21d to the function $\exp[-(E^{\mathrm{f}} - TS^{\mathrm{f}})/k_{\mathrm{B}}T]$.

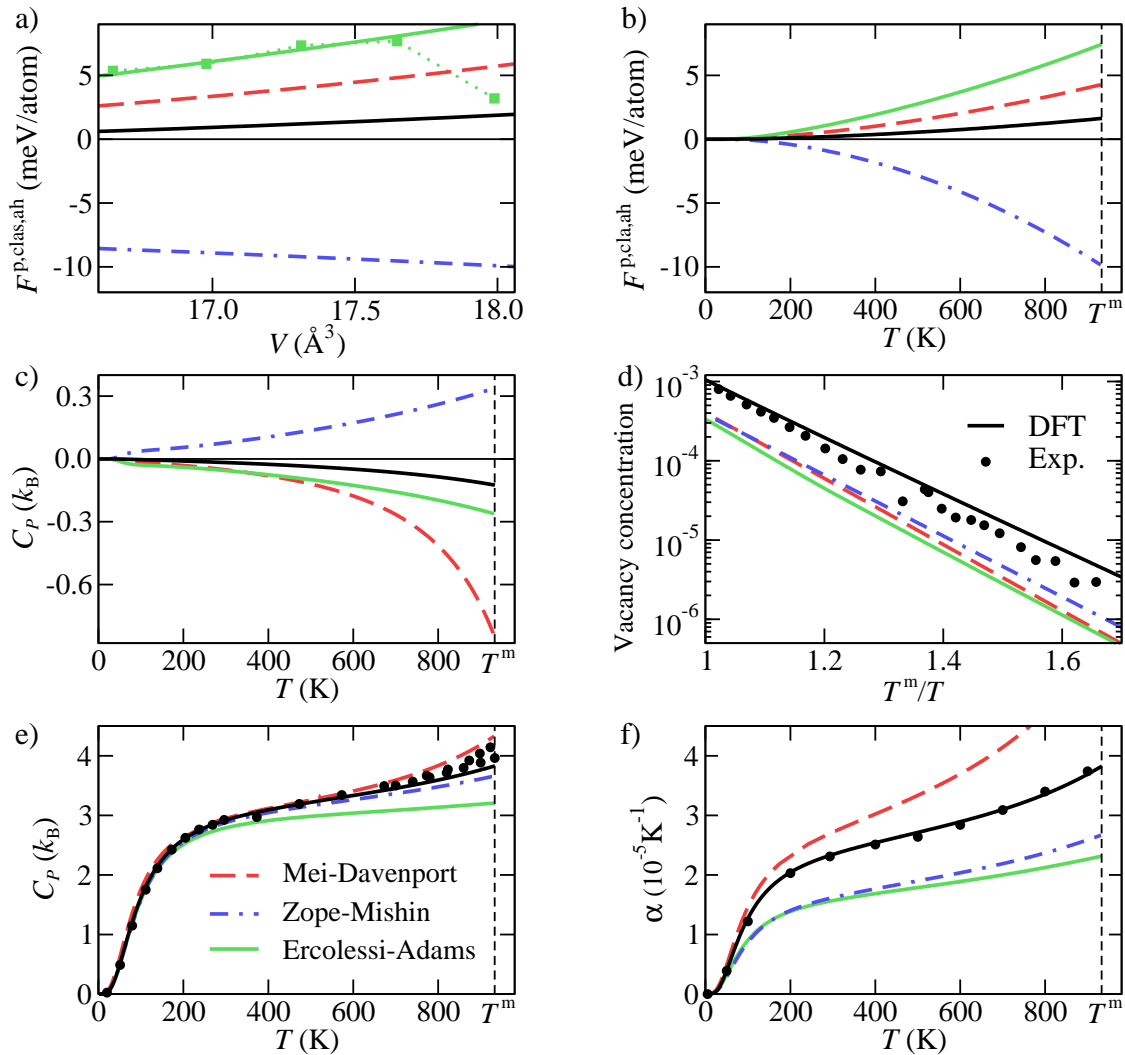| | E^{f} (eV) | | S^{f} (k_{B}) | |
	qh	qh+ah	qh	qh+ah
Mei-Davenport	0.63	0.77	−0.1	1.5
Zope-Mishin	0.68	0.71	0.0	0.1
Ercolessi-Adams	0.69	0.81	0.0	0.2
DFT	0.58	0.68	0.1	1.5
Experiment		0.75		2.4

Figure 4.21: Explicitly anharmonic, vacancy, and the resulting full, i.e., with all excitation mechanisms, properties of aluminum for the investigated EAM potentials (cf. Fig. 4.19) in comparison with DFT (GGA, pseudopotential; cf. Sec. 4.3) and experiment. Experimental data are from Ref. [155] for d), from Refs. [132] and [13] for e), and from Ref. [14] for f). a) Volume dependence of the anharmonic free energy of the perfect crystal $F^{\mathrm{p,clas,ah}}$. The curves are fits through the calculated values based on the model from Sec. 4.3.4. The actually calculated values are shown only for the Ercolessi-Adams potential (filled squares with the dotted line as a guide for the eye) to visualize the kink in the volume dependence discussed at the end of Sec. 4.5. The other, not shown calculated values fall together with the fits on the given scale. b) As a), but showing the temperature dependence. c) The anharmonic contribution to the isobaric heat capacity. d) Vacancy concentration. e) Isobaric heat capacity C_P. f) Expansion coefficient α.

unphysical volume dependence: Since this potential is provided in an analytical form, we enlarged the originally introduced interaction cutoffs [62] which resulted in a potential with a smooth volume dependence. In contrast, the situation is more problematic for the Ercolessi-Adams potential which is provided numerically [64] and therefore not tunable. We solved here the problem by including only the uncorrupted free energy points in our calculations. (For instance, the green solid line in Fig. 4.21a indicates a fit based on the values before the kink.)

From the previous discussions, we draw one major conclusion: Among the investigated potentials, an EAM potential yielding **overall** good thermodynamic properties cannot be identified. Moreover, a clear correlation between the complexity of the construction procedure (see discussion at the beginning of this section) and the accuracy in the thermodynamic properties is not visible. One might argue that the most complex potential, the Ercolessi-Adams one, yields in average the best thermodynamic quantities. This is however not as clear as we would have expected, in particular, due to the fact that it contains $T > 0$ K information.

The most interesting and important question is whether the failure of the EAM potentials is 1) an inherent deficiency of the EAM concept or if 2) it applies only to the here employed parametrizations. We cannot give a decisive answer based only on our results, but we can provide some valuable hints: An argument supporting 1) is the missing correlation discussed above. If the EAM approach was, in principle, able to yield accurate thermodynamic properties, we would expect that increasing the complexity of the potentials leads to a systematic improvement. This is not the case. Inspecting Ref. [64], we found however an issue which still leaves room for hypothesis 2). The reference calculations for the Ercolessi-Adams potential, in particular the 85 MD structures, were not obtained from a "pure" *ab initio* scheme, but rather from a simplified tight binding approximation (developed in Ref. [177]), which is only based on *ab initio* input. This approach was necessary to allow the *ab initio* MD simulations at that time (1994). The tight binding method is however not well suited to describe metallic systems, particularly free-electron systems as aluminum, since it is based on a localized electron picture, i.e., the electrons are assumed to sit close to their host atoms. In contrast, the reference calculations used for the Zope-Mishin potential were obtained using "pure" *ab initio* calculations (LAPW method). It is therefore reasonable to assume that the originally (at the beginning of this section) claimed increasing complexity in the construction procedure of these EAM potentials (including the quality of the reference calculations) does not fully hold. We thus propose to modify the Ercolessi-Adams potential such that it is based on "pure" *ab initio* results (as for instance provided by the UP-TILD method in this study). The evaluation of the corresponding thermodynamics could provide further valuable insight in the general nature and quality of the EAM concept.

Chapter 5

Conclusions

The present work has addressed a major challenge of *ab initio* assisted materials design: The efficient determination of highly accurate materials properties at finite temperatures. For that purpose, various methods have been developed which allow to compute the contribution of all relevant excitation mechanisms to the thermodynamic properties of non-magnetic elementary metals. The developments have been extensively benchmarked by focusing on a set of experimentally well investigated metals. Key findings/messages of this thesis are summarized as follows:

1) *Today's EAM parametrizations are not suited for an accurate prediction of thermodynamic properties of metals.*
   Based on the extensive set of thermodynamic DFT data computed for aluminum, the performance of three state-of-the-art EAM parametrizations in yielding thermodynamic properties was evaluated (Sec. 4.5). None of the EAM potentials is able to yield a satisfactory agreement with DFT for all considered free energy contributions/thermodynamic quantities (Figs. 4.20 and 4.21). For instance, the Ercolessi-Adams potential [64] yields the best quasiharmonic (Fig. 4.20c) *and* anharmonic (Fig. 4.21c) heat capacity compared to DFT. However, the resulting total heat capacity of this potential shows the worst agreement. This rather unintuitive feature can be explained by an error cancellation in the heat capacity contributions predicted by the other potentials. Moreover, a clear correlation between the complexity of the EAM potentials and their predictive power could not be identified. Nonetheless, we were able to suggest a way for improving today's EAM potentials (see end of Sec. 4.5).

2) *Extension of the "usual" phase space by the convergence parameter space boosts your DFT calculations.*
   With the hierarchical UP-TILD method (Sec. 3.2), a conceptually new approach has been opened to combine accuracy and performance in computing thermodynamic averages. The basic idea is to extend the phase space spanned by the set of atomic coordinates ("usual" phase space) with the space of DFT convergence parameters (e.g. k point mesh, plane wave cutoff). The sampling, needed for instance for calculating the anharmonic free energy, is then performed in a hierarchical manner in this extended space. This approach reduces considerably the number of computationally expensive calculations. In our study, we achieved a CPU time reduction of ≈ 30, but we expect that an even larger reduction is possible after optimizing and fully automating the procedure. We therefore believe that a possible future route for improving existing DFT codes could be an automated calculation of physical quantities in the extended space.

3) *The volume optimized or the constant pressure approach should be used for accurate vacancy results.*
Our volume optimized approach (Sec. 3.1) provides an intuitive understanding of the dilute limit point defect concept and allows to derive the typically applied standard approaches as approximations. In the new approach, the usually applied separation of the vacancy contribution by means of a formation free energy was abandoned. The cell containing the point defect and the perfect bulk have to be treated as a coupled system. For vacancies in aluminum, the commonly employed fixed volume approximation results in large error bars in the predicted concentrations (up to 50% too small). The other approximate approach, the constant pressure approach, yields basically the same vacancy concentrations as the general volume optimized method. Hence, for accurate vacancy calculations, one of the latter should be applied.

4) *LDA and GGA provide an ab initio confidence interval for experiment.*
The only approximation in a numerically fully converged DFT calculation is the exchange-correlation (xc) functional. We studied the accuracy of two popular xc functionals, LDA and GGA-PBE, in predicting a wide range of thermodynamic material properties for a large and comparable set of elementary non-magnetic metals (Sec. 4.1). The most important result is that, for all thermodynamic quantities studied here, the two functionals (LDA and GGA) approximate an confidence interval for experiment and may be thus used to estimate *ab initio* error bars. While further tests are needed to check the validity for other materials classes, the existence of such a relation would allow to estimate error bars which are solely based on DFT calculations. The availability of such error bars is a key prerequisite to make truly *ab initio* based materials simulations.[1]

5) *The anharmonic heat capacity is negative and the vacancy contribution is positive in aluminum.*
The developed techniques allowed us to settle a long standing debate about which excitation mechanism dominates thermodynamic quantities in aluminum close to the melting point (Sec. 4.3). This issue has been raised first by Born and Brody [142] almost a century ago and has been heavily debated since then in both experimental and theoretical studies [143, 145, 146]. We found that – in contrast to common belief – explicit anharmonicity gives rise to a negative contribution to the isobaric heat capacity. On the other hand, the heat capacity contribution due to vacancies increases in a strongly non-linear fashion at high temperatures. We therefore conclude that, among these two contributions, only the vacancies can be considered as the origin of the steep positive increase in the Al heat capacity observed in experiment.

6) *Todays ab initio methods, smart statistical approaches, and computer power enable highly accurate predictions up to the melting point.*
Possibly the most important finding of the present work is the recognition that today's computer codes and today's hardware enable a new level of accuracy in simulating realistic physical processes at finite temperatures. Traditionally, *ab initio* approaches such as DFT have

---

[1]Note that the property to form bounds to experiment originates from the $T = 0$ K under(over)estimation of the equilibrium lattice constant by LDA (GGA) (cf. the discussion in Sec. 4.1.8). This phenomenon is well known and investigated in the *ab initio* community. The crucial point made here is the recognition that this $T = 0$ K property translates into an equivalent **finite temperature** property. The latter fact is however of utmost importance for the metal research community.

been applied to calculate $T = 0$ K properties and the extension to $T > 0$ K has been hampered by significantly more expensive calculation times. Including all relevant excitation mechanisms into the free energy, we showed for the example of fcc aluminum that $T > 0$ K quantities are accessible even up to the melting point. Indeed, it turned out that for some thermodynamic quantities the achievable accuracy is in the range of experimental scatter. Thus, for further progress and for a decisive comparison between *ab initio* and experiment, improved experimental techniques are called for.

The results and insights gained in this study are expected to provide a firm basis for the further development of *ab initio* assisted metal design. The importance of the presented investigations has been emphasized, e.g. in Ref. [178]. They can however be only a very first step towards the final goal of metals design on the computer. Further critical points that have to be addressed are:

- We investigated only the temperature independent xc energy functional [e.g., Eq. (2.72)]. Results for a temperature dependent LDA xc functional are available [179, 180] so that its influence should be investigated in a forthcoming study.

- The chemical trends observed in the GGA thermodynamic properties resulted in large errors in particular for the noble metals Ag and Au. The origin of these large errors could be traced back to the inability of present day xc functionals to describe the $T = 0$ K potential energy surface. It is now necessary to determine the physical mechanism causing the errors in the potential energy surface. A possible source might be related to the closed shell structure of the noble metals. For such elements, so called van der Waals, i.e., dipol-dipol, interactions become important, which are not captured by standard DFT functionals (LDA/GGA). Recent developments incorporating these interactions into the DFT approach [181] should therefore be considered.

- A very interesting but also computationally expensive extension would be to include the full excitation spectrum, which was considered here only for Al, also for the other fcc metals. In this respect, one open question is whether the explicitly anharmonic contribution to the heat capacity will turn out to be systematically negative.

- The quantum mechanical perturbation theory calculations were carried out only for a single phonon frequency. These calculations should be extended to other phonon frequencies. Eventually, if a sufficient number of frequencies is available, a quantum mechanical anharmonic free energy can be computed (corresponding equations are given in Ref. [68]) and compared to the classical anharmonic free energy obtained in Sec. 4.3.3.

- Finally, the insight achieved here should be combined with the following related and very active research areas:

    - Inclusion of magnetic excitations [182, 183].
    - Extension to alloys which requires the description of configurational entropy [184].
    - Coupling with homogenization methods allowing to treat polycrystalline materials [185].
    - Atomistic description of (martensitic) phase transitions.

The advancements of these issues will likely result in a new generation of simulation tools that are fully capable of providing finite temperature properties of real materials with hitherto not achievable accuracy and predictive power. The availability of such techniques will open new and exciting routes in computational materials design.

Appendix A

Supplement

A.1 Technical details

A.1.1 Scaling function

We use frequently a symbolic scaling function s (and also s^{el}, s^{DFT}, s^{KS}, s^{qh}) to characterize the dimensions of a problem. In case of matrices, for instance,

$$s = N_1 \cdot (M_1 \times M_1) + N_2 \cdot (M_2 \times M_2) \tag{A.1}$$

means that the corresponding problem consists of solving N_1 times (indicated by "·") the eigenvalue equation of a matrix of size $M_1 \times M_1$ and (indicated by "+") of solving N_2 times the eigenvalue equation of a matrix of size $M_2 \times M_2$. In contrast, in cases where no matrix diagonalization is directly involved to solve the problem, as for instance for the optimized Kohn-Sham equation, Eq. (2.92), the scaling function indicates the dependence of the CPU time and memory, which are needed to solve the problem, on various parameters. Due to these two different characters of the scaling functions, equations involving both types, as for instance Eq. (2.112), should be understood only symbolically as a means of describing the dimensions of a problem. In the same spirit, we do not include constants or negligible terms, as for instance in Eq. (2.187).

A.1.2 Atomic and reduced units

We use in general SI units in the present work. In order to be consistent with customary notation used in the field of DFT, we give the expression for the plane wave cutoff E^{cut}, Eqs. (2.88) and (2.89), in reduced units [186]

$$|\mathbf{G}_{a_0}| = a_0|\mathbf{G}|, \quad \mathbf{k}_{a_0}| = a_0|\mathbf{k}|, \quad E_h^{\text{cut}} = E^{\text{cut}}/E_h, \quad E_r^{\text{cut}} = E^{\text{cut}}/\text{Ry}, \tag{A.2}$$

with the atomic units: the Bohr radius a_0, the Hartree energy $E_h = \hbar^2/(m_e a_0^2)$ [not to be confused with the Hartree energy functional E^{H}, Eq. (2.60)], and the Rydberg energy $\text{Ry} = E_h/2$ [186].

A.1.3 Various definitions

Within the Dirac notation, an abstract, i.e., without a reference to a coordinate system, vector v in Hilbert space is denoted as $|v\rangle$. Its dual counterpart (which is simply the complex conjugate v^* in the real space representation) is denoted as $\langle v|$. A scalar product for vectors $|w\rangle$ and $|v\rangle$ is denoted $\langle w|v\rangle$. In case of discrete vectors, $\langle w|v\rangle = \sum_{i,j} w_i^* v_j$ with w_i and v_i components in a

specific representation. In case of continuous functions, for instance in the real space representation, $\langle w|v\rangle = \int w^*(\mathbf{r})v(\mathbf{r}')\,d\mathbf{r}\,d\mathbf{r}'$.

The commutator $[\hat{A},\hat{B}]$ of two operators $\hat{A}$ and $\hat{B}$ is given by:

$$[\hat{A},\hat{B}] = \hat{A}\hat{B} - \hat{B}\hat{A}. \tag{A.3}$$

The exponential function of an operator $\hat{A}$ is defined by its polynomial series

$$e^{\hat{A}}|\psi\rangle \;=\; \hat{1} + \hat{A}|\psi\rangle + \frac{1}{2}\hat{A}(\hat{A}|\psi\rangle) + \frac{1}{6}\hat{A}(\hat{A}(\hat{A}|\psi\rangle)) + \ldots \tag{A.4}$$

with a general wave function ψ. If $|a\rangle$ is an eigenfunction of $\hat{A}$, it follows from Eq. (A.4):

$$\langle a|e^{\hat{A}}|a\rangle \;=\; e^{\langle a|\hat{A}|a\rangle}. \tag{A.5}$$

The trace of an operator $\hat{A}$ defined by

$$\sum_i \langle b_i|\hat{A}|b_i\rangle, \tag{A.6}$$

where $\{b_i\}$ is a basis and the sum runs over all basis elements, has the property

$$\sum_i \langle b_i|\hat{A}|b_i\rangle = \sum_j \langle g_j|\hat{A}|g_j\rangle, \tag{A.7}$$

which is true for any other basis $\{g_j\}$ [71].

An integral over nuclei coordinates $\{\mathbf{R}_I\}$ is written for short as:

$$\int d\mathbf{R}_I \; := \; \int \ldots \int d\mathbf{R}_1 d\mathbf{R}_2 \ldots d\mathbf{R}_{N_n}. \tag{A.8}$$

A.1.4   Linear response approach to the dynamical matrix

The basic idea (see Ref. [187] for details) behind the method of calculating phonon frequencies from linear response is that the harmonic force constants are entirely determined by their *static* linear electronic response. In fact, within the Born-Oppenheimer approximation, the lattice distortion associated with a phonon can be seen as a static perturbation acting on the electrons. In Ref. [187], it is shown that the reciprocal dynamical matrix $\mathbf{D_q}$ for a certain $\mathbf{q}$ vector can be calculated from the linear variation of the external potential $\partial v(\mathbf{r})/\partial U_{\mathbf{q},\alpha}$, the second derivative of the external potential $\partial^2 v(\mathbf{r})/(\partial U_{\mathbf{q},\alpha}\partial U_{\mathbf{q},\alpha})$ at $\mathbf{q}=0$, and the linear electronic response $\partial\rho(\mathbf{r})/\partial U_{\mathbf{q},\alpha}$ as:

$$D^{\mathrm{el}}_{\mathbf{q},\,\alpha\beta}(\mathbf{q}) = \frac{1}{M_I^{1/2}}\left\{ \int \left[\frac{\partial\rho(\mathbf{r})}{\partial U_{\mathbf{q},\alpha}}\right]^* \frac{\partial v(\mathbf{r})}{\partial U_{\mathbf{q},\beta}}\,d\mathbf{r} \; + \; \delta_{ij}\int \rho_0(\mathbf{r})\frac{\partial^2 v(\mathbf{r})}{\partial U_{\mathbf{q}=0,\alpha}\,\partial U_{\mathbf{q}=0,\beta}}\,d\mathbf{r}\right\}. \tag{A.9}$$

The superscript "el" indicates that Eq. (A.9) describes only the electronic contribution to the dynamical matrix. The additional contribution due to the nucleus-nucleus interaction can be obtained using the Ewald sum. The variation in the external potential $v(\mathbf{r})$ and the electron density $\rho(\mathbf{r})$ is obtained upon a lattice distortion of the form

$$U_\alpha(\mathbf{R}) = U_{\mathbf{q},\alpha}\exp(i\mathbf{q}\cdot\mathbf{R}) \;\;, \tag{A.10}$$

where $\mathbf{R}$ is a primitive lattice vector and where $U_\alpha(\mathbf{R})$ is the displacement of the nucleus at $\mathbf{R}$ into the direction of α (note that, as always in the present thesis, the equations are for elementary materials). In Eq. (A.9), M_I is the mass of the considered element, $\rho_0(\mathbf{r})$ is the unperturbed electron density, and $[.]^*$ denotes the conjugate complex. The variations $\partial v(\mathbf{r})/\partial U_{\mathbf{q},\alpha}$ and $\partial^2 v(\mathbf{r})/(\partial U_{\mathbf{q},\alpha}\partial U_{\mathbf{q},\alpha})$ follow directly from the specific form of the external potential and the distortion. The calculation of the linear electronic response $\partial \rho(\mathbf{r})/\partial U_{\mathbf{q},\alpha}$ is more complex and requires the application of density-functional perturbation-theory (DFPT).

In DFPT, the lattice distortion is superimposed on the unperturbed external potential which produces a change Δv:

$$v \quad \rightarrow \quad v + \Delta v \ . \tag{A.11}$$

This perturbation causes in turn a change Δv^{eff} in the effective Kohn-Sham potential,

$$v^{\mathrm{eff}} \quad \rightarrow \quad v^{\mathrm{eff}} + \Delta v^{\mathrm{eff}} \ , \tag{A.12}$$

which can be used to calculate the change/response in the electron density by means of first order perturbation theory. Since the v^{eff} depends on the the electron density ρ through the Hartree and exchange-correlation potential, the change in ρ will in turn affect v^{eff}, which has to be recalculated. The procedure needs to be continued until self consistency is reached and a converged electronic response $\partial \rho(\mathbf{r})/\partial U_{\mathbf{q},\alpha}$ has been obtained.

A disadvantage of the linear response method is the fact that for each $\mathbf{q}$ vector a separate Kohn-Sham calculation is needed. However, **no** supercell has to be introduced as is the case for the direct force constant method. It suffices to employ the primitive unit cell to obtain the linear electronic response at a certain $\mathbf{q}$ point. The actual number of calculations is determined by the (converged) density of the $\mathbf{q}$ vectors inside the first Brillouin zone and the given crystal symmetries. For crystals with small unit cells, the linear response method is more convenient than the direct force constant method. On the other hand, for sufficiently large primitive unit cells the direct force constant method is better suited. More specifically, "sufficient" means that the primitive unit cell has reached a size for which finite size effects are negligible. In such a case, the supercell can be set equal to the primitive unit cell which favors the direct force constant approach.

An important technical point is the complexity inherent in a DFPT implementation, which requires profound methodological and theoretical skill and is in general very time consuming and error-prone. In contrast, the implementation of the direct force constant method, which can be performed "on top" of an existing *ab initio* code, is relatively straightforward.

A.2   Frequently used notation

In Tabs. A.1 and A.2 (on the following pages), we summarize frequently used abbreviations and symbols, respectively.

Table A.1: Frequently used abbreviations.

Abbreviation	Description
ah	(explicitly) anharmonic (contribution)
augGrid	augmentation grid; for augmentation charges in the PAW method, Sec. 3.4.1
basicGrid	basic grid; used for representing plane waves, Sec. 3.4.1
BZ	first Brillouin zone
DFT	density functional theory
DFC	direct force constant (method); for the calculation of the dynamical matrix
EAM	embedded atom method
EOS	equation-of-state
fcc	face-centered-cubic (lattice)
FEBO	free energy Born-Oppenheimer (approximation); Sec. 2.1.3
FES	(electronic) free energy surface
GGA	generalized gradient approximation
gp/atom	grid points per atom; unit for the augmentation grid, Sec. 3.4.1
kp·atom	k points times number of atoms in the supercell; Sec. 2.1.7
LAPW+lo	linearized augmented plane waves plus local orbitals
LDA	local density approximation
LR	linear response (method);for the calculation of the dynamical matrix
MD	molecular dynamics
PAW	projector augmented wave (method)
PES	(electronic) potential energy surface
PBE	Perdew-Burke-Ernzerhof (parametrization) [37]; for the GGA functional
pp	pseudopotential
prBZ	first Brillouin zone of the primitive unit cell; Sec. 2.3.2
qh	quasiharmonic (contribution)
sc	supercell
scBZ	first Brillouin zone of the supercell; Sec. 2.3.2
TILD	thermodynamic integration based Langevin dynamics; Sec. 2.3.6
UP-TILD	upsampled TILD (method); Sec. 3.2.2
vac	vacancy
xc	exchange-correlation (functional)

Table A.2: Important and frequently used symbols listed in the order: small Latin, capitalized Latin, small Greek, and capitalized Greek characters.

Symbol	Description
a_0	Bohr radius
$\mathbf{a}_1$, $\mathbf{a}_2$, $\mathbf{a}_3$	primitive lattice vectors, Eq. (2.76)
$\mathbf{a}'_1$, $\mathbf{a}'_2$, $\mathbf{a}'_3$	conventional fcc unit cell lattice vectors, Eq. (2.115)
a^{lat}, $a^{\mathrm{lat,eq}}$	(equilibrium) lattice constant
$\mathbf{b}_1$, $\mathbf{b}_2$, $\mathbf{b}_3$	vectors spanning the first BZ of the primitive lattice, Eq. (2.79)
$\mathbf{b}_1^{\mathrm{sc}}$, $\mathbf{b}_2^{\mathrm{sc}}$, $\mathbf{b}_3^{\mathrm{sc}}$	vectors spanning the first BZ of the supercell lattice, Eq. (2.122)
c	vacancy concentration
$c_{\nu,\mathbf{k}+\mathbf{G}}$	expansion coefficients of the Kohn-Sham wave function in reciprocal space
e	elementary charge
f_i, $f_{\nu,\mathbf{k}}$	Kohn-Sham occupation numbers, Eq. (2.65) and Sec. 2.1.7
f^{emb}	embedding function of an EAM parametrization
$\hbar$	reduced Planck constant
$\mathbf{k}$	electronic wave vector inside first BZ
k_{B}	Boltzmann constant
m_e	electron mass
n	number of vacancies
n^{sc}	size of supercell in one dimension, Eq. (2.117)
p_ν	statistical weights of electronic wave function
$\mathbf{q}$	wave vector of nuclei displacements
$\mathbf{r}_i$	coordinates of electrons
s, s^{el}, s^{DFT}, s^{KS}, s^{qh}	scaling functions used to indicate the computational requirements of a problem; see Sec. A.1.1
$\mathbf{s}_1$, $\mathbf{s}_2$, $\mathbf{s}_3$	supercell lattice vectors, Eq. (2.114)
v	external potential, Eq. (2.49)
v^{eff}, $v_{\mathbf{G}}^{\mathrm{eff}}$	effective Kohn-Sham potential, in real and reciprocal space, Eq. (2.58) and Sec. 2.1.7
v^{f}	volume of vacancy formation, Eq. (3.25)
v^{pair}	pair potential of an EAM parametrization
$\mathbf{w}_{\mathbf{G}^{\mathrm{sc}},s}$, $w_{\mathbf{G}^{\mathrm{sc}},s}$	eigenvectors of the reciprocal dynamical matrix $\mathbf{D}_{\mathbf{G}^{\mathrm{sc}}}$ and its components
B_S, B_T	adiabatic, i.e., at constant entropy S, and isothermal bulk modulus, Eq. (2.229)
$B_{T,0}$, $B'_{T,0}$	B_T and the pressure derivative of B_T at $T = 0$ K

Table A.2 (continued).

Symbol	Description
C_P	isobaric heat capacity, i.e., at constant pressure P, Eq. (2.229)
C_V, C_{V_0}	heat capacity at constant and fixed volume; see Sec. 2.4.2
$\mathbf{D}$, $D_{I\alpha,J\beta}$	real space dynamical matrix and its elements, Eq. (2.132)
$\mathbf{D}^{0K}$, $D^{0K}_{I\alpha,J\beta}$	$T = 0$ K approximation to the real space dynamical matrix, Eq. (2.179)
$\mathbf{D}_{\mathbf{G}^{sc}}$, $D_{\mathbf{G}^{sc},\alpha\beta}$	reciprocal dynamical matrix at wave vector $\mathbf{G}^{sc}$ and its elements, Eq. (2.141)
$\mathbf{D}^{0K}_{\mathbf{G}^{sc}}$, $D^{0K}_{\mathbf{G}^{sc},\alpha\beta}$	$T = 0$ K approximation to the reciprocal dynamical matrix, Eq. (2.141)
E_ξ	eigenvalues of the main Hamiltonian $\hat{H}$
E_ω	energy corresponding to the phonon frequency ω
E^{cut}	plane wave cutoff energy
$E^{cut,high}$, $E^{cut,low}$	highly and low converged cutoff, used for the development of the UP-TILD method (Sec. 3.2)
E^f	energy of vacancy formation
E^{el}_ν	eigenvalues of the electronic Hamiltonian $\hat{H}^{el}$
$E^{el}_g(\{\mathbf{R}_I\})$, $E^{el}_{g,0}$	$T = 0$ K ground state of $\hat{H}^{el}$ and $E^{el}_{g,0} = E^{el}_g(\{\mathbf{R}^{0K}_I\})$
$E^H[\rho]$, $E^{xc}[\rho]$	Hartree [Eq. (2.60)] and exchange-correlation [Sec. 2.1.6] energy functional
$E^{nuc}_{\nu,\mu}$	eigenvalues of the nuclei Hamiltonian $\hat{H}^{nuc}_\nu$
E^{zp}, $E^{zp,0K}$	energy of zero-point vibrations [Eq. (2.161)] and its $\mathbf{D}^{0K}$ approximation
$F(V,T)$	full free energy surface including all excitations, Eq. (2.2)
F_P	free energy at constant pressure P
$\widetilde{F}_P$	F_P referenced with respect to $F_P(T = 200K)$ to allow a convenient comparison with CALPHAD data, Eqs. (4.5) and (4.6)
ΔF_P	F_P referenced at each T with respect to the CALPHAD free energy, Eq. (4.7)
F^c	configurational free energy of point defects, Eq. (3.7)
$F^{clas,ah}$	classical explicitly anharmonic free energy, Eq. (2.195)
F^p, F^v	free energy of the perfect crystal and vacancy supercell
$F^{p,clas,ah}$, $F^{v,clas,ah}$	$F^{clas,ah}$ for the perfect crystal and the vacancy supercell
$F^{el}(\{\mathbf{R}_I\})$, F^{el}_0	electronic free energy and $F^{el}_0 = F^{el}(\{\mathbf{R}^{0K}_I\})$
$\widetilde{F}^{el}_0$	temperature dependent part of F^{el}_0, Eq. (3.53)
$\widetilde{F}^{el}[\{p_\nu\},\{\psi_\nu\}]$	free energy functional, Eq. (2.41)
F^{qh}, $F^{qh,0K}$	quasiharmonic free energy [Eq. (2.161)] and its $\mathbf{D}^{0K}$ approximation
F^{vac}	free energy contribution due to vacancies, Sec. 3.1.3

Table A.2 (continued).

Symbol	Description
$\mathbf{F}_I^{\mathrm{HF}}$, $F_{I,\alpha}^{\mathrm{HF}}$	Hellmann-Feynman forces and their components, Eq. (2.164)
$\mathbf{F}_I^{\mathrm{HF,0K}}$, $F_{I,\alpha}^{\mathrm{HF,0K}}$	$\mathbf{F}_I^{\mathrm{HF}}$ and $F_{I,\alpha}^{\mathrm{HF}}$ within the $\mathbf{D}^{\mathrm{0K}}$ approximation, Eq. (2.179)
$\mathcal{F}[\rho]$, $\mathcal{F}^{\mathrm{KS}}[\rho]$	main DFT functional, Eq. (2.48), and the Kohn-Sham functional, Eq. (2.55)
$\mathbf{G}$, $\mathbf{G}^{\mathrm{sc}}$	reciprocal lattice vector of the primitive unit cell and the supercell, Eqs. (2.78) and (2.121)
$\hat{H}$	main Hamiltonian including all interactions, Eq. (2.6); Ψ_ξ, E_ξ
$\hat{H}^{\mathrm{el}}$	electronic Hamiltonian, Eq. (2.15); ψ_ν, E_ν^{el}
$\hat{H}^{\mathrm{KS}}$	Kohn-Sham Hamiltonian, Eq. (2.63); φ_i, ϵ_i
$\hat{H}_\nu^{\mathrm{nuc}}$	nuclei Hamiltonian, Eq. (2.17); $\Lambda_{\nu,\mu}$, $E_{\nu,\mu}^{\mathrm{nuc}}$
$\hat{H}^{\mathrm{qh}}$, $\hat{H}^{\mathrm{3ord}}$, $\hat{H}^{\mathrm{4ord}}$	quasiharmonic, 3. and 4. order Hamiltonian, Eqs. (2.135), (2.209), and (2.210)
$\hat{H}^{\mathrm{rKS}}$	reduced Kohn-Sham Hamiltonian, Eq. (2.101)
M_I	mass of nucleus I
N_e, N_n	number of electrons and nuclei
N_V, N_T	number of V and T points used to parametrize free energy surfaces
N_k, N_k^{irr}	number of (irreducible) $\mathbf{k}$ vectors used for the k sampling
N^{high}, N^{low}	number of $\mathbf{k}$ vectors for a highly and low converged k sampling, used for the development of the UP-TILD method (Sec. 3.2)
N_{mesh}	number of mesh points (1-dim); used for estimations of the CPU requirement
N^{it}, $N^{\mathrm{it,red}}$	number of electronic iterations in a Kohn-Sham calculation and the reduced number (wave function extrapolation; see Sec. 2.3.6)
N^{p}	number of atoms in the perfect crystal [volume optimized approach; Eq. (3.9)]
N^{v}	number of atoms in the vacancy supercell
N^{LD}	number of steps in a Langevin dynamics simulation
N^{PW}	number of plane waves
$O(U^3)$	terms of third and higher order in the Taylor expansion of F^{el}
P	pressure
$\mathbf{P}_{\mathbf{G}^{\mathrm{sc}}}$, $P_{\mathbf{G}^{\mathrm{sc}},s}$	momentum of plane wave with vector $\mathbf{G}^{\mathrm{sc}}$ and its components (branches)
$\hat{\mathbf{P}}_{\mathbf{G}^{\mathrm{sc}}}$, $\hat{P}_{\mathbf{G}^{\mathrm{sc}},s}$	quantum mechanical version of $\mathbf{P}_{\mathbf{G}^{\mathrm{sc}}}$
$\mathbf{R}$	primitive lattice vector, Eq. (2.75)
$\mathbf{R}_I$, $\mathbf{R}_I^{\mathrm{0K}}$	coordinates of nuclei and their $T = 0$ K equilibrium positions
ΔR	displacement used for finite differences
S	entropy

Table A.2 (continued).

Symbol	Description
S^{qh}, $S^{\mathrm{qh,0K}}$	quasiharmonic entropy [Eq. (2.161)] and its $\mathbf{D}^{0\mathrm{K}}$ approximation
S^{f}	entropy of vacancy formation
T	temperature
T^{el}, T^{nuc}	electronic and nuclei temperature, Sec. 3.3.4
$\hat{T}^{\mathrm{el}}$, $\hat{T}^{\mathrm{nuc}}$	electronic and nuclei kinetic energy operator, Eqs. (2.7) and (2.8)
T^{m}	melting temperature
$\mathbf{U}_I$, $U_{I,\alpha}$	classical displacement of nucleus I out of $\mathbf{R}_I^{0\mathrm{K}}$ and its components; $\mathbf{U}(\mathbf{R}_I^{0\mathrm{K}})$ is also used
$\mathbf{U}_{\mathbf{G}^{\mathrm{sc}}}$, $U_{\mathbf{G}^{\mathrm{sc}},s}$	classical reciprocal displacement of nuclei and its components (branches)
$\hat{\mathbf{U}}_{\mathbf{G}^{\mathrm{sc}}}$, $\hat{U}_{\mathbf{G}^{\mathrm{sc}},s}$	quantum mechanical version of $\mathbf{U}_{\mathbf{G}^{\mathrm{sc}}}$
V	volume per atom; equivalent to volume of primitive unit cell
V_0^{eq}	equilibrium volume at $T = 0$ K
$V^{\mathrm{eq}}(T)$	thermal expansion of the equilibrium volume
$\hat{V}^{\mathrm{el}}$	electron-electron repulsion operator, Eq. (2.9)
$\hat{V}^{\mathrm{e\text{-}n}}$	electron-nucleus attraction operator, Eq. (2.11)
V^{nuc}	Ewald contribution, scalar, Eq. (2.50)
$\hat{V}^{\mathrm{nuc}}$	nucleus-nucleus repulsion operator, Eq. (2.10)
Z	full partition function including all excitations, Eq. (2.3)
Z_I	proton number of nucleus I
α	thermal expansion coefficient, Eq. (2.235)
β	thermodynamic beta, $\beta = 1/(k_{\mathrm{B}}T)$
ε	relative thermal expansion, Eq. (2.234)
ϵ_0	electric constant
ϵ_i, $\epsilon_{\nu,\mathbf{k}}$	eigenvalues of the Kohn-Sham Hamiltonian $\hat{H}^{\mathrm{KS}}$ in real and reciprocal space
ζ	friction parameter in a Langevin dynamics simulation
λ	coupling parameter in the thermodynamic integration method
ρ	electronic charge density, Eq. (2.45)
ρ^{at}	atomic charge density for an EAM parametrization
ρ^{aug}	augmentation electronic charge density (PAW method)
σ^{err}	statistical error in molecular/Langevin dynamics calculations, Eq. (2.202)
φ_i, $\varphi_{\nu,\mathbf{k}}$	eigenfunctions of the Kohn-Sham Hamiltonian $\hat{H}^{\mathrm{KS}}$ in real and reciprocal space

Continued.

Table A.2 (continued).

Symbol	Description
ψ_ν	eigenfunction of electronic Hamiltonian $\hat{H}^{\text{el}}$
$\omega_{\mathbf{q},s}$	phonon dispersion
$\omega_{\mathbf{G}^{\text{sc}},s}$, ω_i	phonon frequency at wave vector $\mathbf{G}^{\text{sc}}$ and branch s
$\omega_{\mathbf{G}^{\text{sc}},s}^{0\text{K}}$, $\omega_i^{0\text{K}}$	frequencies within the $\mathbf{D}^{0\text{K}}$ approximation
$\Delta\omega_{\mathbf{G}^{\text{sc}},s}^{\text{qm,ah}}$	quantum mechanical anharmonic phonon shift, Eq. (2.213)
$\Delta\omega_{\mathbf{G}^{\text{sc}},s}^{3\text{ord}}$, $\Delta\omega_{\mathbf{G}^{\text{sc}},s}^{4\text{ord}}$	third and fourth order phonon shift, Eqs. (2.214) and (2.215)
$\Lambda_{\nu,\mu}$	eigenfunctions of nuclei Hamiltonian $\hat{H}_\nu^{\text{nuc}}$
$\Phi^{3\text{ord}}$, $\Phi^{4\text{ord}}$	third and fourth order real space tensor, Eqs. (2.206) and (2.207), with components $\Phi_{I\alpha,J\beta,K\gamma}^{3\text{ord}}$ and $\Phi_{I\alpha,J\beta,K\gamma,L\delta}^{4\text{ord}}$ and with the Fourier transformed elements $\Phi_{\mathbf{G}^{\text{sc}}s,\,\mathbf{G}^{\text{sc}\prime}s\prime,\,\mathbf{G}^{\text{sc}\prime\prime}s\prime\prime}^{3\text{ord}}$ and $\Phi_{\mathbf{G}^{\text{sc}}s,\,\mathbf{G}^{\text{sc}\prime}s\prime,\,\mathbf{G}^{\text{sc}\prime\prime}s\prime\prime,\,\mathbf{G}^{\text{sc}\prime\prime\prime}s\prime\prime\prime}^{4\text{ord}}$, Eqs. (2.211) and (2.212)
Ψ_ξ	eigenfunctions of the main Hamiltonian $\hat{H}$
Ω	volume of a supercell
Ω_I	volume of a sphere around atom I; PAW and LAPW+lo method
Ω^{p}	volume of the perfect crystal in the volume optimized approach, Eq. (3.8)
Ω^{v}	volume of the vacancy supercell

Bibliography

[1] Z. Zhao, F. Roters, W. Mao, and D. Raabe, Adv. Eng. Mater. **3**, 984 (2001).

[2] D. Raabe and F. Roters, Int. J. Plasticity **20**, 339 (2004).

[3] Prof. W. Bleck, Head of the *Department of Ferrous Metallurgy* and Speaker of the Collaborative Research Center "Stahl – *ab initio*" (SFB761), University RWTH Aachen, Germany; private communication (04/19/2009).

[4] Prof. G. Gottstein, President of BV MatWerk, the German Umbrella Association of Materials Science, and Head of the *Institute of Physical Metallurgy and Metal Physics*, University RWTH Aachen, Germany; private communication (04/21/2009).

[5] Dr. H.-P. Schmitz, *Center of Materials Excellence*, ThyssenKrupp Steel AG; private communication (04/27/2009).

[6] Prof. J. Hirsch, *Research and Development Center*, Hydro Aluminium Deutschland GmbH; private communication (07/13/2009).

[7] L. Kaufman and H. Bernstein, *Computer Calculation of Phase Diagrams* (Academic Press, New York, 1970).

[8] T. B. Massalski, Metall. Trans. A **20**, 1295 (1989).

[9] P. E. A. Turchi, I. A. Abrikosov, B. Burton, S. G. Fries, G. Grimvall, et al., CALPHAD **31**, 4 (2007).

[10] J. L. Basdevant and J. Dalibard, *The Quantum Mechanics Solver: How to Apply Quantum Theory to Modern Physics* (Springer, Berlin / Heidelberg, 2006).

[11] K. Ohno, K. Esfarjani, and Y. Kawazoe, *Computational Materials Science: From Ab Initio to Monte Carlo Methods* (Springer, Berlin, 1999).

[12] P. Hohenberg and W. Kohn, Phys. Rev. **136**, B864 (1964).

[13] D. A. Ditmars, C. A. Plint, and R. C. Shukla, Int. J. Thermophys. **6**, 499 (1985).

[14] Y. S. Touloukian, R. K. Kirby, R. E. Taylor, and P. D. Desai, *Thermal Expansion: Metallic Elements and Alloys*, vol. 12 of *Thermophysical Properties of Matter* (IFI/Plenum, New York, 1975).

[15] G. N. Kamm and G. A. Alers, J. Appl. Phys. **35**, 327 (1964).

[16] F. A. Berezin and M. A. Shubin, *The Schrödinger Equation* (Kluwer Ac. Publ., Dordrecht / Boston / London, 1991).

[17] I. W. Sudiarta and D. J. W. Geldart, J. Phys. A: Math. Theor. **40**, 1885 (2007).

[18] G. Farin and D. Hansford, *Practical Linear Algebra: A Geometry Toolbox* (A K Peters, Wellesley, 2005).

[19] D. V. de Jager and J. T. Bradley, *PageRank: Splitting Homogeneous Singular Linear Systems of Index One*, ICTIR (2009), pp. 17-28.

[20] I. Ipsen and R. M. Wills, *Analysis and Computation of Google's PageRank*, 7th IMACS International Symposium on Iterative Methods in Scientific Computing, Fields Institute, Toronto, Canada, 5.-8. May 2005, URL http://www4.ncsu.edu/~ipsen/ps/slides_imacs.pdf.

[21] M. Born and J. R. Oppenheimer, Ann. Phys. **389**, 457 (1927).

[22] B. Grabowski, diploma thesis, Universität Paderborn (2005).

[23] D. Marx and J. Hutter, Mod. Methods Algorithms Quantum Chem. **1**, 301 (2000).

[24] M. Suzuki, Commun. Math. Phys. **57**, 193 (1977).

[25] J. Cao and B. J. Berne, J. Chem. Phys. **99**, 2902 (1993).

[26] N. D. Mermin, Phys. Rev. **137**, A1441 (1965).

[27] M. Levy, Proc. Nat. Acad. Sci. USA **76**, 6062 (1979).

[28] E. H. Lieb, Int. J. Quantum Chem. **24**, 243 (1983).

[29] R. G. Parr and W. Young, *Density-Functional Theory of Atoms and Molecules* (Oxford Science Publications, New York, 1989).

[30] M. J. Gillan, J. Phys. Condens. Matter **1**, 689 (1989).

[31] W. Kohn and L. J. Sham, Phys. Rev. **140**, A1133 (1965).

[32] M. Levy, Phys. Rev. A **26**, 1200 (1982).

[33] C. A. Ullrich and W. Kohn, Phys. Rev. Lett. **87**, 093001 (2001).

[34] H. Englisch and R. Englisch, Physica A **121**, 253 (1983).

[35] M. Levy and J. P. Perdew, in *Density Functional Methods in Physics*, edited by R. M. Dreizler and J. Providencia (Plenum Press, New York, 1985), pp. 11–30.

[36] K. Capelle, Braz. J. Phys. **36**, 1318 (2006).

[37] J. P. Perdew, K. Burke, and M. Ernzerhof, Phys. Rev. Lett. **77**, 3865 (1996).

[38] S. Curtarolo, D. Morgan, and G. Ceder, CALPHAD **29**, 163 (2005).

[39] J. P. Perdew and Y. Wang, Phys. Rev. B **45**, 13244 (1992).

[40] D. M. Ceperley and B. J. Alder, Phys. Rev. Lett. **45**, 566 (1980).

[41] U. von Barth, Phys. Scr. **T109**, 9 (2004).

[42] J. P. Perdew and S. Kurth, in *A Primer in Density Functional Theory*, edited by C. Fiolhais, F. Noqueira, and M. A. L. Marques (Springer, Berlin, 2003), pp. 1–55.

[43] N. W. Ashcroft and N. D. Mermin, *Solid State Physics* (Holt, Rinehart and Winston, New York, 1976).

[44] F. Bloch, Z. Phys. A **52**, 555 (1928).

[45] C. Kittel, *Introduction to Solid State Physics* (Wiley, 2004).

[46] G. Kresse and J. Furthmüller, Phys. Rev. B **54**, 11169 (1996).

[47] M. Bockstedte, A. Kley, J. Neugebauer, and M. Scheffler, Comput. Phys. Commun. **107**, 187 (1997).

[48] E. O. Brigham, *The Fast Fourier Transform* (Prentice-Hall, New York, 1974).

[49] S. Cottenier, *Density Functional Theory and the Family of (L)APW-Methods: A Step-by-Step Introduction* (Instituut voor Kern- en Stralingsfysica, K.U.Leuven, Belgium, 2002), URL http://www.wien2k.at/reg_user/textbooks/.

[50] S. Blügel and G. Bihlmayer, in *Computational Nanoscience: Do It Yourself*, edited by J. Grotendorst, S. Blügel, and D. Marx (John von Neumann Institite for Computing, Jülich, 2006), pp. 85–129.

[51] P. E. Blöchl, Phys. Rev. B **50**, 17953 (1994).

[52] N. A. W. Holzwarth, A. R. Tackett, and G. E. Matthews, Comput. Phys. Commun. **135**, 329 (2001).

[53] G. Kresse and D. Joubert, Phys. Rev. B **59**, 1758 (1999).

[54] M. Marsman and G. Kresse, J. Chem. Phys. **125**, 104101 (2006).

[55] M. Torrent, F. Jollet, F. Bottin, G. Zérah, and X. Gonze, Comput. Mater. Sci. **42**, 337 (2008).

[56] M. Fuchs and M. Scheffler, Comput. Phys. Commun. **119**, 67 (1999).

[57] L. Kleinman and D. M. Bylander, Phys. Rev. Lett. **48**, 1425 (1982).

[58] P. E. Blöchl, C. J. Först, and J. Schimpl, Bull. Mater. Sci. **26**, 33 (2003).

[59] P. M. A. Sloot, D. Abramson, A. V. Bogdanov, J. J. Dongarra, A. Y. Zomaya, et al., *Computational Science - ICCS 2003* (Springer, Berlin / Heidelberg / New York, 2003).

[60] M. Upmanyu, Z. T. Trautt, and B. B. Kappes, Mater. Sci. Forum **467-470**, 715 (2004).

[61] M. S. Daw, S. M. Foiles, and M. I. Baskes, Mater. Sci. Rep. **9**, 251 (1993).

[62] J. Mei and J. W. Davenport, Phys. Rev. B **46**, 21 (1992).

[63] R. R. Zope and Y. Mishin, Phys. Rev. B **68**, 024102 (2003).

[64] F. Ercolessi and J. B. Adams, Europhys. Lett. **26**, 583 (1994).

[65] B. Lee and K. Cho, Surf. Sci. **600**, 1982 (2006).

[66] K. Kadau, T. C. Germann, P. S. Lomdahl, R. C. Albers, J. S. Wark, et al., Phys. Rev. Lett. **98**, 135701 (2007).

[67] J. E. Drut, R. J. Furnstahl, and L. Platter, arXiv:0906.1463v2 [nucl-th] (2009), URL `arxiv.org/abs/0906.1463/`.

[68] D. C. Wallace, *Thermodynamics of Crystals* (Dover, New York, 1998).

[69] M. Born, *Dynamik der Kristallgitter* (Leipzig / Berlin, 1915).

[70] M. Born and K. Huang, *Dynamical Theory of Crystal Lattices* (Oxford, London, 1954).

[71] L. E. Ballentine, *Quantum Mechanics: A Modern Development* (World Scientific, London, 1998).

[72] K. Parlinski, Z. Q. Li, and Y. Kawazoe, Phys. Rev. Lett. **78**, 4063 (1997).

[73] H. Hellmann, *Einführung in die Quantenchemie* (Deuticke, Leipzig, 1937).

[74] R. P. Feynman, Phys. Rev. **56**, 340 (1939).

[75] J. Harris, R. O. Jones, and J. E. Müller, J. Chem. Phys. **75**, 3904 (1981).

[76] P. Pulay, Mol. Phys. **17**, 197 (1969).

[77] W. Nolting, *Statistische Physik*, Grundkurs Theoretische Physik (Springer, Berlin / Heidelberg, 2002).

[78] D. Frenkel and B. Smit, *Understanding Molecular Simulation: From Algorithms to Applications* (Academic Press, San Diego, 2002).

[79] J. M. Haile, *Molecular Dynamics Simulation: Elementary Methods* (Wiley, New York, 1997).

[80] S. Boeck et. al, http://www.sphinxlib.de/.

[81] L. Ismer, Ph.D. thesis, Universität Paderborn (2008).

[82] W. F. van Gunsteren and H. J. C. Berendsen, Mol. Phys. **45**, 637 (1982).

[83] L. Verlet, Phys. Rev. **159**, 98 (1967).

[84] A. Bergström, Normat **20**, 138 (1972).

[85] A. L. Fetter and J. D. Walecka, *Quantum Theory of Many-Particle Systems* (McGraw-Hill, New York, 1971).

[86] M. Zoli, Phys. Rev. B **41**, 7497 (1989).

[87] H. V. Keer, *Principles of the Solid State* (Wiley, New York, 1993).

[88] P. A. Varotsos and K. D. Alexopoulos, *Thermodynamics of Point Defects and Their Relation with Bulk Properties*, vol. 14 of *Defects in Solids* (North-Holland, Amsterdam, 1986).

[89] K. M. Carling, G. Wahnström, T. R. Mattsson, N. Sandberg, and G. Grimvall, Phys. Rev. B **67**, 054101 (2003).

[90] S. Nosé, J. Chem. Phys. **81**, 511 (1984).

[91] W. G. Hoover, Phys. Rev. A **31**, 1695 (1985).

[92] W. Nolting, *Spezielle Relativitätstheorie, Thermodynamik*, Grundkurs Theoretische Physik (Springer, Berlin / Heidelberg / New York, 2002).

[93] M. Forsblom, N. Sandberg, and G. Grimvall, Phys. Rev. B **69**, 165106 (2004).

[94] F. D. Murnaghan, Proc. Nat. Acad. Sci. USA **30**, 244 (1944).

[95] F. Birch, Phys. Rev. **71**, 809 (1947).

[96] P. Vinet, J. Ferrante, J. H. Rose, and J. R. Smith, J. Geophys. Res. [Solid Earth Planets] **92**, 9319 (1987).

[97] R. E. Cohen, O. Gülseren, and R. J. Hemley, Am. Mineral. **85**, 338 (2000).

[98] M. Methfessel and A. T. Paxton, Phys. Rev. B **40**, 3616 (1989).

[99] G. Kresse, M. Marsman, and J. Furthmüller, *Vienna Ab Initio Simulation Package: VASP the Guide*, URL `cms.mpi.univie.ac.at/vasp/vasp.pdf`.

[100] S. de Gironcoli, Phys. Rev. B **51**, 6773 (1995).

[101] K.-H. Hellwege and J. L. Olsen, eds., *Metals: Phonon States, Electron States and Fermi Surfaces*, Landolt-Börnstein (Springer, Berlin, 1981).

[102] P. Blaha, K. Schwarz, G. Madsen, D. Kvasnicka, and J. Luitz, *WIEN2k, An Augmented Plane Wave + Local Orbitals Program for Calculating Crystal Properties* (Technische Universität Wien, Austria, 2001).

[103] H. J. Monkhorst and J. D. Pack, Phys. Rev. B **13**, 5188 (1976).

[104] X. Gonze, J.-M. Beuken, R. Caracas, F. Detraux, M. Fuchs, et al., Comput. Mater. Sci. **25**, 478 (2002).

[105] X. Gonze, G.-M. Rignanese, M. Verstraete, J.-M. Beuken, Y. Pouillon, et al., Z. Kristallogr. **220**, 558 (2005).

[106] X. Gonze, Phys. Rev. B **55**, 10337 (1997).

[107] X. Gonze and C. Lee, Phys. Rev. B **55**, 10335 (1997).

[108] D. R. Hamann, Phys. Rev. B **40**, 2980 (1989).

[109] A. Debernardi, M. Alouani, and H. Dreyssé, Phys. Rev. B **63**, 064305 (2001).

[110] A. A. Quong and A. Y. Liu, Phys. Rev. B **56**, 7767 (1997).

[111] A. Siegel, K. Parlinski, and U. D. Wdowik, Phys. Rev. B **74**, 104116 (2006).

[112] V. L. Moruzzi, J. F. Janak, and K. Schwarz, Phys. Rev. B **37**, 790 (1988).

[113] P. A. Tipler, *Physik* (Spektrum, Heidelberg, 1994).

[114] J. A. Rayne, Phys. Rev. **118**, 1545 (1960).

[115] E. Walker, J. Ashkenazi, and M. Dacorogna, Phys. Rev. B **24**, 2254 (1981).

[116] R. E. Macfarlane, J. A. Rayne, and C. K. Jones, Phys. Lett. **20**, 234 (1966).

[117] J. H. Rose, J. R. Smith, F. Guinea, and J. Ferrante, Phys. Rev. B **29**, 2963 (1984).

[118] A. Eichler, K.-P. Bohnen, W. Reichardt, and J. Hafner, Phys. Rev. B **57**, 324 (1998).

[119] R. Heid, K.-P. Bohnen, K. Felix, K. M. Ho, and W. Reichardt, J. Phys. Condens. Matter **10**, 7967 (1998).

[120] S. Y. Savrasov and D. Y. Savrasov, Phys. Rev. B **54**, 16487 (1996).

[121] F. Favot and A. dal Corso, Phys. Rev. B **60**, 11427 (1999).

[122] S. Narasimhan and S. de Gironcoli, Phys. Rev. B **65**, 064302 (2002).

[123] L. Vočadlo, D. Alfè, G. D. Price, and M. J. Gillan, J. Chem. Phys. **120**, 2872 (2004).

[124] J. Xie, S. de Gironcoli, S. Baroni, and M. Scheffler, Phys. Rev. B **59**, 965 (1999).

[125] A. A. Quong, Phys. Rev. B **49**, 3226 (1994).

[126] R. Bauer, A. Schmid, P. Pavone, and D. Strauch, Phys. Rev. B **57**, 11276 (1998).

[127] T. Takezawa, H. Nagara, and N. Suzuki, Phys. Rev. B **71**, 012515 (2005).

[128] I. Y. Sklyadneva, A. Leonardo, P. M. Echenique, S. V. Eremeev, and E. V. Chulkov, J. Phys. Condens. Matter **18**, 7923 (2006).

[129] R. Heid, K.-P. Bohnen, and K. M. Ho, Phys. Rev. B **57**, 7407 (1998).

[130] L. Vočadlo and D. Alfè, Phys. Rev. B **65**, 214105 (2002).

[131] A. dal Corso, J. Phys. Condens. Matter **20**, 445202 (2008).

[132] Y. S. Touloukian and E. H. Buyco, *Specific Heat - Metallic Elements and Alloys*, vol. 4 of *Thermophysical Properties of Matter* (IFI/Plenum, New York, 1970).

[133] P. E. A. Turchi, V. Drchal, and J. Kudrnovsky, Phys. Rev. B **74**, 064202 (2006).

[134] D. L. Waldorf and G. A. Alers, J. Appl. Phys. **33**, 3266 (1962).

[135] W. C. Overton and J. Gaffney, Phys. Rev. **98**, 969 (1955).

[136] J. R. Neighbours and G. A. Alers, Phys. Rev. **111**, 707 (1958).

[137] D. K. Hsu and R. G. Leisure, Phys. Rev. B **20**, 1339 (1979).

[138] S. M. Collard and R. B. McLellan, Acta Metall. Mater **40**, 699 (1992).

[139] Thermo-Calc Software, Stockholm, URL `http://www.thermocalc.com/`.

157

[140] A. van de Walle and G. Ceder, Phys. Rev. B **59**, 14992 (1999).

[141] A. dal Corso and S. de Gironcoli, Phys. Rev. B **62**, 273 (2000).

[142] M. Born and E. Brody, Z. Phys. **6**, 132 (1921).

[143] T. E. Pochapsky, Acta Metall. **1**, 747 (1953).

[144] Y. Kraftmakher, Phys. Rep. **299**, 79 (1998).

[145] C. R. Brooks and R. E. Bingham, J. Phys. Chem. Solids **29**, 1553 (1968).

[146] R. C. Shukla, C. A. Plint, and D. A. Ditmars, Int. J. Thermophys. **6**, 517 (1985).

[147] D. Alfè, G. A. de Wijs, G. Kresse, and M. J. Gillan, Int. J. Quantum Chem. **77**, 871 (2000).

[148] P. J. H. Denteneer and J. M. Soler, J. Phys. Condens. Matter **3**, 8777 (1991).

[149] T. Gomoll, diploma thesis, Technische Fachhochschule Berlin (2008).

[150] P. H. Dederichs, C. Lehmann, H. R. Schober, A. Scholz, and R. Zeller, J. Nucl. Mater. **69/70**, 176 (1978).

[151] A. De Vita and M. J. Gillan, J. Phys. Condens. Matter **3**, 6225 (1991).

[152] R. Benedek, L. H. Yang, C. Woodward, and B. I. Min, Phys. Rev. B **45**, 2607 (1992).

[153] K. M. Carling, G. Wahnström, T. R. Mattsson, A. E. Mattsson, N. Sandberg, et al., Phys. Rev. Lett. **85**, 3862 (2000).

[154] R. O. Simmons and R. W. Balluffi, Phys. Rev. **117**, 52 (1960).

[155] T. Hehenkamp, J. Phys. Chem. Solids **55**, 907 (1994).

[156] W. Triftshäuser, Phys. Rev. B **12**, 4634 (1975).

[157] E. D. Eastman, A. M. Williams, and T. F. Young, J. Am. Chem. Soc. **46**, 1178 (1924).

[158] S. Umino, Sci. Rep. Tohoku Imp. Univ., Ser. 1 **15**, 597 (1926), (cited from Ref. [168]).

[159] A. Avramescu, Z. Tech. Phys. (Leipzig) **20**, 213 (1939).

[160] K. Honda and Y. Okubo, Sci. Rep. Tohoku Imp. Univ., Ser. 1 **13**, 101 (1924), (cited from Ref. [14]).

[161] F. L. Uffelmann, Philos. Mag. **10**, 633 (1930), (cited from Ref. [14]).

[162] F. C. Nix and D. MacNair, Phys. Rev. **60**, 597 (1941).

[163] A. J. C. Wilson, Proc. Phys. Soc. **54**, 487 (1942).

[164] R. A. McDonald, J. Chem. Eng. Data **12**, 115 (1967).

[165] A. J. Leadbetter, J. Phys. C: Solid State Phys. **1**, 1481 (1968).

[166] U. Schmidt, O. Vollmer, and R. Kohlhaas, Z. Naturforsch. A **A25**, 1258 (1970).

[167] D. I. Marchidan and M. Ciopec, Rev. Roum. Chim. **15**, 1005 (1970), (cited from Ref. [168]).

[168] P. D. Desai, Int. J. Thermophys. **8**, 621 (1987).

[169] Y. Takahashi, T. Azumi, and Y. Sekine, Thermochim. Acta **139**, 133 (1989).

[170] R. M. Nicklow and R. A. Young, Phys. Rev. **129**, 1936 (1963), (cited from Ref. [14]).

[171] P. G. Strelkov and S. I. Novikova, Prib. Tekh. Eksp. (USSR) **5**, 105 (1957), (cited from Ref. [14]).

[172] P. D. Pathak and N. G. Vasavada, J. Phys. C: Solid State Phys. **3**, L44 (1970), (cited from Ref. [14]).

[173] B. von Guérard, H. Peisl, and R. Zitzmann, Appl. Phys. **3**, 37 (1974), numerical differentation of the given experimental expansion data; strongly scattering points were taken out.

[174] F. R. Kroeger and C. A. Swenson, J. Appl. Phys. **48**, 853 (1977).

[175] K. O. McLean, Ph.D. thesis, Iowa State University (1969), (cited from Ref. [14]).

[176] M. Zoli, Philos. Mag. Lett. **62**, 203 (1990).

[177] O. F. Sankey and D. J. Niklewski, Phys. Rev. B **40**, 3979 (1989).

[178] G. Grimvall, Physics **2**, 28 (2009).

[179] F. Perrot and M. W. C. Dharma-Wardana, Phys. Rev. A **30**, 2619 (1984).

[180] D. G. Kanhere, P. V. Panat, A. K. Rajagopal, and J. Callaway, Phys. Rev. A **33**, 490 (1986).

[181] D. C. Langreth, M. Dion, H. Rydberg, E. Schröder, P. Hyldgaard, and B. I. Lundqvist, Int. J. Quantum Chem. **101**, 599 (2004).

[182] F. Körmann, A. Dick, B. Grabowski, B. Hallstedt, T. Hickel, and J. Neugebauer, Phys. Rev. B **78**, 033102 (2008).

[183] F. Körmann, A. Dick, T. Hickel, and J. Neugebauer, Phys. Rev. B **79**, 184406 (2009).

[184] W. A. Counts, M. Friak, D. Raabe, and J. Neugebauer, Acta Mater. **57**, 69 (2009).

[185] M. Friak, W. A. Counts, D. Raabe, and J. Neugebauer, Phys. Status Solidi B **245**, 2636 (2008).

[186] I. Mills, T. Cvitas, K. Homann, N. Kallay, and K. Kuchitsu, *Quantities, Units and Symbols in Physical Chemistry* (Blackwell Science, 1993).

[187] P. Giannozi, S. Gironcoli, P. Pavone, and S. Baroni, Phys. Rev. B **43**, 7231 (1991).

List of Publications

1. B. Grabowski, L. Ismer, T. Hickel, and J. Neugebauer, "*Ab initio* up to the melting point: Anharmonicity and vacancies in aluminum", *Phys. Rev. B* **79**, 134106 (2009).
   See also: G. Grimvall, *Physics* 2, **28** (2009).

2. J. Neugebauer, B. Grabowski, F. Körmann, A. Dick, J. von Pezold, M. Friak, and T. Hickel, "*Ab initio* based multiscale modeling of engineering materials: From a predictive thermodynamic description to tailored mechanical properties", *Asia Steel 2009 Proceedings* (2009).

3. T. Hickel, A. Dick, B. Grabowski, F. Körmann, and J. Neugebauer, "Steel design from fully parameter-free *ab initio* computer simulations", *Steel Res. Int.* **80**, 4 (2009).

4. D. Lencer, M. Salinga, B. Grabowski, T. Hickel, J. Neugebauer, and M. Wuttig, "A map for phase-change materials", *Nat. Mater.* **7**, 972 (2008).

5. F. Körmann, A. Dick, B. Grabowski, B. Hallstedt, T. Hickel, and J. Neugebauer, "Free energy of bcc iron: Integrated *ab initio* derivation of vibrational, electronic, and magnetic contributions", *Phys. Rev. B* **78**, 033102 (2008).

6. T. Hickel, M. Uijttewaal, B. Grabowski, and J. Neugebauer, "Determination of symmetry reduced structures using a soft phonon analysis for magnetic shape memory alloys", *J. Phys.: Condens. Matter* **20**, 064219 (2008).

7. B. Grabowski, T. Hickel, and J. Neugebauer, "*Ab initio* study of the thermodynamic properties of nonmagnetic elementary fcc metals: Exchange-correlation-related error bars and chemical trends", *Phys. Rev. B* **76**, 024309 (2007).